MAGNESIUM ALLOY PARTICULATES USED AS PIGMENTS IN METAL-RICH PRIMER SYSTEM FOR AA2024 T3 CORROSION PROTECTION

A Dissertation
Submitted to the Graduate Faculty
of the
North Dakota State University
of Agriculture and Applied Science

By

Hong Xu

In Partial Fulfillment of the Requirements
for the Degree of
DOCTOR OF PHILOSOPHY

Major Department:
Coatings and Polymeric Materials

December 2010

Fargo, North Dakota

North Dakota State University
Graduate School

Title

Magnesium Alloy Particulates used as Pigments in Metal-rich Primer Systems for AA2024-T3 Corrosion Protection

By

Hong Xu

The Supervisory Committee certifies that this ***disquisition*** complies with North Dakota State University's regulations and meets the accepted standards for the degree of

DOCTOR OF PHILOSOPHY

ABSTRACT

Xu, Hong, Ph. D., Department of Coatings and Polymeric Materials, College of Science and Mathematics, North Dakota State University, December 2010. Magnesium Alloy Particulates Used as Pigments in Metal-rich Primer System for AA2024 T3 Corrosion Protection. Major Professor: Dr. Gordon P. Bierwagen.

As an alternative to the present toxic chromate-based coating system now in use, the Mg-rich primer technology has been designed to protect Al alloys (in particular Al 2024 T3) and developed in analogy to Zn-rich primers for steel substrate. As an expansion of this concept, metal-rich primer systems based on Mg alloy particles as pigments were studied.

Five different Mg alloy pigments, AM60, AZ91B, LNR91, AM503 and AZG, were characterized by using the same epoxy-polyamide polymer as binder, a same dispersion additive and the same solvent. Different Mg alloy-rich primers were formulated by varying the Mg alloy particles and their pigment volume concentrations (PVC).

The electrochemical performance of each Mg alloy-rich primer after the cyclic exposure in Prohesion chamber was investigated by electrochemical impedance Spectroscopy (EIS). The results indicated that all the Mg alloy-rich primers could provide cathodic protection for AA 2024 T3 substrates. However, the Mg alloys as pigments in metal-rich primers seemed to exhibit the different anti-corrosion protection performances, such as the barrier properties, due to the different properties of these pigments. In these investigations, multiple samples of each system were studied and statistical methods were used in analyzing the EIS data. From these results, the recommendation for improved EIS data analysis was made.

CPVC studies were carried out on the Mg alloy-rich primers by using three Mg alloy pigments, AM60, AZ91B and LNR91. A modified model for predicting CPVC is proposed, and the results showed much better agreement between the CPVC values obtained from the experimental and mathematical methods. Using the data from the AM60 alloy pigment system, an estimate of experimental coarseness was done on a coating system, the first time such an estimate has been performed.

By combining various surface analysis techniques, such as scanning electron microscopy (SEM), X-ray photoelectron spectroscopy (XPS) and confocal Raman microscopy, the oxidation products formed after exposure were identified. It was found that variation of Al content in Mg alloy could significantly affect the pH of the microenvironment in the primer films and result in the formation of various oxidation products.

ACKNOWLEDGEMENTS

Here are the many people whose help and support made this dissertation possible:

I would like to show my deepest gratitude to my supervisor, Dr. Gordon Bierwagen, for his guidance, support, and encouragement throughout my Ph. D. study and dissertation writing. My greatest gratitude is to Dr. Dante Battocchi who supported and helped me at every stage of my study.

And it is to these committee members, Dr. Dennis Tallman, Dr. Stuart Croll, and Dr. Zhili Gao, who I would like to give thanks for their advice and support.

To these people I would like to express my gratitude, Heidi Docktor, Scott Payne, Dr. Jinhai Wang, Dr. Xiwen Cai, and Dr. Rebecca de Rosa, who helped me with the experimentation and instrumentation.

It is my pleasure to thank all the faculties, office staff, graduate, and undergraduate students in the Department of Coatings and Polymeric Materials, for providing a wonderful environment for me to learn and grow.

This Ph. D. study was supported by the Air Force Office of Scientific Research under Grant No. 49620-02-1-0398.

Lastly, I wish to dedicate this dissertation to my parents, Jiasong Xu and Songliu Zhao, my husband, Jinhai Wang, and my son, Yiou Wang, for their love and support to me.

TABLE OF CONTENTS

LIST OF TABLES

LIST OF FIGURES

CHAPTER 1. CORROSION PROTECTION FOR THE STRUCTURAL AL ALLOYS (AA2024 T3)

1.1. Structural aluminum alloys for aircraft

Aluminum (Al) and Al alloys have been used in the aeronautical industry since 1900's [1] and become the major structural materials because of their excellent mechanical properties, e.g. high strength, superior toughness, great fatigue resistance, and high strength-to-weight ratio, which satisfy the specific requirements of aircraft materials. [1]

Al alloys have many similar characteristics as the pure Al, such as the light weight (one-third density of steel), the good ductility for extrusion molding, casting or being easily drawn. [1] To be superior to the pure Al, Al alloys have the significantly improved strength [2] and fragile/fatigue resistance, and can withstand high tension and large compression. These distinctive properties make Al alloys be important to the civil engineering construction and aeronautical industry. [2]

The dramatic improvement of the mechanical performance of Al alloys is mainly attributed to the enhanced fabrication processes and the addition of some particular elements, such as Si, Zn and/or Cu. AA2024 T3 is one of the most widely used Al alloys in aircraft industry. [3] AA2024 T3 contains about 4.5% Cu as the secondary element. From Table 1-1, [4] it can be seen that AA2024 T3 has lower density than steel, and has much higher tensile strength/yield strength in comparison to the pure Al. Moreover, the excellent fatigue resistance of AA2024 T3 is absent for the pure Al and many other Al alloys.

The dramatically improved strength of AA2024 T3 is due to its complex metallurgical microstructure. Figure 1-1 shows a SEM image of the microstructure of AA2024 T3. [5]

The dark and bright areas represent the Cu-rich region and Al-rich region, respectively. The black lines are the grain boundaries. The existence of the intermetallic phase separation in the microstructure of AA2024 T3 can be clearly seen.

Table 1-1. Typical mechanical properties of structural metals and alloys* (Data adapted from Kaufman, J.G., **1999**, *ASM International* and Sun, C.T., **1998**, John Wiley & Sons, INC.)

Materials	**Steel**	**Al**	**Al alloy**		**Ti**
Series No. (ANSI)	AISI 4340	1100	2024 T3	7075-O	Ti-6Al-4V
Density (g/cm^3)	7.8	2.7	2.8	2.8	4.46
Tensile strength (MPa)	1790	90	485	550	925
Yield strength (MPa)	1483	34	345	485	869
Modulus of elasticity (GPa)	200	68	72	71	110

*: Testing temperature is 25°C

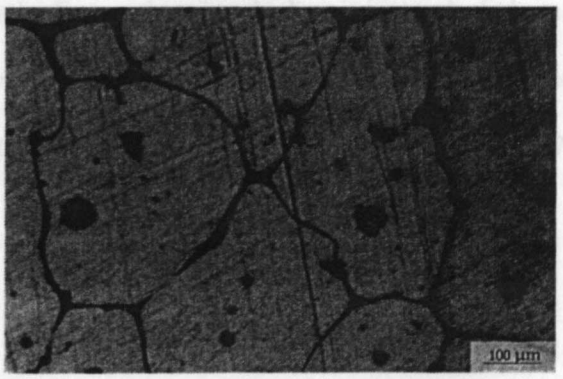

Figure 1-1. Microstructure of AA2024 T3 (Copied from F. M. Khoshnaw, *Materials and Corrosion*, **2007**, 58, 345.)

It is widely accepted that the network formed by the grain boundaries of $CuAl_2$ precipitates contributes the excellent mechanical properties to AA2024 T3. [2] Such metallurgical microstructure of AA2024 T3 is obtained through a particular fabrication

process: a cold precipitation hardening of $CuAl_2$ which is derived from a heat treatment followed by a natural aging (aging at room temperature). [2] In fact, the metallurgical structure and mechanical properties of Al alloys can be significantly affected by heat treatments, quenching temperatures and aging times. [5]

1.2. Corrosion resistance of AA2024 T3

Corrosion is a universal phenomenon that can occur to almost all the metals. Generally speaking, corrosion refers to the chemical reactions between metals/alloys and the service environments in which water and/or oxygen are present. Usually two coupled electrochemical reactions can be used to describe a corrosion mechanism. One is anodic reaction, in which the metal atoms tend to lose their electrons to form more stable oxide compounds. [6] The anodic reaction can be expressed by the following form: [7]

$$M \rightarrow M^{n+} + ne^-$$

The other one is cathodic reaction, in which some adsorbed chemical species from the aqueous solution obtain the electrons via metal surface. The typical reductions occurring in neutral, acid or oxidant-absent solutions are of the following forms: [7]

$$O_2 + 2H_2O + 4e^- \rightarrow 4OH^- \qquad \text{(neutral solution)}$$

$$2H^+ + 2e^- \rightarrow H_2 \uparrow \qquad \text{(acid solution)}$$

$$2H_2O + 2e^- \rightarrow H_2 \uparrow + 2OH^- \qquad \text{(solution lack of oxidants)}$$

For most metals, corrosion occurs spontaneously under most conditions, though the corrosion rates are variable and significantly depended on the inherent activities of metals and the conditions of the service environment. For example, Magnesium (Mg) is an active

metal, and the oxidation of Mg with oxygen or water occurs intensively. But the corrosion of steel usually occurs at a much lower rate in comparison to Mg. For some metals/alloys, such as Al, Ni, and stainless steel, a compact and stable passive layer can be formed over the surface to inhibit the further oxidation of metals. Therefore, passivation can effectively prevent some metals/alloys from the corrosive attacks. Under the normal atmospheric conditions without the presence of Cl^- anions, pure Al needs no corrosion protection. [6, 7]

However, corrosion easily occurs when two or more dissimilar metals are electrically combined together as a galvanic couple and further exposed to the corrosive environment. The difference of the electrical potentials between two dissimilar metals will make the more active metal preferentially corrode at a higher corrosion rate.

In Table 1-2, a galvanic series is listed in which the tendency of a metal/alloy to corrosion is shown in sequence of activity in sea water. [8] A metal will be preferentially oxidized (corrode) if it is located in the top of the series (closer to the "Active") and vice versa. When two metals are coupled together, the farther they are apart from each other in the series, the more severely is the corrosion occurred to the anodic metal. In addition, some metals, such as Al, could lose their passivation protection due to the galvanic coupling with a nobler metal.

In AA2024 T3, most Cu is present in the grain boundaries as the $CuAl_2$ precipitates during the alloy solidification process. The phase separations of Cu-rich regions/grain boundaries and Al-rich regions in the microstructure of AA2024 T3 build up the galvanic couples, [9] as shown in Figure 1-1, and make AA2024 T3 be very susceptible to intergranular corrosion. [2]

A more detailed illustration of the phase separations in the microstructure of AA2024

T3 is shown in Figure 1-2. [10] It can be seen that various intermetallic precipitates, e.g. Al-Cu-Mn-Fe or Al_2-Cu-Mg, are present in the microstructure of AA2024 T3. In fact, the separated phases possess different potentials. Since Cu is much nobler in comparison to Al in the galvanic series, the Cu-rich crystallites embedded in the Al-rich matrix act as cathodes and make the Al anodes corrode more intensively when AA2024 T3 is exposed to corrosive environment. As a result, the Al oxidation products gradually accumulate at the interfaces along the grain boundaries. To a certain extent, the high lifting stress caused by the volume expansions of the accumulated Al oxidation products can break down the grain boundaries and result in delamination and exfoliation. [7] Eventually, the local structural failure caused by corrosion can significantly reduce the strength of AA2024 T3.

Table 1-2. The Galvanic table. (Copied from *Army Missile Command Report RS-TR-67-1*, "Practical Galvanic Series".)

Active End (Anodic)
Magnesium
Mg alloy AZ-31B
Zinc (hot-dip, die cast, or plated)
Al 1100-0
Al 7075-T6
Al 2024-T4
Steel 1010
Iron (cast)
Copper (plated, cast, or wrought)
Nickel (plated)
Chromium (Plated)
Stainless steel 410 (active)
Silver
Gold
Graphite
Noble End (Less Active, Cathodic)

1.3. Significance of corrosion protection for AA2024 T3

As the major structural material of aircraft, AA2024 T3 needs corrosion protection to maintain its excellent mechanical properties. In some cases of aircraft accidents, the occurrence of corrosion on some parts of aircraft, even only limited in a small area, sooner or later induced the serious fatigue or stress corrosion cracks. [11] The consequences of the structure failure of aircraft are disastrous, since it will put the humans and public safety at risk. [9, 11] Therefore, the regular inspection, repairs or replacements of the corroded components of aircraft are requisite in aeronautical industry in order to eliminate any hidden danger. Actually, the improvement of the anti-corrosion performance of AA2024 T3 becomes one of the major tasks for aeronautical industry. [12]

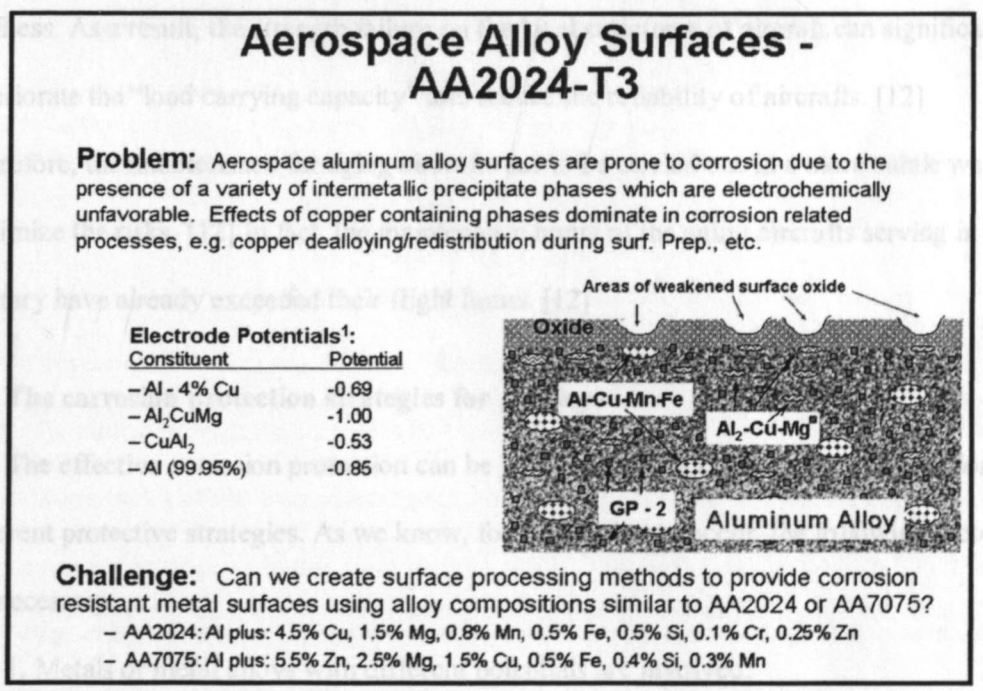

Figure 1-2. Illustration of phase separation in the microstructure of aerospace material AA2024 T3. (Copied from G. Bierwagen, *J. Coat. Technol. Res.*, **2008**, 5, 133.)

The spending on corrosion protection for aircrafts by aeronautical industry is large and

still keeps increasing year after year. In 1996, the estimated annual cost related to the corrosion protection of aircrafts was about $2.2 billion, of which $1.7 billion was used for corrosion maintenance, including corrosion inspection, corroded structure removal, repairing and replacement. [13] Also, the spending on developing new materials with better corrosion resistance and training more experts with the latest corrosion protection knowledge and techniques are also increased extensively. [13]

Furthermore, the costs on the maintenance and replacement for the aging aircrafts are even larger. In United States, one fourth of aircrafts in service are older than 20 years, which is approaching the limitation of service lifetime. [12] The corrosion and degradation of structural materials could make the aging aircrafts lose their original strength and stiffness. As a result, the strength failure on the local structures of aircraft can significantly deteriorate the "load carrying capacity" and reduce the reliability of aircrafts. [12] Therefore, the maintenance for aging aircrafts has to be carried out in a more subtle way to minimize the risks. [12] In fact, the maintenance hours of the aging aircrafts serving in military have already exceeded their flight hours. [12]

1.4. The corrosion protection strategies for Al alloys

The effective corrosion protection can be provided for aircrafts via the combination of different protective strategies. As we know, for a corrosion to occur, the following factors are necessary:

1. Metals or metal alloys with different potentials are involved;
2. Good electrical conductivity is present between the dissimilar metals;
3. Electrolyte is presented to complete the external circuit for corrosion. Some aggressive ions, such as Cl^-, can de-passivate the protective surface layer of Al_2O_3

and result in corrosion.

Therefore, corrosion can be effectively retarded by eliminating any factor mentioned above. In fact, the most commonly used corrosion protection strategies for aircraft are also based on the similar fundamentals, which include, for example: [9]

Cleanliness: keeping aircraft surface to be clean and dry is a very efficient way for corrosion control. A metallic surface without dirt, grease, physical damage, corrosion dust, porous oxide product or the collection of moisture will significantly reduce the risks of corrosion due to the absence of electrolyte.

Surface treatment: surface treatments via electrolytic or chemical processes can provide Al alloys the nonporous oxide layers, such as anodized or chromic acid passive oxide films. These passivation layers can isolate Al alloys from the aggressive environment to retard the occurrence of corrosion. [14, 15]

Protective coatings: the most common approach for corrosion protection is to use different coating systems as the surface finishes. More than for the purpose of aesthetic effects, organic coating can act as a protective barrier to reduce the contact between metals and environment. For example, aircraft topcoat can effectively block the penetration of electrolyte and somewhat the diffusion of O_2 to reach the metal surface due to its excellent barrier properties. For the susceptible areas, e.g. the surface of lap joints, fasteners, bolts and screws, the protective coatings are usually applied on the faying surfaces to avoid the direct contact between the different metals. For instance, the uses of $SrCrO_4$ primer or vinyl tape can break down the possible circuit of corrosion via inhibition or insulation.[9] The main protection mechanism of the $SrCrO_4$ pigmented primer is that, when water penetrates into a primer film and reaches to the interface between the $SrCrO_4$ primer and Al alloy

substrate, the chromate ions can be released from $SrCrO_4$ primer to impede corrosion via inhibiting the surface of Al alloy. [16, 17]

1.5. Challenges of corrosion protection for AA2024 T3

Corrosion protection is a greater issue than simply dealing with the corrosion of metals and alloys. Actually, a wide range of factors are involved in corrosion protection. First, the straightest impact of corrosion protection is to achieve the maximum economic benefits. The decrease of corrosion rate can extend the service time of aircraft and reduce the spending on inspections and maintenances; second, corrosion protection is important for public safety, since corrosion can cause the local structure failure of aircraft and may imperil the security of lives and property; third, both of the fundamental research of corrosion and the new technologies development are of importance to corrosion protection because the thorough understanding of raw materials, service environment and corrosion mechanism can help to develop the novel protection techniques and vice versa; fourth, the replacement for the toxic coating systems always has the top priority for the sack of public safety and the development of the environmental-friendly alternative is imperative.

Therefore, a desirable coating system for AA2024 T3 corrosion protection is able to fulfill the requirements described as follows:

1. To be environmental-friendly, including non-toxic and volatile organic compound (VOC)-compliant;
2. To exhibit excellent anticorrosion performance even under harsh conditions;
3. To have superb mechanical properties and durability to withstand mechanical damages and weathering degradation, e.g. good adhesion with substrates, excellent flexibility and high toughness;

4. To be cost-efficient.

However, it is a big challenge for coating industry to develop an effective coating system which meets all the necessities, especially for the requirements of non-toxicity and low VOC. Traditionally, a large amount of solvent is used in coating formulation to help achieve the expected performance on application and corrosion protection. As the global and nationwide legislation start to limit the amounts of VOC in coating formulation, new coating systems, such as powder coatings and waterborne coatings, have been developed. However, the corrosion protection efficiencies of these new coating systems are not as good as those of solvent-borne coatings when exposed to the harsh conditions.

Furthermore, to develop an alternative to the carcinogenic chromate primer system for AA2024 T3 corrosion protection is an even harder assignment. In aircraft industry, the corrosion protection of Al alloys has relied significantly on the coating systems in which chromates are used as pigments ($SrCrO_4$ pigments) in the primer systems and as the major component in the substrate pretreatment. [18] However, it has been realized that hexavalent chromium Cr(VI) is a human carcinogen and also an precursor to many diseases, e.g. asthma, ulceractions of skin or nasal septum and dermatitis. [17, 19] The handling of Cr (VI)-containing materials has been restricted by OHSA regulations. In Europe, Cr (VI) is one of the six restricted substances which have been banned under Restriction of Hazardous Substances (RoHS) since 2006. [20] Therefore, it becomes considerably costly for aircraft manufacturers, users, or military services [21, 22] to handle the production, application and remediation of the chromate-based primer systems due to the environmental cleanup and the preventive measures required for employees. [23]

In the report of "Aging of U.S. Air Force Aircraft" in 1997, one of the research

recommendations proposed by the committee was to develop "environmentally compatible protective coatings to replace the hazardous materials (e.g. chromates)".[12] Thus, it is an important task for aeronautical industry to develop an alternative to chromate conversion coating. The new aircraft coating system is expected to provide the excellent anti-corrosion performance for Al alloys, to be environmental-friendly, to have good adhesion with the substrate and topcoat and to be easily applied. Also, there is no Cr-containing pretreatment needed for such new coating system. [18, 22, 24, 25]

In fact, in the past decade, many Cr-free candidates have been developed in order to replace the chromate-based primer or pretreatment systems, such as sol-gel pretreatment or cold-cathode plasma-polymerized pretreatment. [26] However, none of them is the true Cr-free protection system, since they still need somewhat Cr-based pretreatment or primer as the auxiliary system in order to obtain the sufficient protection performance. [27]

1.6. Mg-rich primer system for corrosion protection of AA 2024 T3

Mg-rich primer coatings were first developed by Nanna, Bottocchi and Bierwagen at North Dakota State University in 2002. [28-31] In analogy to Zn-rich primers, Mg-rich primer systems have been designed to provide cathodic protection for Al alloy substrate. Mg is more active than Al alloy. [8] Principally, when Mg and Al alloy electrically contact with each other and both of them are exposed to electrolyte, the Mg (more active metal) may work as anode and make Al alloy (nobler metal) be the cathode. [21, 27-30, 32-34] The effective cathodic protection provided by Mg-rich primer has been achieved based on the following factors: [27]

1. Various Mg powders are commercially available. The presence of MgO on the surface of Mg particles makes Mg powder safe to handle; [31]

2. Mg powder is more active than Al and Al alloys and can be used to provide cathodic protection to Al alloys; [28]
3. The organic or inorganic binders used for Mg-rich primer system have provided good adhesion for the entire system and also be stable under alkaline conditions; [31, 35]
4. Mg-rich primer systems have been formulated near CPVC to ensure the good physical contact among Mg particles and also between Mg particles and Al alloy. [31] The necessary conductivity between Mg particles can be obtained when Mg-rich primer is wetted by the penetrated electrolyte.
5. Cathodic protection will be activated when damage of coating system occurs.

So far, Mg-rich primer technology developed in NDSU provides the only true Cr-free corrosion protective coating system, which includes Mg-rich primer and aerospace topcoat and a non-chromate pretreatment. In addition, the performance of the whole Mg-rich system at current formulation seems to equal or even to go beyond the ones of full chromate primer system. [27]

1.7. Goals of this study

The success of Mg-rich primer technology is a milestone in the development of Cr-free alternatives for Al alloy anti-corrosion protection. Moreover, the corrosion protection mechanisms have been studied to obtain a complete understanding of Mg-rich primer system. [21, 28, 32-37]

As the extension of Mg-rich primer technology, [27] the studies of the metal-rich primer systems by using different Mg alloy particles to replace the pure Mg pigment have been carried out in this Ph.D. project.

In the studies of the new Mg alloy pigmented primer systems, several goals have been addressed and studied, they include:

1. The formulation of new Mg alloy-rich primers using various Mg alloy particles as pigment in an epoxy-polyamide binder system;
2. The study of the cathodic protection performance of the Mg alloy-rich primers with different Mg alloys particulates or formulated at various PVC for AA2024 T3 substrate;
3. The studies of the CPVC measurement for Mg alloy-rich primer system and the influences of the various Mg ally particles' properties on the CPVCs;
4. The possible protection mechanisms study of Mg alloy-rich primer systems based on EIS and ENM measurements;
5. The identification of the oxidation products of Mg alloy-rich primers formed during the exposure in Prohesion chamber using different surface analysis methods, such as SEM, EDX, XPS and confocal Raman microscopy.

However, three things needed to be stated before reporting the work of Mg alloy-rich primer system. First, the Mg alloy particulates being investigated in this work are used as received. There was no any modification done to the Mg alloy particulates in this lab.

Second, the major focus of this work is to study the influences of different Mg alloy particulates on the corrosion protection performance of Mg alloy-rich primers rather than to find an optimal Mg alloy-rich primer system. Thus, a constant epoxy-polyamide binder system was used for the formulations of Mg alloy-rich primer systems, and the influences of different binder systems on the performance of Mg alloy-rich primer systems are beyond this Ph. D study.

Third, the raw material supply of each type of Mg alloy pigment was limited by the availability of Mg alloy in particle form from manufactures. For example, the total weight of AM60, AZ91B, LNR91, AM503 and AZG were about 1500 g, 1200 g, 1000 g, 250g and 250 g, respectively. As a result, some studies were subsequently limited due to the short of supply.

1.8. References

1 H. Buhl, *Advanced Aerospace Materials*, ed. B. Ilschner and K. Russell, **1992**, Berlin, Srigner-Verlag.

2 F. M. Mazzolani, *Aluminum Alloy Structures*, **1985**, Pitman Advanced Publishing Program.

3 C. Dole, *Fundamentals of aircraft material factors*, Second ed, **1989**, IAP, Inc.

4 J. G. Kaufman, *Properties of Aluminum alloys: Tensile, creep, and fatigue data at high and low temperatures*, **1999**, ASM International.

5 F. M. Khoshnaw and R. H. Gardi, *Materials and Corrosion* **2007**, 58, 345.

6 D. Talbot and J. Talbot, *Corrosion science and technology*, **1998**, CRC Press LLC.

7 D. A. Jones, *Principles and prevention of corrosion*, **1996**, Prentice-Hall, Inc.

8 *Army Missile Command Report RS-TR-67-1, "Practical Galvanic Series".*

9 *Aircraft corrosion control*, **1985**, IAP, Inc.

10 G. Bierwagen, *J. Coat. Technol. Res.*, **2008**, 5, 133.

11 http://aviation-satety.net/database/record.php?id=19810822-0, *Accident Description.* [cited 2010 09-08].

12 C. o. A. o. U. S. A. F. Aircraft, *Aging of U.S. Air Force Aircraft.* **1997**.

13 G. H. Koch, M. Brongers and N. G. Thompson, *Corrosion costs and preventive strategies in the United States.* [cited 2010 Nov.22].

14 D. Chidambaram, C. R. Clayton, M. W. Kendig and G. P. Haladaa, *J. Electrochem. Soc.*, **2004**, 151, B613.

15 P. Campestrini, E. van Westing and J. de Wit, *Electrochim. Acta*, **2001**, 46, 2631.

16 P. Sorensen, S. Kiil, K. Dam-Johansen and C. Weinell, *J. Coat. Technol. Res.*, **2009**, 6, 135.

17 E. Gaggelli, F. Berti, N. D'Amelio, N. Gaggelli, G. Valensin, L. Bovalini, A. Paffetti and L. Trabalzini, *Environmental Health Perspectives*, **2002**, 110, 733.

18 R. Twite and G. Bierwagen, *Prog. Org. Coat.*, **1998**, 33, 91.

19 K. D. Sugden and B. D. Martin, *Environmental Health Perspectives*, **2002**, 110, 725.

20 www.RoHSGuide.com, *RoHS restricted substances*. **2006**, RoHS & WEEE.

21 G. Bierwagen, D. Battocchi, A. Simoes, A. Stamness and D. Tallman, *Prog. Org. Coat.*, **2007**, 59, 172.

22 J. Osborne, K. Blohowiak, S. RayTaylor, C. Hunter, G. Bierwagen, B. Carslon, D. Bernard and M. Donley, *Prog. Org. Coat.*, **2001**, 41, 217.

23 G. Bierwagen, R. Twite, G. Chen and D. Tallman, *Prog. Org. Coat.*, **1997**, 32, 25.

24 G. Bierwagen and D. Tallman, *Prog. Org. Coat.*, **2001**, 41, 201.

25 J. Janata, D. Baer, G. Bierwagen, H. Birnbaum, A. Davenport, H. Isaacs, Hedberg, M. Kendig, F. Mansfeld, B. Miller, A. Wieckowski and J. Wilkes, *Issues related to chromium replacement*, in *187th Meeting of the electrochemical Society* **1995**, Reno, Nevada.

26 W. J. van Ooij, D. Zhu, V. Palanivel, A. Lamar and M. Stacy, *Silicon Chem*, **2006**, 3.

27 G. Bierwagen, R. Brown, D. Battocchi and S. Hayes, *Prog. Org. Coat.*, **2010**, 67, 195.

28 D. Battocchi, A. Simoes, D. Tallman and G. Bierwagen, *Corrosion Science*, **2006**, 48, 1292.

29 G. Bierwagen, D. Tallman, M. Nanna, D. Battocchi, A. Stamness and V. J. Gelling, *Polymer Preprints (American Chemical Society, Division of Polymer Chemistry)*, **2004**, 45, 144.

30 G. P. Bierwagen, M. E. Nanna and D. Battocchi, *Magnesium rich coatings and coating systems*. **2005**, (NDSU Research Foundation, USA). Application: WO, 65

31 M. Nanna and G. Bierwagen, *J. Coat. Technol. Res.*, **2004**, 1, 69.

32 D. Battocchi, A. M. Simoes, D. E. Tallman and G. P. Bierwagen, *Corrosion Science*, **2006**, 48, 2226.

33 A. Simoes, D. Battocchi, D. Tallman and G. Bierwagen, *Assessment of the corrosion protection of aluminium substrates by a Mg-rich primer: EIS, SVET and SECM study*, **2008**.

34 A. Simoes, D. Battocchi, D. Tallman and G. Bierwagen, *Corrosion Science*, **2007**, 49, 3838.

35 D. Wang, *Organosilane self-assembled layers (SAMs) and hybrid silicate Mg-rich primers for the corrosion protection*, in *Coatings and polymeric materials*. **2007**, North Dakota State University, Fargo.

36 K. N. Allahar, D. Battocchi, M. E. Orazem, G. P. Bierwagen and D. E. Tallman, *J. Electrochem. Soc.*, **2008**, 155, E143.

37 D. Battocchi, G. Bierwagen, M. Zentner and R. Brown, *Mg-rich primer for totally chromate-free protective systems on Al alloys*, in *Nurnberg Coatings Congress*. **2007**, Nurnberg, Germany.

CHAPTER 2. METAL-RICH PRIMER SYSTEMS: A LITERATURE REVIEW

2.1. Introduction

Metal and metal alloys are extensively used as the major materials in modern societies, since they possess many excellent mechanical properties and the matchless flexibility which can satisfy various demands on materials. From the small iPod to the large space station, different metals or alloys play the indispensable roles. However, the biggest problem for a large number of metallic materials is that corrosion will occur spontaneously under most conditions. Corrosion refers to the chemical reactions between metal or metal alloys and the environment. Usually Corrosion results in the disintegration of metals or alloys due to the formation of chemical compounds, such as the oxides or salts of the original metals. [1] Corrosion can cause the structural failures and probably result in property loss and human injury. Therefore, the issue of corrosion is always essential, and the strategies of corrosion protection are of importance.

2.1.1. Fundamentals of corrosion protection

From the thermodynamic view, corrosion is an electrochemical reaction between metal/alloy and water and/or oxygen present in the service environments. In general, corrosion consists of two coupled half reactions: one is an anodic reaction wherein the metal atoms lose their electrons to form more stable oxide compounds. [2] It can be expressed by the following form [1]

$$M \rightarrow M^{n+} + ne^-$$

The other one is cathodic reaction that the chemical species in the aqueous solution or

on the interface of metal surface obtain the electrons to form more stable species. The typical reduction reactions occur in neutral, acid or oxidant-absent solutions are of the following forms, respectively. [1]

$O_2 + 2H_2O + 4e^- \rightarrow 4OH^-$ (neutral solution),

$2H^+ + 2e^- \rightarrow H_2$ (acid solution),

$2H_2O + 2e^- \rightarrow H_2 + 2OH^-$ (oxidant-deficient solution).

Generally, certain requirements should be met for the occurrence of corrosion. First, two separated areas with different potentials should be present as the anodic site and cathodic site; second, there should be two independent electrical connections between these two sites, one is the metallic conductivity between the two sites and the other is the electrolyte solution to which the two areas are exposed. In Figure 2-1, the four necessary linkages for the corrosion of Al alloy to occur are illustrated.

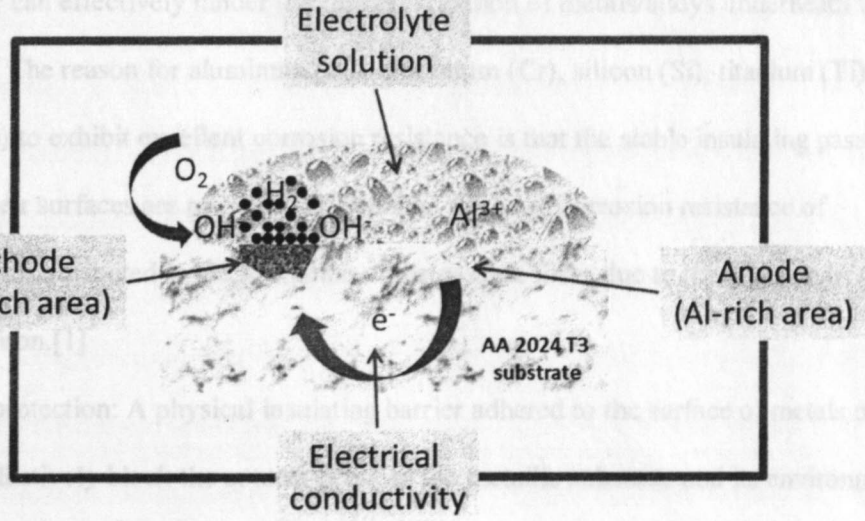

Figure 2-1. Illustration of the four requirements for Al alloy corrosion.

The efficient strategies of corrosion protection are usually those methods which can break one or more linkages of corrosion, such as removal of electrolyte, or a technique to

insulate the different metallic materials from each other. According to the protection mechanisms, the strategies of corrosion protection can be classified as follows: [3]

Environmental modification: Elimination of electrolyte from metal surface can effectively retard corrosion. Thus, the environments with dry air, no moisture aggregation on metal surface or no aggressive species in electrolyte can slow down corrosion.

Proper design of objects: Limitation of the weak sites in the design of objects, such as bolts, rivets, holes, rough surface, joints, sharp edges, can help to avoid corrosion initiation. [1, 3] Since the sites where the dissimilar metals are connected or electrolyte is easily stored tend to activate corrosion.

Passivation: Passivity refers to a particular corrosion resistance behavior possessed by some metals and alloys. A thin, invisible but compact oxide film is formed over the surface of metals or alloys, and it is stable even under the aggressive environment. [1] This thin passive layer can effectively hinder the further oxidation of metals/alloys underneath the passive film. The reason for aluminum (Al), chromium (Cr), silicon (Si), titanium (Ti) and niobium (Nb) to exhibit excellent corrosion resistance is that the stable insulating passive films over their surfaces are present. For example, the good corrosion resistance of stainless steel is attributed to the formation of the passive films due to the addition of Cr and/or Ni to iron.[1]

Barrier protection: A physical insulating barrier adhered to the surface of metals or alloys can effectively block the contact between the metallic substrate and its environment. For example, in a multiple-layer organic coating system, the major function of topcoat is to provide excellent barrier protection, which is to slow down the permeability of water and aggressive species to reach the metal substrates.

Cathodic protection: Cathodic protection is an unique protection technique by which the target metal is forced to act as a cathode. There are two major ways to achieve cathodic protection: one is that an external DC source is used to apply an opposing potential to the target metal and to make it become the cathode to be protected; the other way is to electrically connect a more active metal to the target metal, as a result, the more active metal can work as anode to protect the target metal from corrosion under an aggressive environment.

2.1.2. Corrosion protection coating system

The use of coating system is a major strategy of corrosion protection. For more than one century, different coating systems have been developed and exhibited excellent corrosion protection abilities for a wide range of metals and alloys, such as iron, steel, Al alloys, Ni, Cu and Mg, via different mechanisms. More significantly, the high-performance coating systems can protect heavy duty constructions in the harsh corrosive environments from the dangerous structural failures, such as bridges of river-crossing/highway/railroad, offshore constructions, outdoor containers, decks/ports, gas/liquid pipelines, electrical utilities and telecommunication equipment. [4] Furthermore, the use of coating systems for corrosion protection has many advantages in comparison to many other protection methods. For example, the application of coating system is convenient and economically efficient due to its less limitation in site conditions, application equipment, time or labors. The physical, chemical or mechanical properties of the metal substrates can be maintained in the presence of coating systems.

According to the different protection mechanisms, corrosion protection coatings are usually classified into three major types: [3] barrier coatings, which can provide good

barrier protection to hinder the aggressive species, e.g. water, oxygen, ions, from reaching the surface of metal substrate; inhibitive coatings, which can release inhibitive species to aid the metal substrate to form a dense and stable passive layer; metal-rich coatings with the galvanic effect, in which the more active metallic particles can work as anodes to make the more noble substrates (in comparison to the metallic particles in polymer matrix) act as the cathodes, thus be protected.

Generally speaking, the protection mechanisms for the barrier coating system and the inhibitive coating system are mainly based on blocking the direct contact between the aggressive species and the metal substrates via the elimination of the transport of water and ions or the formation of a passive layer. Therefore, their corrosion protection efficiency and lifetime are significantly dependent on the intactness of the barrier coatings or the passive layers.

However, metal-rich coating system is designed to provide cathodic protection for the underlying metallic substrates in case the intactness of barrier coating or passive layer gets damaged and the substrates are exposed directly to the aggressive environment. Usually, metal-rich coating systems are formulated with high pigment volume concentration (PVC). [5] When the barrier protection fails due to the damages of topcoat, cathodic protection is induced via the oxidative sacrifice of the active pigments.

A metal-rich coating system usually has a porous nature because of the high pigment volume fraction. As a consequence, the poor barrier performance of a metal-rich coating results in the short lifetime of cathodic protection due to the rapid consumptions of the active pigments as well as the electrical conductivity loss among pigments and also between the pigments and the substrates. Therefore, a sophisticated anticorrosive coating

system is usually a multiple-layer system including a metal-rich coating to provide cathodic protection and the topcoat to give a long-term barrier protection. By utilizing the strengths of each type coating, the corrosion protection ability of the whole anticorrosive coating system can be maximized.

A metal-rich primer with a good topcoat usually provides a high-performance coating system, especially in the aggressive service environment. The development of new metal-rich coating systems with the higher anticorrosion efficiency, longer lifetime and environmental-friendly nature is always the goal for coating industry and corrosion engineering. Zn-rich primer (ZRP) system, the most successful example of metal-rich primer system, was developed to provide excellent corrosion protection for steel in 1930's. [6] A lot of research work has been carried out to understand the protection mechanisms, the anticorrosion efficiency and the lifetime prediction of various ZRP systems. [7-13] The studies on ZRP have extended the knowledge of metal-rich coatings and provided the fundamental guidance for the future design and development of new metal-rich coating systems.

This review will provide a brief overview on metal-rich primer system via the description of its corrosion protection principles and anticorrosion function. The influences of some important design parameters on the final anticorrosion performance and durability of metal-rich coating system will be discussed. The studies and experience on the technology of ZRP and Mg-rich primer (MgRP), the successful examples of metal-rich coatings, will be addressed in detail. In addition, the most widely used electrochemical testing methods for evaluating the anticorrosion performance of metal-rich coating, such as electrochemical impedance microscopy (EIS) and electrochemical noise methods (ENM),

will be discussed. Furthermore, the standards of the different corrosive environments and the accelerated weathering methods will be briefly mentioned. Finally, a distinctive study on the new metal-rich primer systems by using Mg alloy particles as pigment will be proposed, and the study procedure will be briefly described in the end of this chapter.

2.2. Metal-rich primer coatings

2.2.1. Principles of galvanic protection provided by metal-rich primer

Generally, metal-rich coating system can provide effective corrosion protection for metal substrates via galvanic effects. It means that the more active metallic pigments in the metal-rich coating can act as anodes and force the more noble substrate to be the cathode, and thus protected. Most importantly, cathodic protection of a metal-rich coating can be induced only when good galvanic contact is maintained among the metallic pigments and also between the pigments and the substrate. It suggests that the high anticorrosion efficiency and long lifetime of a metal-rich coating are dependent on the amount of active pigments in coating system, and whether they act "cooperatively" as anodes due to the good electrical contact among the pigments and also between the pigments and the substrate.

2.2.2. Important design issues of metal-rich primer system

Based on the previous experience and practice of metal-rich coatings, [14, 15] it has been found that the anticorrosion performance and durability of metal-rich coatings are significantly related to five factors in the design and formulation processes. [3] They are four basic components of coatings (metallic pigment, polymer binder, additive and solvent) and one adjustable parameter, pigment volume concentrations (PVC). [14, 16] Although the active metallic pigments in metal-rich primer are those which eventually provide

galvanic protection for the substrates, each of the five factors serves a particular function of providing the metal-rich coatings the proper properties and performance in formulation, application, protection and duration. Therefore, the knowledge of these five factors about their functions, interactions, degradation and limitations can provide abundant and important information to the development of metal-rich coating system.

2.2.2.1. Active metallic pigments

The metallic pigments in metal-rich coating are designed to supply galvanic protection for the substrates. Therefore, the activity of the metallic pigments mainly determines the efficiency of cathodic protection. First, the pigments must be more electrochemically active than the metal substrate so that the pigments can act as anodes to keep the substrate from corrosion when they are galvanically coupled together. Second, the metallic pigments should be available as anodes whenever they are needed in the service environments. It suggests that the metallic pigments should be free of passivation and also maintain good electrical conductivity during the service period. For example, Zn pigments are formulated in ZRP to provide cathodic protection for steel. The oxidations of Zn pigments result in the formation of ZnO layer on the surface which will reduce the activity and conductivity of Zn pigments. Fortunately, ZnO is a semi-conductive material and the electrical conductivity among Zn pigments and between Zn and steel can be still maintained. [17] But, the formation of the non-conductive Al_2O_3 passivative layer over the surface of Al pigments can destroy the electrical conductivity among Al particles. [18]

2.2.2.2. Pigment volume concentration (PVC)

PVC is defined as the volume fraction of pigment in the dry coating film. [19] For a metal-rich coating, the PVC is a very important formulating parameter, because it affects

many important properties of metal-rich coating, such as density, electrical impedance, chemical resistance, impact and tensile strength. [20, 21] For a given pigmented coating system, the abrupt changes of some coating properties can be observed at a specific PVC, which is considered as the critical pigment volume concentration (CPVC). Usually, the CPVC is defined as the point at which there is just enough polymer binder to cover the surface of all the pigments and also to fill all the interstices among particles. [21, 22] Most importantly, the electrical conductivity of metal-rich coating is dependent on the reduced PVC (Λ, capital Greek lambda), which is defined as the ratio of PVC to CPVC (Λ=PVC/CPVC). [20] When Λ <1, it implies that some pigments are isolated from others and will have no contribution to cathodic protection. The small Λ means that the pigments in the metal-rich coating system have less contact between each other, and vice versa. Therefore, in order to obtain high cathodic protection efficiency, the formulating range of Λ for metal-rich primer is generally around 1. However, the choice of Λ should also take into account the other properties of the coating, e.g. good adhesion and mechanical properties.

2.2.2.3. Coating matrix polymers

Coating matrix polymers (polymer binders) are mainly used to combine all the components of metal-rich primer as a whole and also to supply the needed adhesion between the substrate and primer. Good adhesion is the foundation of a successful corrosion protection. The ability of a polymer binder to against delamination and degradation can significantly influence the protection performance and durability of a metal-rich primer. Meanwhile, polymer binders are also responsible for the necessary mechanical properties, such as impact resistance, hardness and toughness. The different

polymer binder systems as well as their major properties have been described in detail in reference [3]. Because of the porous nature of metal-rich primer system, polymer binders cannot provide the excellent barrier protection during the initial service period, such as water resistance and low permeability for gas and liquids. But, the barrier properties of polymer binders probably can be supplemented by the sealing function of the formed oxidation products. [23] However, to obtain the true long-term corrosion protection, metal-rich coatings are best used as primers and then topcoated for barrier protection.

2.2.2.4. Solvents

Although most of solvent will eventually evaporate and only a small amount left in the metal-rich coating system, the solvent has significant influence on the final performance of metal-rich coatings. Solvent can ensure the proper mixing of all the components, adjust the suitable viscosity for coating application, assist in wetting substrates, enable the formation of good film and control the final thickness of coating film. However, the amount of the residual solvent left in coating film should be taken into account in formulation design, since they can influence the T_g of coating and reduce the barrier performance of coating system. [3]

Recently, the uses of organic solvents in coating system have caused more and more concerns due to their negative effects on environment and human health. Now, the development of "VOC-compliant products with high solids content and low amounts of organic solvents" [14] or water-borne coating systems has become an important goal for coating industry but is also a significant challenge to the coating scientists.

2.2.2.5. Additives

The amount of additives used in metal-rich coatings is small and generally less than 2%

by weight. [24] But, the key roles of additives in the property improvement cannot be neglected. Aiming at various requirements and purposes, different additives have been used to improve the properties of coating films. For example, surfactants can assist in pigment wetting and anti-flocculation, thickeners can reduce pigment settling, plasticizers aid the good film formation and curing additives can accelerate the curing processes. [24] Additives can help the formation of defect-free coating films by limiting the presence of the trapped air bubbles, cracks, delaminating interface, and weak cross-linking sites. A defect-free coating film implies excellent protective performance and long durability.

2.2.3. Zinc-rich primer (ZRP) system

The most successful examples of metal-rich coatings are the ZRP systems, which have been used to protect steel or ferrous materials from corrosion since the 1930s. [25] The principle of corrosion protection of ZRP is that Zn dusts can work as anodes to force steel to be cathode and to be protected, because Zn is more electrochemically active than steel. To ensure the cathodic protection being active, ZRPs usually have been formulated at high PVC (around 65% PVC) at which most Zn particles can maintain good electrical connectivity with each other and also with steel substrate. The practical success of ZRPs has clearly demonstrated that metal-rich coatings combined with good topcoats can provide efficient, convenient, safe, economically viable corrosion protection for iron and steel substrates.

In general, ZRPs can be classified into two categories based on the types of matrix polymers used: organic ZRPs and inorganic ZRPs. In Table 2-1, a brief classification of ZRPs is listed according to the different binder systems. In addition, the curing conditions and the major properties of each ZRP system are also described.

Various polymers, such as epoxy/polyamide, epoxy esters, polyurethanes, chlorinated rubbers or alkyd/oil types have been used as binders in organic ZRPs, since they can provide good adhesion and also be capable of withstanding a high pH environment. However, the properties of polymers also can affect the overall performance of ZRPs. For example, ZRPs using alkyd types, epoxy esters or polyurethanes as binder systems usually show quick failure of corrosion protection due to their poor adhesion. [26] However, the epoxy-polyamide based ZRPs exhibit the outstanding anti-corrosion performance in the aggressive environments, such as marine, offshore or sea water. One important reason is that epoxy-polyamide binder can supply good adhesion between ZRP and topcoat as well as between ZRP and steel substrate. The drawbacks of epoxy-polyamide ZRPs are the high VOC's and the toxicity of curing agents.

Inorganic ZRPs usually refer to zinc silicate coatings, in which the more electrically conductive inorganic zinc silicate films can be formed via the chemical reaction between alkali alkyl silicates and Zn particles. [27] In addition, the silicates can react with the steel surface to provide good adhesion between the ZRP primer and the substrate. [28] But the performance of inorganic ZRP's is significantly dependent on the degree of cure. [29-31]

For more than half century, a lot of research work has been carried out on various ZRP systems to understand the protection mechanisms, the key parameters for achieving the effective anticorrosion performance and the degradation/failure modes. The knowledge obtained from these studies is very important for developing new ZRP systems and designing other novel metal-rich coatings.

2.2.4. Protection mechanisms of ZRPs

The protection mechanisms of ZRPs have been extensively investigated. It is widely

accepted that two stages of corrosion protection may contribute to the excellent anti-corrosion performance of ZRPs. In the initial corrosion protection stage, cathodic

Table 2-1. Typical curing conditions and properties of some major ZRPs. (Adapted from P. Sorensen, et al., *J. Coat. Technol. Res.*, **2009**, 135 and D. Wang, **2007**, Ph. D. Dissertation, North Dakota State University.)

	Binder		Curing	Properties	
				Advantages	Limitations
Organic ZRP	Solvent-borne	Epoxy ester	Oxidative reaction	Quick curing Good hardness Low cost	Chalking Poor compatibility to vinyl topcoat
		Polyurethane	Crosslink	Superior UV resistance High gloss	Low corrosion resistance Difficult formulating process
		Siloxane	Crosslink	High gloss Long durability	Poor mechanical properties
		Alkyd	Oxidative reaction	Good adhesion Good flexibility	Low saponification resistance Low zinc content
		Epoxy	Crosslink	Excellent adhesion High chemical resistance Excellent corrosion resistance	Short pot life Slow curing Toxicity
	Water-borne	Epoxy	Crosslink	Low VOC Good adhesion Good flexibility	Short pot life Slow curing Low corrosion resistance Low chemical resistance
	Powder coating	Epoxy	Crosslink	Solvent free Good chemical resistance Low permeability	Low zinc content High capital costs Few availability
Inorganic ZRP		Zinc-silicate	Moisture	Good conductivity Good adhesion Good heat resistance	High RH condition for curing Poor mechanical properties

protection is provided via the sacrifice of zinc particles. In the second stage, the oxidation products of Zn particles enhance the barrier protection and contribute to the long-term corrosion protection of ZRPs. [12, 13, 32, 33] Also, The oxidation of Zn particles help to maintain a high pH environment over the steel surfaces. As a result, the steel substrates under the ZRPs are often passivated.

The cathodic protection provided by ZRPs has been verified by a lot of research work. [10-12, 34-37] Irrespective of the exposure conditions, e.g. salt spray or 3% NaCl immersion, the mixed potentials of the ZRP coated steels reveal the existence of cathodic protection. [11, 12] For example, the open circuit potentials of the bare steels in seawater are around -0.80 to -0.85 v/SCE [versus to the saturated calomel electrode (SCE)]. [11, 35, 38] From the view of thermodynamics, ZRPs can be regarded to provide cathodic protection when the mixed potentials (ε_{mixed}) are more negative than that of bare steels (ε_{steel}). In addition, the duration of cathodic protection can be estimated based on the period when $\varepsilon_{mixed} < \varepsilon_{steel}$. From Knudsen's work, the corrosion potentials of three different ZRPs coated steel samples as a function of exposure time are shown in Figure 2-2. During the one-hundred-day exposure, the mixed potentials of these three ZRPs coated samples are between -1.0v/SCE and -0.8v/SCE, which are lower than ε_{steel}. It indicates that the steel substrates are protected via the sacrifice of Zn particles.

With the increasing exposure time, it can be seen that the mixed potentials gradually rise to close to ε_{steel} (-0.8 v/SCE). It implies the loss of cathodic protection, because Zn particles were consumed and the electrical contacts between zinc particles were lost. According to Knudsen, [38] the area ratio of the exposed steel to the active Zn particles determines the values of the mixed potentials. The exposed steel refers to the steel which is

exposed to electrolyte and acts as cathode: the active Zn particles are those pigments which work as anodes via electrical connection between particles as well as between particles and substrate. The increase of ε_{mixed} implies that the amount of the active zinc particles is reduced and causes the area ratio of anodes to cathodes to decrease. [38]

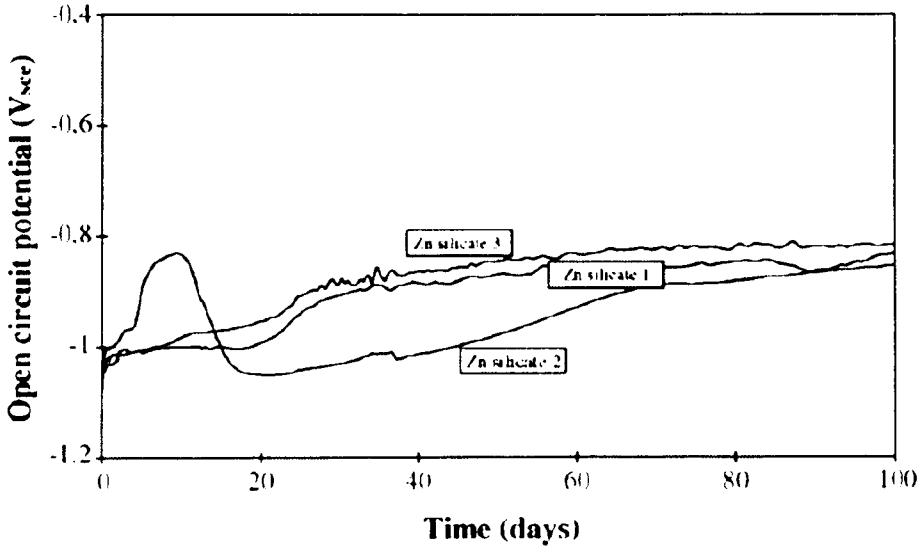

Figure 2-2. Corrosion potential changes of three zinc silicate primers with exposure time in seawater at ambient temperature. (Copied from O. O. Knudsen et al., *Prog. Org. Coat.*, **2005,** 54, 224.)

Cathodic protection through the sacrifice of Zn particles is a short-term protection since the oxidation of Zn particles usually results in the loss of electrical conductivity among zinc particles and also between primer and steel substrate. Therefore, the long-term corrosion protection provided by ZRPs should be assigned to other protection mechanisms. Some research results support the "pore-sealing" mechanism of Felui, [12] which suggests that the formation of Zn corrosion products could improve adhesion and enhance the barrier properties of ZRPs via blocking the pores in primer films. [13, 35, 36, 39] Similarly, Kalendova has suggested that "the neutralization and barrier mechanism" surpasses the

cathodic protection of ZRPs. [40] As a result, the barrier properties as well as the adhesion are enhanced and further contribute to ZRPs the long-term corrosion protection.

One of other views proposed that the basic zinc salts deposited on steel surface could provide inhibitive protection via to block the further attacks of aggressive species. [10, 39, 41, 42] Another possibility of the long-term corrosion protection may be attributed to the passivation of steel due to the oxidation of Zn particles increasing the local pH higher than 9. Regardless of the various opinions about the protection mechanisms, it seems that the coordination of several different anti-corrosion mechanisms result in the excellent protective performance of ZRPs.

2.2.5. Development of high-performance ZRPs

As mentioned before, some design parameters, such as polymer binder, pigment and PVC, can significantly influence the cathodic protection efficiency, the barrier performance and the inhibition properties of ZRPs and in turn affect the overall anticorrosion performance of ZRPs.

A lot of research work has revealed that the effective cathodic protection can be maintained as long as the zinc particles in ZRPs are electrically connected with each other as well as with steel substrate. [43, 44] For example, Feliu et al. have suggested that the durability of cathodic protection "depended on the continuity of the electrical contact between the particles and with the steel base". [12]

Theoretically, several ways can be used to effectively maintain the good electrical conductivity of ZRPs. One is to increase zinc content of ZRPs. In fact, the high PVCs (above 90 wt%) have extensively been applied in ZRPs formulation. The second one is to improve the electrical conductivity for the whole ZRPs via using metallic or inert

conductive extenders or changing the shapes of Zn particles. The third one is to reduce the precipitations of the oxidation products on the surface of Zn particle. [45] The work of Chen et al. has shown that the addition of Al pigments up to 15 wt% in ZRP system can decrease the formation of zinc white. As a result, the resistance to the formation of red rust is improved for the Al-addition ZRP system. The probable reason could be that the high pH of environment induced by the oxidation of Al particles caused the precipitates of ZnO to dissolve. [45]

It has been widely accepted that the efficiency and durability of cathodic protection are closely related to the zinc content of ZRPs. [10] Also, it has been suggested that the durability of cathodic protection is proportional to the thickness of ZRP film. [38, 46] Actually, the high zinc content implies the good physical connection between zinc particles and further the good electrical conductivity of the whole ZRP system. Thus, the high zinc loading in ZRP formulation (usually around or higher than 80 wt% or 65% PVC) seems to be the key requirement for the excellent cathodic protection of ZRPs. [5, 47, 48] As shown in Figure 2-3, the work of Shreepathi et al. has demonstrated that the epoxy ZRP systems containing 80% and 90 wt% Zn dust provided the much more stable and durable cathodic protection for steel in comparison to the ones with lower Zn contents.

One thing should be emphasized is that the criterion value of Zn content for an effective cathodic protection is also related to the type of polymer binder, particle size distribution, particle shape of Zn dust and the application methods. In a sense, the optimal Zn content is related to the dense packing efficiency of Zn particles in a given polymer matrix, where all the Zn particles physically contact with others in the high coordination numbers.

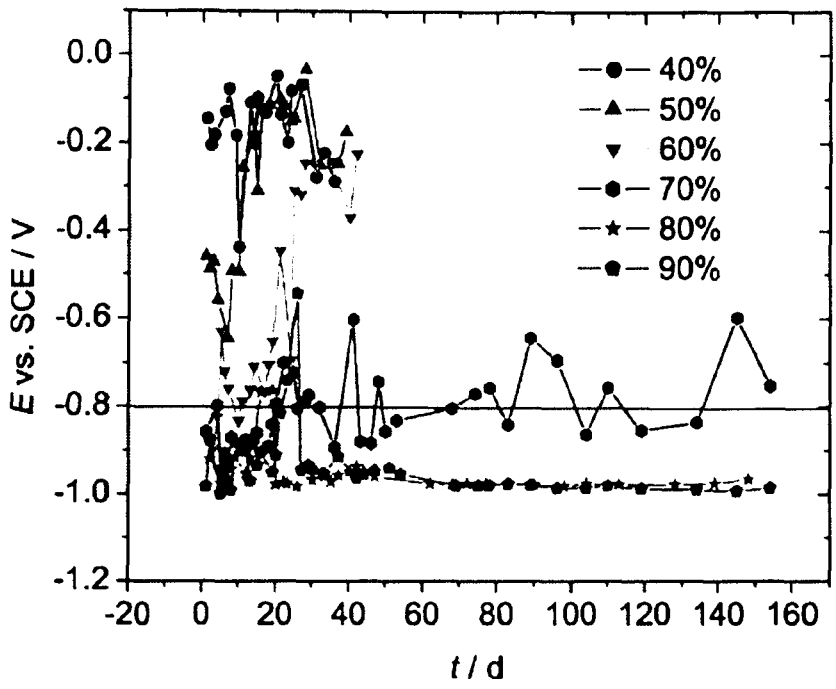

Figure 2-3. OCP (vs. SCE) of ZRPs with different zinc content as a function of immersion time in 3.5% NaCl solution. (Copied from S. Shreepathi, *Electrochim. Acta*, **2010**, 55, 5129)

Some work has been done to investigate the effects of particle size or the particle shape of Zn pigments on the performance of ZRPs. From the work of Kalendova, [44] it seems that the ZRP system containing Zn particles with small particle size or wider particle size distribution provided better anticorrosion properties, since the interstices between Zn particles can be filled by even smaller particles or sealed much easily by corrosion products. ZRPs using the lamellar zinc particles as pigment also exhibit better mechanical properties and anticorrosion behavior in comparison to those containing isometric zinc particles. [44] Moreover, the ZRPs using spherical or lamellar zinc particles as pigments show good performance when the zinc concentration are 50 wt% and 20 wt%, respectively. It implies that the uses of lamellar zinc particles in ZRP system can reduce the zinc content and subsequently the cost without the sacrifice of certain properties. [43, 44]

In fact, the lamellar zinc particles have a wide application in zinc-rich powder coatings. Powder coating systems become more of interest to coating industry due to the zero VOC. But for zinc-rich powder coatings, the homogeneous dispersion of zinc particles becomes difficult when zinc content is above 70 wt%. In order to solve this technological restriction, partial spherical zinc particles have been replaced by the lamellar zinc particles. It has been found that the use of lamellar zinc particles can improve the percolation of Zn particles and make zinc-rich powder coatings exhibit the similar corrosion protection performance as the solvent based ZRPs but in much lower zinc content. [32, 33, 37]

Although the high zinc content can improve the efficiency and durability of cathodic protection for ZRPs, the drawbacks due to the porous nature of ZRPs are also obvious: poor mechanical properties, poor adhesion (between Zn particles and between ZRP and topcoat/substrate), application difficulties (welding and torch cutting) and high cost. Thus, the ways to enhance the efficiency and durability of cathodic protection without increasing the zinc content of ZRPs are also of interest.

Carbon black [32] and carbon nanofiber [49] have been used as extenders in ZRP systems to improve the electrical conductivity. From the work of Marchebois, the mixed potentials of three zinc-rich powder coating samples as a function of seawater-immersion time are shown in Figure 2-4. [32] The ZRP samples of A, B and C contained the same amount of zinc particles (50 wt%) but 0, 2.1 wt% and 5 wt% carbon black, respectively. It is well known that 50 wt% of zinc particles is far below the CPVC of ZRP system. Thus, it indicates that most zinc particles in the 50 wt% ZRP system were isolated by polymer binder and had no physical contact with each other or with steel substrate. In Figure 2-4, it can be seen that sample C, which contained 5 wt% carbon black, provided longer cathodic

protection in comparison to the other samples. As we know, carbon black cannot provide cathodic protection for steel substrate due to its noble activity. Since all the three ZRP samples had the same content of zinc particles, and the addition of carbon black into ZRP system did not increase the amount of active pigments, the improved cathodic protection of sample C indicated that the addition of 5wt% carbon black improved the electrical connection between zinc particles due to its good electrical conductivity. As a result, the longer durability of cathodic protection was achieved without increasing the Zn content. However, the well dispersion of carbon black/carbon nanofiber in polymer matrix is always the key issue for obtaining a uniform ZRP system.

Some other conductive extenders have also been used in ZRPs and their abilities to improve the electrical conductivity of ZRPs are investigated. [43, 50-52] The use of the inert conductive ferrophosphorous (Fe_2P) seems to be of great interest. It has been found that, Fe_2P pigments not only provided good electrical conductivity for ZRP system, but also interacted with Zn^{2+} to co-precipitate with the oxidation products of Zn on the surface of Fe_2P pigments. As a result, the electrochemical activity of Zn particles was maintained longer due to the less oxidation products precipitated over the surface of Zn particles. [52, 53] Experimental results also showed that Fe_2P particles could substitute 25-35 wt% Zn in ZRPs without reducing their corrosion resistance. [51] In fact, ZRPs with the substitution of Fe_2P exhibited better performance on adhesion, welding and gas torch-cutting. However, it's important to point out that the performance of Fe_2P to effectively replace partial Zn particles in ZRPs are related to the distinct nature of polymer binder. [50, 53] The substitution of Fe_2P in ZRPs improves the corrosion resistance for the inorganic and organic ZRPs through different mechanisms. In the porous ethyl silicate ZRP system, good

electrical connection can be observed between zinc and Fe_2P particles. It implies that Fe_2P particles effectively support the cathodic protection of ethyl silicate ZRPs. But the epoxy-polyamide system usually has low porosity and shows less electrical conductivity in comparison to inorganic ZRP system, thus the replacement of Zn by Fe_2P tends to enhance the barrier effect rather than the galvanic property. [50]

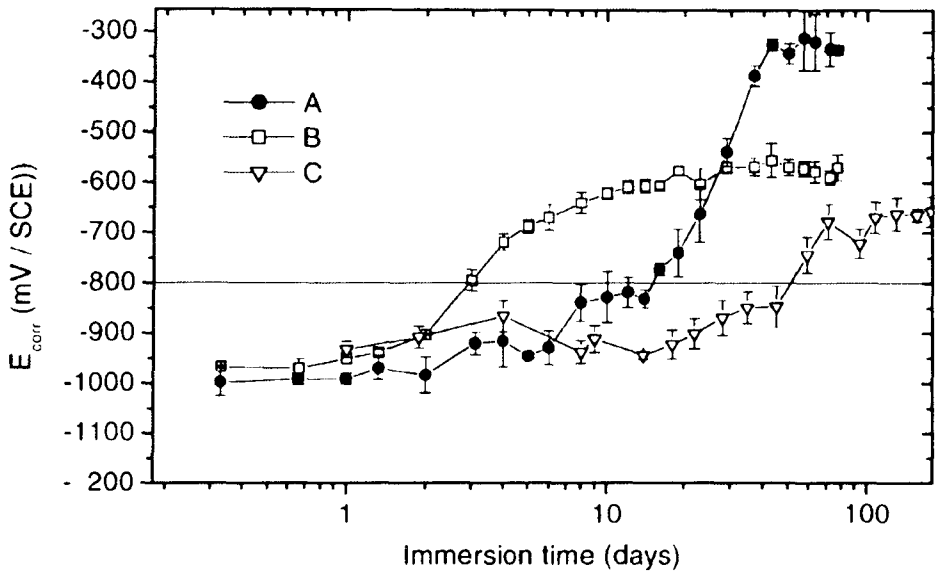

Figure 2-4. Corrosion potentials of different ZRP samples changed with immersion time; sample A: 50% (by wt.) zinc+0 carbon black; sample B: 50% zinc+2.1% carbon black; sample C: 50% zinc+5% carbon black. (Copied from H. Marchebois, et al., *Prog. Org. Coat.*, **2002**, 45, 415.)

Moreover, different metallic pigments, such as cadmium, aluminium, [18, 54] iron [55] , manganese [56], magnesium, [57, 58] and their alloys, have been used as pigments in ZRPs to provide cathodic protection for steel. Chen et al. reported that, in comparison to the ZRPs containing Zn particles alone, the ZRPs with 5 to 25% Al substitution exhibited less effective cathodic protection for steel substrate but better barrier protection after the same salt spray exposure. [45] It seems that Al particles in ZRPs preferred to form the

passive Al_2O_3 film which reduced the electrical conductivity of Al particles. However, the barrier properties were enhanced due to the formation of the passive Al_2O_3. Similar results have been reported by Panossian group. [18] Interestingly, cathodic protection has been observed on Al/Al alloy rich coatings only when they are exposed to the high chloride environment. It seems that the aggressive chloride ions can destroy the passive layer of Al_2O_3 to keep Al particles as anodes. [18]

The addition of various metallic particles into ZRPs not only influence the efficiency of cathodic protection through changing the electrical conductivity of ZRP system, but also affect the barrier properties via forming different oxidation products. When ZRPs are exposed to corrosive environments, e.g. immersion of seawater, salt spray (B117) or wet-dry cycles, different oxidation products of zinc particles consecutively form with time.[25, 33] Generally, the initially formed oxidation products are zinc oxide; with the further exposure, zinc hydroxide can be found in ZRPs; [25] finally, zinc carbonate, simonkolleite [$Zn_5(OH)_8Cl_2 \cdot H_2O$] or sulfated zinc corrosion products [$Zn_4Cl_2(OH)_4SO_4 \cdot 5H_2O$] are developed according to the corrosive conditions. [33] Among those oxidation products, it has been regarded that the formation of zinc carbonate can benefit the long-term protection of ZRPs. [25] Jagtap et al. suggested that the presence of ZnO promoted the electrical conductivity via forming Zn-ZnO p-n junction and further improved the corrosion protection. [17]

One thing has to be mentioned is that the different oxidation products formed in ZRPs actually not only depend on the elemental components of pigment but also closely relate to the conditions of the environment, e.g. the present species, the temperature and wet-dry cycle. [59]

In summary, the high corrosion protection performance of ZRPs can be achieved via different strategies, such as increasing zinc content, changing particle shape, adding conductive extenders or adjusting corrosion products. The studies of ZRPs provide the deep insight into the corrosion protection mechanisms, the key factors and the failure modes, and all the information can be generally applied on metal-rich primer system.

2.2.6. Magnesium-rich primer system

Mg-rich primer (MgRP) system was developed as a new metal-rich primer system by Bierwagen's group in 2002. [47] The motivation of MgRP was inspired by the requirement of developing an environmental-friendly coating system as the alternative to the toxic Cr primer. [23, 60-63] Analogous to ZRPs, MgRP was designed to provide sacrificial protection for Al alloy substrates, especially for AA2024 T3. Since Mg is more electrochemically active than Al and Al alloys, when Mg particles are electrically connected to Al/Al alloys, and further exposed to corrosive environments, Mg particles can act as anodes and force Al or Al alloys to become the cathode and thus be protected. [47, 61, 64, 65]

Due to the same fundamental concepts of metal-rich coatings, some features of MgRP system are similar to ZRP. For example, polymer matrix, either organic or inorganic system, can be used to supply necessary adhesion to substrate and topcoat. [66] The metallic pigments used are more electrochemically active than the metal substrate; high PVCs are chosen for formulation in order to achieve good electrical conductivity. [23, 67] However, MgRP has some specific issues different from ZRPs. First, Mg particles need to be commercially available. Several companies, such as Non Ferrum-Metallpulver GmbH (Salzburg, Austria), [65] Eckart GmbH (Furth, Germany) [47] and Reade, can provide

particulate Mg with the mean particle size from 20 to 50 μm. Second, Mg particles should be safe enough to handle during shipping, storage and formulation. Mg is a very active metal and Mg powders are fire hazardous due to their small particle sizes. But, the experience of Eckart to deliver Mg particle products has alleviated this concern now. [23] The stability of Mg particles is attributed to the thin Mg oxide layer over the surface of Mg particles, which retards the further oxidation of Mg particles under mild conditions. [23, 47] Third, the oxidation of Mg or Zn usually creates high pH conditions, under which iron is likely passivated but Al and Al alloys tend to corrode [1, 68] However, some research results have shown that Mg oxidation products cannot generate an environment which is basic enough for Al or Al alloys to dissolve. [47] Furthermore, different polymer binder systems, such as epoxy-polyamide, silane modified epoxy hybrids, inorganic-organic hybrid sol-gel system, are found to be stable under the basic environment and can still provide good adhesion for MgRP systems. [69, 70]

A lot of studies have been carried out on MgRP systems and the results provide useful information about MgRP, such as the electrochemical performance, protection mechanisms, and the durability and failure modes. [47, 61, 64, 65, 71-74]

Cathodic protection provided by MgRP for AA2024 T3 has been verified by various measurements. The results of the OCP measurements for the MgRP coated AA2024 T3 panels immersed in 0.1% NaCl solution have proved the presence of cathodic protection of MgRP. As shown in Figure 2-5, the OCPs of the MgRP coated samples maintained around -1.0V/SCE, which was between the OCP of bare AA20204 T3 (-0.650V /SCE) and the OCP of Mg particles (-1.6V/SCE). [65]

Scanning vibrating electrode technique (SVET) also has been used to further confirm

the principle of cathodic protection when damage occurred on MgRP. [71, 73, 74] In Figure 2-6 shown is the SVET characterization of an AA2024 T3 sample coated with MgRP. A scribe was made on the surface of sample to expose AA2024 T3 substrate to dilute Harisons' solution (DHS) directly. The shadow areas in Figure 2-6 (A-2) and (B-2) represent the damaged area.

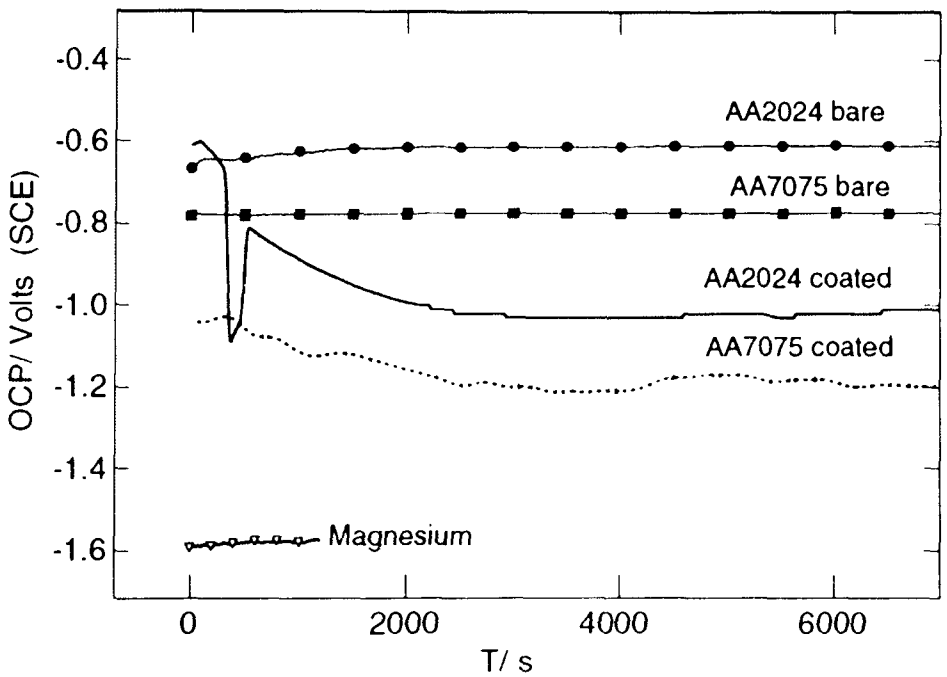

Figure 2-5. Open circuit potential of Mg particles, bare Al alloys (AA2024 T3 and AA7075) and the same Al alloys coated with MgRP when exposed in 0.1% NaCl. (Copied from D. Battocchi, et al., *Corrosion Science*, **2006**, 48, 1292.)

In the beginning of immersion, the anode as the red arrow region can be observed in Figure 2-6 (A-1) and (A-2). It implies that the substrate in the scribed area was corroding. After thirty minutes of DHS immersion, the anodic area disappeared in Figure 2-6 (B-1) and (B-2). It suggests that MgRP did not provide cathodic protection to the damaged area until a certain time of exposure. After the cathodic protection was induced, the damaged

area was under the protection of MgRP.

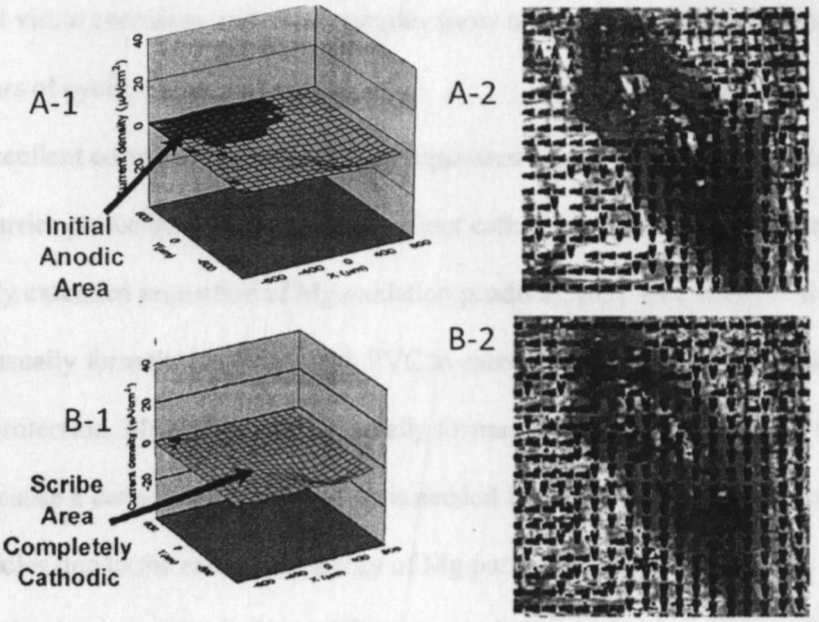

Figure 2-6. 3D SVET plots of current density distribution in the scratched area of Mg-rich primer coated AA2024 T3 sample: (a) immediately after dilute Harrison's solution (DHS) immersion; (b) 30 minutes of DHS immersion. (Copied from G. Bierwagen, et al., *Prog. Org. Coat.*, **2007**, 59, 172.)

Furthermore, the results from potentiodynamic measurements [64, 65] and scanning electrochemical microscopy (SECM) [74] also demonstrated that MgRP provided effective cathodic protection to protect Al alloy substrate from corrosion.

MgRP is a Cr-free coating system since it requires a simple cleaning of substrate and a combination of aerospace topcoat. Many topcoated MgRP samples have been tested in different conditions, such as outdoor weathering, spot test on some parts of airplane, and all sorts of accelerated weathering exposure. [23] The results show that the corrosion protection performance of topcoated MgRP system exceeds the current Cr-based aerospace coating system. For example, the excellent anti-corrosion behavior of the topcoated MgRP has been observed in the outdoor tests on Key West and Daytona Beach; all types of

topcoated MgRP systems have passed 4800 hours of the cyclic exposure (ASTM D 5894-96) without visual corrosion, and some samples show no significant corrosion even after 10,000 hours of cyclic exposure. [23]

The excellent corrosion protection of the topcoated MgRP system can be attributed to the good barrier protection of topcoat, the efficient cathodic protection of Mg particles and the probably extended protection of Mg oxidation products. [65] But different from ZRPs which are usually formulated at very high PVC to extend the efficiency and durability of corrosion protection, MgRP system is generally formulated below but very near the CPVC, [47, 65] because a certain barrier protection is needed for MgRP to reduce the consume rate of Mg particles due to the extensive activity of Mg particles.. Therefore, the way to use various conductive extenders in the MgRP system to improve the electrical conductivity is more necessary.

In summary, as the promising alternative to the current Cr-based aerospace coating system, the MgRP system has been successfully developed and shown excellent corrosion protection for AA2024 T3. The studies of protection mechanism and durability of the MgRP have expanded the knowledge of metal-rich coatings in general.

2.3. Electrochemical testing methods for the studies of metal-rich coatings

Different electrochemical testing methods have been designed and widely used for the purposes of various coating studies, such as film characterization, corrosion mechanism studies, anticorrosion performance evaluation, and protective durability assessment. There are many advantages of using electrochemical testing methods to study coating systems. First, corrosion is a combined phenomenon including many different electrochemical reaction processes. Electrochemical methods have the ability to detect and record the

changes of current and potential occurring in some typical sites. Second, the electrochemical measurements can provide reliable information to demonstrate the failure of coating system even before any visual evidence appears. [14] In fact, the latest electrochemical techniques can help coating scientists to obtain the "true scientific understanding" [16] of organic protective coatings and to make the sophisticated interpretation and predication for coating systems. For example, since 1992 both research groups of Bierwagen and Tallman in NDSU have adapted several new electrochemical techniques in the studies of organic coating system, including electrical impedance spectroscopy (EIS), [15, 47, 64, 65, 71-73, 75-81] electrochemical noise measurement (ENM), [77, 82-89] scanning vibrating electrode technique (SVET), [71, 73, 74, 90-93] scanning electrochemical microscopy (SECM), [71, 74] local electrochemical impedance spectroscopy (LEIS) and conductive atomic force microscopy (CAFM). [5] The research results and the considerable publications have verified that these electrochemical techniques are very useful in testing, interpreting and predicting the anticorrosion performance of organic coatings. Two electrochemical techniques as the routine methods for coating system characterization are briefly discussed as following.

2.3.1. Electrochemical impedance spectroscopy (EIS)

EIS is a powerful electrochemical method. It can be used to characterize the electrical properties of various materials and study the dynamics of solid-solid or solid-liquid interfaces. The principle of EIS was established as early as 1920s and the experimental work of using EIS was developed in 1950s. [94] Since early 1980s, EIS has been extensively applied in coating research.

To date EIS has become one of the most widely used electrochemical methods for

coating characterization, corrosion mechanism studies, performance evaluation and failure detection in coating research. [8, 12, 13, 46, 73, 79, 95-97] A distinct advantage is that EIS is a nondestructive approach because only a very small AC potential signal (about 5 mv) is applied to the tested sample system and the current responses are detected. Therefore, using EIS for measurement would not cause any significant change to the system under study and the detected signals generally reflect the information of non-disturbed system. Furthermore, EIS is a very sensitive measurement so that the small changes in coating system can be detected long before they are visibly noticed. Another attractive ability of EIS to coating research is that EIS can provide correlation between the quantitative data extracted from EIS spectrums and some coating properties, such as the barrier property and the water-uptake of coating. In general, the barrier performance of coating system is related to the impedance modulus at low frequency (lower than 1Hz). [98, 99] The high impedance modulus indicates the good barrier property of coating system. Through modeling EIS data by using equivalent electrical circuits, the properties of the coating film, the substrate, the electrolyte and the interface can be well represented by different electrical circuit components. [100, 101]

2.3.2. Electrochemical noise measurement (ENM)

ENM is another powerful electrochemical method to study the performance of coating system. [77, 84, 102-105] ENM is a true non-intrusive method since there is no external stimulus needed. Only the fluctuations of potential and current generated by the sample itself will be collected. ENM testing does not bring any imposed change to the system under study. Thus, ENM is one of the most preferred techniques for monitoring the performance of coatings.

The most widely used cell configuration of ENM is associated with a three-electrode system, as illustrated in Figure 2-7.

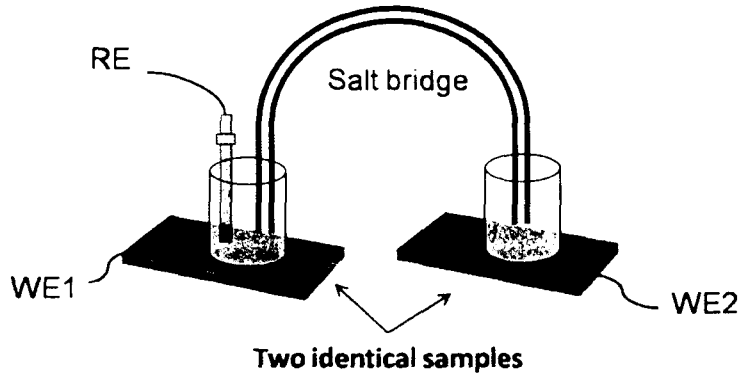

Figure 2-7. Experimental set-up of ENM tests.

Two identical samples used as the working electrodes are coupled, and each of them holds a glass cell by a clamp. A salt bridge is used to connect the electrolyte in the two glass cells. Meanwhile, a reference electrode is placed in one glass cell. The current fluctuations between the two working electrodes and the potential fluctuations between one working electrode and the reference electrode are collected simultaneously.

Noise resistance R_n can be obtained through equation (2.1):

$$R_n = \frac{\sigma_V}{\sigma_I} \qquad (2.1)$$

Where, σ_V and σ_I are the standard deviation of potential and current, respectively.

The origin for the noise signals collected from ENM testing has been of interest to electrochemists. Generally, there are three forms of noise which can be related to the electrochemical processes occurring in the interested system: [106] thermal noise, shot noise and flicker noise. Furthermore, the characteristics of noise via different spectral methods could be used to identify the corrosion type. For example, the localized corrosion processes could result in the increase of transient events if many transient events are

happening, a large f_n could be obtained, which indicates that the uniform corrosion is occurring; in contrast, the small f_n could be related to a localized corrosion. Shot noise is generated from the quantized charge carriers randomly passing through a given point in circuit. Thus the shot noise analysis can be used to identify the type of corrosion via estimating some important parameters, e.g. corrosion current (I_{corr}), characteristic charge (q) and characteristic frequency (f_n). The magnitude of q is considered to be related to the intensity of corrosion process because q implies the "amount of material removed in an individual event". [89, 106]

Although further work is required to establish the relationship between the features obtained from ENM analysis and the parameters related to corrosion type, ENM has become a powerful tool to study the electrochemical processes of corrosion occurring in different systems.

2.4. Classification of corrosive environments

The performance of metal-rich coating, including the protection efficiency and durability, is not only related to the coating system itself but also strongly depends on the service environment. [59] In other words, even the same coating system can exhibit entirely different performance when exposed to different environments. In addition, the corrosion mechanisms could be totally different, too. Thus, the influence of the service environment should be considered in the studies of metal-rich coatings.

2.4.1. Outdoor exposure

The outdoor exposure has been classified into different types of exposure conditions according to ISO 12944 "Coatings and vanishes-Corrosion protection of steel structures by protective coating systems". [107] One classification of outdoor exposure as well as the

major influence factors is illustrated in Figure 2-8. [14]

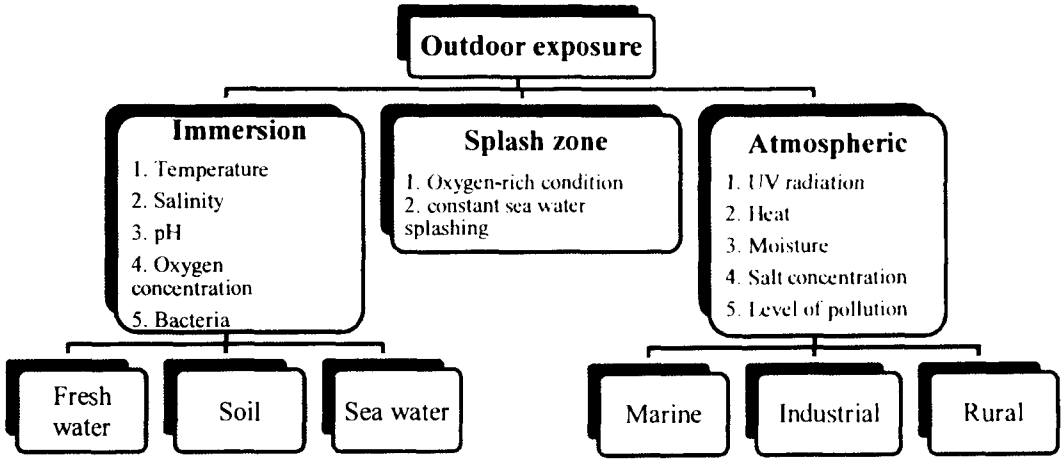

Figure 2-8. Classification of anticorrosive coatings serving conditions and the major environmental influence factors. (Adapted from P. Sorensen, et al., *J. Coat. Technol. Res.*, **2009**, 6, 135.)

2.4.2. Accelerated weathering exposure

Outdoor natural exposures provide the practical and true corrosive environments for evaluating and ranking the anticorrosive performance of protective coatings. But for a high-performance coating, it can take a very long time, e.g. several years, to complete the whole deterioration process. Therefore, the Accelerated weathering methods are designed for the purposes of quickly evaluation, screening, development and comparison of coatings anticorrosive performance. [14] An Accelerated weathering method is to simulate the major environmental factors by amplifying the natural influences. The key target is to shorten the time scale of a coating degradation occurred in natural exposure to a much shorter period without changing the major corrosion processes. Thus, it is important that the Accelerated weathering methods should represent the typical environments but not change the corrosion mechanisms of the coating system under study.

There are many factors which can speed up the corrosion failure of coatings, such as increasing temperature, raising the concentration of corrosive agents, and applying the continuous stress by salt splashing. Historically, ASTM B117 salt spray test [108] is one of the most popular methods for the accelerated exposure. Also, it is the most widely used test to rank the corrosion performance for the coating protected steel in industries. According to ASTM B117, a weathering chamber maintains a constant salt fog at 35°C via a continuous spray of 5% sodium chloride. However, this salt spray test cannot provide reasonable ranking results of the protection performance for the metal-rich coatings, because it hardly reproduces the corrosive conditions that the metal-rich coatings probably encounter. First, the concentration of sodium chloride (about 5% by weight) is too high to reflect the true conditions of natural exposure; second, the continuous salt spray in B117 cabinet differs from the alternate wet-dry cycles of a natural environment. As a result, corrosion mechanisms can be significantly distorted in B117; third, the corrosive agent in B117 is sodium chloride, but in most natural exposure, the present CO_2 and SO_4^{2-} also can influence the corrosion mechanisms and further change the composition of corrosion products.

The Prohesion® weathering method is also a very popular Accelerated weathering exposure. The weathering processes in Prohesion® chamber are made up of the alternative wet-dry cycle, which has one-hour drying cycle at 35°C followed by one-hour salt fog cycle at 25°C. The salt fog is produced by a salt spray of dilute Harrisons' solution (DHS), which contains 0.35% ammonium sulfate and 0.05% sodium chloride with pH of 4-5. [109] In comparison to the salt spray B117, the corrosive conditions produced by Prohesion® weathering are much closer to the natural exposure. First, both the wet-dry cycle and the

low-high temperature cycle imitate the two major climate changes in field exposure. The one-hour alternates of wet-dry or low-high temperature increases the severity of the weathering stress. Second, the DHS has the similar components as the acid rain; as a result, the influence of pollution on corrosion can be taken into account.

In comparison to outdoor exposure, the Accelerated weathering methods can significantly shorten the time period for the degradation of a coating system. However, a suitable Accelerated weathering method should keep the corrosion mechanisms as same as the ones of field exposure.

2.5. Design parameters for metal-rich primer

The development of a high-performance metal-rich primer system is full of challenges. There are many factors, which could significantly influence the final properties of metal-primer system.

The properties of raw materials, such as the types of polymer binders, pigments, particle size distribution and shape, solvents and additives;

The formulation of primer, e.g. PVC or VOC of paint, the content of each components, the formulating procedures, the dispersion of pigments;

The application of primer, e.g. the cleanness and pretreatment processes for substrates, the technique of paint application, viscosity of paint;

The film formation of primer, e.g. temperature, humidity, air cleanliness and air circulation, and curing time;

The service environment of primer, e.g. outdoor exposure, immersion, low-high temperature cycle, Prohesion chamber or salt spray;

Moreover, the combination and interaction of all these factors will cause the further

complexity of metal-rich primer system. As a result, it is extremely difficult to predict the priori effects of each factor.

Therefore, in order to understand how the design parameters influence the final performance of a metal-rich primer system, it is necessary to simplify the system by fixing some factors. For example, if the PVC is the major parameter which needs to be studied, the solvents, additives or even the polymer binders can be held constantly. So, the performance changes of this coating system can be considered as the consequences of the effects of PVC rather than other factors. In addition, a principal characteristic of metal-rich primer system is the electronic conductivity among the metallic particles and also between the particles and the substrate. Thus, the important design parameters are those which can significantly influence the electrical conductivity of metal-rich primer. For instance, high PVC can benefit the galvanic action; the factors of particle size, particle size distribution and shape can affect the packing efficiency of particles; the chemical composition of metallic particles can influence the protection mechanism.

In Figure 2-9, a brief experimental design for developing a high-performance metal-rich coating is shown. [3] The design parameters, e.g. binders, pigments, solvents and additives, need to be defined. Some experimental factors, such as the methods of substrate cleaning, the curing and weathering conditions, are fixed. Through analyzing the data collected from the performance tests, the influences of the design parameters can be evaluated and further provide the useful information for the further development.

2.6. Conclusions

As the major strategy of corrosion protection, various coating systems exhibit the excellent anticorrosion performance for metals and alloys in aggressive environments.

Among them, metal-rich coating systems are very unique since they provide cathodic protection when damage occurs to the coating system. The successes of ZRP and MgRP systems have proved that the desired corrosion protection can be achieved via the combination of different protection mechanisms.

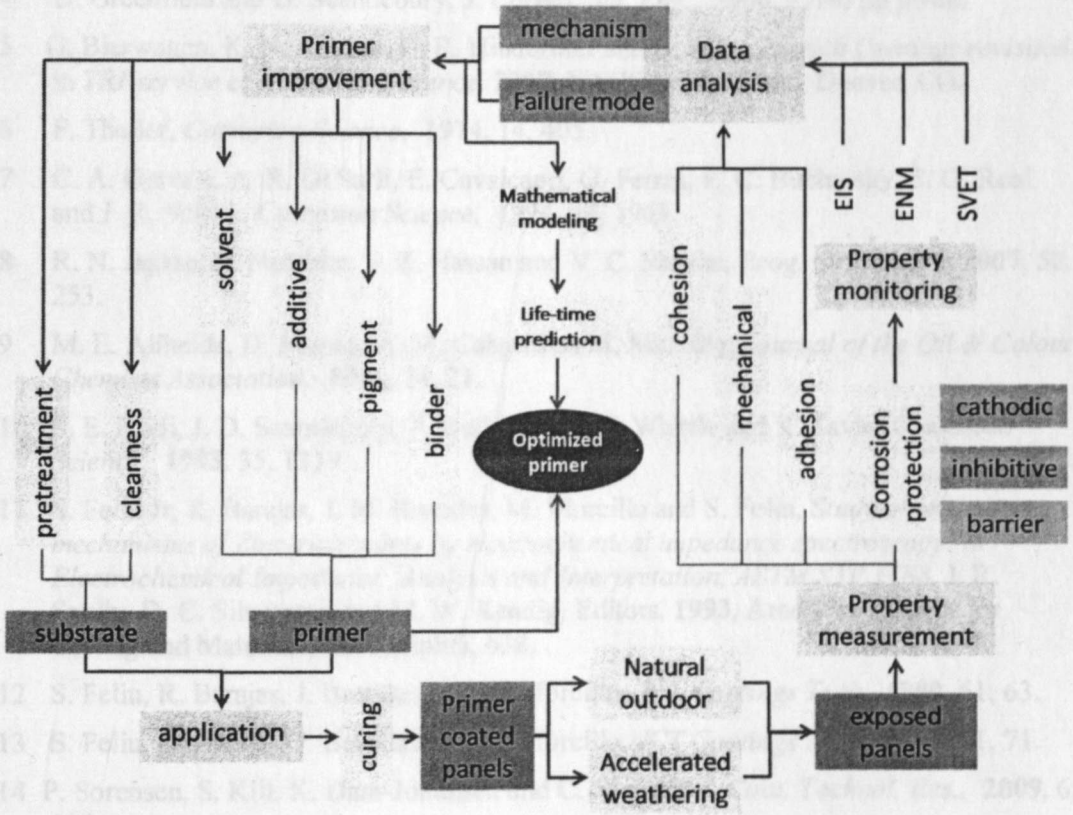

Figure 2-9. Workflow design of high-performance metal-rich primer development.

The research studies on ZRP and MgRP systems have expanded the knowledge of metal-rich primer system and deepened the insight into the relationship between the anticorrosion performance and coating formulation. In addition, the understanding can efficiently and economically benefit the processes of developing new high-performance and environmental-friendly metal-rich primer systems.

2.7. References

1 D. A. Jones, *Principles and prevention of corrosion*, **1996**, Prentice-Hall, Inc.

2 D. Talbot and J. Talbot, *Corrosion science and technology*, **1998**, CRC Press LLC.

3 G. Bierwagen and A. Huovinen, *Paint Formulation*, 4th ed, Shreir's Corrosion, Vol. 4, **2010**, Elsevier B.V.

4 D. Greenfield and D. Scantlebury, *J. Corros. Sci. Eng.*, **2000**, 3, No pp given.

5 G. Bierwagen, K. N. Allahar, B. R. Hinderliter and H. Jung, *Zn-rich Coatings revisited*, in *TRI-service corrosion conference*, **2007**, NACE International, Denver, CO.

6 F. Theiler, *Corrosion Science*, **1974**, 14, 405.

7 C. A. Gervasi, A. R. Di Sarli, E. Cavalcanti, O. Ferraz, E. C. Bucharsky, S. G. Real and J. R. Vilche, *Corrosion Science*, **1994**, 36, 1963.

8 R. N. Jagtap, R. Nambiar, S. Z. Hassan and V. C. Malshe, *Prog. Org. Coat.*, **2007**, 58, 253.

9 M. E. Almeida, D. Pereira, A. M. Cabral and M. Morcillo, *Journal of the Oil & Colour Chemists Association*, **1991**, 74, 21.

10 S. E. Faidi, J. D. Scantlebury, P. Bullivant, N. T. Whittle and R. Savin, *Corrosion Science*, **1993**, 35, 1319.

11 S. Feliu Jr, R. Barajas, J. M. Bastidas, M. Morcillo and S. Feliu, *Study of protection mechanisms of Zinc-rich paints by electrochemical impedance spectroscopy*, in *Electrochemical Impedance: Analysis and Interpretation, ASTM STP 1188*, J. R. Scully, D. C. Silverman and M. W. Kendig, Editors, **1993**, American Society for Testing and Materials, Philadelphia, 438.

12 S. Feliu, R. Barajas, J. Bastidas and M. Morcillo, *JCT Coatings Tech*, **1989**, 61, 63.

13 S. Feliu, R. Barajas, J. Bastidas and M. Morcillo, *JCT Coatings Tech*, **1989**, 61, 71.

14 P. Sorensen, S. Kiil, K. Dam-Johansen and C. Weinell, *J. Coat. Technol. Res.*, **2009**, 6, 135.

15 G. Bierwagen and D. Tallman, *Prog. Org. Coat.*, **2001**, 41, 201.

16 G. Bierwagen, *J. Coat. Technol. Res.*, **2008**, 5, 133.

17 R. N. Jagtap, P. P. Patil and S. Z. Hassan, *Prog. Org. Coat.*, **2008**, 63, 389.

18 Z. Panossian, L. Mariaca, M. Morcillo, S. Flores, J. rocha, J. J. Pena, F. Herrera, F. Corvo, M. sanchez, O. T. Rincon, G. Pridybailo and J. Simancas, *Surface & Coatings Technology*, **2005**, 190, 244.

19 W. K. Asbeck and M. Van Loo, *J. Ind. Eng. Chem. (Washington, D. C.)*, **1949**, 41, 1470.

20 G. Bierwagen and T. Hay, *Prog. Org. Coat.*, **1975**, 3, 281.

21 G. Bierwagen, *JCT Coatings Tech*, **1992**, 64, 71.

22 G. Bierwagen, *J. Paint Tech.*, **1972**, 44, 46.

23 G. Bierwagen, R. Brown, D. Battocchi and S. Hayes, *Prog. Org. Coat.*, **2010**, 67, 195.

24 Z. W. Wicks Jr., F. N. Jones and S. P. Pappas, *Organic Coatings: Science and Technology*, 2rd ed, **1999**, Hoboken, New Jersey, John Wiley & Sons, Inc.

25 J. Krzywicki, *Fastener Technology International*, **2006**, August, 34.

26 C. H. Hare, *Journal of Protective Coatings & Linings* **1998**, July, 17.

27 G. Eccleston, *Journal of Protective Coatings & Linings*, **2000**, October, 85.

28 G. Parashar, D. Srivastava and P. Kumar, *Prog. Org. Coat.*, **2001**, 42, 1.

29 T. Ginsberg, *JCT Coatings Tech.* **1981**, 53, 23.

30 G. Eccleston, *Journal of Protective Coatings & Linings*, **1998**, January, 36.

31 G. B. Byrnes and L. Vincent, *Materials Performance*, **1994**, 33, 31.

32 H. Marchebois, S. Touzain, S. Joiret, J. Bernard and C. Savall, *Prog. Org. Coat.*, **2002**, 45, 415.

33 H. Marchebois, C. Savall, J. Bernard and S. Touzain, *Electrochim. Acta*, **2004**, 49, 2945.

34 D. Pereira and J. D. Scantlebury, *Corrosion Science*, **1990**, 30, 1135.

35 C. M. Abreu, M. Izquierdo, P. Merino, X. R. Novoa and C. Perez, *Corrosion* **1999**, 55, 1173.

36 M. Morcillo, R. Barajas, S. Feliu and J. M. Bastidas, *Journal of Materials Science*, **1990**, 25, 2441.

37 H. Marchebois, S. Joiret, C. Savall, J. Bernard and S. Touzain, *Surf. Coat. Technol.*, **2002**, 157, 151.

38 O. O. Knudsen, U. Steinsmo and M. Bjordal, *Prog. Org. Coat.*, **2005**, 54, 224.

39 D. Schmidt, B. Shaw, E. Sikora, W. shaw and L. Laliberte, *Prog. Org. Coat.*, **2006**, 57, 352.

40 A. Kalendova, *Anti-Corrosion Methods and Materials*, **2002**, 49, 173.

41 N. Fawcett, C. Stearns and B. Bufkin, *JCT Coatings Tech*, **1984**, 56, 49.

42 B. Muller, I. Forster and W. Klager, *Prog. Org. Coat.*, **1997**, 31, 229.

43 C. Giudice, J. Benitez and A. Pereyra, *J. Coat. Technol. Res.*, **2004**, 1, 291.

44 A. Kalendova, *Prog. Org. Coat.*, **2003**, 46, 324.

45 W. Chen, P. Chen, H. Y. Chen, J. Wu and W. Tsai, *Applied Surface Science*, **2002**, 187, 154.

46 E. Cavalcanti, O. Ferraz and A. R. Disarli, *Prog. Org. Coat.*, **1993**, 23, 185.

47 M. Nanna and G. Bierwagen, *J. Coat. Technol. Res.*, **2004**, 1, 69.

48 S. Shreepathi, P. Bajaj and B. Mallik, *Electrochim. Acta*, **2010**, 55, 5129.

49 J. Johnson, M. Barbato, S. Hopkins and M. O'Malley, *Prog. Org. Coat.*, **2003**, 47, 198.

50 S. Feliu Jr. J. Bastidas, M. Morcillo and S. Feliu, *J. Coat. Technol. Res.*, **1991**, 63, 67.

51 F. Simko and V. Simpson, *JCT Coatings Tech*, **1976**, 48, 61.

52 V. P. Simpson and F. A. Simko, *J.Oil Col.Chem. Assoc.*, **1973**, 56, 491.

53 N. Fawcett, C. Stearns and B. Bufkin, *JCT Coatings Tech*, **1984**, 56, 31.

54 S. Gonzalez, F. Caceres and R. Souto, *Prog. Org. Coat.*, **2003**, 46, 317.

55 V. Barranco, S. Feliu Jr and S. Feliu, *Corrosion Science*, **2004**, 46, 2203.

56 M. Selvaraj and S. Guruviah, *Prog. Org. Coat.*, **1996**, 28, 271.

57 K. R. Baldwin, R. I. Bates, R. D. Arnell and C. J. E. Smith, *Corrosion Science*, **1996**, 38, 155.

58 R. Hausbrand, M. Stratmann and M. rohwerder, *Corrosion Science*, **2009**, 51, 2107.

59 N. C. Hosking, M. A. Strom, P. H. Shipway and C. D. Rudd, *Corrosion Science*, **2007**, 49, 3669.

60 G. Bierwagen, D. Tallman, M. Nanna, D. Battocchi, A. Stamness and V. J. Gelling, *Polymer Preprints (American Chemical Society, Division of Polymer Chemistry)*, **2004**, 45, 144.

61 G. P. Bierwagen, M. E. Nanna and D. Battocchi, *Magnesium rich coatings and coating systems*. **2005**, (NDSU Research Foundation, USA). Application: WO, 65

62 J. Janata, D. Baer, G. Bierwagen, H. Birnbaum, A. Davenport, H. Isaacs, Hedberg, M. Kendig, F. Mansfeld, B. Miller, A. Wieckowski and J. Wilkes, *Issues related to chromium replacement*, in *187th Meeting of the electrochemical Society* **1995**, Reno, Nevada.

63 R. Twite and G. Bierwagen, *Prog. Org. Coat.*, **1998**, 33, 91.

64 D. Battocchi, A. M. Simoes, D. E. Tallman and G. P. Bierwagen, *Corrosion Science*, **2006**, 48, 2226.

65 D. Battocchi, A. Simoes, D. Tallman and G. Bierwagen, *Corrosion Science*, **2006**, 48, 1292.

66 C. Hare, *Corrosion control of steel by organic coatings*, 2nd ed, Uhlig's Corrosion Handbook, ed. R. W. Review, **2000**, New York, John Wiley & Sons.

67 G. Bierwagen, R. Fishman, T. Storsved and J. Johnson, *Prog. Org. Coat.*, **1999**, 35, 1.

68 K. B. Oldham and J. C. Myland, *Fundamentals of electrochemical science*, **1994**, San Diego, California, Academic Press, Inc.

69 M. E. Nanna, *Mg-rich coating systems for Al 2024-T3*, in *Coatings and Polymeric Materials*. **2003**, NDSU, Fargo.

70 D. Wang, *Organosilane self-assembled layers (SAMs) and hybrid silicate Mg-rich primers for the corrosion protection*, in *Coatings and polymeric materials*. **2007**, North Dakota State University, Fargo.

71 A. Simoes, D. Battocchi, D. Tallman and G. Bierwagen, *Assessment of the corrosion protection of aluminium substrates by a Mg-rich primer: EIS, SVET and SECM study*, **2008**.

72 K. N. Allahar, D. Battocchi, M. E. Orazem, G. P. Bierwagen and D. E. Tallman, *J. Electrochem. Soc.*, **2008**, 155, E143.

73 G. Bierwagen, D. Battocchi, A. Simoes, A. Stamness and D. Tallman, *Prog. Org. Coat.*, **2007**, 59, 172.

74 A. Simoes, D. Battocchi, D. Tallman and G. Bierwagen, *Corrosion Science*, **2007**, 49, 3838.

75 G. Bierwagen, L. He and D. Tallman, *Macromolecular Symposia*, **2002**, 187, 909.

76 G. Bierwagen, D. Tallman, J. Li and L. He, *Prog. Org. Coat.*, **2003**, 46, 148.

77 R. De Rosa, D. Earl and G. Bierwagen, *Corrosion Science*, **2002**, 44, 1607.

78 L. Ellingson, T. Shedlosky, G. Bierwagen, E. de la Rie and L. Brostoff, *Stud. Conserv.*, **2004**, 49, 53.

79 B. Hinderliter, S. Croll, D. Tallman, Q. Su and G. Bierwagen, *Electrochim. Acta*, **2006**, 51, 4505.

80 C. Jeffcoate, T. Wocken and G. Bierwagen, *J. Materials Eng. & Performance*, **1997**, 6.

81 H. Xu, D. Battocchi, D. E. Tallman and G. P. Bierwagen, *Corrosion*, **2009**, 65, 318.

82 G. Bierwagen, *J. Electrochem. Soc.*, **1994**, **14**, L155.

83 G. Bierwagen, V. Balbyshev, D. Mills and D. Tallman, *Fundamental considerations on electrochemical noise methods to examine corrosion under organic coatings*, in *Proc. of the Symposium on Advances in Corrosion Protection by Organic Coatings II*, **1995**, Special Publication of The Electrochemical Society.

84 G. Bierwagen, C. Jeffcoate, J. Li, S. Balbyshev, D. Tallman and D. Mills, *Prog. Org. Coat.*, **1996**, 29, 21.

85 G. Bierwagen, D. Mills and D. Tallman, *Electrochemical Noise Methods as a Possible In Situ Corrosion Sensing Technique*, **1993**, Houston, TX, 12th International Corrosion Congress.

86 G. Bierwagen, D. Tallman, S. Touzain, A. Smith, R. Twite, V. Balbyshev and Y. Pae, *Electrochemical Noise Methods Applied to the Study of Organic Coatings and Pretreatment*, in *Corrosion 98*, **1998**, NACE Int., San Diego, CA.

87 G. Bierwagen, X. Wang and D. Tallman, *Prog. Org. Coat.*, **2003**, 46, 163.

88 D. Mills, G. Bierwagen, D. Tallman and B. Skerry, *Materials Performance*, **1995**, 34, 33.

89 Q. Su, K. Allahar and G. Bierwagen, *Electrochim. Acta*, **2008**, 53, 2825.

90 J. He, V. Gelling, D. Tallman and G. Bierwagen, *J. Electrochem. Soc.*, **2000**, 147, 3661.

91 J. He, V. Gelling, D. Tallman, G. Bierwagen and G. Wallace, *J. Electrochem. Soc.*, **2000**, 147, 3667.

92 J. He, D. E. Tallman and G. P. Bierwagen, *J. Electrochem. Soc.*, **2004**, 151, B644.

93 D. Tallman, J. He, V. Gelling, G. Bierwagen and G. Wallace, *Scanning Vibrating Electrode Studies of Electroactive Conducting Polymers on Active Metals*, in *Conductive/Electroactive Polymers for Corrosion Prevention*, P. Zarras, Editor. **2003**, ACS Symposium Series, 228.

94 E. Barsoukov and J. R. Macdonald, *Impedance Spectroscopy Theory, Experiment, and Application*, second ed, **2005**, Hoboken, New Jersey, John Wiley & Sons, Inc.

95 E. Akbarinezhad, H. R. Faridi and A. Ghanbarzadeh, *Surface Engineering*, **2009**, 25, 163.

96 G. Baril, G. Galicia, C. Deslouis, N. Pebere, B. Tribollet and V. Vivier, *J. Electrochem. Soc.*, **2007**, 154, C108.

97 G. Grundmeier, W. Schmidt and M. Stratmann, *Electrochim. Acta*, **2000**, 45, 2515.

98 D. Loveday, P. Peterson and B. Rodgers, *JCT Coatings Tech*, **2004**, August, 46.

99 D. Loveday, P. Peterson and B. Rodgers, *JCT Coatings Tech*, **2004**, October, 88.

100 R. E. Lobnig, V. Bonitz, K. Goll, W. Villalba, R. Schmidt, P. Zanger, J. Vogelsang and I. Winkels, *Prog. Org. Coat.*, **2007**, 60, 77.

101 R. E. Lobnig, W. Villalba, K. Goll, J. Vogelsang, I. Winkels, R. Schmidt, R. Zanger and J. Soetemann, *Prog. Org. Coat.*, **2006**, 55, 363.

102 O. Duran, E. Vera, C. A. Ortiz and A. Heyn, *Materials and Corrosion*, **2007**, 58, 997.

103 S. Mabbutt, D. Mills and C. Woodcock, *Prog. Org. Coat.*, **2007**, 59, 192.

104 D. Mills, S. Mabbutt and G. Bierwagen, *Prog. Org. Coat.*, **2003**, 46, 176.

105 J. Sanchez-Amaya, R. Osuna, M. Bethencourt and F. Botana, *Prog. Org. Coat.*, **2007**, 60, 248.

106 R. A. Cottis, *Corrosion*, **2001**, 57, 265.

107 *ISO 12944. International Standards Organization*, **1998**.

108 ***B117-97**, Standard Practice for Operating Salt Spray (Fog) Apparatus*, **1997**, American Society for Test and Materials.

109 ***ASTM G85-98**, Standard Practice for Modified Salt Spray (Fog) Testing*, **1998**, ASTM International.

CHAPTER 3. EFFECTS OF PIGMENTATION ON THE CRITICAL PIGMENT VOLUME CONCENTRATION (CPVC) OF MG ALLOY-RICH COATING SYSTEMS

3.1. Introduction

In the coating industry, a variety of different pigments are used in the coating system to modify the rheological properties of paints for aiding application, accomplishing the optimal aesthetic appearance, hiding the underlying substrate or primer, achieving desirable performance, e.g. anti-corrosion, solvent resistance and durability, or reducing cost. [1] The final performance of the pigmented coating system is not only related to the inherent properties of pigments, e.g. physical and chemical properties, particle size, particle shape but also the amount of pigments used, which is usually valued as pigment volume concentrations (PVC) in coating industry, and the way of the particles packing in polymer matrix. Therefore, it is of importance to study the relationship between the final properties of the pigmented coating systems and the influencing factors to gain an insight into the coating systems under study.

3.1.1. Significance of the studies of PVC and CPVC in coating industry

The relationship between the coating performance and PVC has been studied since the 1920's. Asbeck and Van Loo [2] quantitatively studied how some physical properties of coating film varied as the function of PVC in 1940's. For example, the mechanical properties, permeability, gloss, or electrical conductivity of coating films have been found to be closely related to PVC: with the increase of PVC, the gloss and tensile strength of coating films decrease, however, the roughness, permeability and density of coating films

increase. In addition, a specific PVC has been studied as the critical pigment volume concentration (CPVC), since many coating properties, such as gloss, mechanical properties, water and ion permeability or electrical conductivity, exhibit dramatically discontinuous changes at this PVC. [3, 4]

The CPVC is a transition point at which there is just enough polymer binder to cover the surface of pigments as well as to fill all the interstices between the pigments. [3, 4] For a pigmented coating film, when its PVC is below the CPVC, it indicates that polymer binder not only covers the surface of pigments but also fills the interstitial spaces between pigments. In other words, the polymer binder is a continuous phase in which pigments are homogeneously dispersed. However, when a PVC is above the CPVC, there is no enough polymer binder to fill all the interstitial spaces between pigments. As a result, voids start to emerge in coating film and break down the continuous phase of polymer binder. The presence of voids changes the microstructure of coating film and further causes the abrupt changes of film properties around the point of CPVC. Therefore, CPVC is a very useful coating design/formulation parameter.

Actually, a better way to utilize CPVC information is to use the reduced pigment volume concentration (Λ/capital Greek lambda). Λ, which is defined as the ratio of the PVC to the CPVC, was first suggested by Bierwagen. [5] One of the advantages to use Λ is that the values of Λ are comparable even for the coating systems using different polymers and pigments. Λ takes into account both the effects of the adsorbed layer over the particles and the packing efficiency of pigments. [6]

The study of PVC and CPVC is of great significance for coating formulation, especially for metal-rich primer coatings. The efficiency of corrosion protection is not only

dependent on the types of metallic pigment used, but also related to the electrical conductivity between the metallic pigments as well as between the substrate and pigments. The particle packing efficiency of pigments in metal-rich primer affects the physical contacts between the metallic particles and further determines the conductivity of the whole system.

For Zn-rich primer systems (ZRPs), the electrical conductivity among Zn dusts will affect the efficiencies of cathodic protection. It is generally believed that the PVCs of ZRPs should be above the CPVC to ensure Zn particles have good electrical connection with each other. [7, 8] In other words, the value of Λ for a ZRP system is usually above 1. Similarly, Mg-rich primer (MgrP) system should be formulated at high PVCs to achieve good performance. However, due to the high activity of Mg and the large surface area of Mg paricles, it has been found that the suitable Λ value is lower but close to 1 ($\Lambda \sim 0.95$, etc). [9-11]

The study of PVC and CPVC are necessary and indispensable for the new metal-rich primer system using Mg-alloy particles as pigments. First, the study can help to determine the CPVC as well as a reasonable PVC range for formulation; secondly, the study can give insight into the particle packing efficiency of Mg alloy particles in polymer binder; third, the study can provide useful information and criteria for suitable pigment selection; fourth, the study can suggest the relationship between particle packing and particle' properties, such as particle shape, particle size and particle size distribution (PSD) for the modeling of CPVC prediction.

3.1.2. Experimental methods for CPVC determination and their limitations

Theoretically speaking, the CPVC of a given coating system can be determined by any

method which can detect the point of PVC where the abrupt changes of coating properties occur. As shown in Figure 3-1, some coating properties, such as gloss, blistering, rusting and permeability, exhibit the abrupt changes for determining CPVC. [5] The reason for the abrupt changes of many coating properties is the emergence of voids in the microstructure of coating system at CPVC. [4] In the following sections, several experimental methods used to determine CPVC of coating system are briefly introduced.

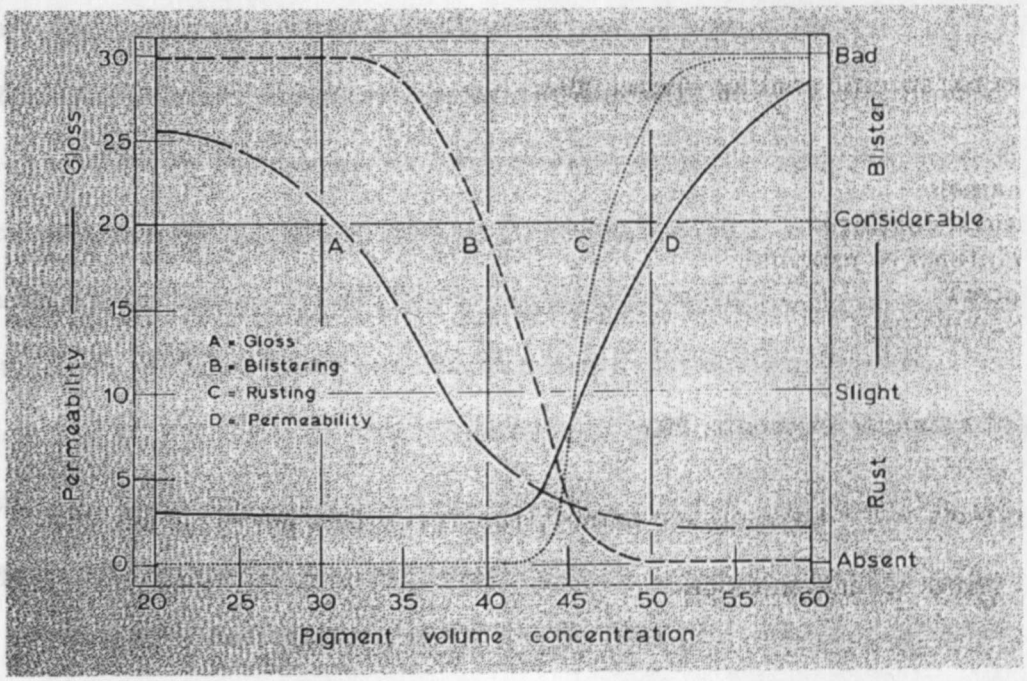

Figure 3-1. Influence of CPVC on some properties of coating film. (Copied from W. K. Asbeck and M. Van Loo, *J. Ind. Eng. Chem.*, **1949**, 41, 1470)

3.1.2.1. CPVC obtained from EIS measurement

The determination of CPVC by using electrochemical impedance spectroscopy (EIS) is based on detecting an abrupt impedance modulus drop with the increase PVCs of coating samples. [12-14] When PVC is below CPVC, the porosity of coating is generally low and the polymer binder with a continuous phase contributes the coating film high impedance modulus; but when PVC is above CPVC, polymer binder cannot fill all the interstitial

spaces between pigments and the voids start to emerge in coating film. As a result, an abrupt drop of the impedance modulus of coating film due to the increase of porosity can be observed. EIS has been found to be a suitable method for CPVC experimental determination. [15, 16] For a solvent base epoxy coating system, the highest impedance modulus ($|Z|_{maximum}$) or the impedance modulus at 0.01Hz ($|Z|_{0.01Hz}$) is approximate to the pore resistance of coating film and can be used as CPVC indicator; [16] also, in the work of Ahadi et al, open circuit potential (OCP) has been used to estimate CPVC. [17]

3.1.2.2. CPVC obtained from fluorescence microscopy measurement

The way to use fluorescence microscopy measurement to determine CPVC is a new method developed in our lab. The voids in a dry coating film can be decorated by fluorescence dye and then detected by fluorescence microscope due to its high sensitivity to the fluorescence dye. However, coating films are not uniform, especially at the microstructural level due to the particle agglomeration and the random distribution of voids, a statistical design and a proper choice of a statistically valid number of samples are important and necessary to limit the testing errors.

Besides the methods mentioned above, there are many other methods developed for the determination of CPVC experimentally. These include gloss measurement, scanning laser acoustic microscopy, water vapor permeability or Gilsonite staining. The details of these methods are briefly introduced in a review of Braunshausen. [18]

However, it is still a significant challenge for coating industry to establish a suitable method, by which the accurate CPVC for a given system can be determined. The reasons for the difficulties to determine the "true" CPVC of coating system can be mainly attributed to the following factors: first, CPVC is sensitive to the quality of the free film

preparation, such as pigment dispersion and film formation. In practice, the agglomeration due to the inadequate dispersion or poor film formation often occurs and results in a low CPVC value; second, the CPVC determination is related to the sensitivity of the particular testing method. For example, both the gloss measurement and Gilsonite staining are based on monitoring the roughness variation of the testing samples with the increase of PVCs. In fact, the point of inflexion is more ambiguous for the gloss measurement in comparison to the Gilsonite staining since the former one has the lower sensitivity; third, a particular property of coating film used as CPVC indictor can be influenced by other factors rather than PVC alone. For example, the impedance modulus of a coating film can be affected by the addition of conductive pigments; the roughness of a coating surface can be influenced by the poor film formation; fourth, the presence of the local concentration fluctuations (coarseness) of PVC [19] can also affect the accuracy of CPVC determination.

3.1.3. Mathematical methods for CPVC prediction

In the past few decades, it has been realized by the coating industry that the mathematical predication of CPVC has many advantages.[18] Compared with the experimental methods, the way to predict the CPVC values via a mathematical model requires less time and no bench work. [3] Furthermore, the CPVC obtained mathematically is based on the inherent properties of the raw pigments, e.g. OA, and is not affected by the types of polymer binders, the formulating procedures and the testing methods. Thus, to develop the models for mathematically predicting the CPVC is of high interest for coating industry. [18]

3.1.3.1. CPVC calculated from oil absorption (OA) data

The way to use OA value to predict the single pigment CPVC has been utilized for

many years. [20] The relationship between OA and CPVC can be expressed as the following equation: [1]

$$CPVC = \frac{1}{1 + \frac{OA \times \rho}{0.935}} \times 100\% \qquad (3.1)$$

Where ρ is the density of the pigment in g/ml, and 0.935 is the density of linseed oil in g/ml, and OA has the unit of grams of linseed oil per 100 grams of pigment.

In fact, equation (3.1) is a rough method for mathematically predicting CPVC, it holds true only when many critical conditions are met: a single type pigment; all the particles are spherical and of the same size; the endpoint of OA measurement is considered as same as the point of CPVC; the particle packing reaches the maximum efficiency at the endpoint of OA measurement; the relation between the weight of adsorbed linseed oil and the amount of mixed pigments is linear. In other words, the surface area for a certain weight of pigments is constant.

But, in practice these assumptions hardly hold true. In general, the OA consists of two parts: one is the strongly adsorbed linseed oil layer which covers all the surface of particles and the other is the part which fills all the interstices between the randomly dense packed pigments. The former part can be significantly influenced by the surface area, the surface roughness, the porosity of particles and the chemical properties of pigment. The latter one is strongly dependent on the particle packing efficiency, and it can be considerably affected by particle size, particle size distribution, particle shape and interparticle friction.

OA can be experimentally measured via different methods. Spatula rub-out (ASTM D281) [21] and Gardner-Coleman (ASTM D1483) [22] are the most common methods. However, the accuracies of OA measurements are still under debate. Many factors other

than the inherent properties of pigment can affect the values of OA, [23] such as the testing procedure, the strength and the time of rubbing, the level of aggregation /agglomeration, the tools used and the operators. For example, the presence of aggregates or agglomerates of pigments could reduce the OA value since some pigments in the aggregate cannot be wetted by linseed oil. Some results have showed that the variation of OA values between different operators could be ±25% due to the different interpretation of the endpoint of OA. [20]

However, the way to use OA for predicting CPVC is still widely applied in coating industry since it is simple and inexpensive. Although the low accuracy of OA method might be not suitable to determine the exact CPVC for a given pigment, it's still helpful to provide a reasonable range where the CPVC is probably located.

3.1.3.2. A numerical method for CPVC prediction

A very useful mathematical model for CPVC calculation based on pigments' properties was developed by Bierwagen in 1972 [3] and improved in 1999. [19] According to the suggestions of Bierwagen, the CPVC value for a given coating system is essentially affected by two factors : [3, 24] one is the adsorption of polymer binder on pigment particles' surface, which can increase the diameters of particles and in turn change the particle size distribution of pigments; [19] the other is the packing efficiency of these polymer-adsorbed pigment particles, from which the volume fraction of pigment in the total volume of coating film can be obtained. When the thickness of the adsorbed layer and the corresponding packing efficiency are known, CPVC value can be calculated. [3, 25] In fact, CPVC value can be predicted via the equation as following: [3, 19]

$$CPVC = \frac{\Phi_{wet}}{(1 + V_a)} \qquad (3.2)$$

where Φ_{wet} is the random densest packing efficiency, and V_a, the adsorbed oil volume fraction, can be expressed as

$$V_a = \frac{V_{absorbed\ oil}}{V_{pigment}} \tag{3.3}$$

There are two important assumptions for this computational model: [3]

1. All pigment particles are spherical. Based on the particle size distribution data, the random dense packing factor for a given pigment can be obtained by using an algorithm suggested by Lee.[26]
2. The thickness of the absorbed layer only depends on the nature of pigments irrespective of the polymer binder used, and the thickness of the absorbed layer is uniform irrespective of the shape and particle size of pigments.[3] Thus, the thickness value can be calculated from OA data.

The successful CPVC calculation through this model will be highly dependent on the accuracy of experimental measurement of particle size distribution and OA. From the work of Bierwagen, the CPVC value calculated from this model exhibited very good agreement with the experimental results for both solution polymer system and latex system.[25] It has verified that the modification of CPVC calculation to take into account of both the particle size distribution and the thickness of the adsorbed layer is practical, necessary and significant.

3.1.4. Essential elements influencing particle packing

For mathematical prediction of CPVC, a very important component is the particle packing efficiency, which refers to how particles are assembled in a space with a certain volume. For a spherical particle system, the particle packing characteristics have been well

studied.[27] It has been accepted that, for the monosize spheres, the maximum packing density of "an ordered close-packed array with a coordination number of twelve" is 0.7405. [28] However, it is very complicated to calculate the packing efficiency for the practical particles, since the pigments used in coating systems are hardly uniform in particle size and shape. In addition, many variables, such as packing order, particle size distribution, particle shape, surface texture and interparticle friction, can affect the ways of particle packing and further the packing efficiency. [28] Therefore, the particle packing of the practical pigments generally diverges away from the monosize sphere system. Some influencing factors are briefly discussed here:

3.1.4.1. Packing mode

Packing mode refers to the way how the particles assemble in a given space. It can be affected by the exterior vibration as well as the interior friction between particles. Different packing modes have dissimilar packing efficiency. In general, there are two extreme random packing modes: random close packing (RCP), which is the most compact mode when particles are packed randomly, has the highest packing efficiency; the other one is random loose packing (RLP), which is regarded to have the lowest packing efficiency. An aggressive agitation or vibration is necessary for obtaining the RCP. Furthermore, all the particles should move freely without interparticle friction. [29] Particles tend to have RLP when there is no exterior force applied. [28] Based on the experimental results of Scott et al. [30] the packing densities for the monosize hard spheres in RCP and RLP are 0.637 and 0.60, respectively.

The work of using molecular simulation to study particle packing mode have been done by several groups. Frith and Buscall [31] simulated a model which had a fixed size

box filled with the randomly close-packed and monosize hard spherical particles. By increasing the size of the spherical particles in a controlled rate, the variance of the coordination numbers (how many neighbors each particle contacts with) were studied to help the understanding of percolation threshold and critical exponents. The model of Frith and Buscall assumed that the particle size increased in a constant changing rate could cause the variance of particle packing. However, in the realistic condition, the sizes of the given particles are usually constant. The compression rate on the interstices among the particles actually varies. In the work of Fishman et al., [32] a more reasonable model was proposed: the particles' sizes were constant, the size of the box was gradually compressed by moving a wall of the box toward the center at different speeds, which imitated the drying rates of a coating film in the practical situation. The study of the computer simulations suggested that the packing density was influenced by the compression rate: a compression at a fast rate resulted in a low packing efficiency but with homogeneous distribution of pigments; but the slow compression generated a high packing density but at a large heterogeneity. [32]

3.1.4.2. Particle size distribution

A broad particle size distribution will benefit high packing density. With the highly ordered and homogenized packing, each smaller particle can always fill into the voids between the packed large particles. A broad particle size distribution means that there are always smaller particles to fill up the remaining interstice spaces and result in a higher packing density. In addition, it is found that the optimal particle size distribution does not depend on the mean particle size but is related to both the volume fraction of the large particles and the roundness of particles.[28]

3.1.4.3. Particle shape

Particle shape can significantly influence the packing efficiency. Generally speaking, the irregularly shaped pigments can reduce the packing efficiency due to the irregular shapes increase the interparticle friction and further hinder the particles to move freely to achieve a high packing efficiency. [28]

The regularity of a particle can be reflected by two parameters: sphericity (S) and roundness (R). [33] Sphericity describes the global shape of a particle and its similarity to a sphere, which can be expressed by the ratio of surface area of an ideal sphere to the real surface area of a particle when both of them have the equivalent volume; [33] roundness refers to the small curvature on a particle surface whose magnitude is typically one order smaller than the particle size. [34]

There are different ways to quantify the sphericity and roundness for a particle. According to the method suggested by Krumbein and Sloss, where the maximum 2D projection of particle has been used, [34] sphericity (S) can be measured as the ratio of the diameter of the largest inscribed circle ($R_{max\text{-}in}$) to the diameter of the smallest circumscribed circle ($R_{min\text{-}cir}$), and roundness (R) can be given by the average diameter of the surface curvatures (r_i) to the diameter of the maximum inscribed circle ($R_{min\text{-}cir}$), as shown in Figure 3-2.

Furthermore, Cho et. al. has proposed an equation to calculate the regularity (ρ) for a particle,

$$\rho = (S + R) / 2 \qquad (3.4)$$

where S and R are the sphericity and roundness, respectively.

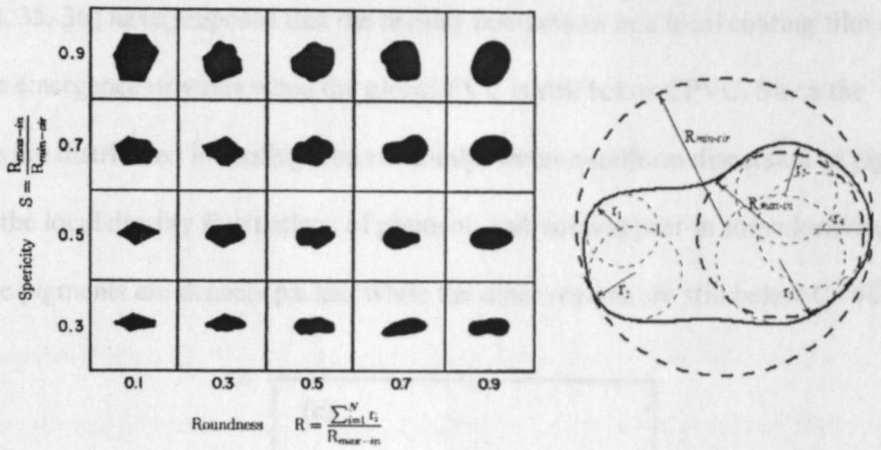

Figure 3-2. Particle shape measurement and Krumbein chart. (Reproduced form G. C. Cho et al., *J. Geotechnical. & Geoenviornmental Eng.*, **2006**, 132, 591)

3.1.4.4. Void ratio

Cho et. al. also defined the void ratio (e) as the volume of void (V_{void}) divided by the volume of particle ($V_{particle}$) in a given space: [33]

$$e = \frac{V_{void}}{V_{particle}} \tag{3.5}$$

Two extreme void ratios, e_{max} and e_{min}, have been used to represent the least efficient random packing and the most efficient random packing, respectively. The empirical relationships between the regularity and the extreme void ratios are shown in Figure 3-3.

3.1.4.5. Coarseness

Theoretically, the emergence of voids in a coating film when the PVC exceeds the CPVC can result in the abrupt changes of some coating properties. However, it has been noticed that most coating films exhibit the continuing property changes instead of the abrupt ones. In other words, some coating properties start to change before the PVC reaches the CPVC. [35] Furthermore, for a given pigment-polymer system, the value of CPVC is still sensitive to the sample preparation and the coating film formation. Fishman

et al. [32, 35, 36] have proposed that the density fluctuations in a local coating film can cause the emergence of voids when the global PVC is still below CPVC. Since the pigments are distributed in coating film randomly, the non-uniform dispersion of pigment result in the local density fluctuations of pigment, and voids appear in some local regions where the pigments are densely packed while the other regions are still below CPVC.

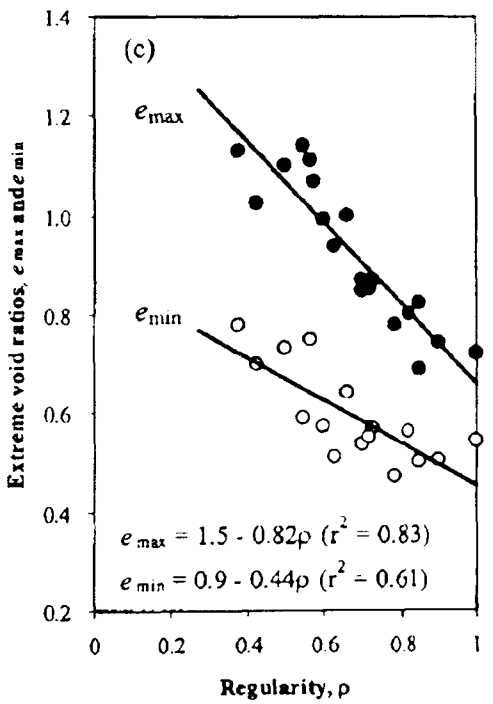

Figure 3-3. Effect of particle shape on extreme void ratios. (Copied from G. C. Cho et al., *J. Geotechnical. & Geoenviornmental Eng.*, **2006**. 132, 591)

Coarseness $C_p(V)$ is a parameter defined as [37]

$$C_p(V) = \frac{\sigma_p(V)}{<\phi_p(V)>} \tag{3.6}$$

Where $\sigma_p(V)$ is the standard deviation of the local PVCs, and $<\phi_p(V)>$ is the global PVC (average) for the whole system.

Coarseness can affect the onset of voids and how the behavior of coating property varying as a function of PVC, thus it can be used to measure the variation of local PVC's from the global PVC.

The theory of the influence of density fluctuations on the properties of organic coatings has been well developed by Fishman et al. [19, 35, 36] But, due to the difficulties of the proper definition for the minimum size of pigment cluster and the accurate estimation of local pigment volume concentration, the experimental measurement of coarseness for a pigmented coating system is still a great challenge. [37]

In this chapter, the CPVC studies of the new Mg alloy-rich primer systems will be reported. Three Mg alloy pigments as received, AM60, AZ91B and LNR, were used as pigments in an epoxy-polyamide binder to formulate Mg alloy-rich primers with different PVC values. Several methods were utilized for experimental determining the CPVC's of the three primer systems. To be more exact, the possible range, where the true CPVC might locate, is estimated for each Mg alloy-rich primer system based on the experimental results.

Three major problems have been attacked in the CPVC studies. First, development a description of the deviation between the CPVC data obtained from different testing methods. Second, based on the mathematical model developed by Bierwagen,[3, 19] development of a modified model to take into account the influences of particle shape and particle packing mode. The comparison between the predicted and experimental CPVC values is carried out to check the applicability of the new model. Third, an initial try at using florescence spectroscopy images to experimentally measure coarseness of Mg alloy pigmented primer is introduced. This is the first attempt at experimentally measuring coarseness in paint films. Based on the results of CPVC studies and the particle

characteristics, some useful criteria for optimal particle selection are proposed for future work.

3.2. Experimental

Three different Mg alloys granules used in this study were supplied by Reade (READE Advanced Materials, East Providence, Rhode Island, USA). They are AM60, AZ91B, and LNR91/96. The data of the chemical composition and density of each Mg alloy particle shown in Table 3-1were obtained from the manufacturers' data sheets.

3.2.1. Scanning electron microscope – Shape and morphological characterization

Scanning electron microscope (SEM) is a microscope technique with significantly high magnification and resolution due to the use of high energy electrons as light source. The schematic drawing of SEM is shown in Figure 3-4. In a vacuum column, electrons are generated by an electron gun, and then an electric potential is used to accelerate the electrons. Several condensing lenses made of "a coil of current-carrying wire" collimate the electrons into a beam and their magnetic fields speed up the movement of electrons. A

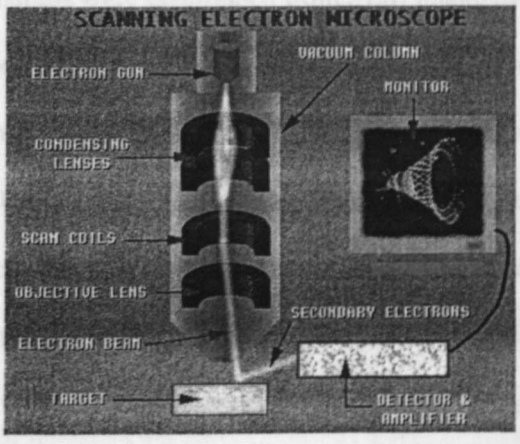

Figure 3-4. Schematic of SEM. (Copied from http://materialscience.uoregon.edu/ttsem/SEMbasics.html)

followed scan coil is used to scan the electron beam before it hit the sample. An objective lens is used to focus the electron beam into a small volume which finally hits the sample. The backscattered or secondary electrons escaped from the sample due to the bombard of electron beam are detected by the detector. SEM images are generated after the electrical signal transformation.

The shape and surface morphology of Mg alloy granules were studied by SEM. Mg alloy particles were softly laid on a piece of carbon tape, then a suction bulb was used to blow away the loose Mg alloy particles and a thin layer of Mg alloy particles was left on the surface of carbon tape. An ultra-thin gold film was coated over the surface of particles for SEM test.

SEM surface images were taken by using a JEOL JSM-6300 (JEOL Ltd., Tokyo, Japan) with 15KeV acceleration voltage, at 3000× magnification for the Mg alloy samples. All SEM measurements were carried out by Panny, S. in USDA.

3.2.2. Mg alloy pigments' sphericity and roughness calculation

Sphericity and roundness were determined from SEM image of pigments. The image was opened by Photoshop® (Abode Systems Incorporated) and the maximum inscribed circle, minimum circumscribed circle and circles fitting curvatures were manually plotted for individual particle. The diameters of these circles were read for calculating sphericity and roundness. The calculated values were verified by visual comparison with Krumbein chart (reproduced in figure 3-2). [34] For each pigment, more than 50 particles were measured and the mean sphericity and roundness were used. Calculation work was carried by Wang, J. in CPM.

3.2.3. Particle size measurement

Particle size and particle size distribution (PSD) of pigments were measured by using Accusizer 780 optical particle sizer (Lab Recyclers Inc., Gaithersburg, MD, USA), which is based on a single particle optical sensing (SPOS) method. The magnesium alloy particles suspended in acetone passed through a "photozone" one after the other; meanwhile, the signal (a pulse) was recorded when an individual particle obscured the photozone, the blocked area of which was related to the mean diameter of the particle. The PSD was obtained by comparing the single signal strength with a standard calibration curve.

3.2.4. Oil absorption (OA) measurements

3.2.4.1. Gardner-Coleman method (ASTM D1483)

A known quantity of Mg alloy pigments was placed on a glass culture dish. Linseed oil with acid number of 3 was added drop-wise to the pigments from a burette. Meanwhile a steel spatula was used to gently fold the oil-pigment mixture. The end point was reached when the mixture of pigments and oil eventually formed a paste that could be scooped with the help of the spatula. The amount of linseed oil used was obtained by subtracting the weight of dry pigments from the total weight of the mixture. The value of OA was calculated from equation (3.7)

$$OA = [\frac{wt.1 - wt.2}{wt.2}] \times 100 \qquad (3.7)$$

Where $wt.1$ was the total weight of oil-pigment mixture at the end-point, $wt.2$ was the weight of dry pigments used in test. The final expression of OA is grams of linseed oil per 100 grams of pigment. [23]

3.2.4.2. Spatula rub-out method (ASTM 281)

A known weight of pigment was placed on a large glass panel and linseed oil was

added in a drop-wise manner. After each drop of oil was added, a steel spatula was used to intensely rub the oil and the pigments to ensure thorough mixing. The end point was obtained when the mixture of pigment and linseed oil became an unbroken "stiff, putty-like paste". [20] The weight in grams of linseed oil mixed with the known-weight pigments to reach the end-point was obtained by subtracting the weight of linseed oil which was left in the container from the original weight of linseed oil in the container. Again, the unit for OA is grams of linseed oil/100 grams of pigment.

3.2.5. Electrochemical impedance spectroscopy (EIS) method

A series of Mg alloy-rich primers were formulated at different PVC's and applied on the AA2024 T3 panels by air spray. EIS tests were carried out through three-electrode setup: primer coated AA2024 T3 panels were clamped to a glass cell with a 7.06 cm^2 exposure area and used as the working electrode; a saturated calomel electrode (SCE) was used as the reference electrode and a Pt mesh as the counter electrode; DHS was the working electrolyte. All the EIS data were collected through a frequency range from 10^5 Hz to 0.01Hz by using a Gamry PCL4-300 in potentiostatic mode (Gamry Instruments, Inc. Warminster, PA, USA).

3.2.6. Fluorescence microscopy method

The panels coated with Mg-rich primers were cut into 0.75 in × 0.75 in coupons for fluorescence dye staining: the coupons were first immersed in 0.1% Rhodamine-B (Sigma, St. Louis, MO) aqueous solution for 4 hours followed by de-ionized water rinsing, then the air-dried coupons were ready for ultra low angle microtome (ULAM) sample preparation. The description of ULAM sample preparation is shown in Appendix. A cross-section at 1.64° away from surface plane was used in our sample preparation and the finally obtained

cross-section was about 35 times wider than the one of using normal cross-section.

An Olympus LM60 fluorescence microscope (Olympus American Inc., Center Valley, PA) equipped with U/B/G filter (Chroma Technology Corp., Rockingham, VT) was used to detect the fluorescence emitting from fluorescence dye left in the voids of Mg-rich primer films. The fluorescence microscope images of the low angle cross-section samples were analyzed by using ImageJ software (National Institute of Health, http://rsbweb.nih.gov/ij/) to obtain the fraction data of fluorescence stained area at red channel. The low angle cross-cutting of samples and the measurements of fluorescence microscope were done by Wang, J in CPM.

3.2.7. Local volume fraction analysis based on fluorescence images

In Figure 3-5, an image analysis procedure is introduced. First, an original picture of fluorescence image (Figure 3-5 A) is split into twelve small tiles, and each tile represents a local area of primer film. Image of each tile passed through color (Red, Green and Blue) channels for splitting. Voids have highest contrast in red channel and pigments show highest contrast in blue channel. Therefore, by masking the image in red channel, a binary image of voids was obtained where the black area represented the voids, as shown in Figure 3-5 (C-2); similarly, in the binary image of Figure 3-5 (D-2) after being masked in blue channel, the black region shows the pigments.

ImageJ software (National Institute of Health, http://rsbweb.nih.gov/ij/) was used to obtain the fraction data of voids or pigments in a local area of primer film based on the binary images. For each sample with particular PVC, six to eight fluorescence images were taken, each of them was split into 12 tiles for analysis. Therefore, seventy-two to ninety-six of local void or pigment fractions were calculated on one PVC primer sample for

coarseness measurement.

3.3. Results and discussions

3.3.1. Characterization of Mg alloy particles

AM60, AZ91B, and LNR91 are the three Mg alloy pigments used for studying the formulation of candidate Mg alloy-rich primer systems. Figure 3-6 shows the morphology and particle shape of three Mg alloy pigments. It can be seen that the three Mg alloy particles have dissimilar shapes: AM60 particles have plate-like shapes with the smooth edges, AZ91B particles have chip-like shapes with sharp edges, LNR91 particles have cubic-like shapes with pointed edges. Figure 3-7 exhibits the plots of PSD of three Mg alloy pigments, among which AZ91B had the broadest PSD.

In Table 3-1, the data of particle size, OA, density and chemical composition for three Mg alloy pigments are listed. The mean volume diameters of AM60 and AZ91B are 66.95 μm and 62.94 μm, respectively, which are larger than the one of LNR91 (47 μm). In addition, the ratios of mean volume diameter to mean number diameter for AM60, AZ91B, and LNR91 were 4.08, 6.07, and 3.21, respectively. It indicates that the amount of AZ91B particles with small size is large. This phenomenon can also be evidenced by SEM image of AZ91B (Figure 3-6 AZ91B) and its particle size plot (Figure 3-7 AZ91B), where the number percentage of particles with small size (less than 5μm) is extremely high. Based on the data obtained from spatula rub-out method in Table 3-1, the trend of OA value from small to large is LNR91, AM60 and AZ91B. The low OA of LNR91 might be due to its high density and good wetting ability of linseed oil on the surface of LNR91 particles. The reasons for AM60 and AZ91B to have large OA might be due to the large percentage of small particles.

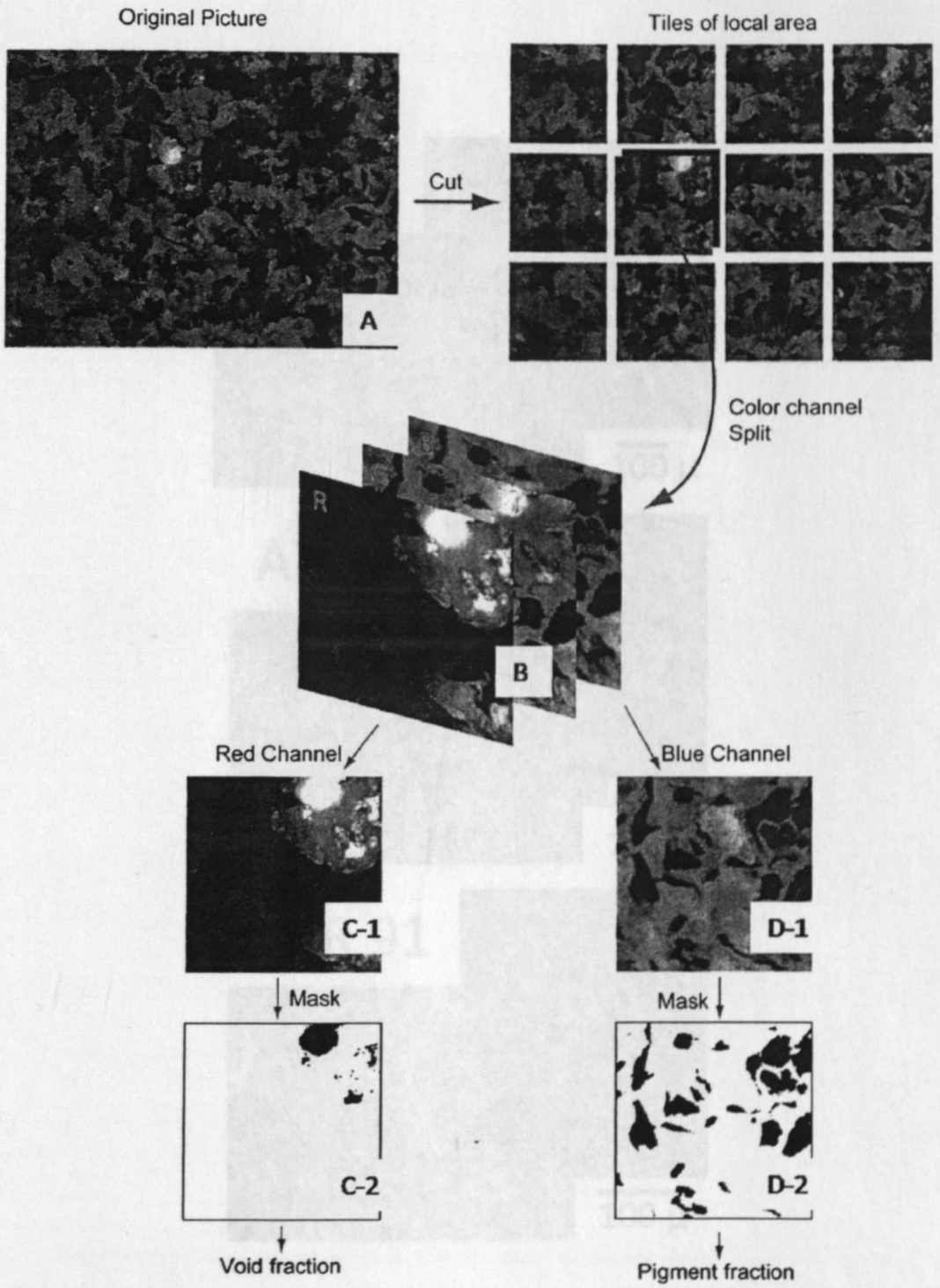

Figure 3-5. Fluorescence image analysis procedure for obtaining the data of void fraction and pigment fraction of a Mg alloy pigmented primer sample.

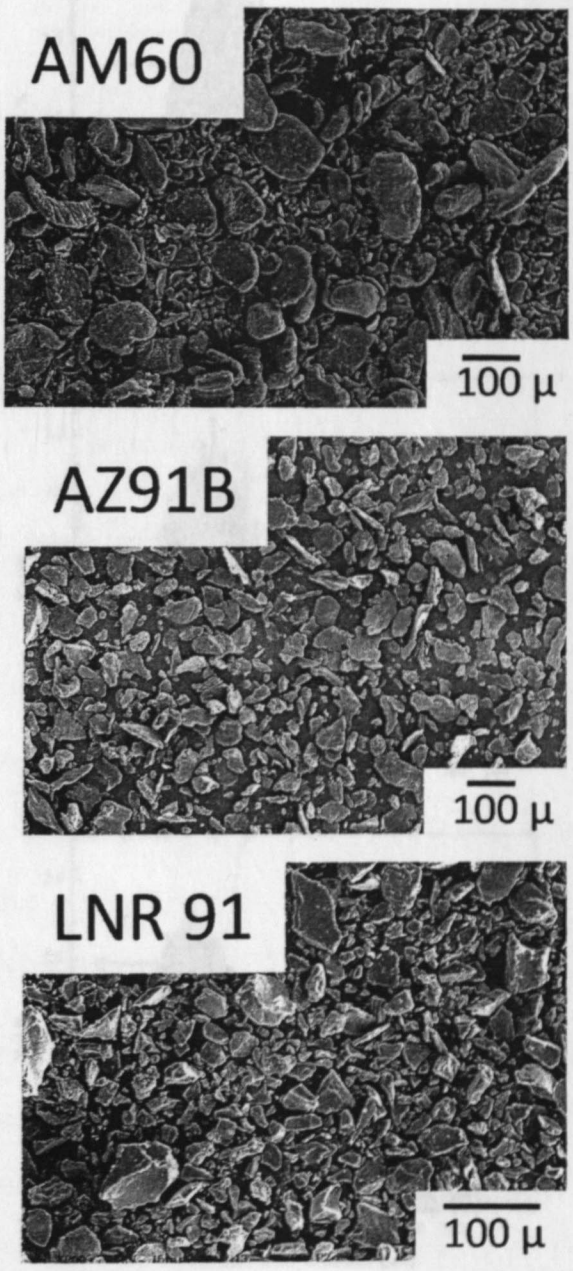

Figure 3-6. Particle shape and morphology of Mg alloy pigments: AM60, AZ91B and LNR91.

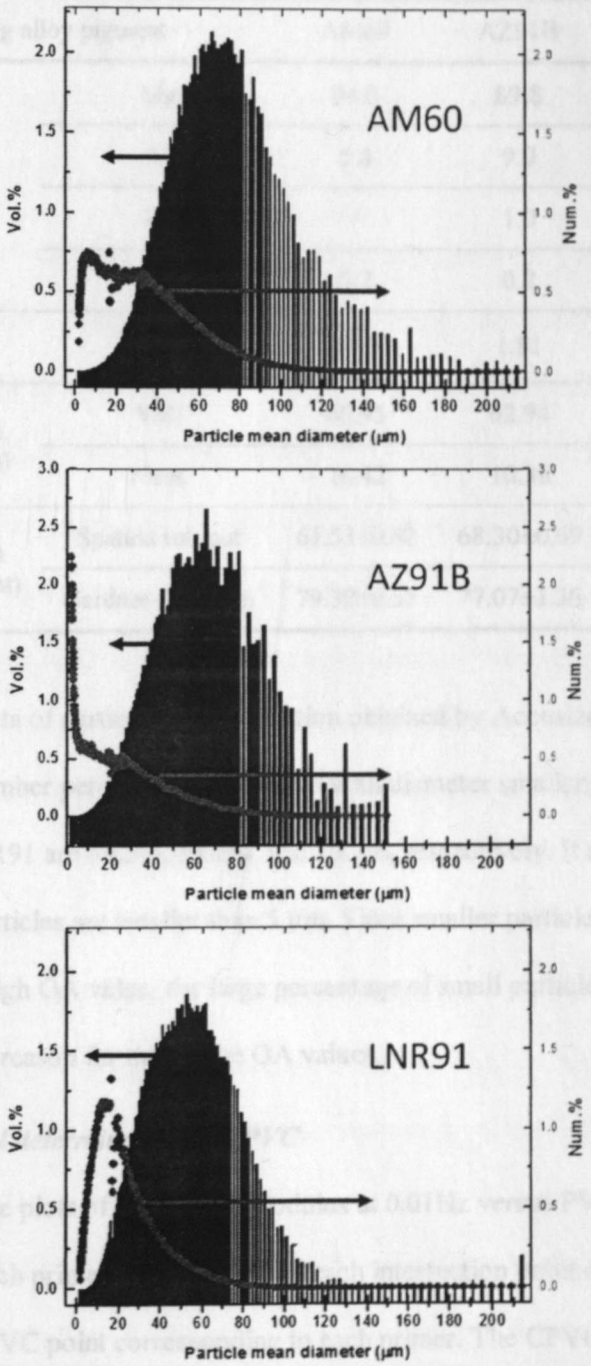

Figure 3-7. Particle size distribution plots of Mg alloy pigments: AM60, AZ91B and LNR91. (Instrument: Accusizer 780 optical particle sizer)

Table 3-1. Properties of Mg alloy particles.

Mg alloy pigment		AM60	AZ91B	LNR91
Chemical composition (% by wt.)	Mg	94.0	89.8	50
	Al	5.8	9.0	50
	Zn		1.0	/
	Mn	0.2	0.2	/
Density (g/cm^2)		1.80	1.81	2.22
Particle mean diameters (μm)	Vol.	66.95	62.94	47.00
	Num.	16.42	10.36	14.63
Oil absorption (g/100g pigment)	Spatula rub-out	61.53±0.62	68.30±0.69	33.45±1.14
	Gardner-Coleman	79.32±0.57	77.07±1.36	42.57±1.86

From the raw data of particle size distribution obtained by Accusizer 780 optical particle sizer, the number percentage of particles with diameter smaller than 5 μm for AM60, AZ91B, LNR91 are 49.5%, 54.1%, and 29.7%, respectively. It suggests that half of AM60 or AZ91B particles are smaller than 5 μm. Since smaller particles have large huge surface to result in high OA value, the large percentage of small particles in AM60 and AZ91B could be the reason for their large OA values.

3.3.2. Experimental determination of CPVC

In Figure 3-8, the plots of impedance modulus at 0.01Hz versus PVC for three different Mg alloy-rich primers are shown, and each intersection point of the red lines is considered as the CPVC point corresponding to each primer. The CPVC values of the different Mg alloy-rich primers obtained from EIS measurements are listed in Table 3-2.

The plots of the fraction of fluorescent area as function of PVCs for three Mg alloy-

rich primer systems are shown in Figure 3-9. The experimentally obtained CPVC values for each primer system are listed in Table 3-2. In addition, the OA values obtained from spatula rub-out and Gardner-Coleman methods were used to calculate the predicted CPVC via equation (3.1) and GPB method, and the results are listed in Table 3-2.

3.3.3. Limitations of experimental CPVC determination methods

In Table 3-2, it can be seen that the CPVC values vary significantly from each other. The CPVCs obtained experimentally from EIS and Fluorescence microscopy are similar with each other but much smaller in comparison to the ones calculated from OA; the predicted CPVCs from spatula rub-out method are much larger than those from Gardner-Coleman; the CPVC values calculated via GPB method are smaller than the ones from equation (3.1). Assumed that the random bias was limited by the statistical measurements and expressed by standard deviation, the differences between the CPVC's are considered as the systematic bias, which could be caused by the variations from method to method. The probably systematic bias is discussed from several aspects.

3.3.3.1. Sample preparation

In Table 3-2, it can be seen that the CPVC results obtained from EIS and fluorescence microscopy measurements are similar with each other. But they are much lower than the CPVCs from OA calculation. The most probably reasons could be due to the different sample preparation. The cured coating samples were used to determine CPVC in both of EIS and fluorescence microscopy methods. For OA calculation methods, the raw Mg alloy particles were tested in a linseed oil matrix. It has been realized that the CPVC is not only influenced by the inherent properties of pigment but also the interaction between pigments and polymer binders. [24] [18]

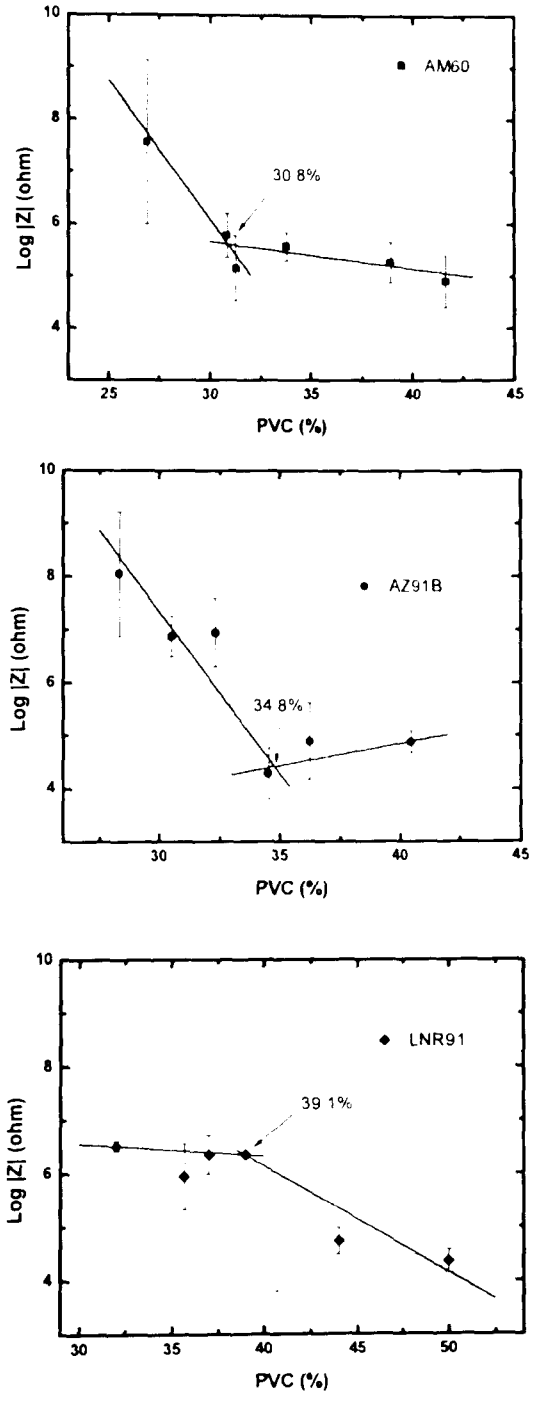

Figure 3-8. Impedance modulus at 0.01Hz ($|Z|_{0.01Hz}$) of primer samples as a function of PVC.

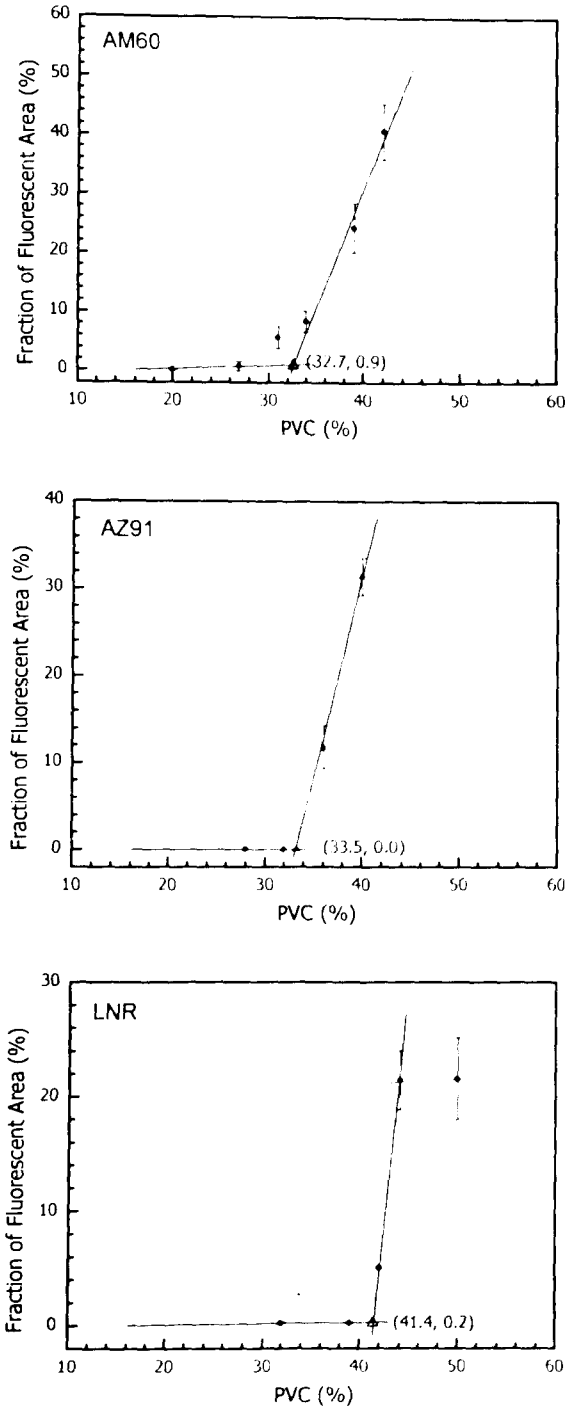

Figure 3-9. Fraction of fluorescent area of primer samples as the functions of PVC.

Table 3-2. CPVC values from different testing methods.

Mg alloy pigment	Density (g/cm^3)	CPVC (%)			
		Predicted value (GPB method)		Experimental value	
		Spatula rub-out	Gardner-Coleman	EIS	Fluorescence microscopy
AM60	1.80	45.8	39.6	30.8	32.7
AZ91B	1.81	43.0	40.1	34.8	33.5
LNR91	2.22	55.7	49.7	39.1	41.4

Moreover, Bierwagen has pointed out that the film formation has considerable effects on the apparent CPVC, such as latex coating. [24] Therefore, the way of using OA to predict CPVC is mainly related to the properties of pigment; but the particle packing in a cured coating film can be affected by the inherent properties of pigments, polymer binder, pigment dispersion and film formation.

3.3.3.2. Estimation of mathematical model

In the mathematic model of equation (3.1), it is assumed that all the particles are spherical, and there is no roughness of particles' surface and friction between particles. But in practice, the pigments are irregularity in shape and have rough surface, thus the large friction between particles can drastically affect the particle packing and introduce positive errors to the CPVC values. As a result, the CPVCs obtained from EIS and fluorescence microscopy are much lower in comparison to the ones from OA calculation. The CPVCs from GPB method are smaller than those obtained from equation (3.1), since more reasonable estimations were made in GPB method: pigments had a continuous particle size distribution and a polymer layer was tightly adsorbed on the surface of pigments.

3.3.3.3. Coarseness and percolation

The local density fluctuations result in the presence of coarseness in coating films. As a result, voids can emerge in a coating film even when its PVC is still below the CPVC. Usually, the presence of coarseness in a coating system has no significant effects on the systematic bias for CPVC determination. However, for some micro-level testing methods, such as fluorescence microscopy, the presence of coarseness can cause large errors on CPVC determination due to the high sensitivity to the existence of voids. Therefore, the results of CPVC obtained from fluorescence microscopy may be smaller than the "true" one. Somehow, the experimental errors can be reduced by using the statistical measurement.

Generally, a pigmented coating film can be considered as a disordered system, where a "dispersed phase" (pigments) in a "dispersion medium" (polymer binder). [38] Thus, the concept of percolation can be used to describe the "degree of connectivity" for a whole film, and here the percolation threshold refers to the PVC at which a continuous path of conduction through the whole film is just formed. [38] Theoretically, the conduction percolation threshold is different from the CPVC and usually has a lower value than CPVC. Conduction percolation threshold is closely dependent on the structure where a continuous connected path is randomly built-up in coating film, [24] but CPVC is mainly related to the pigmentation of a given coating system and the adsorbed layer of pigments. At the point of CPVC, all the particles in a coating film involve in the conduction. Therefore, for a given coating system, the CPVC is exclusive but the percolation threshold can be multiple.

The existence of the multiple conduction percolation thresholds can cause systematic errors to CPVC determination in EIS method. The CPVC indicator of EIS method is the abrupt drop of impedance of coating system. In fact, the drop of impedance of primer film

can occur before the CPVC due to the conduction percolation of particles. As a result, the accuracy of using EIS to determine CPVC can be affected, since an ambiguous impedance modulus changing range can be observed instead of a sharp drop of impedance modulus at the point of CPVC.

3.3.3.4. Endpoint determination

The CPVC values obtained from Spatula rub-out method (ASTM 281) and Gardner-Coleman method (ASTM D1483) are different because of their different OA values. Two possible reasons might be attributed to the variations: one is the different endpoint determination. In spatula rub-out method, the endpoint was made when an unbroken "stiff, putty-like paste"[20] was formed. Since the adsorbed linseed oil on particle surface had enough cohesion to hold particles together, it was possible that some interstices in the putty-like paste were not actually filled with linseed oil. As a result, the endpoint could be determined earlier than the true one. In Gardner-Coleman method, the endpoint was determined when a single ball was formed. In fact, over a very the surface of the ball and on the surface of glass container a small amount of overloaded linseed oil was observed. Thus, the endpoint could be determined later than the true one. As a result, the OA values obtained from Gardner-Coleman method were larger than the ones from spatula rub-out method.

The other one is the different ways of rubbing and mixing pigments and linseed oil. In Gardner-Coleman method, a very gentle fold of oil and pigments by spatula is required; in spatula rub-out method, a vigorous and thorough rubbing to mix pigments and oil is necessary. Therefore, very gentle exterior forces were used in Gardner-Coleman method which could cause loose particle packing. On the contrary, the strong rubbing was applied

to mix the pigments and linseed oil in spatula rub-out method to improve the particle packing of the mixture and reduce the amount of linseed oil absorbed on the surface of pigments. Again, the different rubbing ways could cause the OA values from Gardner-Coleman method to be larger than the ones from spatula rub-out method.

Each method for the experimental determination of CPVC has its limitations and errors. It is still a challenge to find a proper way to determine the exact CPVC for coating system.[18] However, the experimental determination of CPVC is very useful in coating industry. At least, they can provide the reasonable ranges where the true CPVCs are probably located. Also, the CPVC obtained from experiments can take into account the effects of coating formulation procedures and film formation situations. Thus, the CPVC ranges of Mg alloy-rich primer systems obtained from different experiments can provide the information of Mg alloy particles' packing efficiency and also help to formulating the new Mg alloy pigmented primers.

3.3.4. Mathematical model by taking particle shape and packing mode into account

As mentioned before, the mathematical model proposed by Bierwagen has taken two factors into account in the predication of particle packing efficiency: the random close packing of spheres and a continuous particle size distribution. [3, 25] The CPVC values can be predicted via the equation (3.2).

In Table 3-3, the calculated CPVC values of three Mg alloy-rich primer systems by using Bierwagen's model are listed. To better understand the effects of particle shape on the CPVC values, the data of two pure Mg-rich primers (Mg3820 and Mg1-11) are also adopted in Table 3-3 from Nie's work. [39] The experimental CPVC values obtained from fluorescence microscopy as well as the relative errors between the mathematical and

experimental ones are shown, too.

Table 3-3. The comparison of calculated CPVC values by Bierwagen's model and experimental value for various Mg-rich coatings.

Mg alloy pigment	Predicted value (GPB method)				Experimental
	Spatula rub-out		Gardner-Coleman		Fluorescence microscopy
	CPVC (%)	Relative error*[1]	CPVC (%)	Relative error*[1]	CPVC (%)
AM60	45.8	40.0%	39.6	21.1%	32.7
AZ91B	43.0	28.6%	40.1	19.7%	33.5
LNR91	55.7	34.5%	49.7	20.0%	41.4
Mg 3820	46.9	16.1%		/	40.4*[2]
Mg 1-11	50.1	3.3%		/	48.5*[2]

*[1] Relative error = $|CPVC_{cal} - CPVC_{exp}|/CPVC_{exp}$

*[2] Experimental data adopted from Nie's work [39]

From Table 3-3, it can be seen that the relative errors are very large. According to the data based on the Spatula rub-out method, the relative errors between the predicted and the fluorescence microscopy CPVCs vary from 15% to as large as 40%. However, for the Mg 1-11 which has near-spherical shape, the relative error is much smaller in comparison to others. It indicates that the non-spherical shape of particles might be the major cause for the large relative error.

Therefore, based on GPB model, two variables, particle shape and particle packing mode, have been taken into account in the mathematical model to reduce the errors.

It is well known that the random packing efficiency for the monosized spheres is around 0.639. [28, 29, 40-42] However, some research work has showed that, as the particle shape becomes more irregular, packing efficiency can gradually decrease to 0.40.

[28] In our case, all the three Mg alloy particles have irregular particle shapes, thus the packing efficiency could be lower than 0.639 of the spherical particles.

As mentioned before, RCP and RLP generally represent the two extreme packing modes with the highest and lowest packing efficiency, respectively. For RCP packing mode, it assumes that there is no interparticle friction and all the particles can move freely under agitation and vibration; but for RLP packing mode, the high interparticle friction hinders the free move of particles. In practice, Mg alloy particles were wrapped by a tightly adsorbed polymer layer, thus, the interparticle friction was dependent on the properties of the adsorbed layer and also the application procedure, e.g. air spray or draw-down. Therefore, it is reasonable to consider that the true packing mode is locate somewhere between RCP and RLP. [21, 22]

Therefore, in the modified mathematic model, a correction term (ϕ) is added to the GPB's model,

$$\mathrm{CPVC} = \mathrm{CPVC}_{\mathrm{GPB}} \times \frac{\phi_{\mathrm{correct}}}{0.639} \tag{3.8}$$

$\phi_{correct}$ is a correcting item which has taken into account two factors: the regularity of pigments and the packing mode, and 0.639 is the random densest packing efficiency used in GPB's model.

$\phi_{correct}$ can be obtained based on the two equations listed in Figure 3-3, the extreme void ratio for RLP (e_{max}) can be expressed as

$$e_{max} = 1.5 - 0.82\rho \tag{3.9}$$

And the extreme void ratio for RCP (e_{min}) can be calculated

$$e_{min} = 0.9 - 0.44\rho \tag{3.10}$$

The regularity (ρ) can be obtained through equation (3.4)

where, S and R are the sphericity and the roughness of particles, respectively. In experimental section, the details of calculating S and R have been described.

Since

$$e_{max}(\text{or } e_{min}) = \frac{V_{void}}{V_{particle}} \tag{3.11}$$

and

$$\phi_{packing} = \frac{V_{particle}}{V_{particle} + V_{void}} \tag{3.12}$$

so

$$\phi_{RLP} = \frac{V_{particle}}{V_{particle} + e_{max} \times V_{particle}} = \frac{1}{1 + e_{max}} = \frac{1}{2.5 - 0.82\rho} \tag{3.13}$$

and

$$\phi_{RCP} = \frac{V_{particle}}{V_{particle} + e_{min} \times V_{particle}} = \frac{1}{1 + e_{min}} = \frac{1}{1.9 - 0.44\rho} \tag{3.14}$$

Third, the final predicted CPVC value for a given pigment is expressed by:

$$CPVC_{RLP} = CPVC_{GPB} \times \frac{\phi_{RLP}}{0.639} \tag{3.15}$$

$$CPVC_{RCP} = CPVC_{GPB} \times \frac{\phi_{RCP}}{0.639} \tag{3.16}$$

In Table 3-4, the calculated $CPVC_{GPB}$, the regularity for Mg/Mg alloy particle, ϕ_{RLP}, ϕ_{RCP}, the $CPVC_{RLP}$ and $CPVC_{RCP}$, the fluorescence microscope CPVC values and their relative errors (E) are listed.

It can be seen that the relative errors become smaller in the order from E_{GPB}, E_{RCP} to E_{RLP}. The reduced relative errors of E_{RCP} to E_{RLP} indicate that a fairly good correlation between the predicted and experimental CPVC values can be achieved when taking the

effects of particle shape into account. In other hand, the differences between E_{RCP} to E_{RLP} imply that the packing mode also can influence the packing efficiency of Mg alloy-rich primer system, and the true packing mode may locate between RCP and RLP, probably near RLP.

Table 3-4. Comparison of calculated CPVC values from this work's model with experimental values for various Mg-rich coatings.

Pigments	AM60	AZ91B	LNR91	Mg 3820	Mg 1-11
Regularity	0.4337	0.5284	0.4681	0.6256	1
ϕ_{RLP}	0.4663	0.4839	0.4725	0.5033	0.5952
ϕ_{RCP}	0.5851	0.5997	0.5903	0.6155	0.6849
$CPVC_{RLP}$ (%)	33.4	32.6	41.2	36.9	46.7
E_{RLP}	2.2%	2.6%	0.5%	8.6%	3.8%
$CPVC_{RCP}$ (%)	41.9	40.4	51.4	45.2	53.7
E_{RCP}	28.1%	20.6%	24.2%	11.9%	10.7%
$CPVC_{GPB}$ (%)	45.8	43.1	55.7	46.9	50.1
E_{GPB}	40.0%	28.6%	34.5%	16.1%	3.3%
$CPVC_{exp}$ (%)	32.7	33.5	41.4	40.4	48.5

* E is Relative error = $|CPVC_{cal} - CPVC_{exp}|/CPVC_{exp}$, subscripts represent the different calculation methods.

However, more work of applying this mathematical model on different particles should be done in the future in order to confirm the universality of this modified model for CPVC calculation. Moreover, there are two aspects that are needed to be emphasized:

(1) This model is based on the mathematical model developed by Bierwagen. Therefore, it inherited the assumptions that the dispersion of particles in coating film was ideal, and the OA measurement by spatula rub-out was also assumed to have nearly ideal dispersion. So, the calculated CPVC value is based on a coating system with an ideal

dispersion of particles. But, in the real practical coating system, the flocculation and agglomeration are usually inevitable. Thus, the presence of coarseness can result in large error to the experimental CPVC value.

(2) In this model, sphericity and roundness are determined from SEM image. This process includes manual estimates of maximum inscribed circle, minimum circumscribed circle and curvature cycles, which are subjective and may result in some variation among different observers, especially for the estimates of individual particles. However, it has been proved that, if there are 50 or more particles are measured, the average value tends to be similar because the bias from different operators are compensated by in numbers of estimates.[34]

3.3.5. Attempt of experimental coarseness measurement

In early of 1990s, Bierwagen and his coworkers proposed the theory of local density fluctuation of pigment.[35, 36] It has theoretically predicted that, in practice, the dispersion of pigments in the polymer matrix of organic coating is inhomogeneous. In some regions, voids can emerge due to the random dense packing of pigment though the global PVC is still below CPVC.

In Figure 3-10, a ULAM cross-section image of AM60 pigmented primer via fluorescence microscopy is shown. The black areas represent the pigments; the gray region is the binder, and the bright spots show the presence of voids. It can be seen that, for 31% AM60 primer PVC of which is below CPVC, the regions marked with yellow circles contain some voids due to the local random dense packing of AM60 pigments. It confirms the predication of Fishman et al of which the "densely-packed cluster" of pigments causes the voids to form even when the global PVC is below CPVC. [35]

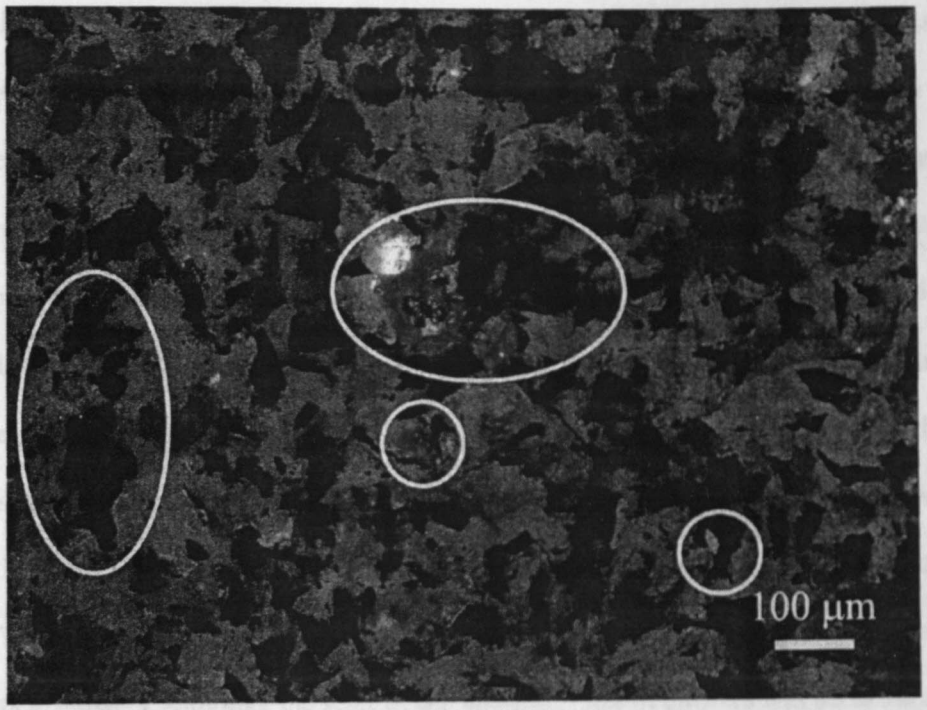

Figure 3-10. Fluorescence image of the presence of coarseness in a 31% PVC AM60 pigmented primer sample: black areas are pigments; gray region is polymer binder; bright spots are voids; the regions marked by white circles show the presence of voids in pigment dense-packing areas (coarseness).

The coarseness has been theoretically used to provide information on how it affects the local density fluctuation of pigments. [35, 36] However, experimental estimation of coarseness is still a challenge due to the difficulties of properly defining the minimum size of pigment cluster and practically applying 3D analysis of local PVC based on 2D images. [37]

In the CPVC studies of Mg alloy-rich primer systems, the work of experimentally coarseness measurement was carried out for the first time. Two preconditions have been proposed in order to fulfill the work: first, it is assumed that the images taken from the primer samples are considered to represent the structures of samples, where the dispersion of pigments or voids is random and homogenous. Under this condition, from the view of

stereological measurement, the area fraction from 2D image can be considered to be the same as the 3D volume fraction. [43] In our case, the fluorescence images were taken from different spots of a sample, and the micro-structures of Mg alloy-rich primer shown in the images are similar. It suggests that the first assumption holds true; second, the scale of the minimum size of particle cluster has been determined as ~300 μm so that there are 10 to 20 particles presented in each tile. According to the work of Bierwagen et al. [35] the particle numbers in a cluster is about 10. [43] since the coordination number is usually 9 for the monosize pigments packed in a random dense-packing mode. In addition, the formation of voids in clusters is affected by the large particles (around 100 μm) rather than the small ones. Therefore, ~300 μm was chosen as the scale of one tile to represent the minimum size of particle clusters. Although the scale of the minimum size of clusters was set arbitrarily, as the first attempt of experimentally coarseness measurement, the reasonability of this selection will be checked by the experimental results later.

Through the analysis by ImageJ program (National Institute of Health, http://rsbweb.nih.gov/ij/), the data of local Φ_{void} and $\Phi_{particle}$ for each Mg alloy-rich primer sample can be obtained. The sum of the local volume fractions is 1 due to

$$\Phi_{binder} + \Phi_{pigment} + \Phi_{voids} = 1 \tag{3.17}$$

According to Reference [36], the volume fraction of polymer [$q(x)$] in the region not occupied by pigment can be described as

$$q(x) = \frac{\Phi_{binder}}{\Phi_{binder} + \Phi_{voids}} \tag{3.18}$$

and the coarseness of the "polymer space-filling" can be obtained by

$$C_q = \frac{\sigma_q}{< q(x) >} \tag{3.19}$$

where C_q is the coarseness of polymer binder, σ_q is the standard deviation of $q(x)$ via

$$\sigma_q^2 = < q(x)^2 > - < q(x) >^2 \qquad (3.20)$$

Therefore, for each tile, a value of local $q(x)$ can be obtained. Thus, a population of seventy-two to ninety-six values of local $q(x)$ and its standard deviation σ_q were obtained via equation (3.18) and equation (3.20). At the same time, the mean value of local PVC ($\langle \phi_p(V) \rangle$) can be obtained by

$$< \phi_p(V) >= \sum_{i=1}^{n} \phi_p(V) / n \qquad (3.21)$$

where $\phi_p(V)$ is the local PVC in each tile via

$$\phi_p(V) = \frac{\phi_{pigment}}{\phi_{binder} + \phi_{pigment}} \qquad (3.22)$$

Based on equation (3.19), the coarseness of polymer binder (C_q) for Mg alloy-rich primers at different PVC was calculated. The results of experimentally coarseness measurement are listed in Table 3-5.

Table 3-5. Coarseness data of AM60 pigmented primers at different PVCs.

Pigments	PVC	Λ	C_q	$\langle \phi_p(V) \rangle$
AM60	27%	0.825	0.066	25.7%
	31%	0.948	0.169	30.5%
	34%	1.040	0.219	32.7%

From Table 3-5, it can be seen that the coarseness is increasing with PVC. When Λ is smaller than 0.85, coarseness is very small; but in the range of Λ from 0.85 to 1.15, coarseness is large. These results confirmed the suggestion of Bierwagen that the probability for voids presenting in coating system increases when Λ is above 0.85. [5, 37]

In addition, it can be seen that the values of PVC and its corresponding $\langle \phi_p(V) \rangle$ are

very close. The PVC value is the formulation PVC, and $\langle\phi_p(V)\rangle$ is the calculated mean PVC from the fluorescence image. The small differences between these two sets of values imply that the assumption, that the area friction of 2D is equal to the volume fraction of 3D, is reasonable. The formulation PVC is a volume fraction for 3D system, and $\langle\phi_p(V)\rangle$ was obtained from the area fraction of 2D. Moreover, the values of C_q are in agreement with the theoretical predictions in reference. [32] It indicates that the scale of minimum size of clusters (~300μm) is suitable. When the scale of tile is too small, the standard deviation $\sigma_p(V)$ tends to be very large, but when the scale is too large, $\sigma_p(V)$ tends to zero.

Of course, being the first attempt, the method of experimentally coarseness measurement still needs more examination and verification. The application of this method in different systems should be checked in order to understand the requirement of statistic measurement, the relationship between the particle size and the scale of minimum cluster, the validation and limitation of this new method. However, from the coarseness studies, it can be seen that the two assumptions proposed before are reasonable, and some theoretical predictions can be defined by our experimental results.

3.4. The optimal properties of Mg alloy particles

One of the major purposes for our CPVC studies on the Mg alloy-rich primer system was to understand how the particles' properties influence particle packing efficiency and further affect the CPVCs. The knowledge of the relationship between particle properties and packing efficiency is very useful for choosing the metallic particles with optimal properties, which can maximize packing efficiency of particles in polymer matrix and enhance the final performance of primer system.

As we know, the practical application of Mg alloy-rich primer is to provide cathodic

protection to the Al alloy substrate. For the effective cathodic protection and the durability of primer, the good electrical conductivity among the Mg alloy particles should be maintained as long as possible. Thus, a high packing density of Mg alloy particles in primer is extensively desirable.

To obtain a high packing density for a pigmented system, the optimization of particle properties is necessary and essential, since the packing efficiency is significantly affected by the properties of particles. Based on the understanding obtained from these CPVC studies, the preferred particle properties, which can benefit the high packing efficiency and further the good electrical conductivity of metal-rich primer system, are discussed as follows:

1. From the numerical simulation studies, objects with shape of cube, ellipsoid or cylinder have much higher random packing efficiency (0.78, 0.74 or 0.72, respectively) than sphere (0.64) if the pigments can be aligned properly. However, in practice of coating industry, the pigments are randomly settled in polymer matrix and the viscosity of the absorbed layer hinders the further alignment of pigments. As a result, spherical particles or near-spherical particles tend to have high alignment efficiency due to their 3D symmetry, and the good alignment of pigments helps system to have high packing efficiency. With the increases of asymmetry of particles, the coordination number reduces, and the differences between the densest and loose random packing increase, the probability of system having low packing density increases. [28] Thus, the uses of spherical particles in coating formulation will aid coating system to obtain constant packing efficiency, which can benefit the reproducibility of coating properties batch from batch and

overall quality control. Of course, if the alignment of pigments with cube, ellipsoid or cylinder in coating systems can be solved via new techniques, the packing efficiency of pigmented coating system can be improved by using non-spherical particles.

2. The broad particle size distribution will benefit the high packing efficiency, since the small particles usually fill into the interstices of big particles. But two practical difficulties could hinder the achievement of optimized packing. First, the alignment of particles in coating system is random and the optimal alignment of particles is difficult to achieve; second, the size ratio of big particles to small particles, or the shape of the particle size distribution can affect the packing efficiency. In general, the larger size ratio will result in higher packing efficiency. From the work of Furnus, [28, 44], if the size ratio is higher than 100, good packing efficiency can be obtained. For the particles with continuous size, the shape of particle size distribution is important. The volume fraction of large particles should be big enough to form a continuous framework. [28]
3. Interparticle friction is the resistance required to overcome so that particles can move freely. In the process of particle packing, free movement is necessary for particles to fit into the interstices to achieve high packing efficiency. The interparticle friction is affected by the viscosity of polymer binder, the density of pigments and particle size. High viscosity will hinder the freedom of particles' movements; the low density of pigment will reduce the moving of particles in polymer media; and the decrease of particle size will increase the surface area of particles and result in the increase of resistance to moving. For high density

pigments, the influence of interparticle friction can be overcome by the weight of pigments, such as zinc, its large weight of particles can overcome the increased interparticle friction; but for light metallic pigments, such as carbon, Al and Mg, the momentum of particle is usually not big enough to overcome the interparticle friction, as a result, the serious fluctuations of local pigment concentration can occur and reduce the packing efficiency. Thus, in comparison to the particle size of the Zn dust (about 5-7 μm) used in Zn-rich primer, the particle size of Mg or Mg alloy pigments should be larger. The work on Mg-rich primer system has showed that the Mg particles with mean diameter of 15-20 μm have the best performance. [9, 10]

For the practical purpose of Mg alloy-rich primer system, to obtain the highest packing efficiency, the particles are preferred to be spherical and have a continuous particle size distribution. Thus, the currently used Mg alloy particles should be improved to meet those optimal properties in order to obtain the high packing efficiency and good electrical connections among particles.

3.5. Conclusions

In this chapter, the CPVC studies were carried out on different Mg alloy-rich primer systems. It was found that the differences between the CPVC values obtained from different test methods were large. The large variation can be caused by many factors: the coating preparation, film formation, the determination of end-point of testing methods, and the sensitivity of the indicating properties. To find a suitable method for accurate CPVC determination is still a big challenge for the coating industry.

Based on the model developed by Bierwagen, two extra factors have been taken into

account for mathematically predicting CPVC of coating film: particle shape and random loose packing. Modified model reduced the relative errors of CPVC results between experimental ones and the predicted ones, the good agreement indicated that the influence of particle shape was necessary to be considered for Mg alloy-rich primer systems.

For the first time, the experimentally coarseness measurement was carried out on AM60 pigmented primer samples. The experimental results confirmed the theoretical predictions of Bierwagen that coarseness is a function of PVC, and the coarseness increases when Λ is above 0.85.

Moreover, some suggestions were given for the selection of optimal particles based on the effective enhancement of packing efficiency.

3.6. Appendix: Ultra Low Angle Microtome (ULAM)

ULAM is a sample preparation technique with which the coating panel sample can be cut at a defined angle away from the coating surface to produce a cross section across the coating layer. It has been used in studying the interface of polyester/polyurethane (PU) primer/poly(vinylidene difluoride) (PVdF) topcoat multilayer coating and the species migration between these layers. [45, 46]

A scheme of ULAM is shown in Figure 3-11. The panels are first cut into 0.75 × 0.75 inch coupon. The coupon is fixed by double-sided tape on an internally developed stainless steel stage with a tapered surface. The assembly is glued to a polyethylene block, which is clamped on the base plate of a Leica SM 2500 sliding microtome (Leica Microsystem Inc., Bannockburn, IL) for sectioning operation. The coupon is cut at a step between 1 – 10 μm until the Al alloy substrate is exposed. [47]

With this procedure, a tapered section between air interface and substrate interface can

be obtained for measurement. Its width, w, is equal to d/sin(α), where d is the thickness of coating layer and α is the angle between section plane and coating surface plane. Since α is a small angle, w can be several ten times the magnitude of d. Hence, the structure of the coating layer is directly exposed and can be easily accessed by different surface analysis techniques. At the same time, the microstructures of the coating, such as pigments, pores and voids, are reproduced with respect to their shape and size on the sectioned surface. Therefore, by studying the sectioned surface that is exposed by ULAM, the inner structure of coating layer and its change during exposure can be obtained.

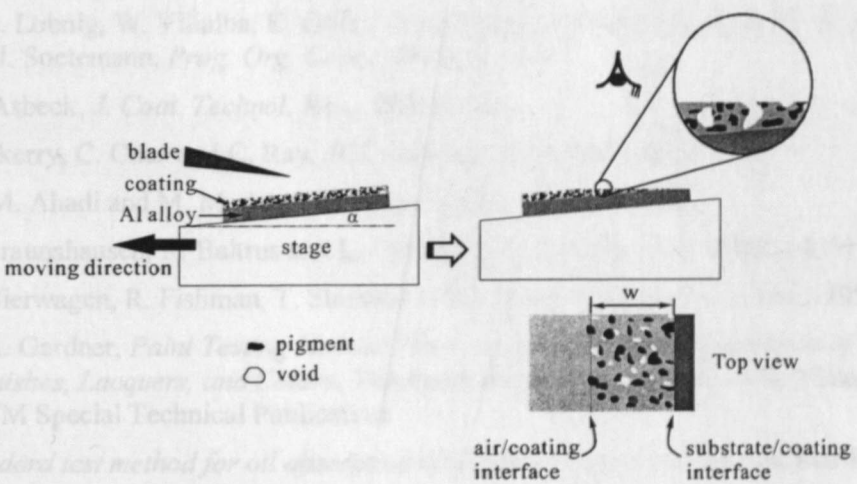

Figure 3-11. Scheme of ultra low angle microtome setup.

3.7. References

1 Z. W. Wicks Jr., F. N. Jones and S. P. Pappas, *Organic Coatings: Science and Technology*, 2rd ed, **1999**, Hoboken, New Jersey, John Wiley & Sons, Inc.

2 W. K. Asbeck and M. Van Loo, *J. Ind. Eng. Chem. (Washington, D. C.)*, **1949**, 41, 1470.

3 G. Bierwagen, *J. Paint Tech.*, **1972**, 44, 46.

4 G. Bierwagen, *JCT Coatings Tech*, **1992**, 64, 71.

5 G. Bierwagen and T. Hay, *Prog. Org. Coat.*, **1975**, 3, 281.

6 G. Bierwagen, R. Fishman, T. Storsved and J. Johnson, *Prog. Org. Coat.*, **1999**, 35, 1.

7 C. A. Gervasi, A. R. Di Sarli, E. Cavalcanti, O. Ferraz, E. C. Bucharsky, S. G. Real and J. R. Vilche, *Corrosion Science*, **1994**, 36, 1963.

8 H. Marchebois, C. Savall, J. Bernard and S. Touzain, *Electrochim. Acta*, **2004**, 49, 2945.

9 D. Battocchi, A. M. Simoes, D. E. Tallman and G. P. Bierwagen, *Corrosion Science*, **2006**, 48, 2226.

10 D. Battocchi, A. Simoes, D. Tallman and G. Bierwagen, *Corrosion Science*, **2006**, 48, 1292.

11 M. Nanna and G. Bierwagen, *J. Coat. Technol. Res.*, **2004**, 1, 69.

12 R. E. Lobnig, V. Bonitz, K. Goll, M. Single, W. Villalba, J. Vogelsang, I. Winkels, R. Schmidt and P. Zanger, *Prog. Org. Coat.*, **2007**, 60, 1.

13 R. E. Lobnig, V. Bonitz, K. Goll, W. Villalba, R. Schmidt, P. Zanger, J. Vogelsang and I. Winkels, *Prog. Org. Coat.*, **2007**, 60, 77.

14 R. E. Lobnig, W. Villalba, K. Goll, J. Vogelsang, I. Winkels, R. Schmidt, R. Zanger and J. Soetemann, *Prog. Org. Coat.*, **2006**, 55, 363.

15 W. Asbeck, *J. Coat. Technol. Res.*, **2005**, 2, 64.

16 B. Skerry, C. Chen and C. Ray, *JCT Coatings Tech*, **1992**, 64, 77.

17 M. M. Ahadi and M. M. Attar, *Scientia Iranica*, **2007**, 14, 369.

18 R. Braunshausen, R. Baltrus and L. Debolt, *JCT Coatings Tech*, **1992**, 64, 51.

19 G. Bierwagen, R. Fishman, T. Storsved and J. Johnson, *Prog. Org. Coat.*, **1999**, 35, 1.

20 H. A. Gardner, *Paint Testing Manual Physical and Chemical Examination of Paints, Varnishes, Lacquers, and Colors*, Thirteenth ed, ed. G. G. Sward, **1972**, Philadelphia, ASTM Special Technical Publication.

21 *Standard test method for oil absorption of pigments by spatula rub-out*, **Feb 15, 1995**.

22 *Standard test method for oil absorption of pigments by Gardner-Coleman method*, **Feb 15, 1995**.

23 J. V. Koleske, *Paint and Coating Testing Manual*, 14th ed, ASTM International, **1995**.

24 G. Bierwagen and D. Rich, *Prog. Org. Coat.*, **1983**, 11, 339.

25 G. Bierwagen, *JCT Coatings Tech*, **1975**, 47, 36.

26 D. I. Lee, *Journal of Paint Technology*, **1970**, 42, 579.

27 J. E. O. Mayne and U. R. Evans, *Soc. Chem. Ind. Rev.*, **1944**, 22, 109.

28 R. M. German, *Particle Packing Characteristics*, First ed, **1989**, Princeton, New Jersey, Metal powder industries federation.

29 C. Song, P. Wang and H. A. Makse, *Nature*, **2008**, 453, 629.

30 G. D. Scott, *Nature*, **1960**, 188, 908.

31 W. J. Frith and R. Buscall, *J.Chem. Phys.*, **1991**, 95, 5983.

32 R. Fishman, E. Hill, T. Storsved and G. Bierwagen, *J. Appl. Phys.*, **1996**, 79, 729.

33 G.-C. Cho, J. Dodds and J. C. Santamarina, *Journal of Geotechnical and Geoenvironmental Engineering*, **2006**, **132**, 591.

34 W. C. Krumbein and L. L. Sloss, *Stratigraphy and Sedimentation*, Second ed, **1963**, San Francisco and London, W. H. Freeman and Company.

35 R. Fishman, D. Kurtze and G. Bierwagen, *Prog. Org. Coat.*, **1993**, 21, 387.

36 R. Fishman, D. Kurtze and G. Bierwagen, *J. Appl. Phys.*, **1992**, 72, 3116.

37 G. Bierwagen, *J. Coat. Technol. Res.*, **2008**, 5, 133.

38 V. I. Roldughin and V. V. Vysotskii, *Prog. Org. Coat.*, **2000**, 39, 81.

39 J. Nie, *Improvements in the use of Mg pigments in corrosion protective coatings*, in *Coatings and Polymeric Materials*. **2010**, North Dakota State University, Fargo.

40 J. D. Bernal and J. Mason, *Nature*, **1960**, 188, 910.

41 J. D. Berryman, *Phys. Rev. A*, **1983**, 27, 1053.

42 G. D. Scott and D. M. Kilgour, *J. Phys. D*, **1969**, 2, 863.

43 J. C. Russ, *The image processing handbook*, Fifth ed, **2007**, Boca Ryton, CRC Press.

44 C. C. Furnas, *Industrial and Engineering Chemistry*, **1931**, 23, 1052.

45 S. J. Hinder, C. Lowe, J. T. Maxted and J. E. Watts, *Prog. Org. Coat.*, **2005**, 54, 104.

46 S. J. Hinder, C. Lowe, J. T. Maxted and J. F. Watts, *Journal of Materials Science*, **2005**, 40, 285.

47 J. Wang, H. Xu, D. Bottocchi and G. P. Bierwagen, **in preparation**.

CHAPTER 4. ANTICORROSION PERFORMANCE STUDIES OF THE NEW METAL-RICH PRIMER SYSTEMS PIGMENTED WITH FIVE MAGNESIUM ALLOYS AS PIGMENTS BY USING ELECTROCHEMICAL IMPEDANCE SPECTROSCOPY

4.1. Introduction

Aluminum alloys, especially AA2024 T3, are widely used in the airspace industry as the major structural materials due to their excellent mechanical properties, e.g. excellent strength and stiffness, and high strength-to-weight ratio. However, while the addition of Cu to the Al alloys provides the improvement in strength, the high copper content (about 4.5 wt.%) in AA2024 T3 also can cause Al alloy to be susceptible to the corrosion attacks. It is because of the phase separation of $CuAl_2$ which precipitates out from the Al region in the microstructure of AA2024 T3. [1] Therefore, unlike the pure Al with the inherent resistance to corrosion due to the dense layer of Al_2O_3, Al alloys need external corrosion protection.

For several decades, chromate pre-treatment and chromate primer coatings have been used to successfully protect Al alloys from corrosive attacks. [2] When the aggressive species, e.g. water, ions or oxygen, permeate through the topcoat and reach the layer of chromate primer, the soluble chromate ions can form chromate complexes on the surface of Al alloys to inhibit corrosion. [3-5] However, it has been confirmed that hexavalent Cr(VI) is carcinogenic and responsible for inducing asthma, ulceractions of skin or nasal septum. [6, 7] Thus, the use of toxic chromate based coatings (including chromate pigments and chromate metal pretreatments) has been restricted by OHSA regulation [8] and European

restriction of the use of certain hazardous substances (RoHS) [9] due to the increasing environmental and human health concerns.[10] It becomes very important and urgent to develop a new coating system which not only can provide good corrosion protection for Al alloy substrates but also is non-toxic and environmental-friendly.

Analogous to Zinc-rich primer (ZRP) coatings which can protect steel from corrosion through cathodic protection, a promising alternative, Mg-rich primer coating, has been designed, examined and developed by M. E. Nanna, D. Battocchi and G. P. Bierwagen at NDSU. [11-15] By using the pure magnesium pigments which are more active than Al alloy substrate, Mg-rich primers have been formulated around critical pigment volume concentration (CPVC) to provide cathodic protection to Al alloy substrate. The AA2024 T3 panels coated by Mg-rich primer and combined with a topcoat successfully passed 10000 hours exposure in Prohesion chamber and exhibited excellent corrosion protection. In addition, various electrochemical techniques, such as electrochemical impedance spectroscopy (EIS), scanning vibrating electrode technique (SVET) and scanning electrochemical microscopy (SECM), have been used to assess the global and local corrosion protection mechanisms of various Mg-rich primer systems. [12, 16-18] Results have shown that Mg-rich primer can provide good cathodic protection to AA 2024 T3 when damages occur to coating system, and the certain barrier protection possibly ascribed to the reaction products has been observed. [12, 18]

From the previous studies, it has been demonstrated that pure Mg particles can be used as pigments and formulated in different polymer binder system to provide cathodic protection for AA2024 T3 substrate. The success of Mg-rich primer not only has provided a promising alternative to Cr-free protective coating system, but has also expanded the

knowledge of applying different metallic pigments in metal-rich primer system for corrosion protection.

Mg alloys possess some properties similar to pure Mg, such as light weight, and high activity. The addition of other elements, e.g. Al, Mn or Zn, [19, 20] can change the corrosion resistance of these alloys drastically. [19] For example, trace amounts of iron or copper can dramatically increase the corrosion rate of Mg alloys; but the addition of zinc or manganese can effectively reduce the corrosion rate of Mg alloys. [21-23] Moreover, the presence of some rare earth elements in Mg alloys, such as Ce, Nd or Y, can improve the corrosion resistance. [23, 24] When Mg alloy particles are used as pigments in Mg-rich primer system, the performance of Mg-rich primer system will be greatly affected by the properties of Mg alloys, such as the different chemical composition, surface morphology, particle size and particle size distribution (PSD).

As an extension of the studies of Mg-rich primer system, metal-rich primer systems using Mg alloy particles as pigment have been formulated. Furthermore, how the corrosion protection behaviour affected by the inherent properties of the Mg alloy pigments have been investigated. Certainly, the corrosion protection performance provided by metal-rich primers are not only dependent on the metal pigments but also closely related to the synergy of different factors, such as the interactions between polymer binders and the active pigments, PVC, additives, solvents, application procedures, substrate pretreatment and the adhesion to topcoat and to substrate. [25] In order to determine the effects of different Mg alloys on the corrosion protection performance of metal-rich primers, it is necessary to fix some variables other than those related to Mg alloy pigment.

EIS is a powerful technique which has been extensively applied in coating research to

study a wide variety of coating systems. [26-30] In the previous work of our lab, EIS is a major tool to study Mg-rich primer system. [11-13, 15-17, 31-33] Generally, there are three important parameters obtained from EIS tests to understand the studied systems. They are open circuit potential (OCP), impedance modulus at low frequency ($|Z|_{0.01Hz}$) and capacitance at high frequency ($|C|_{10^4 Hz}$). For a metal-rich primer system, the value of OCP as well as its changing with exposure time is an important indicator for cathodic protection. [12, 15, 17, 29, 34, 35]

One advantage of using EIS in coating research is that the performance of a protective organic coating can be monitored and evaluated via $|Z|_{0.01Hz}$. It is an element near DC response [36] so that can be obtained without equivalent circuit modeling. $|Z|_{0.01Hz}$ can be related to the pore resistance R_{pore} and the polarization resistance R_p in a common circuit mode. [37, 38] Also, $|C|_{10^4 Hz}$ can be associated with water uptake via coating capacitance ($C_c = \varepsilon\varepsilon_0 A/d$). Since the dielectric constant of water (ε_{water} = 80 F/cm) is much larger than $\varepsilon_{polymer}$ (2~8 F/cm), the C_c will increase when water penetrates a coating system.

However, the ways to display EIS data are various when several duplicates for the same coating system are tested. Usually, a set of data obtained from a single sample is displayed as the representative. [39-42] The possible reasons could be that, the data of duplicates are very similar with each other, or most of them are comparable, or all the data are hard to display together. In the case of metal-rich coating, especially for those using Mg/Mg alloy particles as pigments, the active nature of metallic pigments and the local percolation make the coating system more complicate. As a result, the variations of EIS data among the duplicates become much larger. Therefore, it's necessary to give a try of using some statistical methods to analysis EIS data in order to avoid any subjective

judgment.

In statistic data analysis, there are two major approaches used to fit data: parametric and nonparametric. [43] Parametric approach needs a correct model and a good understanding on the studied system for data fitting. The advantages of parametric approach are good prediction and less plausible function. But to a new system with little information available, nonparametric approach is more useful. First, it is more flexible and can provide a wide "range of potential fits to the data" [43]; second, it is less subjective and can avoid choosing wrong model. But nonparametric approach cannot describe the relationship between "the predictors and the responses". [43]

In this work, new Mg alloy-rich primer systems have been formulated at 32% PVC and 42% PVC by using five different Mg alloy particles as pigment in an epoxy-polyamide system. They are AM60, AZ91B, LNR91/96, AM503 and AZG Mg alloys. The Mg alloy-rich primer coated AA2024 T3 samples have been exposed in Prohesion chamber. The corrosion protection performance of each Mg alloy-rich primer at different exposure times has been studied using OCP and EIS. Nonparametric approach has been applied to analysis EIS data. Also, Scanning Electron Microscopy (SEM) has been used to study the shapes of Mg alloy pigments and the surface morphology of exposed Mg alloy primers.

4.2. Experimental

4.2.1. Particle size measurements of Mg alloy particles

Particle size and particle size distribution (PSD) of Mg alloy pigments were measured by using Accusizer 780 optical particle sizer (Lab Recyclers Inc., Gaithersburg, MD, USA), which is based on a single particle optical sensing (SPOS) method. [44] The magnesium alloy particles suspended in acetone passed through a "photozone" one by one; meanwhile,

the signal (a pulse) was recorded when an individual particle obscured the photozone by a certain area that is related to the mean diameter of the particle. The PSD was obtained by comparing the single signal strength with a standard calibration curve.

4.2.2. Oil absorption (OA) measurements of Mg alloy particles

OAs of Mg alloy particles were tested according to ASTM D281[45] by using the method of Spatula Rub-out. Linseed oil was added to a known quantity of pigment in a drop-wise manner, and the pigments and linseed oil were mixed thoroughly with a spatula. When the spatula could hold all pigments together, the end point was reached. OA was expressed as gram of oil per 100 grams of pigment. Theoretical CPVC was calculated using OA value and pigment density. [46]

4.2.3. Experimental flow of the formulation and test processes

A workflow chart for the experimental procedure for formulation, the accelerated weathering exposure and EIS tests is illustrated in Figure 4-1.

The AA2024 T3 panels were supplied by Q Panel Lab products. (Cleveland, OH, USA) before being coated by Mg alloy-rich primer, the panels were polished by 220 grit and 600 grit sand papers to remove the oxide layer and followed by a hexane rinse. The Mg alloy granulates were supplied by READE Advanced Materials (East Providence, Rhode Island, USA).

An epoxy-polyamide organic coating system previously used in Zn-rich primers for many years was chosen as the binder. The Mg alloy primer paints were formulated near their CPVCs. Methyl ethyl ketone was used as the solvent to give the appropriate viscosity for air spray application.

Mg alloy-rich primers were applied on the panels by air spray. Four to eight panels

were prepared for each type of primer system. Mg alloy-rich primer films were cured at room temperature for two days and the thickness of the dry primer was approximately 150 μm.

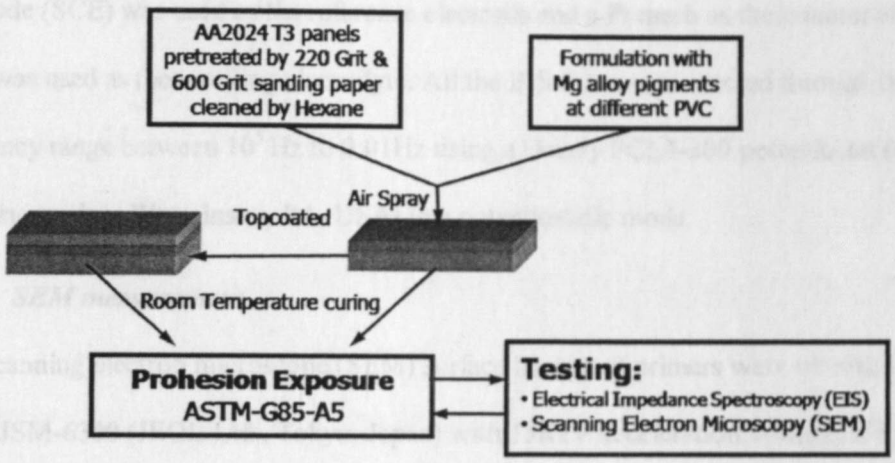

Figure 4-1. Experimental flow of Mg alloy-rich primers' formulation, exposure and tests.

Two to four panels for each type of primers were topcoated using Akzo Nobel polyurethane topcoat. AM60 and AZ91B primers were topcoated by Deft 03-GY-321 low gloss polyurethane topcoat (supplied by DEFT INC, Irvine, CA, USA) and cured at room temperature for two days. The thickness of the dried topcoat was approximately 100 μm.

All the cured non-topcoated and topcoated test panels were put into Prohesion chamber for accelerated exposure tests. Prohesion chamber consists of one-hour fog cycle of dilute Harrison's solution (DHS) fog (0.05% sodium chloride and 0.35% ammonium sulphate) at 25°C and one-hour dry-off cycle at 35°C. The panels were removed from the Prohesion chamber at dry cycle in a weekly interval for the electrochemical testing (EIS) and put back into chamber after EIS testing was conducted.

4.2.4. EIS measurement setup

In all the EIS measurements, a glass cell with a 7.06 cm^2 exposure area was clamped to the test panel, and the panel was used as the working electrode; a saturated calomel electrode (SCE) was used as the reference electrode and a Pt mesh as the counter electrode. DHS was used as the working electrolyte. All the EIS data was collected through the frequency range between 10^5 Hz to 0.01Hz using a Gamry PCI4-300 potentiostat (Gamry Instruments, Inc. Warminster, PA, USA) in a potentiostatic mode.

4.2.5. SEM measurement

Scanning electron microscope (SEM) surface images of primers were obtained using a JEOL JSM-6300 (JEOL Ltd., Tokyo, Japan) with 15KeV acceleration voltage. If it is not noted, a secondary electron detector was used to obtain the images. The images of Mg alloy particles were taken at 250× magnification and images of samples after exposed in Prohesion chamber were taken at 3000× magnification.

4.3. Results and discussion

4.3.1. Properties of Magnesium alloy pigments

The five Mg alloy particles used as pigment in Mg alloy-rich primer system are AM60, AZ91B, LNR91, AM503 and AZG. They have dissimilar chemical composition, e.g. different elements at varying concentrations, and also they possess different physical properties of particle shape, particle size, particle size distribution (PSD) and surface roughness. The data of their chemical composition, density, mean volume and number particle size, and OA obtained from Spatula Rub-out method for five magnesium alloy pigments, are listed in Table 4-1. In addition, the morphologies and particle size plots of the five Mg alloy particles are shown in Figure 4-2 and 4-3, respectively.

In Figure 4-2, it can be seen that the five Mg alloy particles have different shapes: the AM60 particles have plate-like shapes with smooth edges; the AZ91B particles have chip-like shapes with sharp edges; the LNR91 particles have polyhedral-like shapes with pointed edges; the AM503 particles have smooth plate-like shapes similar to AM60; the AZG particles have random flake-like shapes but the edges are less sharp in comparison to AZ91B particles.

From Table 4-1, it can be seen that AM60 and AZ91B particles have the largest sizes with a mean volume diameters of 66.95 μm and 62.94 μm, respectively; AM503 and AZG have the smallest particles with mean volume diameters of 30.26 μm and 29.15 μm, respectively; LNR91 has the mean volume diameter of 47 μm. In Figure 4-3, it can be clearly seen that the width of PSD for each Mg alloy particle is different from others: AM503 and AZG have the narrowest widths and AZ91B has the broadest one. In addition, the ratios of mean volume diameter to mean number diameter for AM60, AZ91B, LNR91, AM503 and AZG are 4.08, 6.07, 3.21, 3.13 and 3.10, respectively. It indicates that AZ91B contained a large amount of very small particles. This phenomenon was not only evidenced by the SEM image of AZ91B but also by its particle size distribution plot, where the number percentage of small particles (less than 5μm) was very high.

OA for a specific particle is closely related to its surface area, size, PSD, surface roughness and porosity, and the wetting ability by linseed oil. [47] From Table 4-1, it can be seen that the progressive increase in OA value is of the order of LNR91, AM503, AZG, AM60 and AZ91B. The low OA of LNR91 might be due to its high density.

In Figure 4-3, the number percentage of the particles with diameter smaller than 5 μm for AM60, AZ91B, LNR91, AM503 and AZG is 49.5%, 54.1%, 29.7%, 23.5% and 26.6%,

respectively. It can be seen that half of AM60 and AZ91B particles have small particle size. The presence of large amount of small particles is very likely the reason for AM60 and AZ91B having large OA values because the smaller particles usually have high surface area to volume ratios.

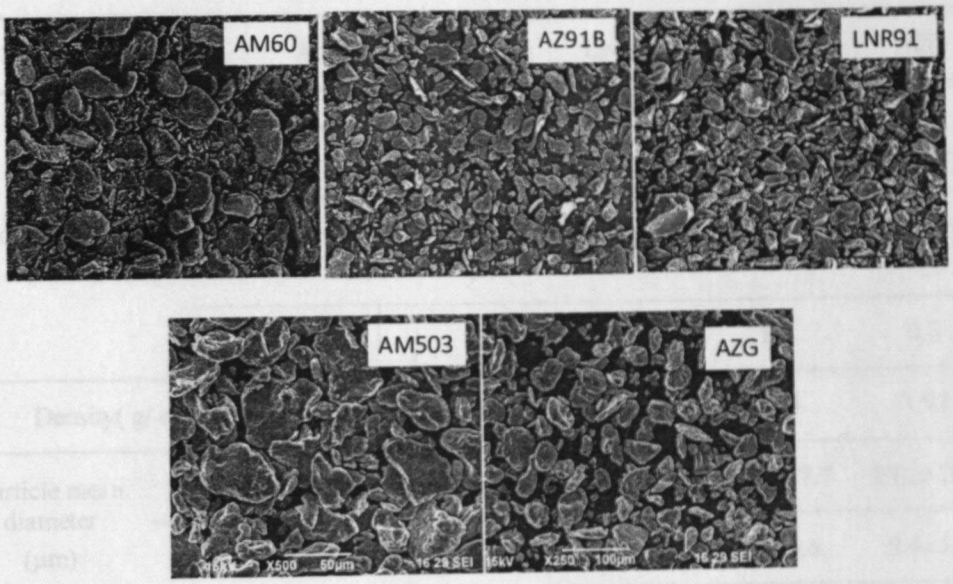

Figure 4-2. SEM images of Mg alloy particles: AM60, AZ91B, LNR91, AM503 and AZG.

4.3.2. Non-paramatric regression analysis of EIS data

Figure 4-4 shows the results of OCP changing as a function of exposure time obtained from eight 42% PVC AM60 primer coated AA2024 T3 panels. Each symbol represents an individual panel at different exposure time. It can be seen that the eight samples showed some similar trends in OCP changing, since most spots are located close with others. But the scattering of the data can be observed, too. Because there was no exact reason for excluding any data, all the data should be treated on an equal footing. Therefore, the nonparametric approach is used to fit these data. [43] The nonlinear regression model can be expressed as

$$y_i = f(x_i) + \varepsilon_i \qquad (4.1)$$

where the unspecific function f is assumed to be continuous and smooth, and $\varepsilon_i \sim$ NID (0, σ^2).

Table 4-1. Physical and chemical properties of Mg alloy particles.

Mg Alloy Pigment		AM60	AZ91B	LNR91	AM503	AZG
Chemical composition (wt.%)	Mg	94.0	89.8	50	98.1	91.1
	Al	5.8	9.0	50	/	5.7
	Zn	/	1.0	/	/	2.9
	Mn	0.2	0.2	/	1.9	0.3
Density(g/ cm^3)		1.80	1.81	2.22	1.84	1.97
Particle mean diameter (μm)	Vol	66.9±31.8	62.9±29.9	47.0±41.6	30.3±17.7	29.2±18.1
	Num	16.4±27.6	10.4±33.8	14.6±8.2	9.7±6.6	9.4±5.7
Oil absorption (g/100g pigment)		61.53±0.62	68.30±0.69	33.45±1.14	46.07±1.51	39.25±0.64

To fulfill the data fitting, R-project was downloaded from http://www.R-project.org, [48] including the packages of "survival", [49] "KernSmooth", [50] "splines", [48]"lattice", [51] "MASS", [52]"Matrix", [53] "mgcv", [52, 54-58] "fields", [59] "nlme".[60]

As a first attempt to use nonparametric approach to fit our data, three different methods are used. They are Kernel estimators, smoothing splines and local polynomials. The results of the data fitting obtained from these three methods are compared in order to choose a suitable one to be applied in our EIS data analysis.

4.3.2.1. Kernel estimators (Moving average estimation)

The Kernel estimator [43] has a simple form as

$$\hat{f} = \frac{1}{nh}\sum_{i=1}^{n} K(\frac{x - x_i}{h}),\ K(x) \geq 0,\ \int_{-\infty}^{\infty} K(x)dx = 1,\ K(x) = K(-x) \qquad (4.2)$$

K is the Kernel constant, and h is the bandwidth which determines the smoothness of the fitted curve.

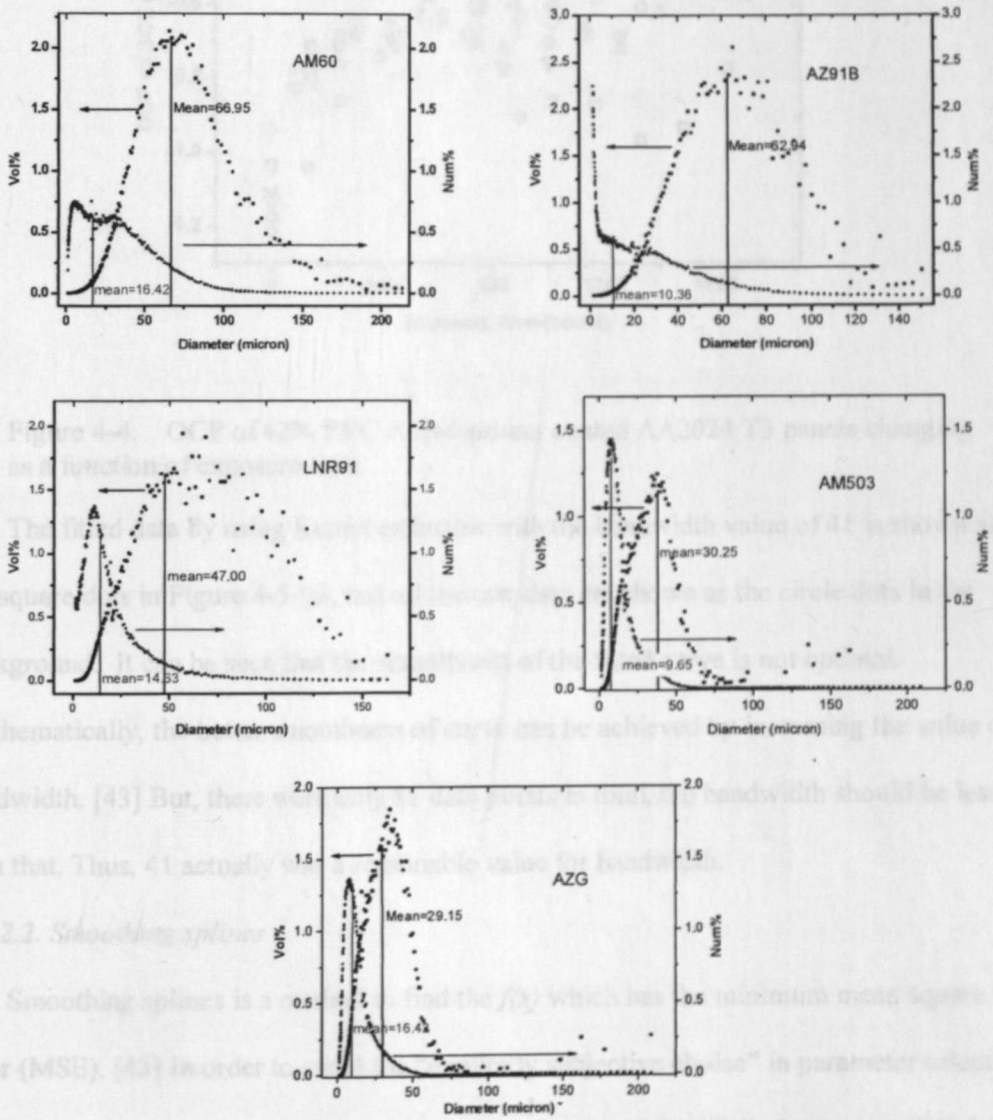

Figure 4-3. Particle size distribution of Mg alloy particles: AM60, AZ91B, LNR91, AM503 and AZG.

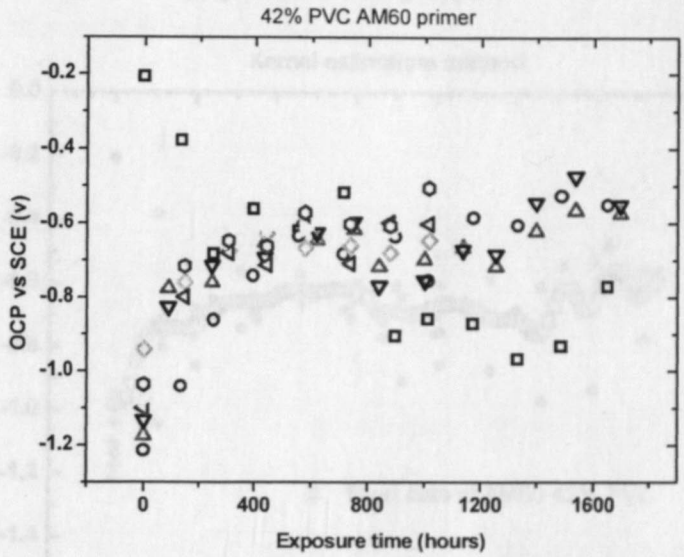

Figure 4-4. OCP of 42% PVC AM60 primer coated AA2024 T3 panels changing as a function of exposure time.

The fitted data by using Kernel estimator with the bandwidth value of 41 is shown as the square dots in Figure 4-5 (a), and all the raw data are shown as the circle dots in the background. It can be seen that the smoothness of the fitted curve is not optimal. Mathematically, the better smoothness of curve can be achieved by increasing the value of bandwidth. [43] But, there were only 81 data points in total, the bandwidth should be less than that. Thus, 41 actually was a reasonable value for bandwidth.

4.3.2.2. Smoothing splines

Smoothing splines is a method to find the $f(x)$ which has the minimum mean square error (MSE). [43] In order to avoid the "explicitly subjective choice" in parameter selection, cross-validation is a common method used by statistician. [43] Similarly, cross-validation is used to choose the smoothing parameter of smoothing splines in R-project. The fitted results are shown in Figure 4-5 (b) as the square dots with 95% confidential interval.

Similarly, the raw data are displayed as the background.

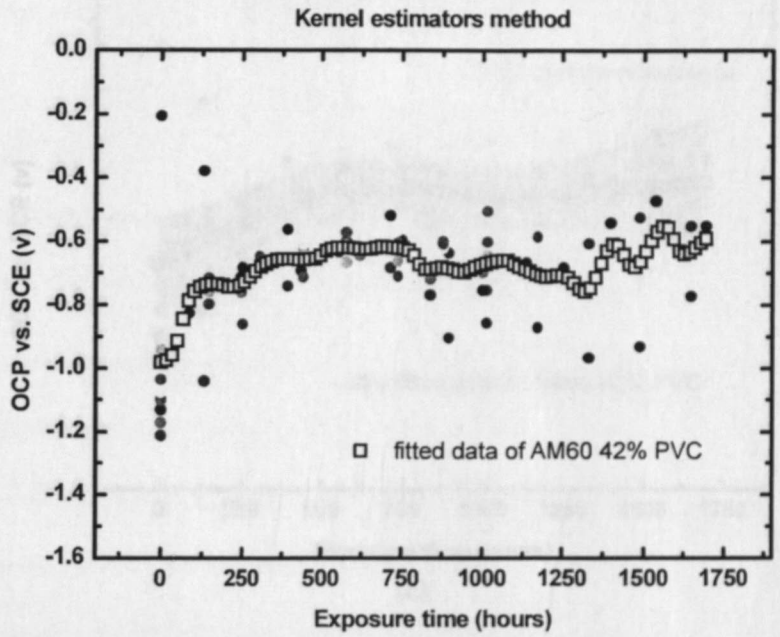

(a)

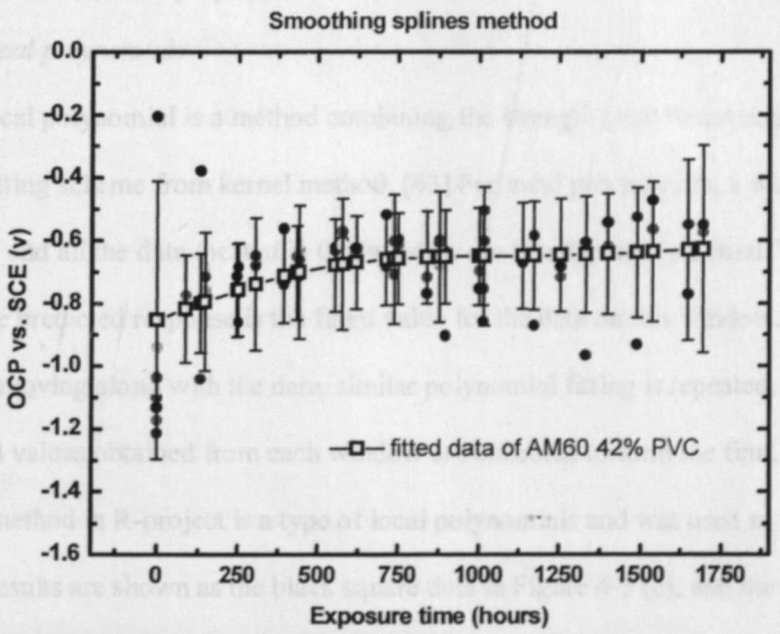

(b)

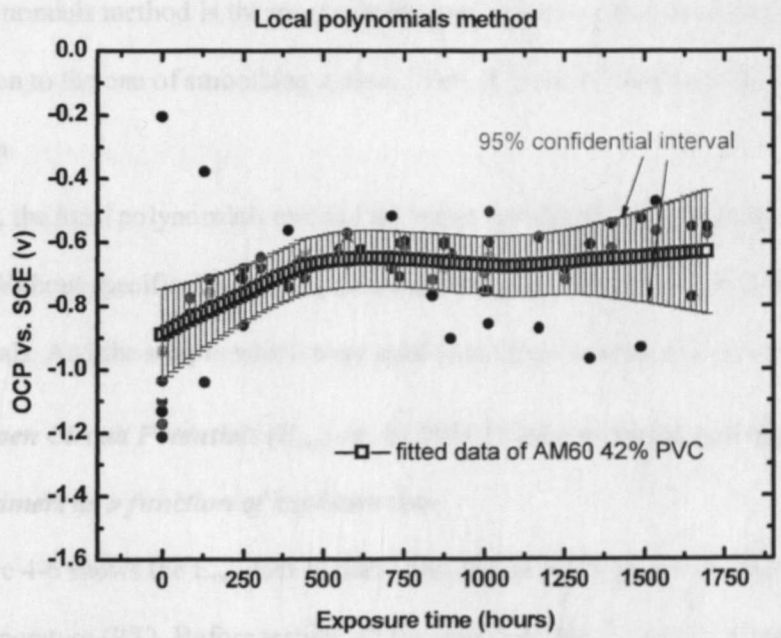

(c)

Figure 4-5. Data fitting plots by using (a) kernel estimators (h=41), (b) smooth splines, and (c) local polynomials.

4.3.2.3. Local polynomials

The local polynomial is a method combining the strength from linear regression and the local fitting scheme from kernel method. [43] For local polynomials, a window is set artificially, and all the data located in this window are fitted to a polynomial. The middle value of the predicted response is the fitted value for the data on this window. When this window is moving along with the data, similar polynomial fitting is repeated. As a result, many fitted values obtained from each window are collected to form the final fitted curve. The loess method in R-project is a type of local polynomials and was used to fit the EIS data. The results are shown as the black square dots in Figure 4-5 (c), and the 95% confidential interval is shown as the green shadows.

By comparing these three methods, it seems that the fitted results obtained from the

local polynomials method is the most suitable one, since its curve maintains more details in comparison to the one of smoothing splines. Also, it is not as rough as the one of kernel estimation.

Thus, the local polynomials method is chosen for all the EIS data analysis in this chapter. Without specific description, all the data lines are the fitted curves by using local polynomials. And the scripts which were used to analysis data are shown in the Appendix.

4.3.3. Open Circuit Potentials (E_{ocp}) of AA2024 T3 panels coated with Mg alloy rich primers as a function of exposure time

Figure 4-6 shows the E_{ocp} data of thirty bare AA2024 T3 panels in DHS solution at room temperature (RT). Before testing, all the bare AA2024 T3 were polished by using 220 grit sand paper and then followed hexane rinse to eliminate the oxide layer on the surface. From Figure 4-6, it can be seen that the average E_{ocp} value of AA2024 T3 panel and its standard deviation are -0.4976 V/SCE and ± 0.021 V/SCE, respectively. Therefore, the OCP range between -0.48 and -0.52 V/SCE is considered as the E_{ocp} region for bare AA2024 T3.

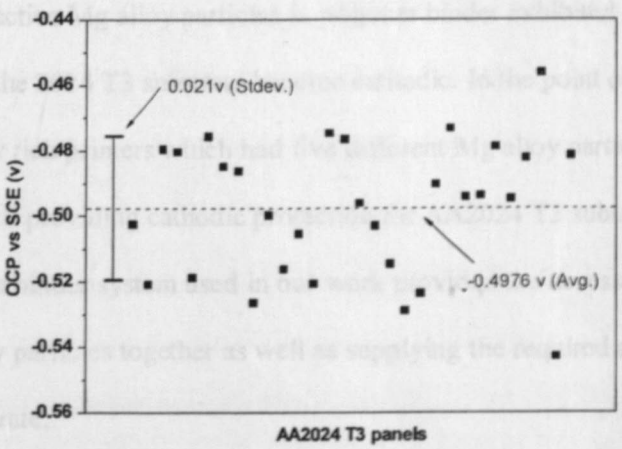

Figure 4-6. Open circuit potentials of thirty AA2024 T3 panels.

When an AA2024 T3 panel was coated with an Mg alloy rich primer, a mixed E_{ocp}^{mix} of this coated AA2024 T3 panel was obtained. When the E_{ocp}^{mix} was smaller than the E_{ocp} of bare AA2024 T3, the AA2024 T3 substrate was under cathodic protection; when E_{ocp}^{mix} was higher than the E_{ocp} of bare AA2024 T3, the corrosion of AA2024 T3 was undergoing. Therefore, as long as E_{ocp}^{mix} was more negative than E_{ocp}, it can be regarded that cathodic protection provided by Mg alloy rich primer was in place. [16, 61]

In our work, the values of E_{ocp}^{mix} of AA2024 T3 panels coated with various Mg alloy rich primers were recorded with exposure time. Figure 4-7 shows the plots of the E_{ocp}^{mix} change as a function of exposure time for each Mg alloy rich primer coated AA2024 T3 samples (42% PVC and without topcoat) and the gray shadow denotes the 95% confidential interval for each Mg alloy rich primer.

From Figure 4-7, it can be seen that the E_{ocp}^{mix} values of AA2024 T3 panels coated with Mg alloy rich primers were located at a potential between -1.20 V/SCE (E_{ocp} of Mg alloy) and -0.5 V/SCE (E_{ocp} of bare AA2024 T3). It clearly indicates that the Mg alloy rich primers have provided cathodic protection for AA2024 T3 substrate. Similar to pure Mg-rich primer, the active Mg alloy particles in polymer binder exhibited that they could act as anodes to make the 2024 T3 substrate become cathodic. In the point of metal-rich primer system, Mg alloy rich primers which had five different Mg alloy particles as pigments met the requirement of providing cathodic protection for AA2024 T3 substrate. Also, the epoxy-polyamide binder system used in our work provided the necessary matrix for holding Mg alloy particles together as well as supplying the required adhesion between primer and substrate.

Furthermore, the changes of E_{ocp}^{mix} of Mg alloy rich primers coated AA2024 T3

samples with exposure time were studied. Three major periods can be distinguished based on Figure 4-7.

4.3.3.1. Initial period: sharp increase of E_{ocp}^{mix}

The E_{ocp}^{mix} of the unexposed samples coated with various Mg alloy rich primers are close to the ones of Mg alloys, which is in agreement with the high content of Mg alloy particles in unexposed primer films. From 0 to 300 hours of exposure time, all the samples show the quick increase of E_{ocp}^{mix} from very negative values (between -1.25V/SCE and -1.0V/SCE) to -0.75V/SCE. It indicates the quick activation and oxidation of Mg alloy particles. Such quick increases of E_{ocp}^{mix} in the beginning of exposure were also observed in Mg-rich primer systems.[12, 13, 15] However, for ZRP systems, the sharp increases of E_{ocp}^{mix} are usually observed in the later stage of exposure.[29, 61, 62] This difference might be explained by the different activities between Mg/Mg alloys and Zn. Since Mg/Mg alloys are more active than Zn, the direct reaction between electrolyte and Mg/Mg alloy probably occur while Mg/Mg alloy particles also act as the sacrificial anodes. This "side-reaction" will cause the oxidation of Mg/Mg alloy in parallel. To reduce the consumption of Mg/Mg alloy particles caused by side-reaction, it suggests that the proper PVC for the formulation of Mg/Mg alloy rich primer systems is near but lower than CPVC so that the barrier property of polymer binder can hinder the direct reactions between Mg/Mg alloy particles and electrolyte. [12] However, the effective cathodic protection provided by each Mg alloy rich primer was obtained due to the good electrical connection between Mg alloy particles via the electrolyte as well as the particle-to-particle connectivity.

4.3.3.2. Second period: plateau of E_{ocp}^{mix}

With the further exposure after three hours, the E_{ocp}^{mix} of samples increased slowly

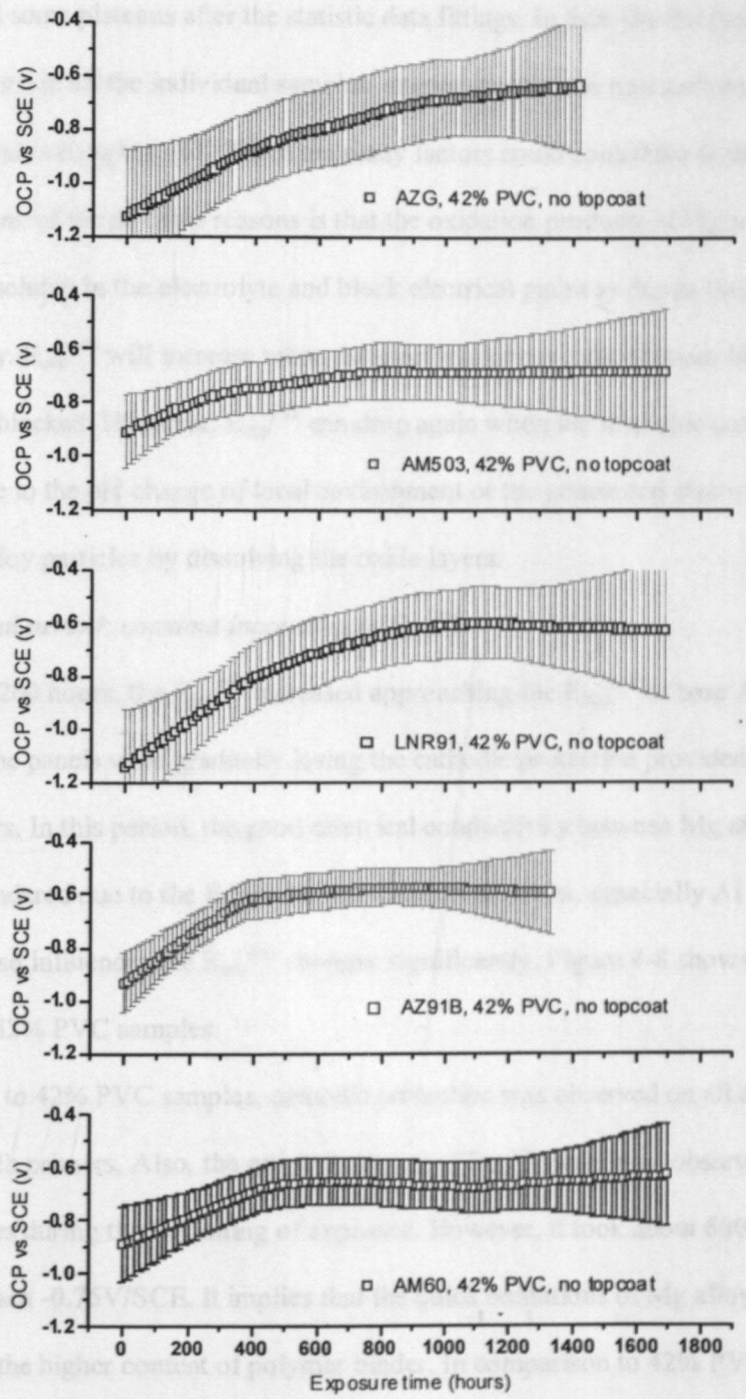

Figure 4-7. OCP of AA2024 T3 panels coated with different Mg alloy rich primers with 42% PVC changing as function of exposure time.

and showed some plateaus after the statistic data fittings. In fact, the fluctuation of E_{ocp}^{mix} were observed in all the individual samples, suggesting that the ratios of exposed A_{par}/A_{sub} were randomly changing. [61] There are many factors could contribute to the fluctuations of E_{ocp}^{mix}, one of the possible reasons is that the oxidation products of Mg and Al formed could be insoluble in the electrolyte and block electrical pathway due to their reduced conductivity. E_{ocp}^{mix} will increase when the electrical connection between Mg alloy particles is blocked. However, E_{ocp}^{mix} can drop again when the insoluble oxidation products dissolve due to the pH change of local environment or the penetrated electrolyte active more Mg alloy particles by dissolving the oxide layers.

4.3.3.3. Final period: constant increasing of E_{ocp}^{mix}

After 1200 hours, the E_{ocp}^{mix} increased approaching the E_{ocp}^{mix} of bare AA2024 T3, indicating the panels were gradually losing the cathodic protection provided by the Mg alloy primers. In this period, the good electrical conductivity between Mg alloy particles might be hindered due to the formation of oxidation products, especially Al oxides.

PVC also influences the E_{ocp}^{mix} changes significantly. Figure 4-8 shows the E_{ocp}^{mix} changes of 32% PVC samples.

Similar to 42% PVC samples, cathodic protection was observed on all the 32% PVC Mg alloy rich primers. Also, the quick increases of E_{ocp}^{mix} were also observed on all the 32% PVC samples during the beginning of exposure. However, it took about 600 hours for the E_{ocp}^{mix} to reach -0.75V/SCE. It implies that the quick oxidations of Mg alloy particles were retarded by the higher content of polymer binder. In comparison to 42% PVC samples, it's more difficult to distinguish the plateaus of E_{ocp}^{mix} to 32% PVC samples, since the continuous increases of E_{ocp}^{mix} were still observed for AZ91B and LNR91 samples. In

addition, the E_{ocp}^{mix} of AM503 samples even dropped during the further exposure, and AZG samples showed much fast increases of E_{ocp}^{mix} in the last stage of exposure.

The 32% PVC Mg alloy primers exhibited different behaviour of the E_{ocp}^{mix} changes with exposure time. One probable reason is that the microstructures of 32% PVC Mg alloy primers were more various in comparison to the 42% PVC samples. As what mentioned in the studies of CPVC, the CPVCs of these five Mg alloy rich primer systems were different. When Mg alloy rich primers were formulated at high PVC (>CPVC), the major differences of the microstructures were the thickness of the absorbed layer and the percentage of polymer filled interstices. However, when they were formulated at low PVC (<CPVC), the connection of Mg alloy particles in polymer matrix actually depended on Λ (the reduced PVC = PVC/CPVC). Since the CPVCs of AM503, AZG and LNR91 were much higher than the ones of AM60 and AZ91B, the former primer systems might have better barrier properties than the latter ones. However, more studies should be done to confirm the effects of Λ on the behaviour of E_{ocp}^{mix} changes.

With the further exposure, serious delamination was observed to the 32% PVC Mg alloy rich primers even their E_{ocp}^{mix} values didn't show dramatic changes. It might be due to the low content of Mg alloy particles in 32% PVC primers, which made the electrolyte play an important role in the electrical conductivity between particles as well as between primers and AA2024 T3 substrates.

E_{ocp}^{mix} is a very useful and intuitive indicator to monitor the presence and the duration of cathodic protection. Based on the change of E_{ocp}^{mix} vs. exposure time, it is clearly showed that all the Mg alloy-rich primers studied can provide cathodic protection to AA2024 T3 substrate and the performance and duration of cathodic protection are

appreciably affected by the type of Mg alloys and the PVC of formulation.

4.3.4. Impedances at 0.01Hz ($|Z|_{0.01Hz}$) of AA2024 T3 panels coated with Mg alloy rich primers as a function of exposure time

In Figure 4-9 (a) and (b), the impedance modulus ($|Z(\omega)|$) and phase angle ($\theta(\omega)$) diagrams of 31%PVC AM60 primer at different exposure time are shown, respectively. In coating system, the impedance at low frequency is usually related to the sum of polarization resistance (R_p), pore resistance (R_{pore}) and solution resistance (R_s), [63] especially when defects, such as pores, are presented in the coating system. Because Mg alloy rich primer systems without topcoat were porous, $|Z(\omega)|$ at low frequency can be regarded as the sum of R_p and R_{pore} (R_s was ignored because it was very small).

From Figure 4-9 (a) and (b), it can be seen that the impedance at low frequency (0.01Hz) decreased with exposure time. Meanwhile, the phase angle at low frequency (0.01Hz) was about -10 degrees in the first 100 hours exposure and increased to -40 degrees at 506 hours exposure; after 600 hours exposure, the phase angle at low frequencies dropped to -20 degree again.

Figure 4-10 (a) and (b) show the Bode modulus and phase angle diagrams for the panels coated with different Mg alloy primers and a clear (unpigmented) coating (black lines) after 500 hours exposure. It can be seen that the phase angles of the clear coating, 36% PVC AZ91B, and 50% PVC LNR91 were less than -10 degree at low frequencies, and the ones of others samples were between -20 degree and -40 degree. The non-zero of phase angle at low frequency indicates that the capacitance of Mg alloy rich primer system also contributed to the impedance at low frequency.

However, since the phase angles at low frequencies did not vary significantly and the

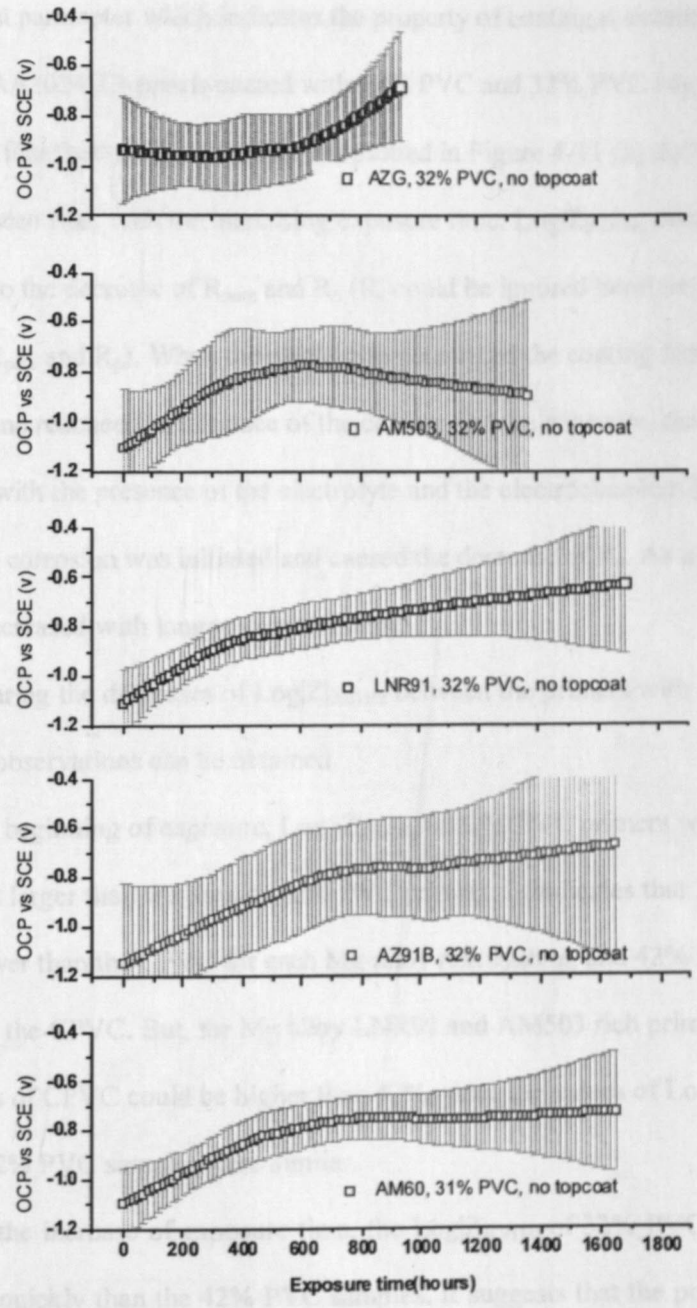

Figure 4-8. OCP of AA2024 T3 panels coated with different Mg alloy rich primers with 32% PVC changing as function of exposure time.

phase angles decreased with the increasing exposure time, the changes of impedance modulus at low frequency ($|Z|_{0.01Hz}$) dominated by the alteration of coating resistance. Thus,

as an important parameter which indicates the property of coating resistance, the changes of $|Z|_{0.01Hz}$ of AA2024 T3 panels coated with 42% PVC and 32% PVC Mg alloy rich primers as the function of exposure time are plotted in Figure 4-11 (a) and (b), respectively.

It can be seen that, with the increasing exposure time, $Log|Z|_{0.01Hz}$ decreased. This might be due to the decrease of R_{pore} and R_p (R_s could be ignored because it was very low compared to R_{pore} and R_p). When the electrolyte penetrated the coating film through the porous paths and reached the interface of the coating and the substrate, the R_{pore} decreased. Furthermore, with the presence of the electrolyte and the electrochemically active species, the under-film corrosion was initiated and caused the decrease of R_p. As a result, $Log|Z|_{0.01Hz}$ decreased with longer exposure time.

By comparing the decreases of $Log|Z|_{0.01Hz}$ between the primers with 42% PVC and 32% PVC, several observations can be obtained.

1. In the beginning of exposure, Log $|Z|_{0.01Hz}$ of 32% PVC primers were about two orders larger than the ones of 42% PVC primers. It indicates that 32% PVC might be lower than the CPVC for each Mg alloy rich system, and 42% PVC might be above the CPVC. But, for Mg alloy LNR91 and AM503 rich primer systems, the values of CPVC could be higher than 42%, since the values of $Log|Z|_{0.01Hz}$ of 32% and 42% PVC samples were similar.
2. With the increase of exposure time, the $Log|Z|_{0.01Hz}$ of 32% PVC primers dropped more quickly than the 42% PVC samples. It suggests that the porous nature made the high PVC primers saturated with electrolyte very quickly. In the contrary, the high percentage of polymer binder in low PVC primers slowed down the penetration of electrolyte, which resulted in the graduate decrease of $Log|Z|_{0.01Hz}$.

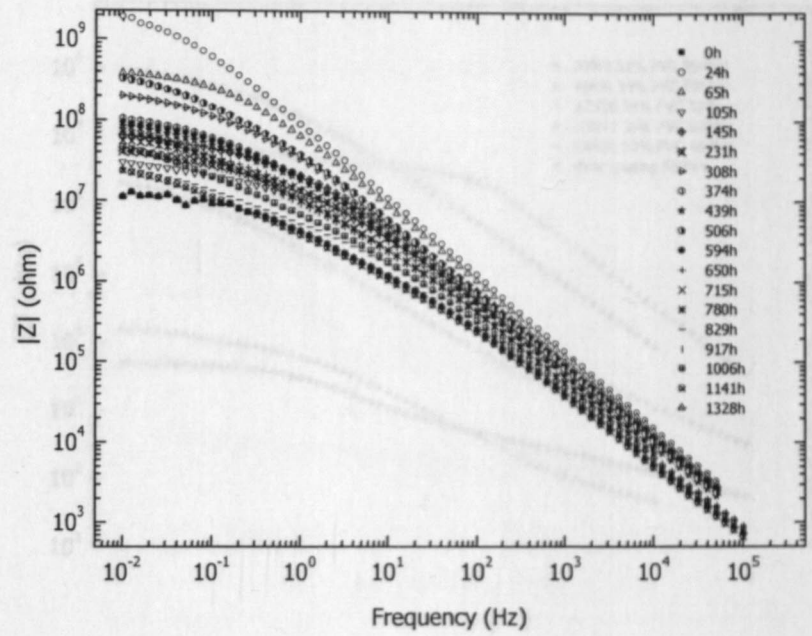

(a)

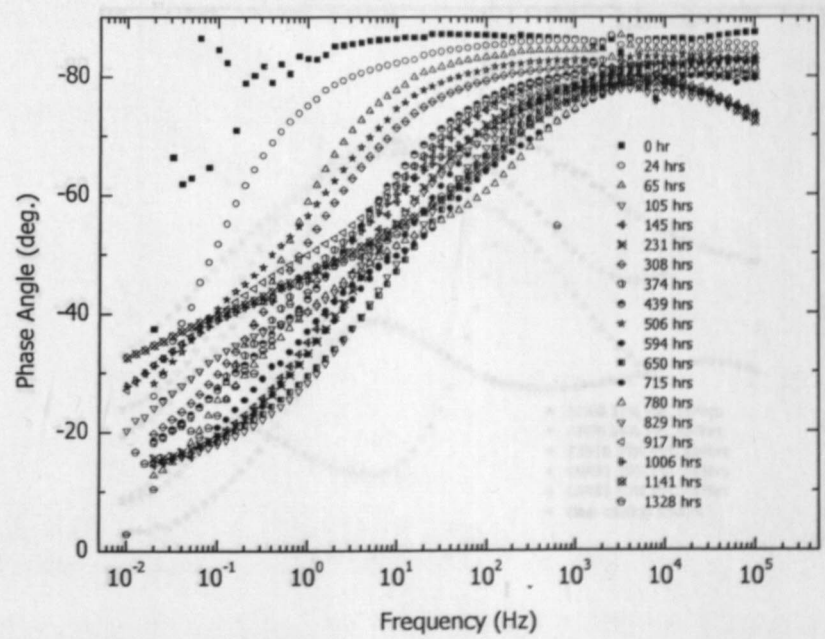

(b)

Figure 4-9. (a) Bode plots, and (b) phase angle diagrams of AA2024 T3 panel coated with 31% PVC AM60 primer at different exposure times.

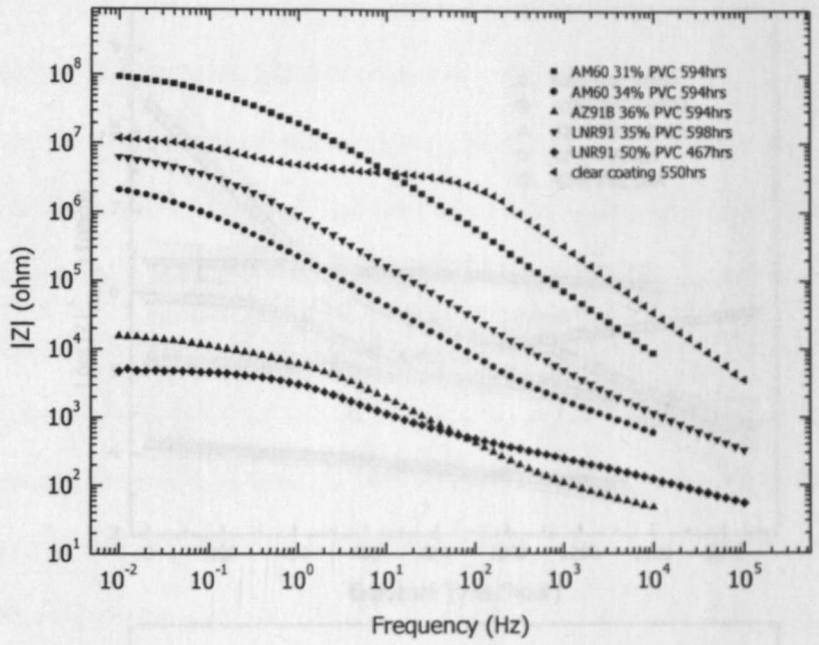

(a)

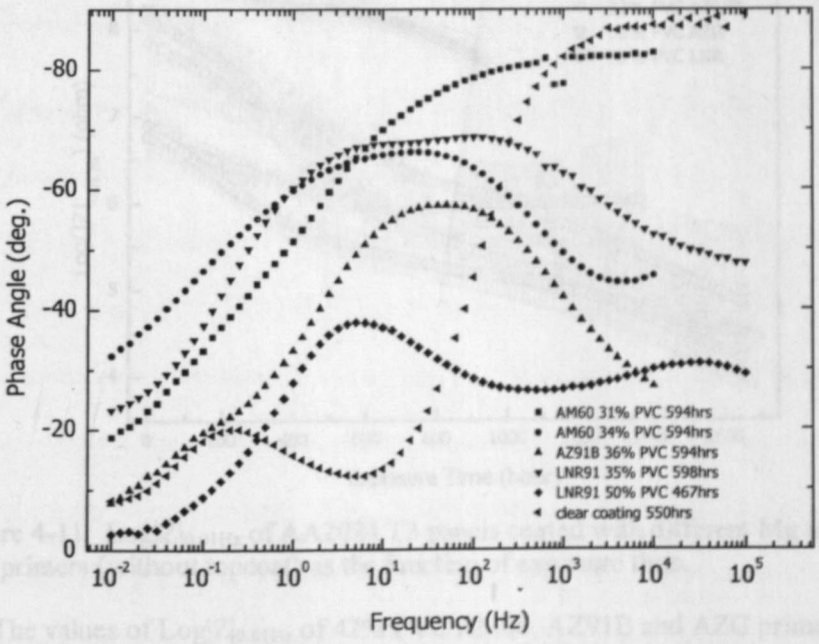

(b)

Figure 4-10. (a) Bode plots, and (b) phase angle diagrams of AA2024 T3 panel coated with different Mg alloy rich primers after about 600 hours exposure.

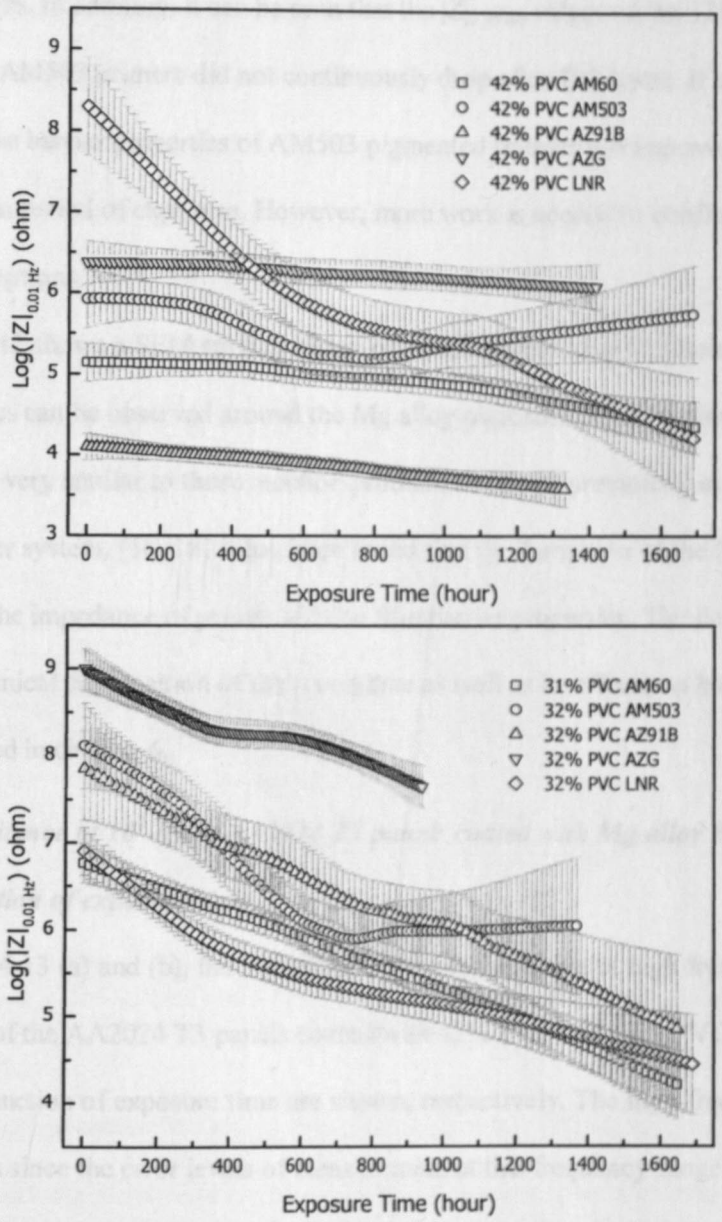

Figure 4-11. $Log|Z|_{0.01Hz}$ of AA2024 T3 panels coated with different Mg alloy rich primers (without topcoat) as the function of exposure time.

The values of $Log|Z|_{0.01Hz}$ of 42% PVC AM60, AZ91B and AZG primers did not drop much with the increase of exposure time, though their primer films were porous. It indicates that the formation of oxidation products of Mg or Al in Mg alloy particles probably contributed some barrier properties to these primer

systems. In addition, it can be seen that the $|Z|_{0.01Hz}$ values of the 32% and 42% PVC AM503 primers did not continuously drop after 700 hours. It might imply that the barrier properties of AM503 pigmented primers got improved after a certain period of exposure. However, more work is needed to confirm these assumptions.

Figure 4-12 shows a SEM surface image of AM60 primer after 715 hours exposure. Mg precipitates can be observed around the Mg alloy pigments. The morphology of the Mg precipitates is very similar to those reaction products observed previously in the studies of Mg-rich primer system. [16, 18] It has been found that the formation of the Mg precipitate would affect the impedance of primer and the film barrier properties. The determination of the actual chemical composition of the precipitate as well as its effects on barrier protection will be reported in chapter 6.

4.3.5. Capacitance at 10^4 Hz of AA2024 T3 panels coated with Mg alloy rich primers as a function of exposure time

In Figure 4-13 (a) and (b), the logarithms of the capacitances at high frequency ($Log|C|_{10^4\ Hz}$) of the AA2024 T3 panels coated with 42% PVC and 32% PVC Mg alloy rich primers as a function of exposure time are shown, respectively. The high frequency of 10^4 Hz was chosen since the error levels of measurement at this frequency range are low and the system is usually locally stable. Also, the capacitance at high frequency of a coating system is relative to the water uptake of the coating film. [64] since the high dielectric constant of water (~80 F/cm^2) is much larger than the ones of polymers (2~8 F/cm^2), and the water uptake of coating film can result in the increase of coating capacitance.

From Figure 4-13, it can be observed that, with the increase of exposure time, all the

$Log|C|_{10^4Hz}$ increased gradually. In addition, for AM60 and AZ91B primers, the $Log|C|_{10^4Hz}$ values of 42% PVC primers were one order higher than the ones of 32% PVC, but for AM503, LNR91 and AZG primers, their $Log|C|_{10^4Hz}$ values were similar whatever they were 42%PVC or 32% PVC. It might imply that the CPVCs of LNR91, AM503 and AZG primer systems could be higher than 42%. Furthermore, irrespective of the type of pigments used or the PVC formulated at, the increasing rates of $|C|_{10^4Hz}$ were similar. It might indicate that the water uptake tended to be related to the property of polymer binder rather than Mg alloy particles.

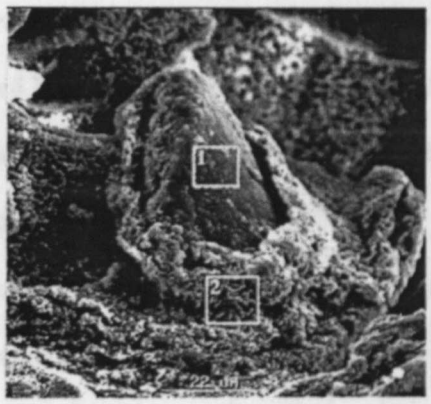

Figure 4-12. SEM surface image of 34% PVC AM60 primer coated panel after 715 hours exposure: (Area 1) Mg alloy pigment and (Area 2) Structure of Mg precipitate.

4.3.6. E_{ocp}^{mix} of topcoated Mg alloy primers as a function of exposure time

A complete metal-rich primer system at least contains a layer of primer film and a layer of topcoat, which will be applied over the primer to provide the barrier protection. In order to understand the anti-corrosion behavior and the durability of an aerospace coating system, Mg alloy-rich primer system with two different types of topcoat have been studied by EIS after being exposed in Prohesion chamber. The duplicates of testing samples were limited by the shortness of the Mg alloy particles supplies, two or four samples had been

tested for each type of Mg alloy rich primers. Thus, the following data analysis and discussions are based on the available results. More works need to be done in the future to confirm the performance of the topcoated Mg alloy rich primer systems.

Figure 4-14 and 4-15 show the E_{ocp}^{mix} of AA2024 T3 panels coated with 42% and 32% PVC Mg alloy primers and a topcoat as the function of exposure time. It can be observed that, irrespective of the type or PVC of Mg alloy rich primer, the E_{ocp}^{mix} of all samples were between -1.5 and -0.8 V/SCE in the early exposure time, and gradually increased to approach to the E_{ocp} of bare AA2024 T3 with the increasing exposure time. which indicates the existence of cathodic protection for all the topcoated Mg alloy rich primers. These results showed that topcoated Mg alloy rich primers provided cathodic protection for AA 2024 T3 substrate. However, the existence of topcoat had some influence on the performance of Mg alloy rich primers.

In comparison to the non-topcoated primers, it took longer time for the E_{ocp}^{mix} of topcoated Mg alloy rich primers to reach -0.55V/SCE. It indicates that the barrier protection provided by the topcoat reduced the direct reaction between the porous primer and the electrolyte, since the penetration of electrolyte into the primer films were retarded by the topcoat. As a result, the lifetime of the topcoated Mg alloy rich primers were extended.

4.3.7. $|Z|_{0.01Hz}$ of topcoated Mg alloy primers as a function of exposure time

Figure 4-16 (a) and (b) showed the impedance at low frequency as function of exposure time for topcoated AA2024 T3 panels with 42% and 32% PVC Mg alloy rich primers, respectively.

It can be observed that $|Z|_{0.01Hz}$ remained at 5×10^{8} to 10^{10} ohm irrespective of the type

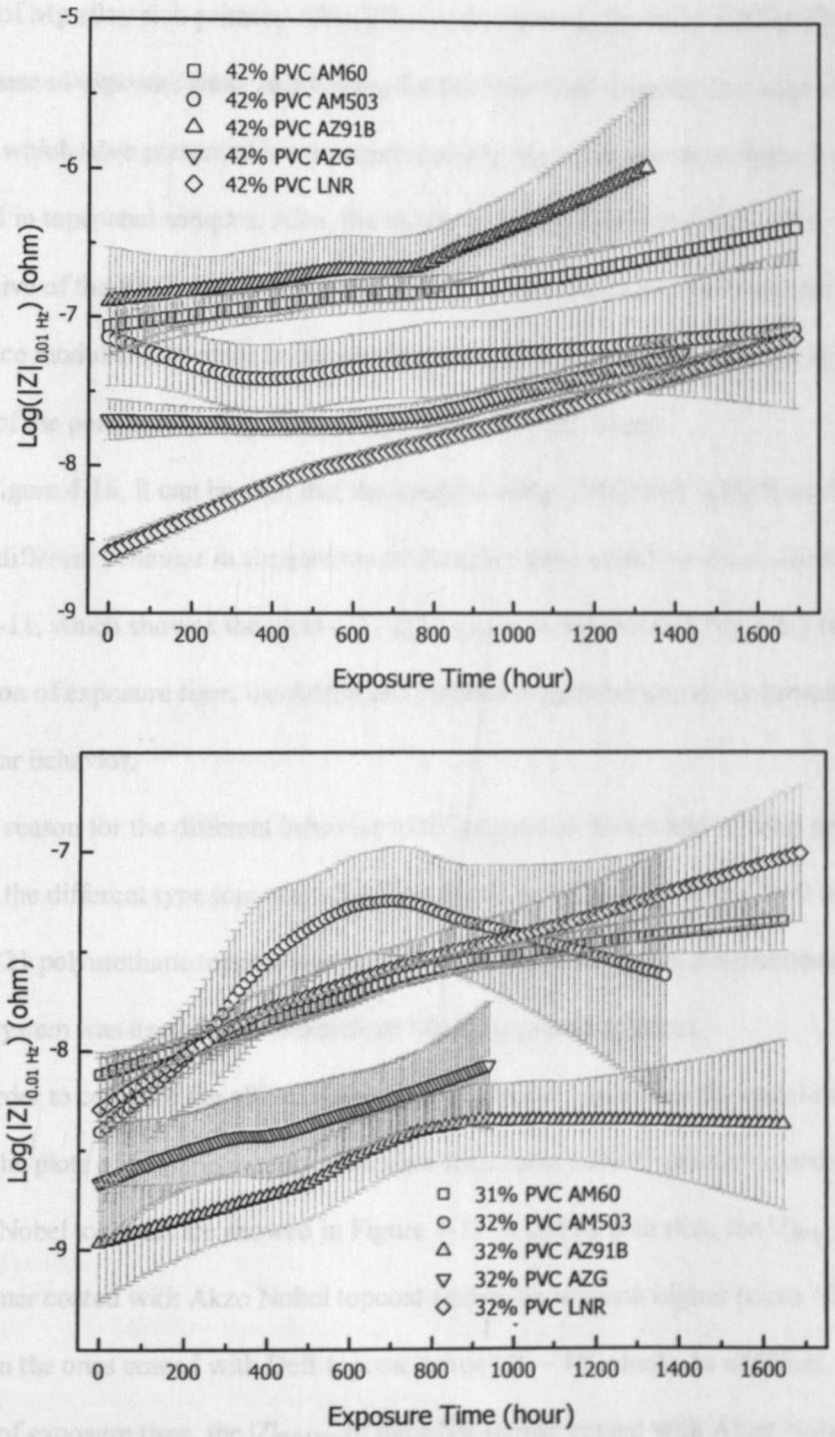

Figure 4-13. Log $|C|_{10^4\ Hz}$ of AA2024 T3 panels coated with different Mg alloy primers (without topcoat) as a function of exposure time.

or PVC of Mg alloy rich primers. Also, $|Z|_{0.01Hz}$ for topcoated primers did not decrease with the increase of exposure time. In addition, for the individual samples, the large variation of $|Z|_{0.01Hz}$, which have presented in non-topcoated Mg alloy rich primer systems were not observed in topcoated samples. Also, the values of $|Z|_{0.01Hz}$ were above 10^9 ohm irrespective of the PVC of primers. It may imply that the topcoat contributed the high impedance modulus (10^9 ohm) to the whole coating system by overriding the various $|Z|_{0.01Hz}$ of the porous Mg alloy rich primers (circa 10^6 - 10^7 ohm).

In Figure 4-16, it can be seen that the samples using AM60 and AZ91B as pigments showed different behavior in comparison to the other three primer systems. However, from Figure 4-11, which showed the plots of $Log|Z|_{0.01Hz}$ of non-topcoated Mg alloy rich primers as function of exposure time, the AM60 and AZ91B pigmented primer systems exhibited the similar behavior.

One reason for the different behavior of the topcoated AM60 and AZ91B primers could be the different type topcoats used. For AM60 and AZ91B primers, Deft low gloss 03-GY-321 polyurethane topcoat was applied. And the Akzo Nobel Polyurethane glossy topcoat system was used for the other three Mg alloy primer systems.

In order to compare the effects of topcoat as a barrier protection for metal-rich primer system, the plots of $|Z|_{0.01Hz}$ vs. exposure time for a same LNR91 primer coated with Deft or Akzo Nobel topcoats are showed in Figure 4-17. It can be seen that, the $|Z|_{0.01Hz}$ of the LNR primer coated with Akzo Nobel topcoat system were much higher (circa 10^9 -10^{10} ohm) than the ones coated with Deft topcoat (circa 10^6 – 10^7 ohm). In addition, with the increase of exposure time, the $|Z|_{0.01Hz}$ of the LNR primer coated with Akzo Nobel topcoat remained constantly. But, the LNR91 primers coated with Deft topcoat showed much lower

$|Z|_{0.01Hz}$, and were found to be failed in 700 hours exposure due to the loss of adhesion. Although the reason for adhesion loss is not clear yet, but the performance of the Deft topcoated primers implies that Deft topcoat cannot provide the good barrier protection to the whole coating system as the Akzo Nobel topcoat does.

Also, in Figure 4-16 (a) and (b), the increase of $Log|Z|_{0.01Hz}$ of the topcoated AM60 and AZ91B primers can be observed. This phenomenon was actually caused by the statistic analysis, since the changes of $Log|Z|_{0.01Hz}$ of the individual samples did not exhibit such dramatic increase of $|Z|_{0.01Hz}$. Probably, more raw data are needed in order to obtain the reasonable statistic results.

The comparison of Mg alloy rich primers coated with good and poor topcoat emphasizes that the anticorrosion performance of Mg alloy rich primer is dependent on the synergy of the different components in the whole system. In the initial exposure period, the topcoat can protect Al alloy substrate via its good barrier protection. When the electrolyte gradually penetrates the topcoat and primer film, Mg alloy pigments can be induced to provide cathodic protection for Al alloy substrates. With the further exposure, the formation of the oxidation products of Mg or Al in Mg alloy particles may reinforce the barrier protection of Mg alloy rich primer systems, which will be discussed in chapter 6. As a result, the lifetime of the Mg alloy-rich coating can be significantly extended.

4.4. Conclusions

Similar to the pure Mg particles, the Mg alloy pigments formulated in metal-rich primer coatings can provide cathodic protection for Al alloy substrates. OCP results showed that the E_{ocp}^{mix} of AA 2024 T3 panels coated with Mg alloy rich primers were between the E_{ocp}s of Mg alloy particles and bare Al 2024 T3. For the five Mg alloy

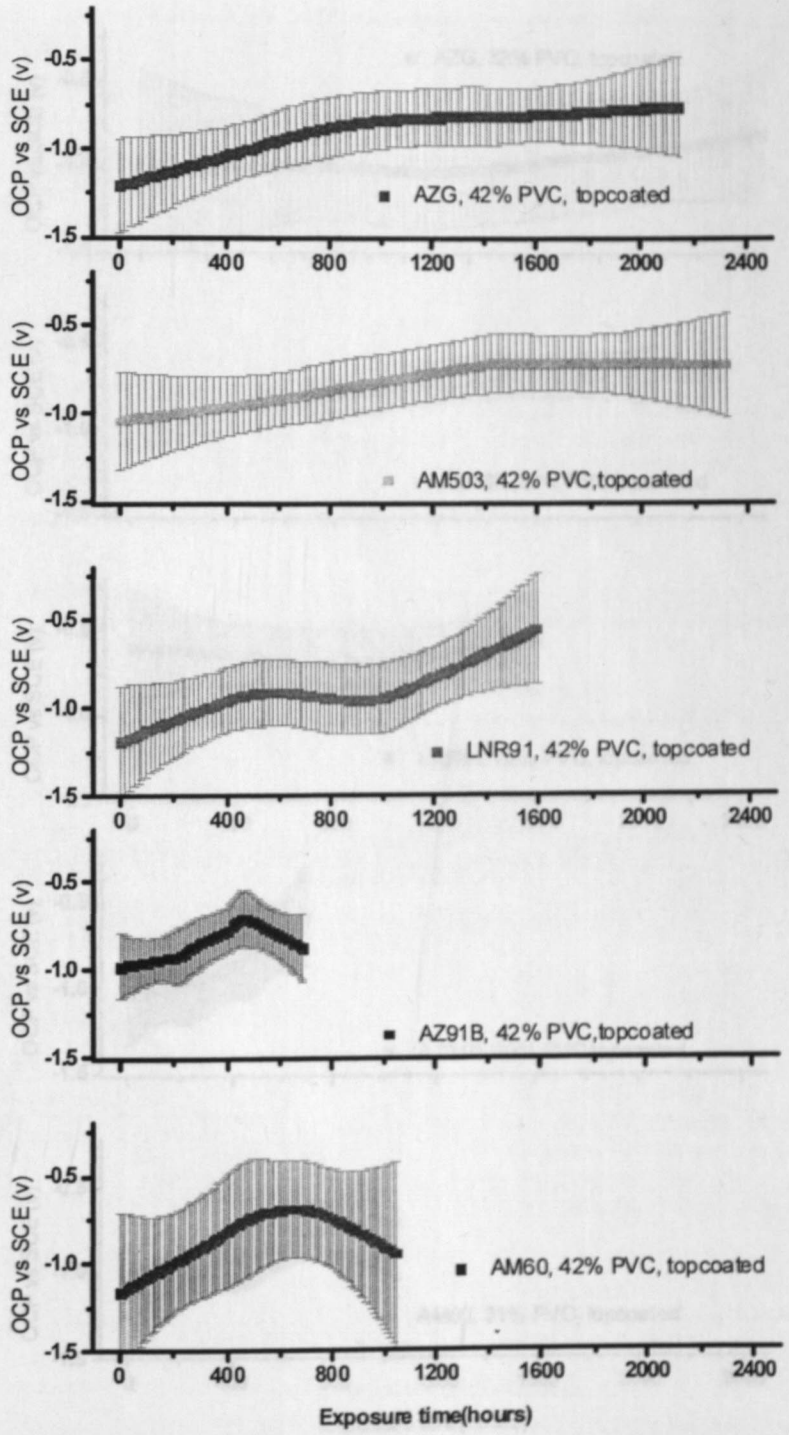

Figure 4-14. OCPs of 42% Mg alloy primer coated panels (with topcoat) as the function of exposure time.

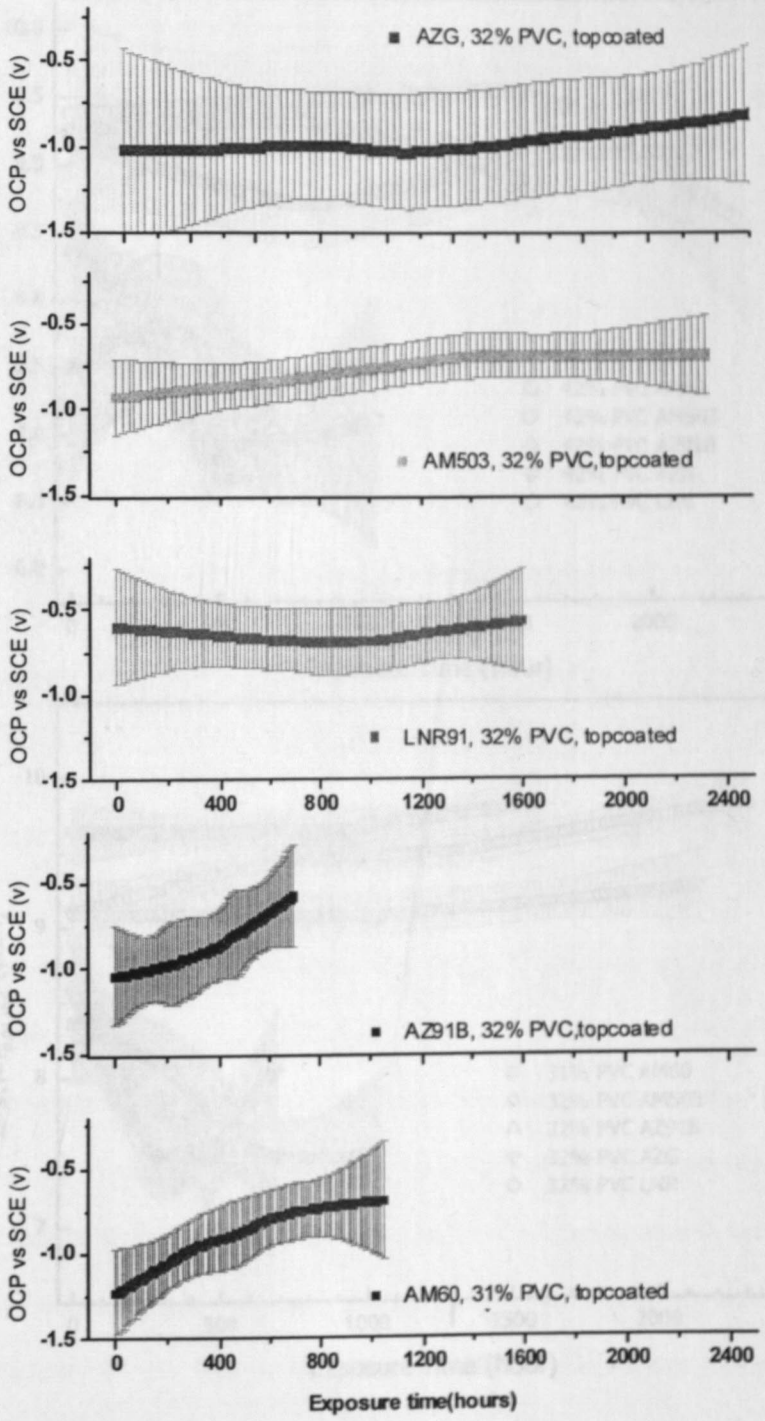

Figure 4-15. OCPs of 32% Mg alloy primer coated panels (with topcoat) as the function of exposure time.

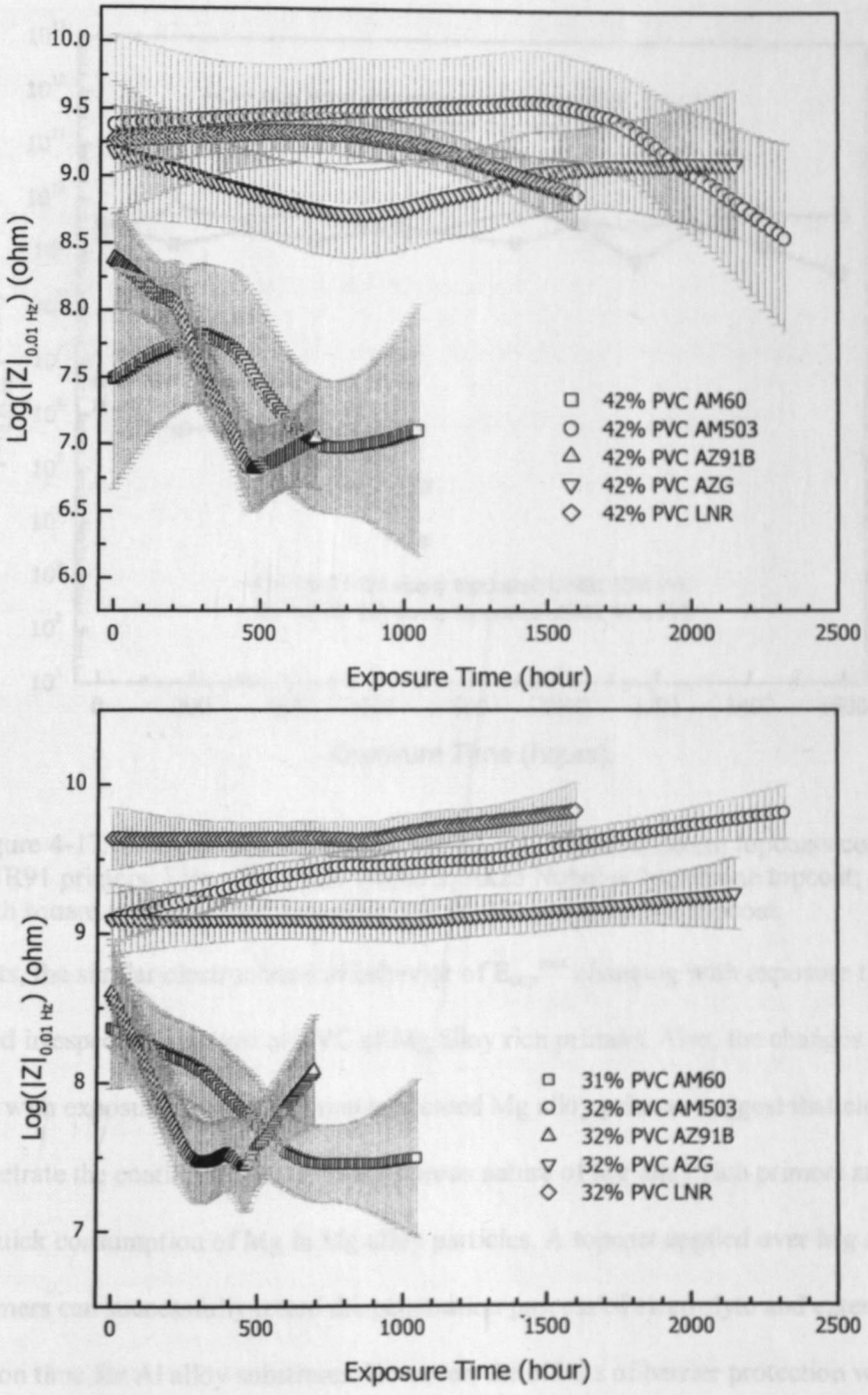

Figure 4-16. $|Z|_{0.01Hz}$ of Mg alloy primer coated panels (with topcoat) as the function of exposure time.

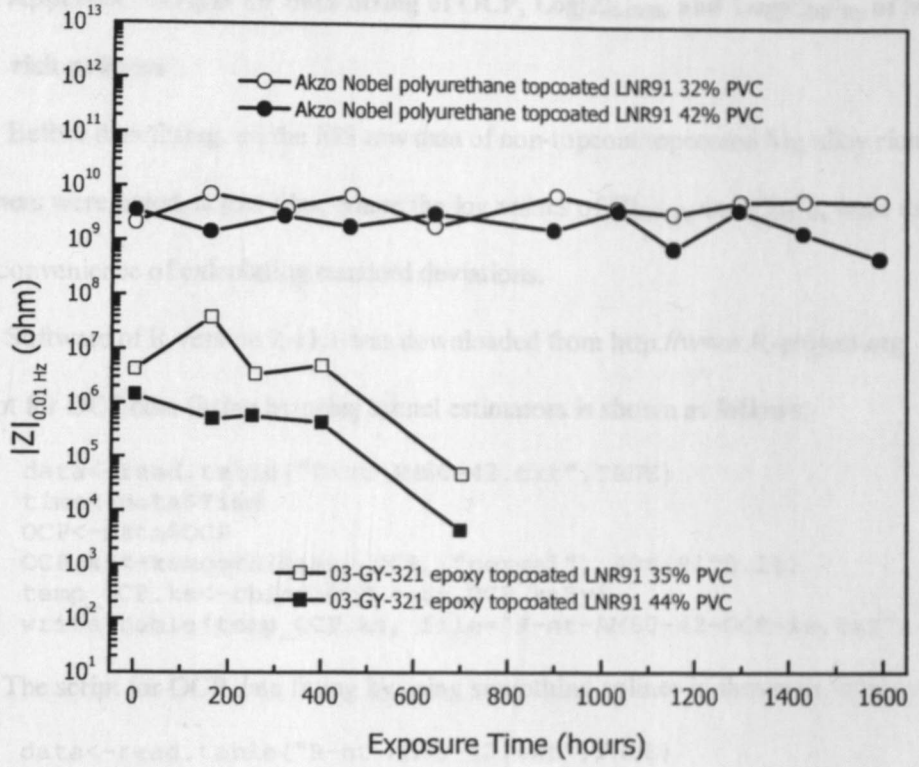

Figure 4-17. Comparison of the values of $|Z|_{0.01Hz}$ of two different topcoats coated LNR91 primers. Line with circle symbols: Akzo Nobel polyurethane topcoat; line with square symbols: Deft low gloss 03-GY-321 polyurethane topcoat.

pigments, the similar electrochemical behavior of E_{ocp}^{mix} changing with exposure time was observed irrespective the type or PVC of Mg alloy rich primers. Also, the changes of $|Z|_{0.01Hz}$ with exposure time for the non-topcoated Mg alloy primers suggest that electrolyte can penetrate the coating films due to the porous nature of Mg alloy rich primers and result in the quick consumption of Mg in Mg alloy particles. A topcoat applied over Mg alloy rich primers can successfully retard the penetration process of electrolyte and extend the protection time for Al alloy substrates. However, the effects of barrier protection were also depended on the type of topcoat, for example, Akzo Nobel topcoat showed much better performance in comparison to Deft topcoat system.

4.5. Appendix: Scripts for data fitting of OCP, Log$|Z|_{0.01Hz}$ and Log$|C|_{10^4Hz}$ of Mg alloy rich primers

Before data fitting, all the EIS raw data of non-topcoat/topcoated Mg alloy rich primers were saved as text files, where the log values of $|Z|_{0.01Hz}$ and $|C|_{10^4Hz}$ were used for the convenience of calculating standard deviations.

Software of R version 2.11.1 was downloaded from http://www.R-project.org. The script for OCP data fitting by using kernel estimators is shown as follows:

```
data<-read.table("R-nt-AM60-42.txt",TRUE)
time<-data$Time
OCP<-data$OCP
OCP.ks<-ksmooth(time, OCP, "normal", 40*(81^0.2))
temp_OCP.ks<-cbind(OCP.ks$x,OCP.ks$y)
write.table(temp_OCP.ks, file="R-nt-AM60-42-OCP-ks.txt")
```

The script for OCP data fitting by using smoothing splines is shown as follows:

```
data<-read.table("R-nt-AM60-42.txt",TRUE)
time<-data$Time
OCP<-data$OCP
OCP.sp<-smooth.spline(time, OCP, df=3)
fit_OCP.sp<-sreg(time,OCP)
fit_OCP.sp$shat.GCV*sqrt(fit_OCP.sp$diagA)
temp_OCP.sp<cbind(OCP.sp$x,OCP.sp$y,1.96*fit_OCP.sp$shat.GCV*s
qrt(fit_OCP.sp$diagA))
write.table(temp_OCP.sp, file="R-nt-AM60-42-OCP-sp.txt")
```

The script for OCP data fitting by using Local polynomials is shown as follows:

```
data<-read.table("R-nt-AM60-42.txt",TRUE)
time<-data$Time
inc.100<-seq(min(time), max(time), len=100)
OCP<-data$OCP
OCP.lo<-loess(formula=OCP~time, span=0.7, degree=1)
pred_OCP.lo<-predict(OCP.lo,data.frame(time=inc.100),se=TRUE)
temp_OCP.lo<-cbind(inc.100,pred_OCP.lo$fit,
pred_OCP.lo$se.fit*1.96)
write.table(temp_OCP.lo, file="R-nt-AM60-42-OCP-lo.txt")
```

The script for Log$|Z|_{0.01Hz}$ data fitting by using Local polynomials is shown as follows:

```
data<-read.table("R-nt-AM60-42.txt",TRUE)
time<-data$Time
```

```
Z<-data$Z
inc.100<-seq(min(time), max(time), len=100)
Z.lo<-loess(formula=Z~time, span=0.7, degree=1)
pred_Z.lo<-predict(Z.lo,data.frame(time=inc.100),se=TRUE)
temp_Z.lo<-cbind(inc.100,pred_Z.lo$fit, pred_Z.lo$se.fit*1.96)
write.table(temp_Z.lo, file="R-nt-AM60-42-Z-lo.txt")
```

The script for Log$|C|_{10^4 Hz}$ data fitting by using Local polynomials is shown as follows:

```
data<-read.table("R-nt-AM60-42.txt",TRUE)
time<-data$Time
C<-data$C
inc.100<-seq(min(time), max(time), len=100)
C.lo<-loess(formula=C~time, span=0.7, degree=1)
pred_C.lo<-predict(C.lo,data.frame(time=inc.100),se=TRUE)
temp_C.lo<-cbind(inc.100,pred_C.lo$fit, pred_C.lo$se.fit*1.96)
write.table(temp_C.lo, file="R-nt-AM60-42-C-lo.txt")
```

The author gratefully acknowledges Prof. Gang Shen in the department of Statistic, NDSU for his introducing R-project and amending the scripts of data fitting programs.

Also, the author wants to give grateful acknowledgements to Dr. Jinhai Wang for his OriginLab program used in EIS data extraction.

4.6. References

1 F. M. Khoshnaw and R. H. Gardi, *Materials and Corrosion* **2007**, 58, 345.

2 O. O. Knudsen, U. Steinsmo and M. Bjordal, *Progress in Organic Coatings*, **2005**, 54, 224.

3 T. Kamimura and M. Stratmann, *Corrosion Science*, **2001**, 43, 429.

4 F. Scholes, S. Furman, A. Hughes, T. Nikpour, N. Wright, P. Curtis, C. Macrae, S. Intem and A. Hill, *Prog. Org. Coat.*, **2006**, 56, 23.

5 J. Zhao, L. Xia, A. Sehgal, D. Lu, R. L. McCreery and G. S. Frankel, *Surf. Coat. Technol.*, **2001**, 140, 51.

6 K. D. Sugden and B. D. Martin, *Environmental Health Perspectives*, **2002**, 110, 725.

7 E. Gaggelli, F. Berti, N. D'Amelio, N. Gaggelli, G. Valensin, L. Bovalini, A. Paffetti and L. Trabalzini, *Environmental Health Perspectives*, **2002**, 110, 733.

8 *Occup. Safety and Health Standards for Construction*, in *Standards -29 CFR*, O. S. H. Admistration, Editor.

9 *Directive 2002/95/EC of the European Parliament and of the Council of 27 January 2003 on the restriction of the use of certain hazardous substances in electrical and electronic equipment*, in *32002L0095*, E. P. a. t. C. o. t. E. Union, Editor. **2003**, Official Journal of the European Union, Brussels.

10 R. Twite and G. Bierwagen, *Prog. Org. Coat.*, **1998**, 33, 91.

11 D. Battocchi, G. Bierwagen, M. Zentner and R. Brown, *Mg-rich primer for totally chromate-free protective systems on Al alloys*, in *Nurnberg Coatings Congress*. **2007**, Nurnberg, Germany.

12 D. Battocchi, A. Simoes, D. Tallman and G. Bierwagen, *Corrosion Science*, **2006**, 48, 1292.

13 D. Battocchi, A. M. Simoes, D. E. Tallman and G. P. Bierwagen, *Corrosion Science*, **2006**, 48, 2226.

14 G. P. Bierwagen, M. E. Nanna and D. Battocchi, *Magnesium rich coatings and coating systems*. **2005**, (NDSU Research Foundation, USA). Application: WO, 65

15 M. Nanna and G. Bierwagen, *J. Coat. Technol. Res.*, **2004**, 1, 69.

16 G. Bierwagen, D. Battocchi, A. Simoes, A. Stamness and D. Tallman, *Prog. Org. Coat.*, **2007**, 59, 172.

17 A. Simoes, D. Battocchi, D. Tallman and G. Bierwagen, *Assessment of the corrosion protection of aluminium substrates by a Mg-rich primer: EIS, SVET and SECM study*, **2008**.

18 A. Simoes, D. Battocchi, D. Tallman and G. Bierwagen, *Corrosion Science*, **2007**, 49, 3838.

19 B. A. Shaw, *ASM Hand book*, **2003**, 13A, 692.

20 G. Song, A. L. Bowles and D. H. StJohn, *Materials Science and Engineering A*, **2004**, 366, 74.

21 J. G. Kim and S. J. Koo, *Corrosion*, **2000**, 56.

22 E. Ghali, *Mater. Sci. Forum*, **2000**, 350-351, 261.

23 G. L. Makar and J. Kruger, *Int. Mater. Rev.*, **1993**, 38, 138.

24 H. Alves, U. Koster, E. Aghion and D. Eliezer, *Mater. Technol. (Poulton-le-Fylde, U. K.)*, **2001**, 16, 110.

25 P. Sorensen, S. Kiil, K. Dam-Johansen and C. Weinell, *J. Coat. Technol. Res.*, **2009**, 6, 135.

26 C. I. Elsner, E. Cavalcanti, O. Ferraz and A. R. Di Sarli, *Prog. Org. Coat.*, **2003**, 48, 50.

27 P. E. Hintze and L. M. Calle, *Electrochim. Acta*, **2006**, 51, 1761.

28 X. W. Liu, J. P. Xiong, Y. W. Lv and Y. Zuo, *Prog. Org. Coat.*, **2009**, 64, 497.

29 H. Marchebois, C. Savall, J. Bernard and S. Touzain, *Electrochim. Acta*, **2004**, 49, 2945.

30 S. Sack, R. Ramagnoli, V. Vetere, C. Elsner, O. Pardini, J. Amalvy and A. Di Sarli, *JCT Coatings Tech*, **2002**, 74, 63.

31 K. N. Allahar, D. Battocchi, M. E. Orazem, G. P. Bierwagen and D. E. Tallman, *J. Electrochem. Soc.*, **2008**, 155, E143.

32 G. Bierwagen, R. Brown, D. Battocchi and S. Hayes, *Prog. Org. Coat.*, **2010**, 67, 195.

33 B. Hinderliter, S. Croll, D. Tallman, Q. Su and G. Bierwagen, *Electrochim. Acta*, **2006**, 51, 4505.

34 J. Havlik, A. Kalendova and D. Vesely, *Journal of Physics and Chemistry of Solids*, **2007**.

35 H. Marchebois, S. Touzain, S. Joiret, J. Bernard and C. Savall, *Prog. Org. Coat.*, **2002**, 45, 415.

36 M. Mahdavian and M. M. Attar, *Corros. Sci.*, **2006**, 48, 4152.

37 J. Kittel, N. Celati, M. Keddam and H. Takenouti, *Prog. Org. Coat.*, **2001**, 41, 93.

38 R. De Rosa, D. Earl and G. Bierwagen, *Corrosion Science*, **2002**, 44, 1607.

39 R. A. Armas, C. A. Gervasi, A. Di Sarli, S. G. Real and J. R. Vilche, *Corrosion*, **1992**, 48, 379.

40 I. Martinez and C. Andrade, *Corros. Sci.*, **2008**, 50, 2948.

41 V. Barranco, S. Feliu Jr and S. Feliu, *Corrosion Science*, **2004**, 46, 2203.

42 S. Feliu Jr, M. Morcillo and S. Feliu, *Corrosion*, **2001**, 57, 591.

43 J. J. Faraway, *Extending the linear model with R: generalized linear, mixed effects and nonparametric regression models*, 2nd ed, Tests in statistical science series, **2006**, Boca Raton, FL, Chapman& Hall/CRC

44 E. Kissa, *Dispersions characterization, testing, and measurement*, Surfactant science series, **1999**, New York, Mareel Dekker, Inc.

45 *ASTM D281 -95(2007) Standard Test Method for Oil Absorption of Pigments by Spatula Rub-out*, **2007**, ASTM International.

46 G.P.Bierwagen, R.S.Fishman, T. Storsved and J. Johnson, *Prog. Organic Coatings*, **1999**, 35, 1.

47 H. A. Gardner, *Paint Testing Manual Physical and Chemical Examination of Paints, Varnishes, Lacquers, and Colors*, Thirteenth ed, ed. G. G. Sward, **1972**, Philadelphia, ASTM Special Technical Publication.

48 R. D. C. Team, *R: A language and environment for statistical computing*, R. F. f. S. Computing, Editor. **2010**, Vienna, Austria.

49 T. Therneau and T. Lumley, *survival: Survival analysis, including penalised likelihood.* **2009**.

50 M. Wand and B. Ripley, *KernSmooth: Functions for kernel smoothing for Wand & Jones (1995)*. **2009**.

51 D. Sarkar, *lattice: Lattice Graphics*. **2010**.

52 W. N. Venables and B. D. Ripley, *Modern Applied Statistics with S*, Fourth Edition ed, **2002**, New York, Springer.

53 D. Bates and M. Maechler, *Matrix: Sparse and Dense*, in *Matrix Classes and Methods*. **2010**.

54 S. N. Wood, *Journal of the American Statistical Association*, **2004**, 99, 673.

55 S. N. Wood, *Journal of the Royal Statistical Society*, **2008**, 70, 495.

56 S. N. Wood, *Generalized Additive Models: An Introduction with R*, **2006**, Chapman and Hall/CRC.

57 S. N. Wood, *Journal of the Royal Statistical Society (B)*, **2003**, 65, 95.

58 S. N. Wood, *Journal of the Royal Statistical Society (B)*, **2000**, 62, 413.

59 R. Furrer, D. Nychaka and S. Sain, *fields: Tools for spatial data*. **2010**.

60 J. Pinheiro, D. Bates, S. DebRoy, D. Sarkar and R. C. team, *nlme: Linear and Nonlinear Mixed Effects Models*. **2009**.

61 C. M. Abreu, M. Izquierdo, P. Merino, X. R. Novoa and C. Perez, *Corrosion* **1999**, 55, 1173.

62 H. Marchebois, S. Joiret, C. Savall, J. Bernard and S. Touzain, *Surf. Coat. Technol.*, **2002**, 157, 151.

63 D. Loveday, P. Peterson and B. Rodgers, *JCT Coatings Tech*, **2004**, October, 88.

64 S. Gonzalez, F. Caceres and R. Souto, *Prog. Org. Coat.*, **2003**, 46, 317.

CHAPTER 5. STUDIES OF APPLYING ENM IN A MG ALLOY RICH PRIMER SYSTEM USING LNR91 AS PIGMENT AND THE CORRELATION BETWEEN ENM AND EIS RESULTS

5.1. Introduction

Testing techniques are very important to the development of the corrosion protective coating system. They can not only quantitatively monitor the performance of a coating system but also effectively provide the information of protection mechanisms, coating degradations, and the probable interactions between environments and coating systems. With the help of a variety of testing techniques, the understanding of the current coating system can be expanded and lead to the ongoing improvements of a coating system. [1]

In the past several decades, many electrochemical techniques have been developed and applied in coating systems to aid the studies of corrosion processes and protective characteristics, such as electrochemical impedance spectroscopy (EIS) and linear polarization. [2-4] Electrochemical noise methods (ENM) have been used in corrosion research since 1968, when Iverson found that the magnitude of electrochemical noise heard by a loudspeaker as strong or weak sound was related to the corrosion rate. [5] Actually, in an electrochemical system, the occurrence of corrosion is always accompanied with the spontaneous fluctuations of potential and current, which can be collected and analyzed by ENM.

ENM has many advantages and is an attractive electrochemical technique in corrosion studies. [6-8] First, ENM is a non-intrusive technique because there is no signal imposed on the system under examination. The fluctuations of potential and current due to the

corrosion processes freely occurred on working electrodes (WEs) can be monitored by ENM instantly. Second, ENM has the unique ability to identify various corrosion modes, e.g. uniform corrosion, pitting and crevice corrosion through ENM data analysis. It is absent for many other electrochemical techniques. Third, ENM is a fast and straightforward test method and it has the advantages of low equipment cost, ease of data collection and operation.

In fact, the significant achievements of ENM instrumentation, experimental methods and data analysis in 1990's resulted in the wide application of ENM in corrosion studies. For example, the high accuracy/low-noise amplifiers, the potentiostat and galvanostat devices became commercially available. As a result, ENM is able to collect the small signals in the frequency range about 1 Hz, which are usually related to the corrosion processes. [9] In addition, a new experimental design based on a three-electrode system was developed at the University of Manchester Institute of Science and Technology (UMIST). [10] Two identical working electrodes (WE) were coupled via a zero resistance ammeter (ZRA), and the current noise between the two WEs was monitored by the ZRA. Simultaneously, the potential noise of the coupled WEs was measured with respect to a reference electrode (RE). Such cell configuration can keep the average of the current noise between two WEs approximate to zero so that to avoid the polarization of WEs caused by the variation of open circuit potential (OCP). [9]

On the other hand, the methods used for ENM data analysis have been improved, too. The statistical methods of mean, standard deviation (SD), correlation function with time-domain, power spectral density (PSD) and amplitude spectral density (ASD) with frequency-domain have been developed for characterizing ENM data. [9] Furthermore, the

developed computer technology has significantly improved the techniques of ENM data acquisition and data analysis.

In 1990's, ENM started to be applied in the studies of organic coating system. [11-15] For example, Bierwagen et al. applied ENM to monitor the performance of a variety of organic coatings as a function of exposure time in Prohesion chamber or cyclic thermal immersion.[16-18] The results showed that ENM could provide the fast and easy measurement to the coating studies. Now, ENM has become a popular technique for evaluating the coating performance, monitoring the film degradations and studying the protection mechanisms.

Since ENM is non-destructive, fast and easy of installation, it has a unique application in sensing techniques for in-field monitoring coating systems. [19] For instance, the group of Bierwagen has designed an embedded sensor system. It is made of platinum and placed between the primer and the topcoat.[20-23] ENM has been used via this sensor system to study the performance of various protective coatings exposed in different environments, such as salt fog, Prohesion, and a constant humidity conditions. [23, 24] Results showed that ENM was appropriate to be combined with the embedded sensor system since the noise resistance (R_n) acquired from ENM data was a suitable indicator for monitoring the degradations of organic coating systems.

However, as opposed to its ease of ENM operation and ENM data collection, the mathematical treatments required for ENM data analysis are very complex. Many studies have been carried out on the interpretation of ENM data to understand the internal relationship between the ENM data and the corrosion processes. These have recently been reviewed by Cottis. [8]

Various mathematic methods can be used to interpret ENM data to extract the useful information. [9] Generally, ENM data in time domain and in frequency domain are the most common ones. The shape, amplitude and time constant of the time transients can reveal the information related to the kinetics of the corrosion processes. [6, 9, 25] In Figure 5-1 shown are the typical shapes of the time transients for pitting corrosion and uniform corrosion.

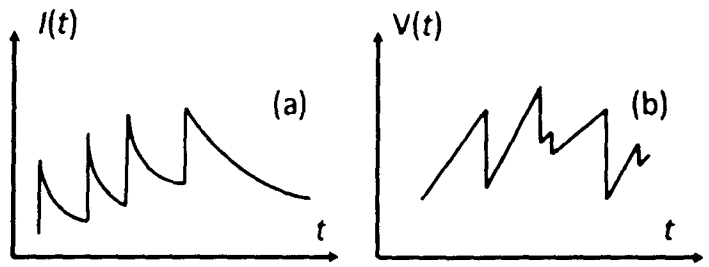

Figure 5-1. Typical time transients of (a) pitting corrosion and (b) uniform corrosion with hydrogen bubble evolution. (Reproduced from F. Huet. *Electrochemical Noise Technique*, **2006**)

Noise resistance (R_n) is a most widely used parameter of ENM. It can be derived from the ENM data in time domains by using the Ohm's law via equation (5.1):

$$R_n = \frac{\sigma_E}{\sigma_I} \tag{5.1}$$

where, σ_E and σ_I are the standard derivation of potential noise and current noise, respectively.

R_n can be used as a good screening parameter for evaluating the corrosion protection performance of coating systems. Some research work showed that R_n had the good correlation with the DC resistance in the system of organic paint coated metal substrates. [19] In coating industry, DC resistance has been regarded as an indicator of corrosion protection ability of coating system. A coating system with DC resistance higher than 10^8

Ωcm^2 usually exhibits the excellent corrosion protection, but the one with DC resistance lower than 10^6 Ωcm^2 has a poor performance. [19] Therefore, R_n can be probably used as an indicator, too. In addition, some authors have suggested that R_n is proportional to the polarization resistance R_p when the corrosion rate of the system is low.[26, 27] Thus, R_n can be used to estimate the corrosion rate via Stern-Geary equation instead of R_p. [9] However, the work of Gouveia-Caridade et al. showed that the presence of the localized corrosion could cause R_n to deviate from R_p. [28]

ENM data can also be analyzed in the frequency domain by calculating power spectral density (PSD) of potential and current noise. In corrosion studies, maximum entropy method (MEM) and fast Fourier transform (FFT) are the most common ways used to estimate a power spectrum. [8, 29] In comparison to FFT, MEM is faster and can give smoother spectra with the extended low frequency range. However, it is also noticed that "the arbitrary choice" of the number of the coefficients (M) in the MEM computation can significantly affect the spectrum accuracy. In addition, the validity of the spectrum at the extended low frequency range is still in question. Thus, any method used for ENM data analysis should be carefully selected.

From the PSD plots of potential noise, $PSD_E(f)$, and current noise, $PSD_I(f)$, two parameters, A_E/A_I and S_E/S_I, can be obtained by fitting the linear parts of $PSD_E(f)$ and $PSD_I(f)$: [30]

$$\log(PSD_E(f)) = A_E + S_E \log(f) \text{ and } \log(PSD_I(f)) = A_I + S_I \log(f) \qquad (5.2)$$

The S_E and S_I are the slope values of the fitting linear parts for $PSD_E(f)$ and $PSD_I(f)$, respectively, and their intercepts are A_E and A_I. Some studies show that the slopes can be related to typical corrosion mechanisms of corrosion processes, and the intercepts are

related to the protective properties of coating systems. [30, 31]

In addition, the PSD of noise resistance, $R_{sn}(f)$, can be obtained via equation (5.3),

$$R_{sn}(f) = \sqrt{\frac{PSD_E(f)}{PSD_I(f)}} \tag{5.3}$$

Based on $R_{sn}(f)$, some useful parameters can be obtained, such as R_{sn}^0 or $R_{sn(0.1Hz)}$. In fact, R_{sn}^0 is the dc limit of $R_{sn}(f)$

$$R_{sn}^0 = \lim_{f \to 0}[R_{sn}(f)] \tag{5.4}.$$

And the noise impedance $R_{sn(0.1Hz)}$ can be obtained via equation (5.3) at 0.1 Hz. In the work of Sanchez-Amaya et al., [12] a close correlation between R_n, $R_{sn(0.1Hz)}$ and $|Z|_{0.1Hz}$ from EIS measurement was observed.

In our work of developing Mg alloy rich primer systems to protect AA2024 T3, the technique of ENM was used to monitor the performance of Mg alloy rich primer system in addition to EIS. The systems under study were the metal-rich primers by using Mg alloy particles, such as AM60, AZ91B and LNR91, as pigments in an epoxy-polyamide polymer binder. There was no topcoat applied over the primers. As we known, Mg alloys are very active, and they become particularly reactive when in the form of particles, since the surface area is increased dramatically. Although the polymer binder covered partial surface area of Mg alloy particles in primer film, the reactions between the penetrating electrolyte and the exposed particles were significant when there was no barrier protection provided by topcoat.

Therefore, for an active Mg alloy rich primer systems, the application of ENM had a lot of challenges. The following questions needed to be considered. Is the assumption of a stationary system still valid? If not, what can be determined in an unstable system? Is the

interpretation of ENM data available for steady-state system still suitable to explain the behavior of the active Mg alloy rich primer systems? When the two coupled samples used for ENM measurement are not identical, how the ENM results will be affected? Is the extracted information from ENM data analysis still reliable and reproducible?

In this chapter, the work of applying ENM to the characterization of Mg alloy rich primer systems is reported. Due to the extensively large amounts of ENM data, only that resulted in a typical measurement, such as the systems of Al alloy 2024 T3 substrates coated with 35%, 39% and 50% PVC LNR91 primers without topcoat, were chosen. Also, the work reported and discussed in this chapter mostly focuses on the application of ENM in the active Mg alloy rich primer systems rather than the evaluation of the performances of the different primer systems. Moreover, less H_2 was generated on the surface of the primers using LNR91 as pigment, and there were more ENM data obtained from the LNR91 primers available.

EIS and ENM were both used to monitor the performance of these three Mg alloy rich primer systems as the samples were exposed in Prohesion chamber. The ENM data in time domain is demonstrated and the possible corrosion kinetic information is interpreted. Meanwhile, the general protection performances of these primers are discussed based on the PSD spectra transformed via MEM and FFT. Furthermore, the comparison between the FFT and MEM spectral analysis for the Mg alloy rich primer systems is made. Importantly, the correlation study between the ENM and EIS results obtained from Mg alloy rich primer systems is carried out. As an important technique, EIS not only evaluated the new Mg alloy rich primer system from various aspects (in chapter four), but also provided useful reference data for ENM study. The parameters, R_n, $R_{sn(0.1Hz)}{}^f$ (via FFT), and $R_{sn(0.1Hz)}{}^m$ (via

MEM) from ENM data are compared with $|Z|_{0.1Hz}$ of EIS as a function of exposure time to better understand the performances of the LNR91 primer systems. In addition, some probable answers to the previous questions are discussed via the comparison of ENM and EIS data.

5.2. Experimental

5.2.1. Sample preparation

The chemical composition of Mg alloy LNR91 particles is 50 wt% Mg and 50 wt% Al. The volume average particle size of LNR91 is about 47 μm. LNR91 primers were formulated by using Mg alloy particles, LNR91, as pigment in an epoxy-polyamide polymer binder at PVC's of 35%, 39% and 50%. The primer paints were applied by air spray on the cleaned AA2024 T3 substrates. After two days of curing at room temperature, the thicknesses of LNR91 primer films were around 150 μm. More details of the sample preparation have been described in chapter four.

One LNR91 primer coated panel with dimension of 3 inch × 6 inch was cut into two 3 inch × 3 inch panels as two fairly identical samples for ENM measurement. All the samples were exposed in Prohesion chamber, and taken out for ENM and EIS tests after a period of time.

5.2.2. Experimental arrangement of ENM tests

The test system of three-electrode cell, illustrated in Figure 5-2, was used for ENM measurement. Two identical samples were used as WEs, and each of them was clamped by a glass cell with a 7.06 cm^2 exposure area. These two glass cells were filled with dilute Harrison's solution (DHS) as electrolyte and connected with each other by a 3% NaCl agar salt bridge. A saturated calomel electrode (SCE) was placed in one glass cell as RE.

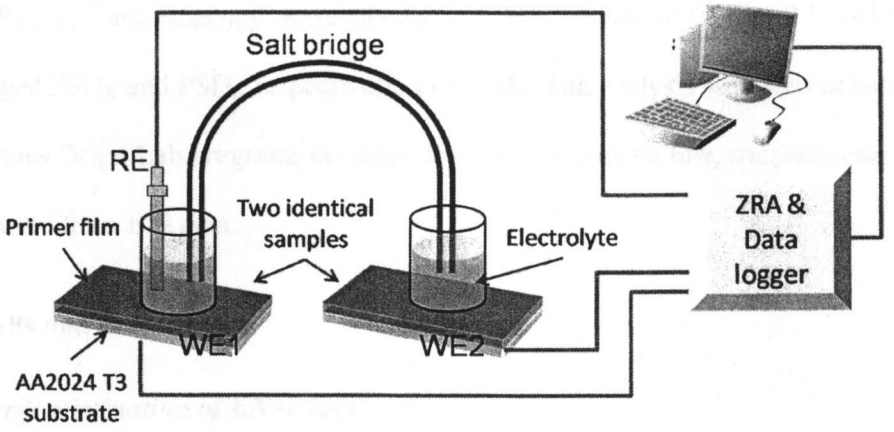

Figure 5-2. Electrochemical cell configuration of three-electrode ENM.

ENM raw data was collected by using Gamry PCL4-300 in ZRA mode. For the test at every exposure time, there were five consecutive ENM data sets collected. Each ENM data set had 256 points with a sampling frequency of 10 Hz. Right after ENM test, these two samples were measured by EIS separately. A potentiostat 32012 controlled Gamry PCL4-300 was used to collect EIS data.

5.2.3. Data analysis of EIS and ENM results

Every plot of ENM data in time domain consisted of five time records, each of them was displayed after the linear drift removal. [21, 22]

The plots of PSD_E and PSD_I were transformed from the detrended ENM data in time domain via FFT or MEM. For each test, there were five PSD_E or PSD_I spectra obtained corresponding to the five time records. By averaging the five consecutive time records of PSD_E or PSD_I, a single averaged PSD_E or PSD_I was obtained and discussed in this chapter. The values of A_E/S_E or A_I/S_I were obtained by using OriginLab for linear fitting the slope of each PSD_V or PSD_I.

The parameter of R_n was estimated via equation (5.1) from the raw ENM data in time

domain. $R_{sn(0.1Hz)}^{f}$ and $R_{sn(0.1Hz)}^{m}$ were calculated through equation (5.3) at 0.1 Hz based on the averaged PSD_V and PSD_I, respectively. The ENM data analysis was accomplished by using various OriginLab programs developed in our lab. Meanwhile, the parameter $|Z|_{0.1Hz}$ was extracted from EIS data.

5.3. Results and discussions

5.3.1. Drift elimination of ENM data

In Figure 5-3 (a), the potential noise (black line) and current noise (gray line) as a function of exposure time are plotted together for the sample coated with 39% PVC LNR91primer over a 356-hour exposure time. It can be seen that the signals were not stationary: a "drift" of potential noise or current noise was present in the raw ENM data. In fact, the drifting signals were observed on most ENM raw data in our ENM study.

For ENM measurement, one of the important assumptions is that the system under study should be stationary during the measurement time so that the statistical analysis methods, such as standard deviation (SD) or power spectral density (PSD) can be applied. [9, 32] Therefore, the presence of the signal drifting will distort the true information of the systems under study.

On the other hand, it is found that the drifting signals can be caused by various reasons rather than the unstable system. For example, the signals with low frequency (<1/T) may cause the drifting, or some slow alterations occur in the system under study. Especially in corrosion studies, the systems tend to be non-stationary since the working electrodes usually undergo "progressive deterioration". [21, 22, 32]

So far the nature of the drifting is not clear yet and much work needs to be done to identify the reasons. [32] However, there is a consensus in the relevant literature that it is

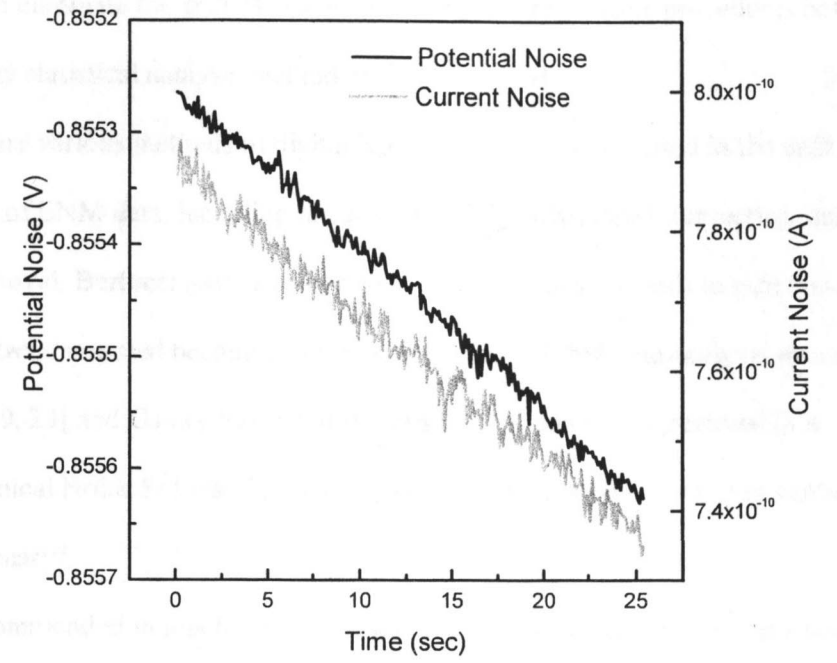

(a)

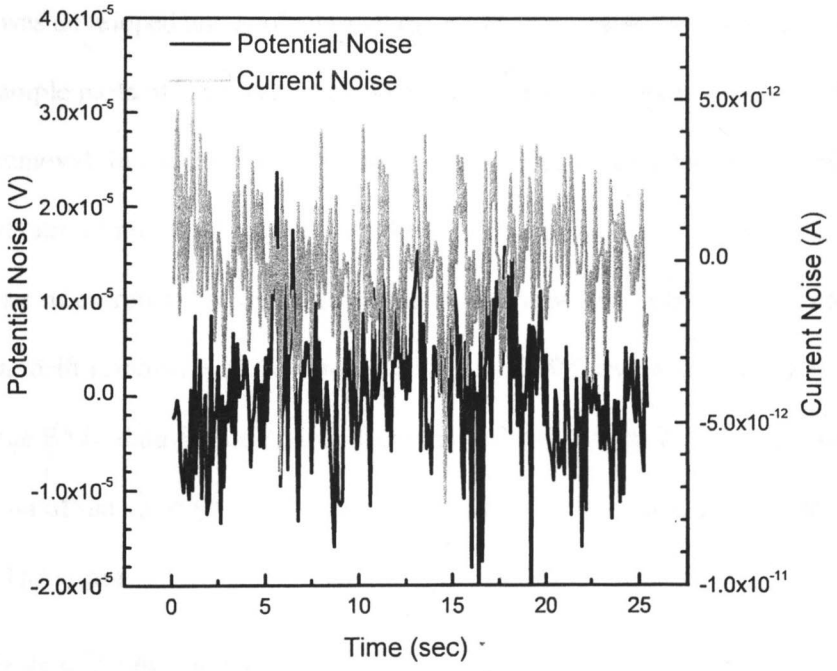

(b)

Figure 5-3. ENM data in time domain for the sample coated with 39% PVC LNR91 primer at 356-hour exposure before (a) and after (b) linear trend removal.

necessary to eliminate the drift of signals through some reasonable procedures before applying any statistical analysis method to ENM data. [9]

There are various methods of digital high-pass (HP) filtering used in the drift elimination of ENM data, including linear subtracting, polynomial subtracting, and moving average removal. Bertocci gave a good review of the various methods in reference [32]. In fact, linear trend removal becomes a common method in ENM data analysis in corrosion studies, [8, 9, 23] and Gamry has added the function of linear trend removal in its "EN120 Electrochemical Noise Software". This appears to be because few corrosion studies are truly "stationary".

As recommended in much ENM literature [7, 32] and the previous experiences of in our lab, [21, 22] a program of linear drift removal based on the method of linear subtracting was developed and applied to all the ENM raw data in our study. Figure 5-3 (b) shows the sample plots of the potential noise and current noise in time domains after the linear drift removal. In comparison to Figure 5-3 (a), it can be seen that the values of potential and current noise in Figure 5-3 (b) become much smaller, and the average of potential noise or current noise in the time transients is near zero. These results indicate that the linear drift removal is suitable to eliminate the ENM data drift in our study. In this chapter, all the ENM data demonstrated, except Figure 5-3 (a) and R_n, were derived after the elimination of the constant drifts of potential/current noise by using the same linear drift removal program.

5.3.2. ENM data in time domain

The ENM data in time domain for the samples coated with 35% PVC LNR91primer at 157, 356, 663, 856 and 1012 hour exposure are plotted in Figure 5-4 (a), (b), (c), (d) and (e),

respectively.

For each figure, there are five time records separated by black vertical dash lines. In each record, 255 points was recorded during 25.4 second acquisition time. The interval between each time record was about 34.6 seconds. But, in Figure 5-4, the five time records are displayed together in a sequence of continuous time. For a truly stable system, similar patterns of the potential or current transients should be observed in the five time records. The shape, amplitude and time constant of the time transients can provide useful information about the electrochemical processes of the system under study. [6] [9]

In Figure 5-4 (a), fast, small current transients and large, slow potential transients are observed. In addition, the similar patterns in five time records indicate that the system was relatively stationary during the measurement time.

In Figure 5-4(b), the values of the current noise were similar to the ones of Figure 5-4 (a), but the amplitude of potential noise decreased by three orders of magnitude, from

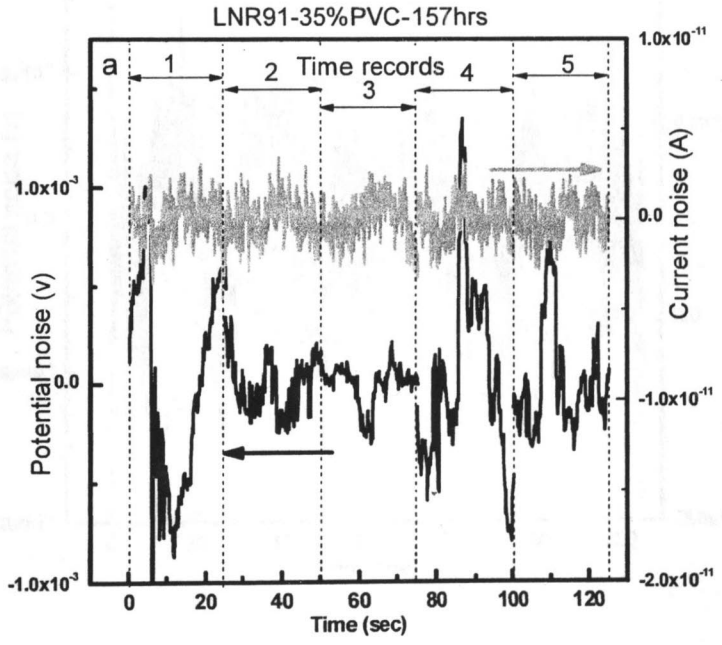

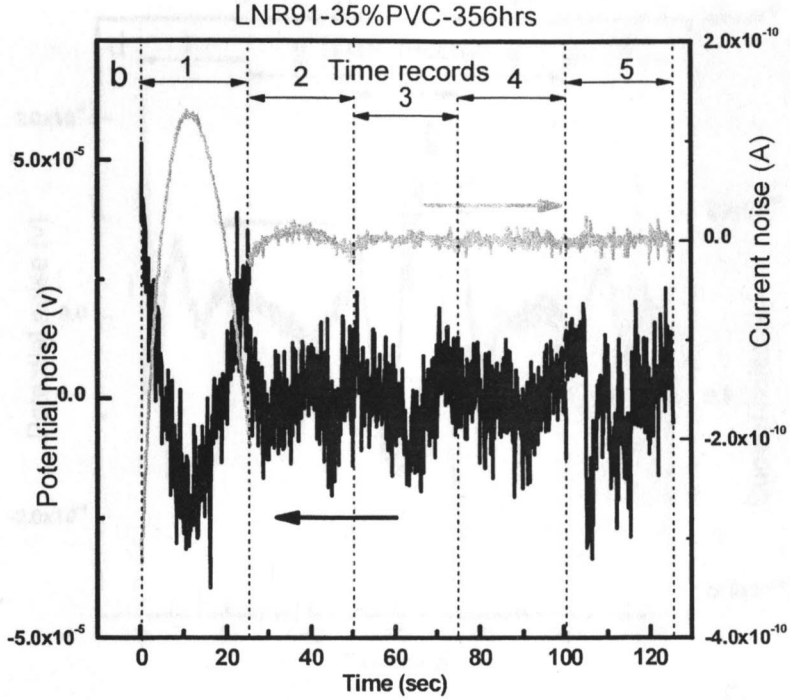
LNR91-35%PVC-356hrs
b
1
2
3
4
5
Time records
Potential noise (v)
Current noise (A)
5.0x10-5
0.0
-5.0x10-5
2.0x10-10
0.0
-2.0x10-10
-4.0x10-10
0
20
40
60
80
100
120
Time (sec)

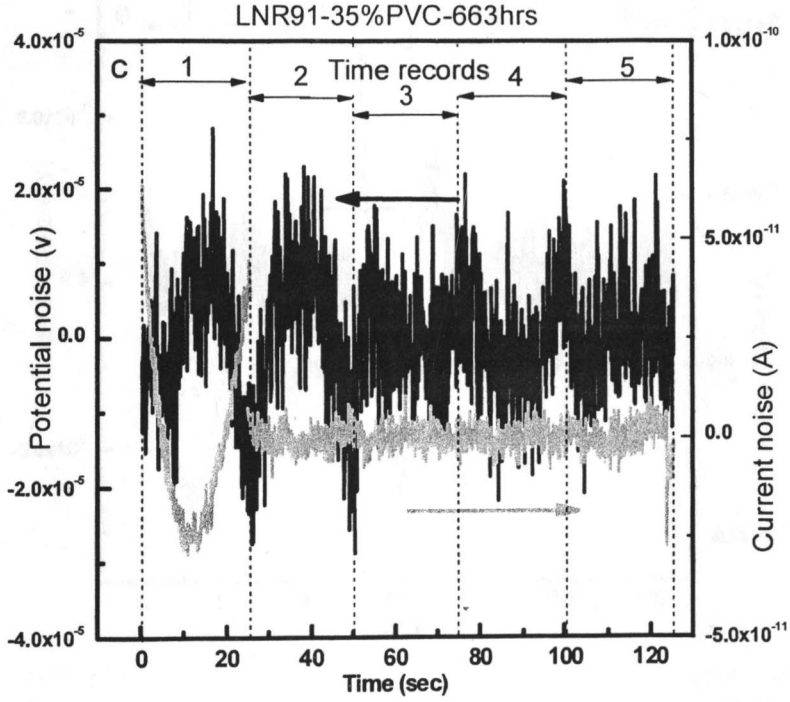
LNR91-35%PVC-663hrs
c
1
2
3
4
5
Time records
Potential noise (v)
Current noise (A)
4.0x10-5
2.0x10-5
0.0
-2.0x10-5
-4.0x10-5
1.0x10-10
5.0x10-11
0.0
-5.0x10-11
0
20
40
60
80
100
120
Time (sec)

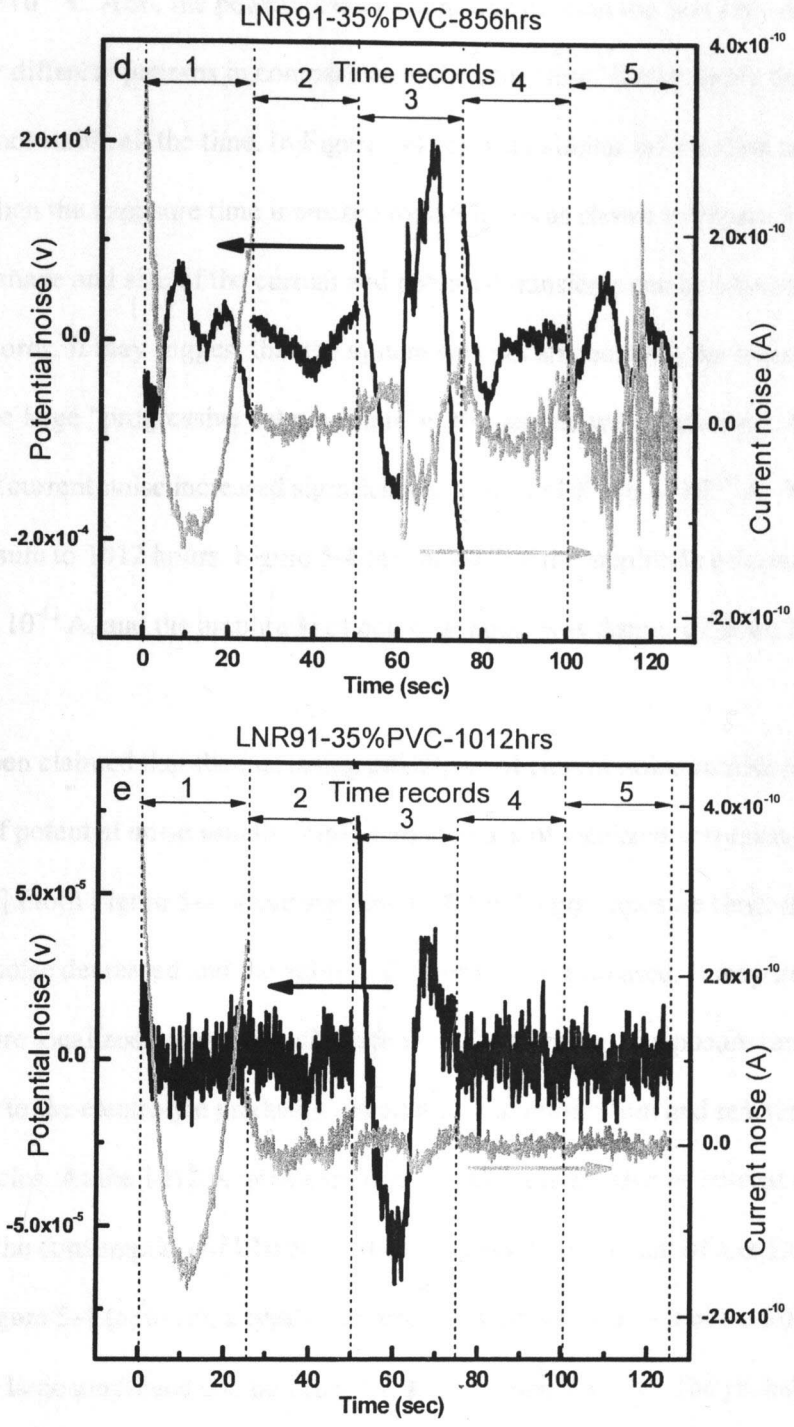

Figure 5-4. ENM data in time domain for the samples coated with 39% PVC LNR91 primer at (a) 157, (b) 356, (c) 663, (d) 856 and (e) 1012 hours exposure. Black lines: potential noise; gray lines: current noise.

2×10^{-3} to 1×10^{-6} V. Also, the potential and current transients in the first time record showed very different patterns in comparison to the other four. It may imply that the system was not stable all the time. In Figure 5-4 (c), very similar information can be obtained. When the exposure time increased to 856 hours as shown in Figure 5-4 (d), large variation of shape and size of the current and potential transients can be observed in the five time records. It may suggest that the system was not stationary at the measurement time, or some large "progressive deterioration" of the sample were occurring. Also, the amplitude of current noise increased significantly, from 1×10^{-11} to 4×10^{-10} A. With the further exposure to 1012 hours, Figure 5-4 (e) shows that the amplitude of current noise decreased to 10^{-12} A, and the amplitude of potential noise was decreased from 2×10^{-4} to 5×10^{-6} V.

It has been claimed that the increasing amplitude of current noise combined by a decreasing of potential noise usually implies an increase of localized corrosion in the system. [6, 9] From Figure 5-4, it can see that, with the longer exposure time, the amplitude of potential noise decreased and the values of current noise increased. It may indicate that more and more localized corrosion took place with the increase of exposure time. This could be due to the electrolyte gradually penetrating the primer film and reacting with more LNR91 particles. At the 1012 hour of exposure, the decreased value of current noise may suggest that the consumption of LNR91 particles reduced the amount of localized corrosion.

From Figure 5-4 (a) to (e), a typical pattern of an increase current noise followed by a decrease in a large amplitude can be observed in many time records. The probable reason could be the H_2 evolution. The growth and detachment of H_2 bubbles in the surface of primer film resulted in the fluctuations of the active surface area, or the electrolyte

concentration of the microenvironments. [9]

The ENM data in time domain for the samples coated with 39% PVC LNR91primer at 157, 356, 663, 856 and 1012 hour exposure is shown as Figure 5-5 (a), (b), (c), (d) and (e), respectively.

In Figure 5-6 (a), (b), (c), (d) and (e), the ENM data in time domain for the samples coated with 50% PVC LNR91primer at 50,157, 245, 356, and 467 hour exposure are shown, respectively. Different patterns of the transients on the fluctuations of potential and current noise can be observed in comparison to the samples of 35% PVC and 39% PVC. They became slower in frequency and larger in the amplitude: a sharp increase followed by a decrease in the fluctuations of current noise can be observed except Figure 5-6 (b) at 157 hours. Also, the amplitudes of the fluctuations of potential and current for the 50% PVC sample became large. Moreover, the interval of the peaks was about 10 seconds at 50-hour exposure and increased to 25 seconds at 467-hour exposure.

For the 39% PVC samples, fast, small transients of potential and current noise are observed in Figure 5-5 (a), (b), (c), and (d). The amplitude of potential and current noise at these four exposure time, 157, 356, 663 and 1012 hour, are very similar, about 5×10^{-6} V and 10^{-11} A, respectively. Only at 856-hour exposure, the potential and current noise increased to 4×10^{-4} V and 2×10^{-10} A, respectively. Meanwhile, it can see that the patterns of the time transients at 856-hour exposure were not similar in the five time records. It may indicate that the system of 39% PVC sample had no significant changes during the whole exposure period, except the increasing amount of localized corrosion at 856-hour exposure.

For the 50% PVC sample, the amplitudes of potential noise kept decreasing from 2×10^{-3} V to 5×10^{-5} V, and the amplitudes of current noise were stable between 4×10^{-9} A

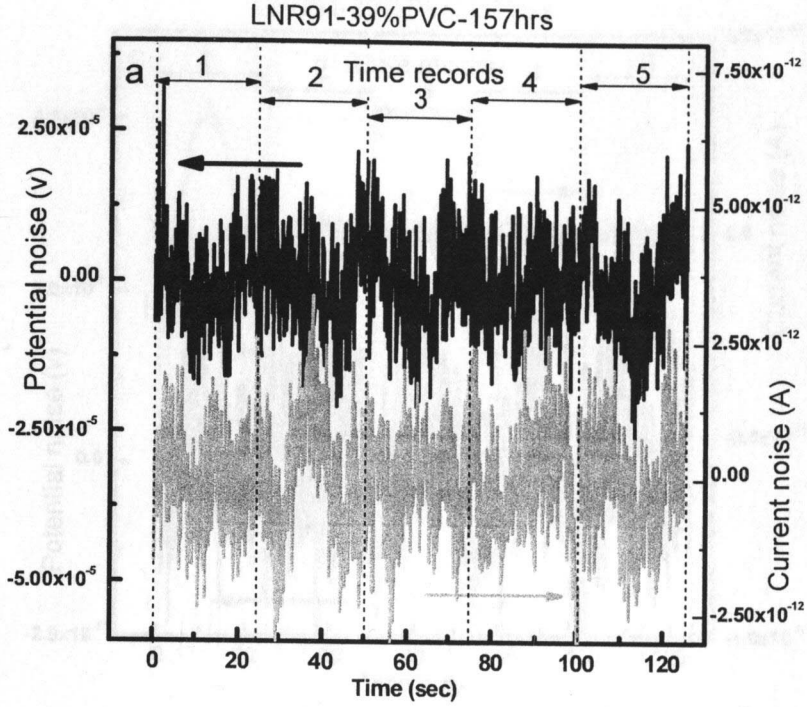
LNR91-39%PVC-157hrs
a
1
2
Time records
3
4
5
2.50x10-5
0.00
-2.50x10-5
-5.00x10-5
Potential noise (v)
7.50x10-12
5.00x10-12
2.50x10-12
0.00
-2.50x10-12
Current noise (A)
0
20
40
60
80
100
120
Time (sec)

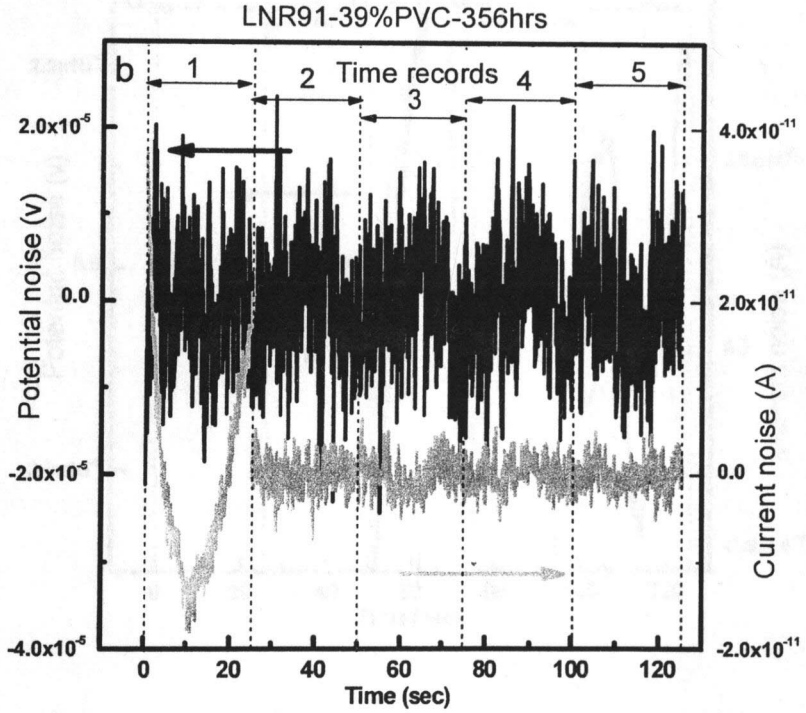
LNR91-39%PVC-356hrs
b
1
2
Time records
3
4
5
2.0x10-5
0.0
-2.0x10-5
-4.0x10-5
Potential noise (v)
4.0x10-11
2.0x10-11
0.0
-2.0x10-11
Current noise (A)
0
20
40
60
80
100
120
Time (sec)

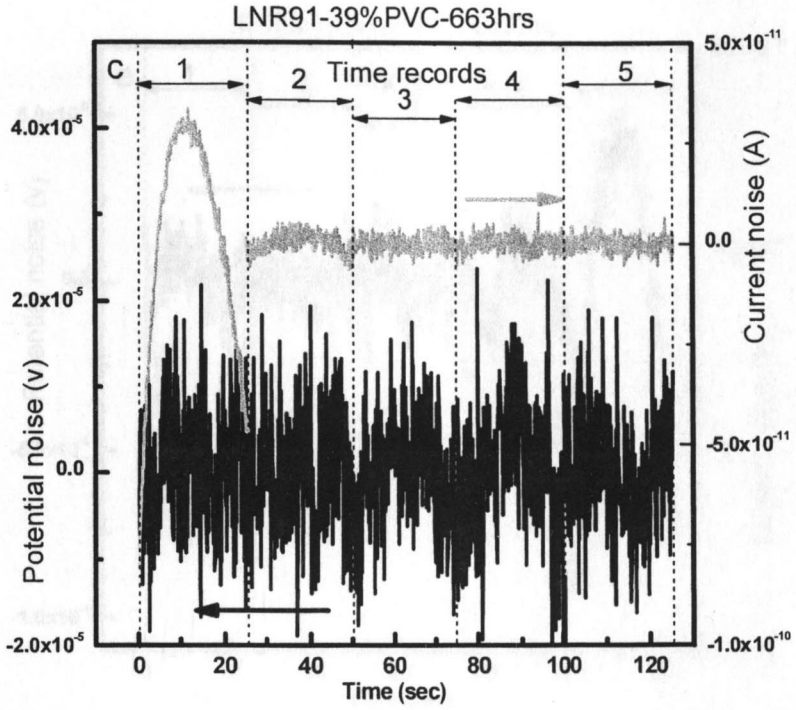
LNR91-39%PVC-663hrs
c
1
2
Time records
3
4
5
4.0x10-5
2.0x10-5
0.0
-2.0x10-5
Potential noise (v)
5.0x10-11
0.0
-5.0x10-11
-1.0x10-10
Current noise (A)
0
20
40
60
80
100
120
Time (sec)

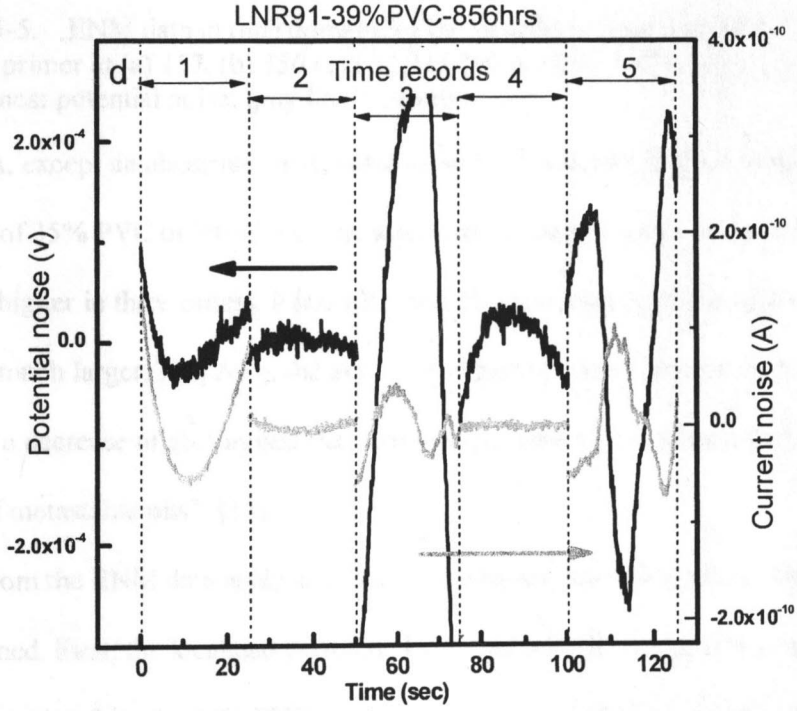
LNR91-39%PVC-856hrs
d
1
2
Time records
3
4
5
2.0x10-4
0.0
-2.0x10-4
Potential noise (v)
4.0x10-10
2.0x10-10
0.0
-2.0x10-10
Current noise (A)
0
20
40
60
80
100
120
Time (sec)

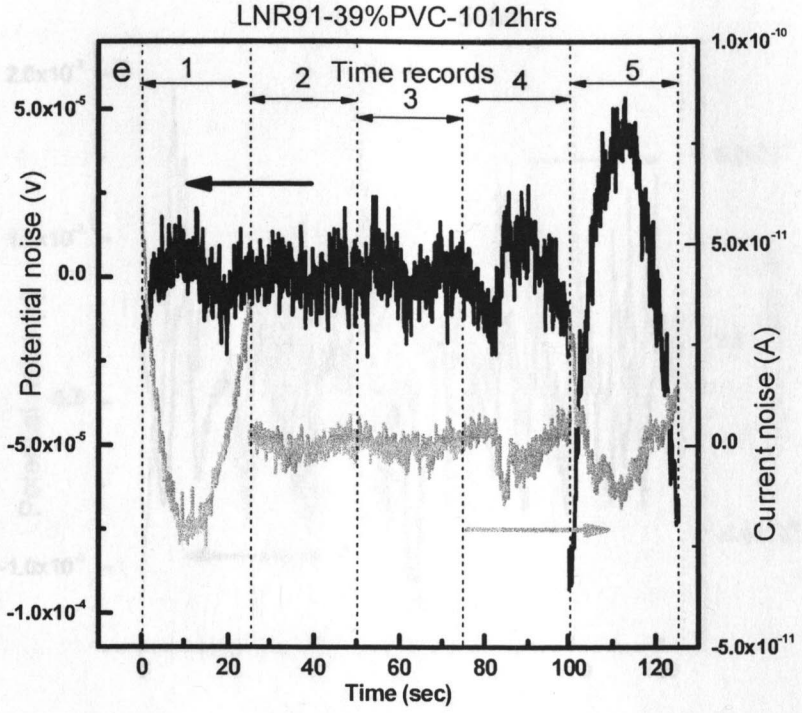

Figure 5-5. ENM data in time domain for the samples coated with 39% PVC LNR91 primer at (a) 157, (b) 356 (c) 663, (d) 856 and (e) 1012 hours exposure. Black lines: potential noise; gray lines: current noise.

and 7×10^{-9} A, except an abnormal small value of 4×10^{-12} A at 157 hour. In comparison to the samples of 35% PVC or 39% PVC, the amplitude of current noise in the 50% PVC sample was higher in three orders. It indicates that the corrosion intensity of the 50% PVC sample was much larger. [12] Also, the asymmetric patterns of an increased current followed by a decrease might suggest the corrosion processes were related to "the formation of metastable pits". [28]

Thus, from the ENM data analysis in the time domain, some interesting information can be obtained. First, the localized corrosion increased with the longer exposure time for 35% PVC sample while the 39% PVC sample showed no significant change, and the50% PVC sample had the highest corrosion intensity due to the highest amplitude of current

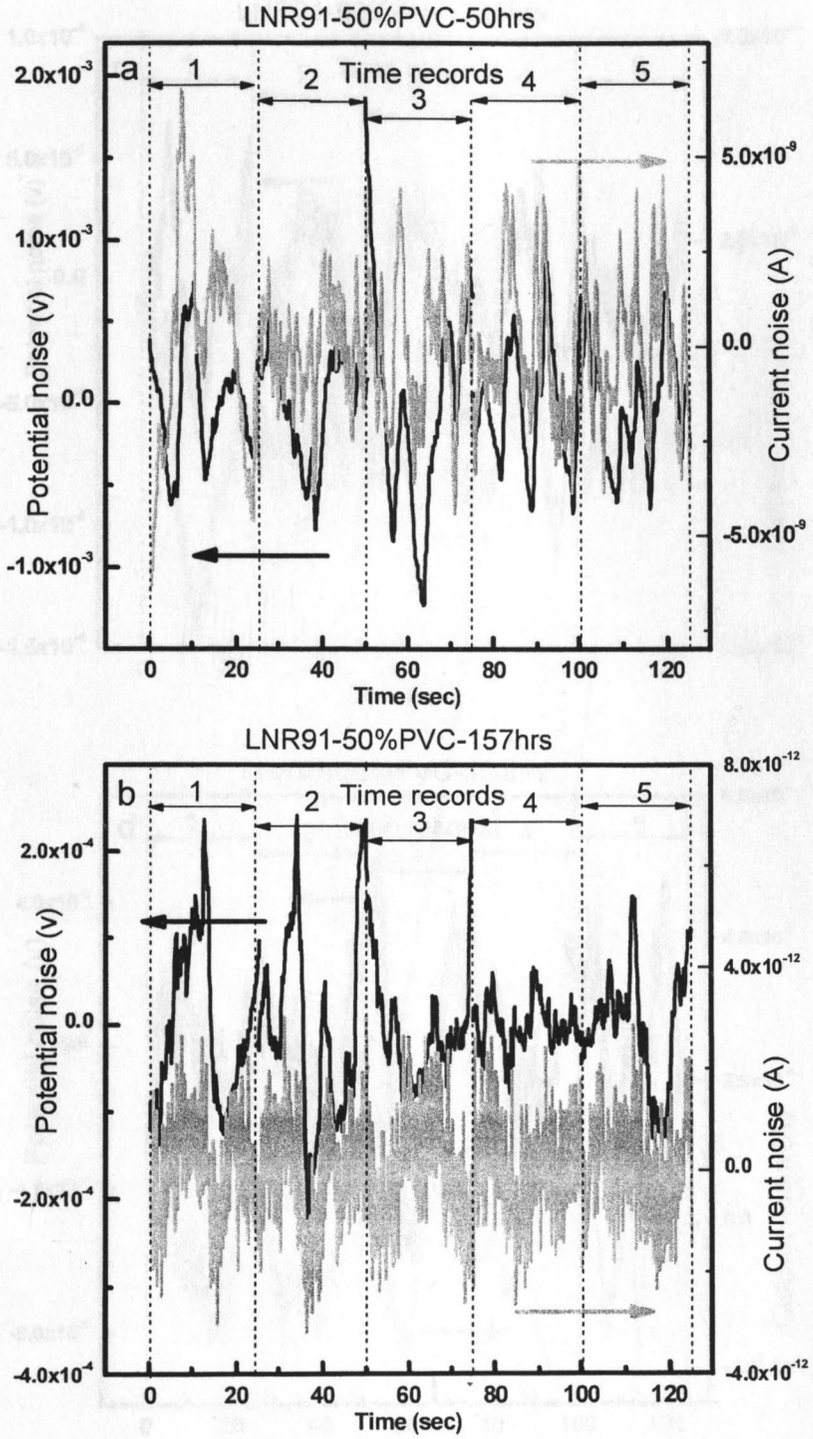
LNR91-50%PVC-50hrs
a
Time records
1
2
3
4
5
2.0x10-3
1.0x10-3
0.0
-1.0x10-3
Potential noise (v)
5.0x10-9
0.0
-5.0x10-9
Current noise (A)
0
20
40
60
80
100
120
Time (sec)
LNR91-50%PVC-157hrs
b
Time records
1
2
3
4
5
2.0x10-4
0.0
-2.0x10-4
-4.0x10-4
Potential noise (v)
8.0x10-12
4.0x10-12
0.0
-4.0x10-12
Current noise (A)
0
20
40
60
80
100
120
Time (sec)

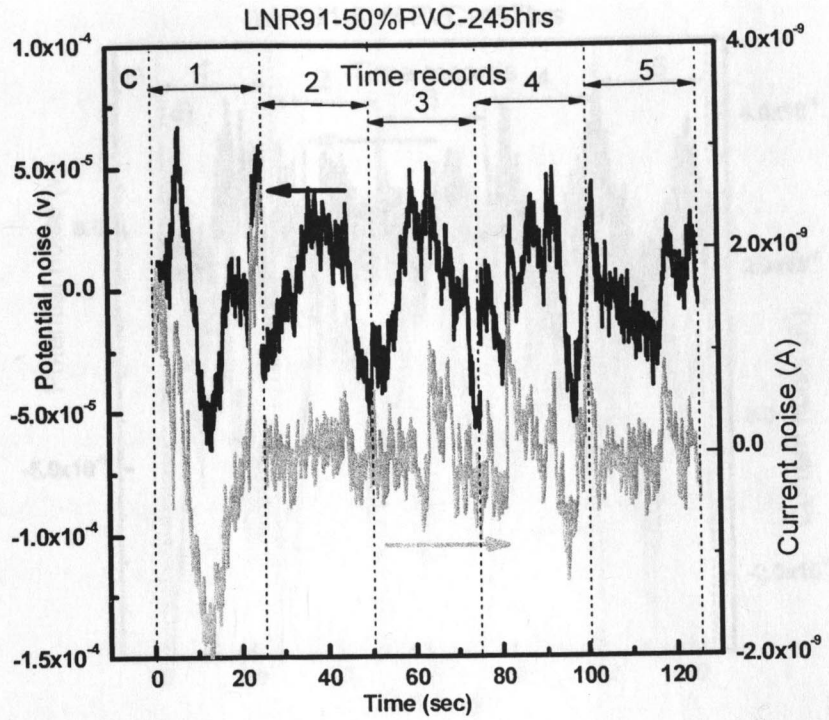
LNR91-50%PVC-245hrs
c
Time records
1
2
3
4
5
Potential noise (v)
Current noise (A)
Time (sec)
1.0x10-4
5.0x10-5
0.0
-5.0x10-5
-1.0x10-4
-1.5x10-4
4.0x10-9
2.0x10-9
0.0
-2.0x10-9
0
20
40
60
80
100
120

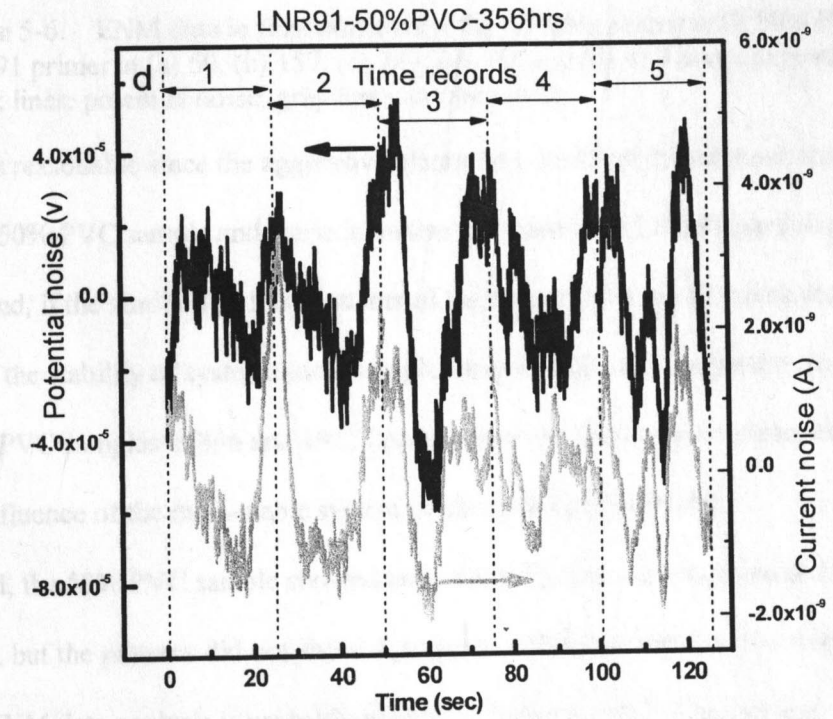
LNR91-50%PVC-356hrs
d
Time records
1
2
3
4
5
Potential noise (v)
Current noise (A)
Time (sec)
4.0x10-5
0.0
-4.0x10-5
-8.0x10-5
6.0x10-9
4.0x10-9
2.0x10-9
0.0
-2.0x10-9
0
20
40
60
80
100
120

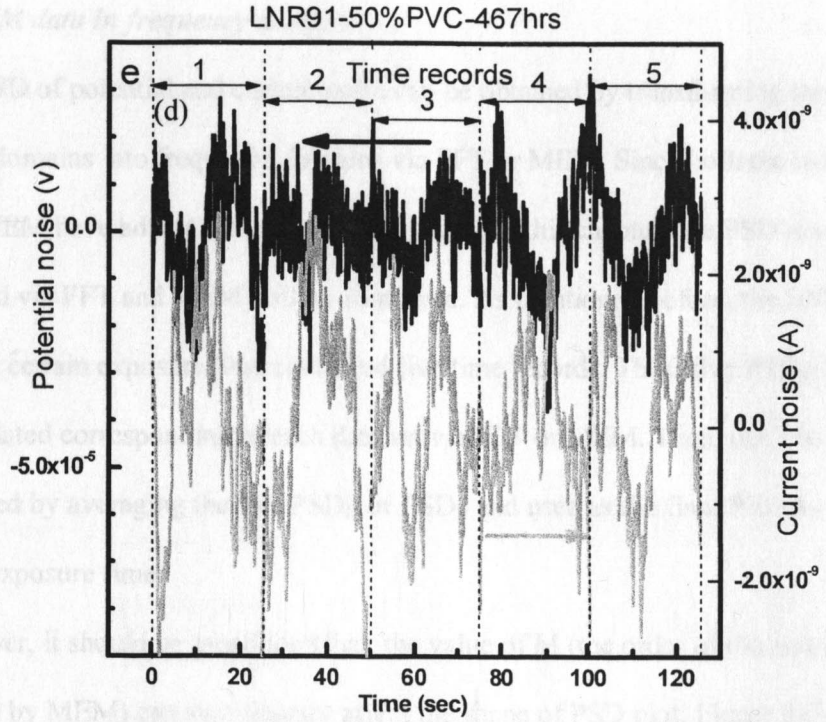

Figure 5-6. ENM data in time domain for the samples coated with 50% PVC LNR91 primer at (a) 50, (b) 157, (c) 245, (d) 356 and (e) 467 hours exposure. Black lines: potential noise; gray lines: current noise.

noise. It is reasonable since the aggressive electrolyte could easily penetrate the porous nature of 50% PVC sample and cause intensive reactions with LNR91 particles.

Second, if the similarity of the patterns of the transients in the five time records is related to the stability of system, some samples might not be at steady-state, such as 35% and 39% PVC samples at 856 and 1012 hours. However, there was no direct evidence to tell the influence of the meta-stable system on the collected ENM data.

Third, the 50% PVC sample showed an abnormally low current noise at 157 hour exposure, but the patterns did not show significant difference between the five time records. Further ENM data analysis is probably needed to figure out this phenomenon.

5.3.3. ENM data in frequency domain

The PSD of potential and current noise can be obtained by transforming the ENM data from time domains into frequency domains via FFT or MEM. Since both the methods of FFT and MEM have advantages and disadvantages, in this chapter, the PSD results transformed via FFT and MEM will be compared. As mentioned before, the ENM data of a sample at a certain exposure time contained five time records. Thus, five PSD_{Ei} or PSD_{Ii} were calculated corresponding to each data set via FFT or MEM. Then, one PSD_E or PSD_I was obtained by averaging the five PSD_{Ei} or PSD_{Ii} and used as the final PSD for this particular exposure time.

However, it should be mentioned that, the value of M (the order of the autoregressive model used by MEM) can significantly affect the shape of PSD plot. Figure 5-7 shows the PSD_{MEM} plots calculated from the same ENM data by using the various M values of 10, 30, 50, 100 and 200. It can see that, a smaller M value resulted in a smoother PSD_{MEM} plot, but some useful information in the high frequency region could be lost due to smoothness. Thus, the PSD_{FFT} plot was used as a reference plot to help choosing the suitable M value. From Figure 5-7, it seems that the PSD_{MEM} plot with M value of 30 exhibits a good smoothness as well as the necessary details at high frequency. Thus, the M value of 30 was chosen for MEM calculation.

In Figure 5-8 (a) and (b), the PSD_E/PSD_I of the 35% PVC sample at different exposure hours via FFT and MEM are shown, respectively. Similarly, the PSD_E/PSD_I of the 39% and 50% PVC samples at different exposure hours are plotted in Figure 5-9 and 5-10, respectively. The different colors of the PSD plots represent the various exposure hours.

By comparing the PSD_E/PSD_I plots obtained via FFT with the ones via MEM in Figure

5-8 to 5-10, it can be found that the corresponding plots of PSD_{FFT} and PSD_{MEM} are very similar with each other, though the lines of PSD_{MEM} are much smoother than the ones of PSD_{FFT}. It indicates that the methods of FFT and MEM have very good consistency in ENM data analysis, and both of them are suitable to be used to transform the ENM data from time domains to frequency domains. To avoid the arbitrary choice of M value for MEM computation, PSD_{FFT} plot was used as reference and a reasonable M value of 30 was chosen.

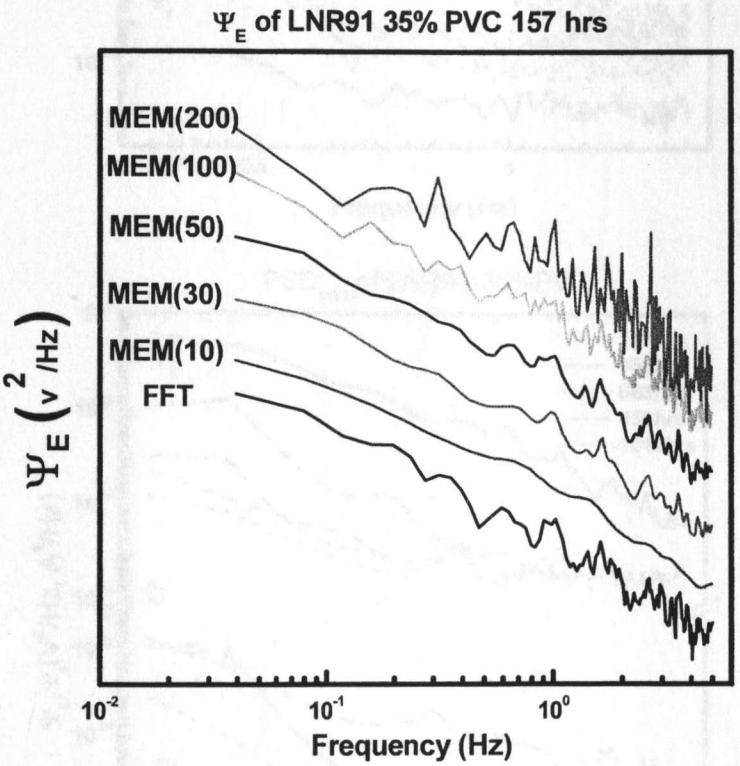

Figure 5-7. PSD_E of the sample coated with 35% PVC LNR91 primer at 157 hours exposure calculated by FFT, MEM (M) with the M value of 10, 30, 50, 100 and 200.

In Figure 5-11, the values of A_E and A_I for the samples at various exposure hours are plotted, and the values of S_E and S_I are listed in Table 5-1.

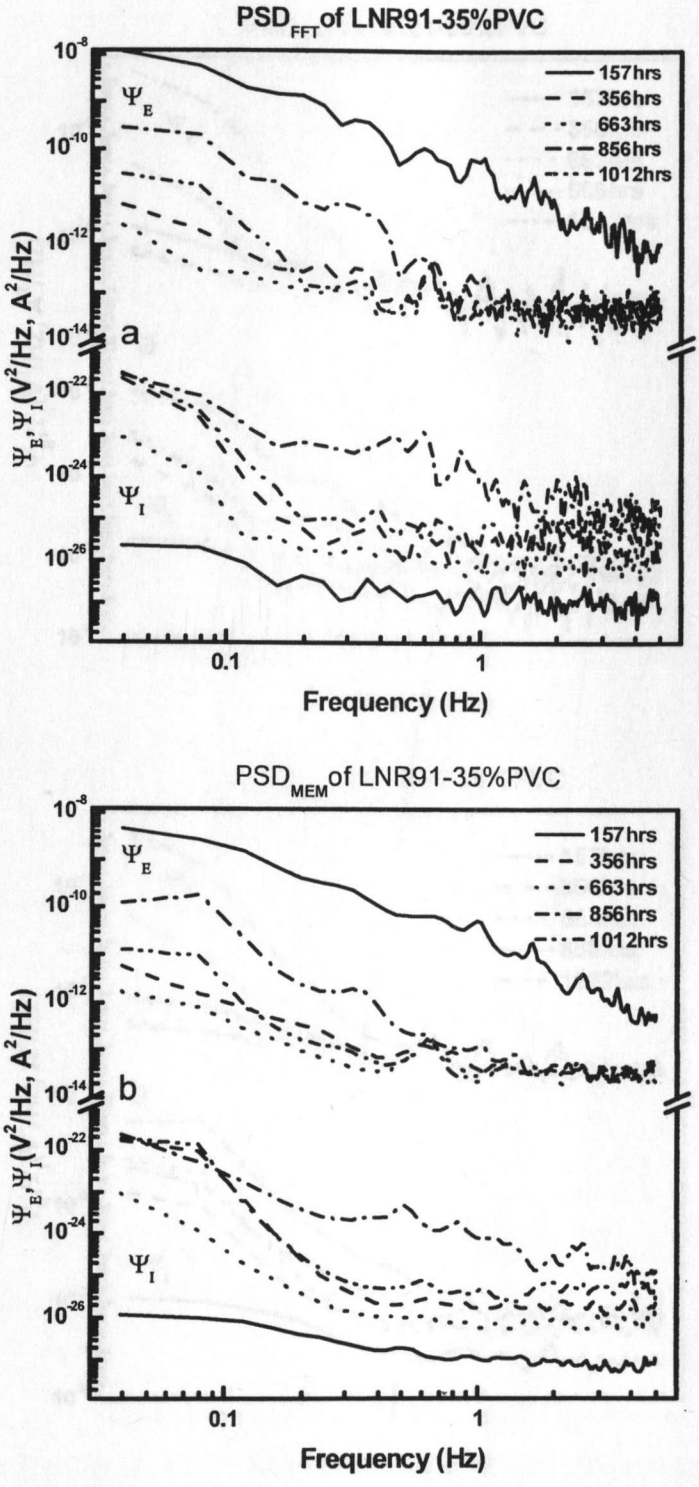

Figure 5-8. PSD_E and PSD_I of the samples coated with 35% PVC LNR91 primers at different exposure time obtained via (a) FFT, and (b) MEM (30).

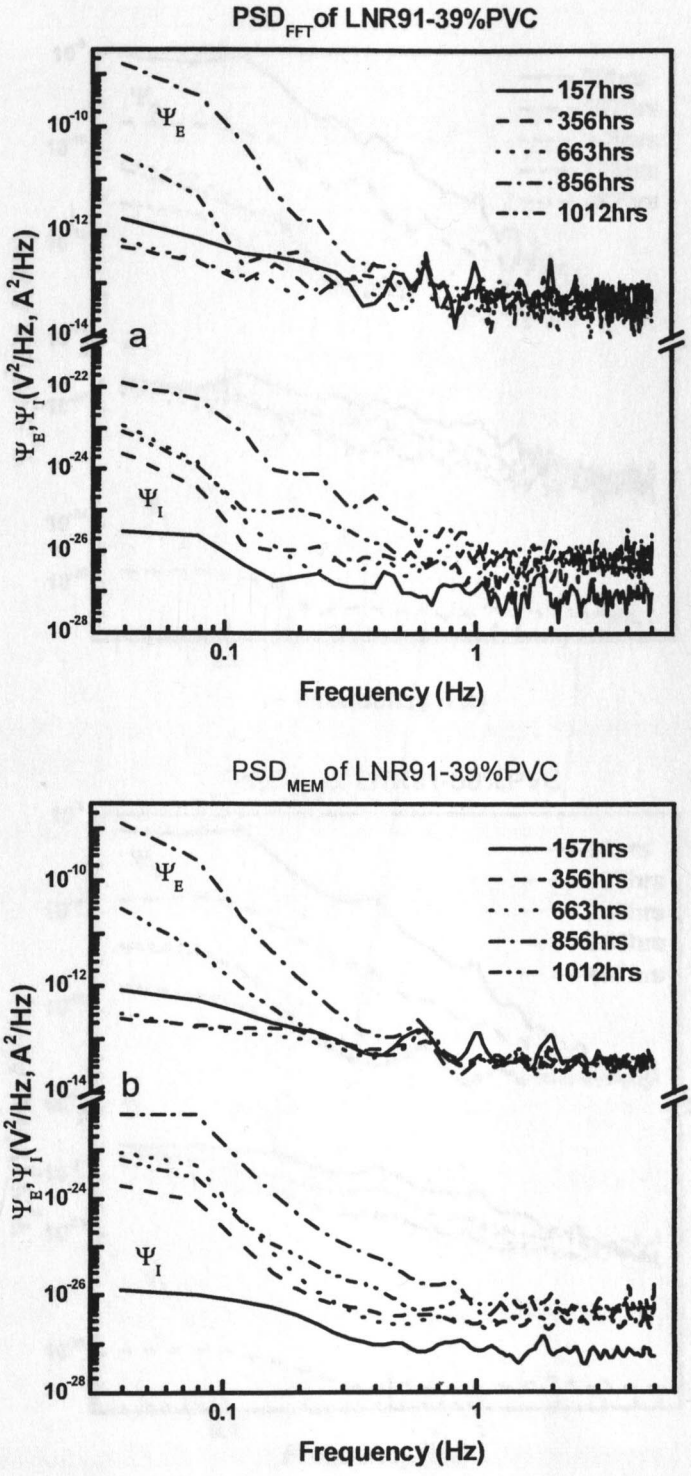

Figure 5-9. PSD_E and PSD_I of the samples coated with 39% PVC LNR91 primers at different exposure time obtained via (a) FFT, and (b) MEM (30).

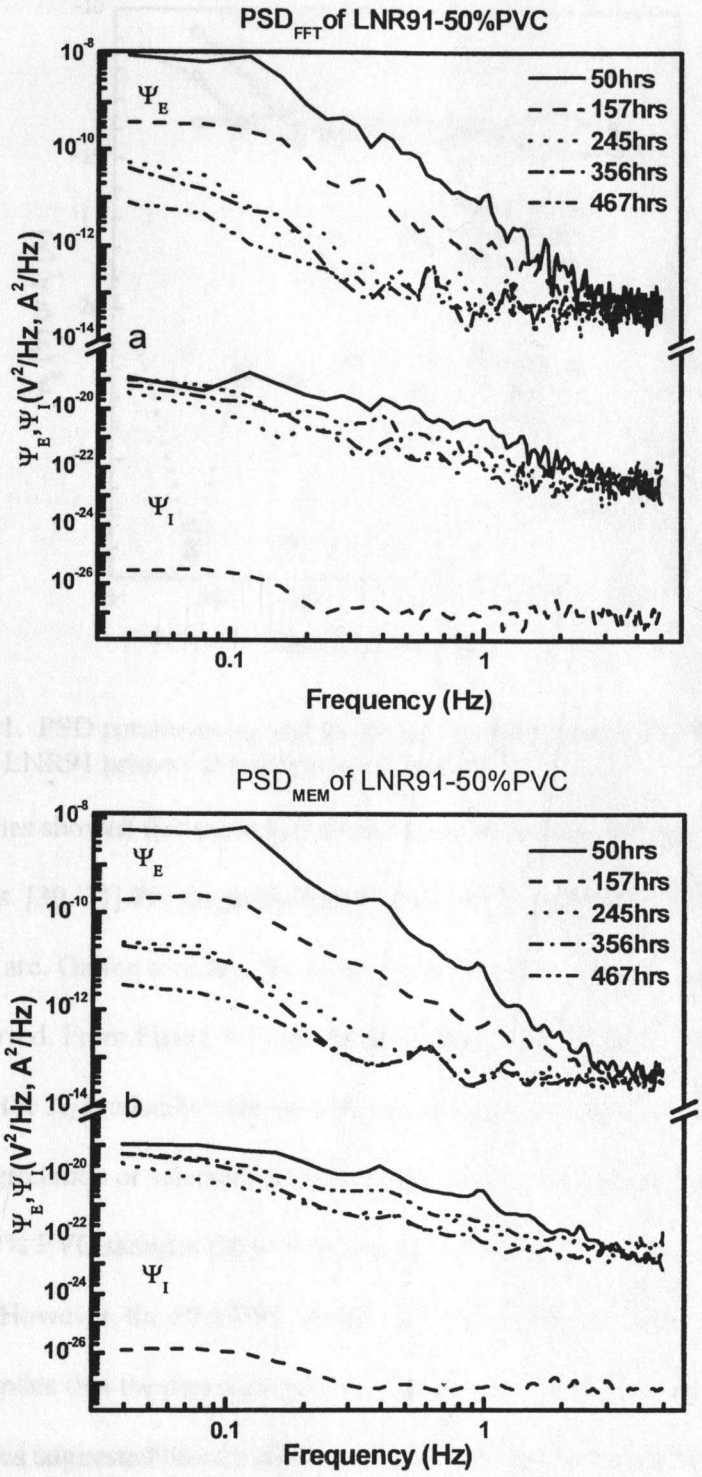

Figure 5-10. PSD_E and PSD_I of the samples coated with 50% PVC LNR91 primers at different exposure time obtained via (a) FFT, and (b) MEM (30).

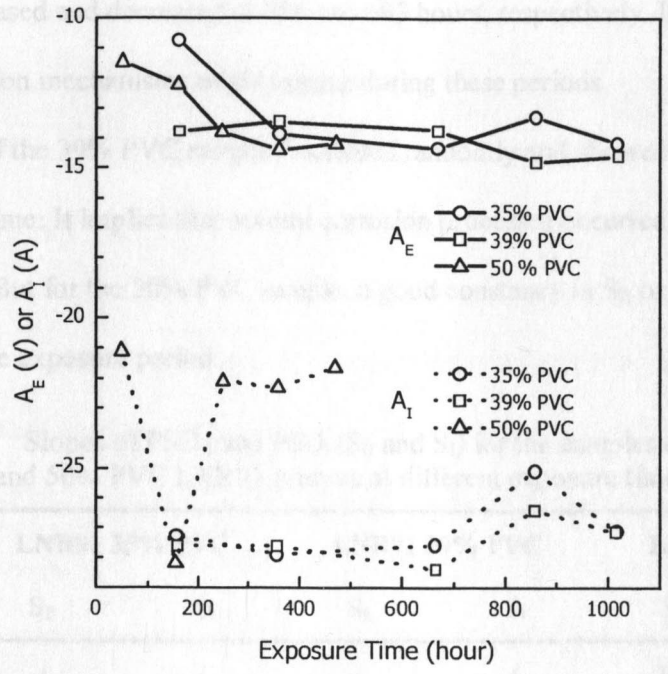

Figure 5-11. PSD parameter A_E and A_I for the samples coated with 35%, 39% and 50% PVC LNR91 primers at various exposure time.

Some studies showed that the values of A_E/A_I are related to the protective properties of coating systems. [30, 31] The larger the value of A_E is, the better the protection properties of coating film are. On the contrary, the larger A_I value means the more intensive corrosion processes occurred. From Figure 5-11, it can be seen that the values of A_E for the samples decrease while the A_I gradually increase with the increases of exposure time. It suggests that coating degradation or substrate corrosion had occurred to these coatings. Moreover, the 35% and 39% PVC samples show very similar trend of A_E or A_I as a function of exposure time. However, the 50% PVC sample exhibited much larger A_I values than the other two. It implies that the corrosion processes of 50% PVC sample were much intensive.

Some studies suggested that the different values of the PSD slopes (S_E/S_I) reflected the various corrosion mechanisms irrespective of the corrosion activity. [30, 31] In Table 5-1, it can be seen that, for the 35% PVC sample, S_E and S_I were constant at 157, 856 and 1012

hours, but increased and decreased at 356 and 663 hours, respectively. It suggests that different corrosion mechanisms might appear during these periods.

S_E and S_I of the 39% PVC sample fluctuated randomly and showed no obvious relation with exposure time. It implies that several corrosion processes occurred during the exposure time. But for the 50% PVC sample, a good constancy in S_E or S_I can be seen during the whole exposure period.

Table 5-1. Slopes of PSD_E and PSD_I (S_E and S_I) for the samples coated with 35%, 39% and 50% PVC LNR91 primers at different exposure time.

Exposure time (hours)	**LNR91 35% PVC**		**LNR91 39% PVC**		**LNR91 50% PVC**	
	S_E	S_I	S_E	S_I	S_E	S_I
50	/	/	/	/	-3.56	-2.64
157	-2.23	-1.18	-1.28	-1.44	-2.06	-2.23
245	/	/	/	/	-2.79	-1.79
356	-1.87	-4.36	-0.58	-2.72	-2.94	-2.28
467	/	/	/	/	-2.3	-1.93
663	-1.82	-3.16	-0.81	-4.16	/	/
856	-2.62	-2.39	-4.29	-3.01	/	/
1012	-2.07	-3.87	-2.77	-2.8	/	/

Therefore, the 39% PVC sample exhibited the most stable corrosion rate but might have many different corrosion mechanisms. The 50% PVC sample had very constant corrosion processes with a large corrosion rate. The probable reasons can be that the penetrating electrolyte caused the changes of the local microenvironments of the 39% PVC sample and resulted in the variation of corrosion mechanisms. But for the 50% PVC sample, the penetration of electrolyte into the porous film did not cause any change in the

local microenvironment over time, the steady state condition formed rapidly for the porous 50% PVC sample.

In Figure 5-11, a large decrease of A_I of 50% PVC LNR91 sample at 157 hour followed by a large increase at 245 hours can be observed though their S_I values were very similar (Table 5-1). It indicates that the 50% PVC LNR91 sample had a very small corrosion rate at 157 hours. The reason for such phenomenon was not clear yet. But in Figure 5-6 (b), an abnormal small current noise in time domain is observed, too.

In Figure 5-12 (a), (b) and (c) shown are the plots of log $R_{sn}(f)$ for 35%, 39% and 50% PVC samples. The large decrease of log R_{sn} (f) from 157 to 356 hour exposure of the 35% PVC sample revealed coating degradation. For the 39% PVC sample, the decrease of log $R_{sn}(f)$ with longer exposure time was not significant. But, a large increase of log $R_{sn}(f)$ at 157 hour of 50% PVC sample can be observed in Figure 5-12 (c).

Again, the information from $R_{sn}(f)$ is also in agreement with the abnormal small corrosion rate observed in the ENM data in time domain in Figure 5-6 (b) and the large decrease of A_I values in Figure 5-11.

From both the ENM data analysis in time and frequency domains, it can see that the 35% and 39% PVC samples showed very similar performance after exposure: low corrosion rate, slow coating degradation and various corrosion mechanisms. On the contrary, the 50% PVC sample exhibited high corrosion intensity, rapid coating degradation and a constant corrosion mechanism. The porous nature of the 50% PVC sample could be the reason. Electrolyte could easily penetrate into the porous primer film and react with the active LNR91 particles.

However, it needs to mention that the information obtained from ENM data is still not

enough for identifying the exact corrosion processes or mechanisms of the systems under study, lot of more work is needed to do this with any confidence. It should be emphasized that the application of ENM on the active Mg alloy-rich primer systems has lots of challenges. Due to the high activity of Mg alloy particles, the stability of the primer system during measurement is always in question. Therefore, all the ENM results should be treated with care.

As a first attempt to use ENM to study Mg alloy rich primer systems, all the conclusions and discussions are based on the previous work and experience carried out on the totally different systems. Very little prior work has been done on metal-rich coatings, such as the less active Zn-rich systems. Therefore, more work needs to be done on the similar systems by using ENM. In addition, EIS provides the comparative data that is very helpful in ENM data analysis. [11, 12, 30, 31]

In our study, the comparison between the EIS and ENM data was very important for studying the correlation between EIS and ENM, but helped show the utility of applying ENM to the Mg alloy rich primer systems.

5.3.4. Correlation studies of EIS and ENM on LNR91 primer systems

As mentioned before, examining the correlation between ENM and EIS data is very important to ENM study. According to the literature studies, several important parameters derived from EIS are usually used to evaluate the coating properties: impedance modulus at low frequency ($|Z|_{0.01Hz}$), polarization resistance (R_p), the minimum phase angle (Φ_{min}) and its frequency (f_{min}). On the other hand, the parameters of R_n and R_{sn}^0 have been shown valuable in studying coating properties, though their mathematical natures are totally different. The former is obtained by statistical analysis and the latter is based on spectral

noise analysis.

(a)

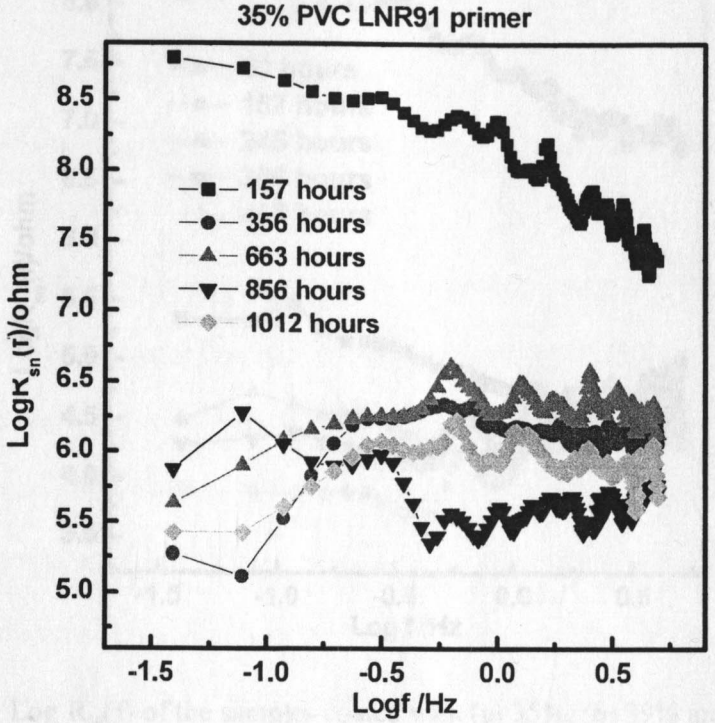

(b)

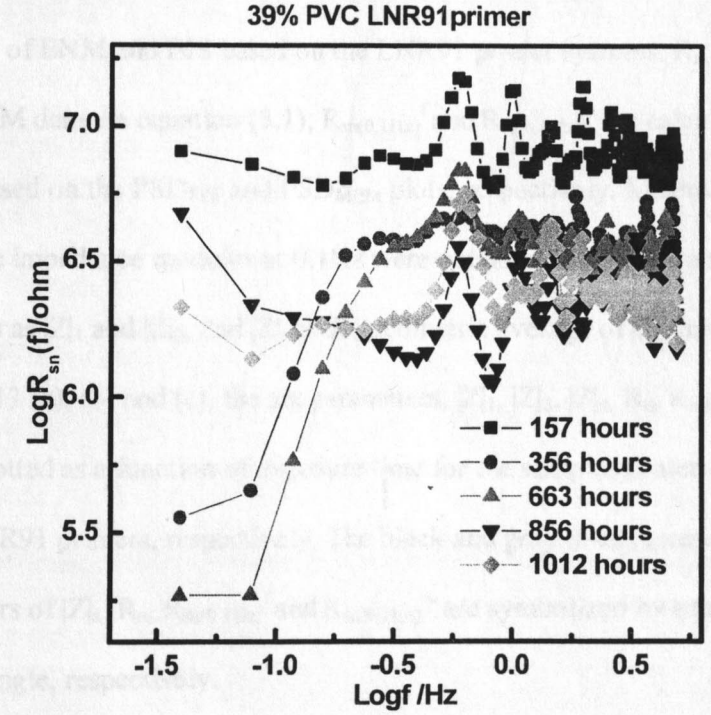

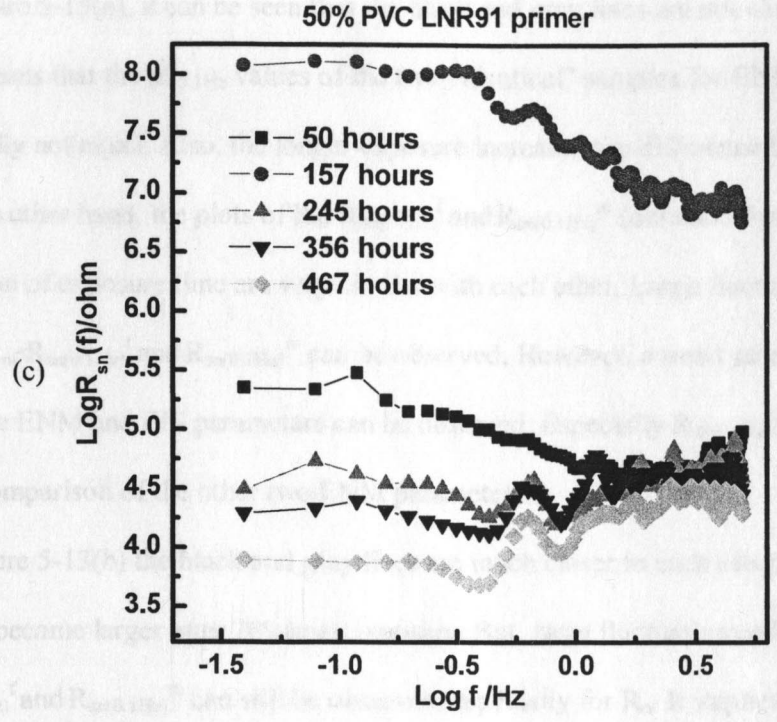

Figure 5-12. Log $R_{sn}(f)$ of the samples coated with (a) 35%, (b) 39% and (c) 50% PVC LNR91 primers at different exposure time.

In this work, four parameters, R_n, $R_{sn(0.1Hz)}{}^f$, $R_{sn(0.1Hz)}{}^m$ and $|Z|_{0.1Hz}$, were chosen for the correlation study of ENM and EIS based on the LNR91 primer systems. R_n is obtained from the raw ENM data via equation (5.1); $R_{sn(0.1Hz)}{}^f$ and $R_{sn(0.1Hz)}{}^m$ are calculated via equation (5.3) based on the PSD_{FFT} and PSD_{MEM} plots, respectively. Meanwhile, the two parameters of the impedance modulus at 0.1Hz were obtained from EIS data of the two identical samples as $|Z|_1$ and $|Z|_2$, and $|Z|_a$ is the geometric average of $|Z|_1$ and $|Z|_2$.

In Figure 5-13 (a), (b) and (c), the six parameters, $|Z|_1$, $|Z|_2$, $|Z|_a$, R_n, $R_{sn(0.1Hz)}{}^f$ and $R_{sn(0.1Hz)}{}^m$, are plotted as a function of exposure time for the samples coated with 35%, 39% an 50% PVC LNR91 primers, respectively. The black and gray lines represent $|Z|_1$and $|Z|_2$, and the parameters of $|Z|_a$, R_n, $R_{sn(0.1Hz)}{}^f$ and $R_{sn(0.1Hz)}{}^m$ are symbolized by square, circle, diamond and triangle, respectively.

In Figure 5-13(a), it can be seen that the black and gray lines are not close to each other. It means that the $|Z|_{0.1Hz}$ values of the two "identical" samples for ENM measurement were actually not equal. Also, the longer exposure increased the difference between $|Z|_1$ and $|Z|_2$. On the other hand, the plots of R_n, $R_{sn(0.1Hz)}{}^f$ and $R_{sn(0.1Hz)}{}^m$ (obtained from ENM data) as a function of exposure time are very similar with each other. Large fluctuations of the values of R_n, $R_{sn(0.1Hz)}{}^f$ and $R_{sn(0.1Hz)}{}^m$ can be observed. However, a trend correlation between the ENM and EIS parameters can be observed. Especially $R_{sn(0.1Hz)}{}^f$ is more closer to $|Z|_a$ in comparison of the other two ENM parameters.

In Figure 5-13(b) the black and gray lines are much closer to each other though the difference became larger after 700-hour exposure. But, large fluctuations of the values of R_n, $R_{sn(0.1Hz)}{}^f$ and $R_{sn(0.1Hz)}{}^m$ can still be observed, especially for R_n. It implies that there is no certain relationship between the unequal samples and the deviations between R_n/ $R_{sn(0.1Hz)}{}^f$/$R_{sn(0.1Hz)}{}^m$ and $|Z|_{0.1Hz}$. Again, it can see that $R_{sn(0.1Hz)}{}^f$ showed a better trend correlation with $|Z|_a$ in comparison of R_n/$R_{sn(0.1Hz)}{}^m$.

In Figure 5-13 (c), it can be found that the two samples of 50% PVC LNR91 primers for ENM measurement were almost identical since the black and gray lines are very close. In addition, the values of $R_{sn(0.1Hz)}{}^f$/$R_{sn(0.1Hz)}{}^m$ are overlapping with $|Z|_a$ except the large fluctuation at 157 hours.

The results of the comparison between the six parameters provide interesting information not only about the LNR91 primer systems but also the correlation between ENM and EIS methods. First, the six parameters, $|Z|_1$, $|Z|_2$, $|Z|_a$, R_n, $R_{sn(0.1Hz)}{}^f$ and $R_{sn(0.1Hz)}{}^m$, exhibited the similar trend of the gradual decreased values with the increase of exposure time, though the large and random fluctuations in R_n, $R_{sn(0.1Hz)}{}^f$ and $R_{sn(0.1Hz)}{}^m$ were always

observed. Second, the variations between the two "identical" samples for ENM measurement were present and increased with the longer exposure. However, so far the there was no evidence came from this study to relate the asymmetry of samples with the large fluctuations of ENM data or the deviations between EIS and ENM data. Since the two samples of 39% PVC had very similar $|Z|_1$ and $|Z|_2$, but the deviations between $R_n/R_{sn(0.1Hz)}^{f}$ / $R_{sn(0.1Hz)}^{m}$ and $|Z|_a$ were still significant. Third, the parameter of $R_{sn(0.1Hz)}^{f}$ showed a better correlation with $|Z|_a$ in comparison to R_n or $R_{sn(0.1Hz)}^{m}$. The probable reason could be that R_n was statistically obtained from the raw ENM data, which was not detrended. For $R_{sn(0.1Hz)}^{m}$, the smoothing of the MEM method might cause some information loss. Fourth, the presence of abnormal data, such as the ENM data of the 50% PVC sample at 157 hour, also contributed to the random fluctuations in the plots of $R_n/R_{sn(0.1Hz)}^{f}$ / $R_{sn(0.1Hz)}^{m}$ as a function of exposure time, which is shown as large peaks at 157 hours in Figure 5-13 (c). But the origins of such abnormal data were hard to tell. Thus, a dense sampling by shortening the periods between two ENM testing might help to find the true trend of coating degradation.

The differences present between the parameters of ENM ($R_n/R_{sn(0.1Hz)}^{f}$ / $R_{sn(0.1Hz)}^{m}$) and $|Z|_a$ is reasonable. ENM data are acquired at a freely floating OCP, but EIS data are obtained under a fixed OCP. The two unequal working electrodes in ENM measurement can cause the testing condition to deviate from the important assumption of "activation control". [33] Moreover, the ENM data acquisition is always more sensitive to environmental disturbances, such as the H_2 bubble growth and breakup, in comparison to EIS data collection.

However, from the results of this study, the ENM parameters, $R_{sn(0.1Hz)}^{f}$ / $R_{sn(0.1Hz)}^{m}$, exhibited good trend correlation with the impedance modulus $|Z|_a$. It indicates that the

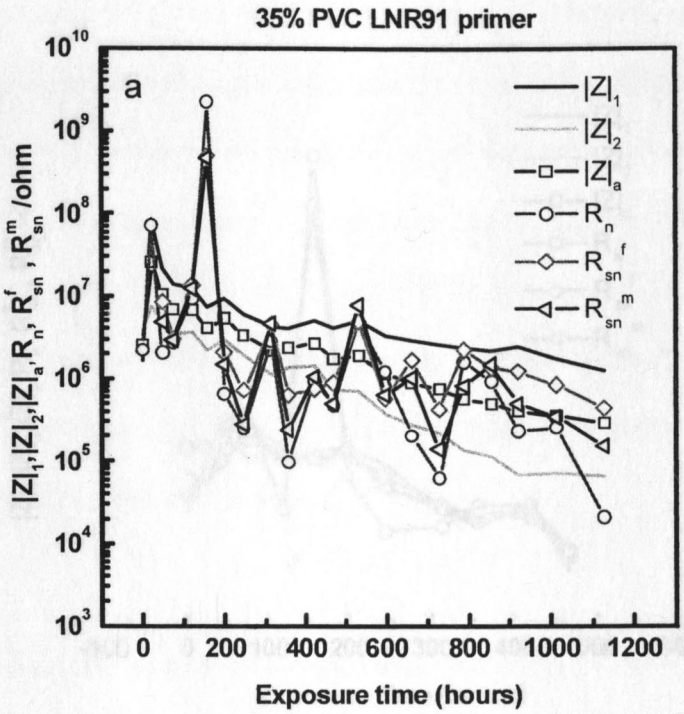
35% PVC LNR91 primer
a
$|Z|_1$
$|Z|_2$
$|Z|_a$
R_n
R_{sn}^f
R_{sn}^m
$|Z|_1, |Z|_2, |Z|_a, R_n, R_{sn}^f, R_{sn}^m$ /ohm
Exposure time (hours)

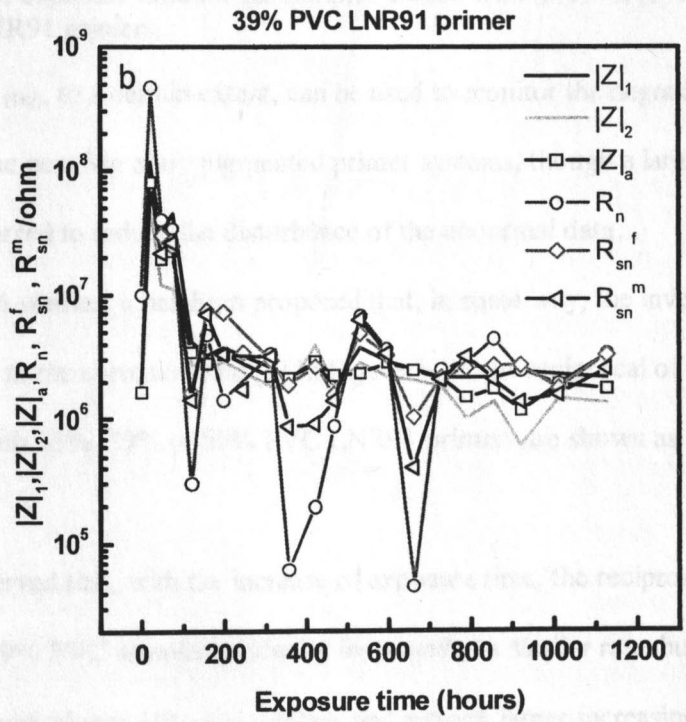
39% PVC LNR91 primer
b
$|Z|_1$
$|Z|_2$
$|Z|_a$
R_n
R_{sn}^f
R_{sn}^m
$|Z|_1, |Z|_2, |Z|_a, R_n, R_{sn}^f, R_{sn}^m$ /ohm
Exposure time (hours)

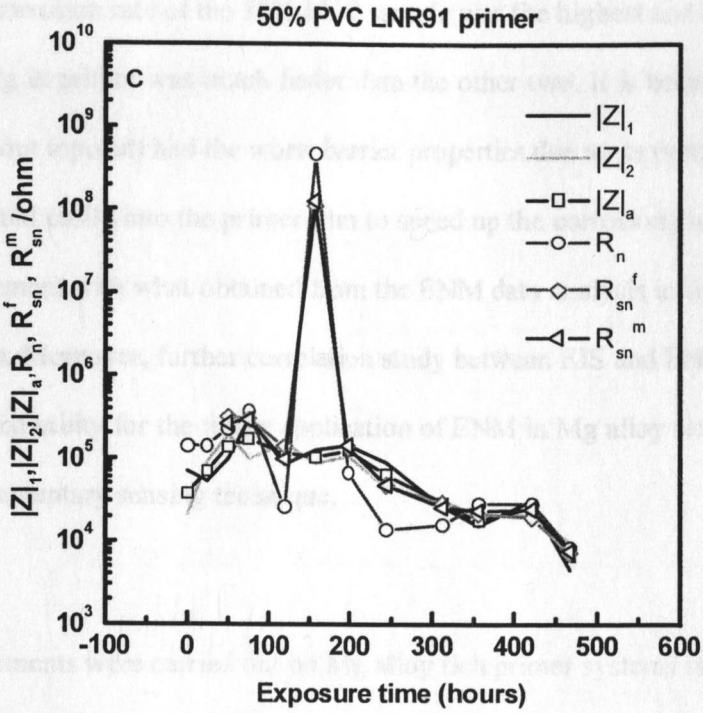

Figure 5-13. Parameters of $|Z|_1$, $|Z|_2$, $|Z|_a$, R_n, $R_{sn(0.1Hz)}{}^f$ and $R_{sn(0.1Hz)}{}^m$ changes as the function of exposure time for the samples coated with (a)35%, (b) 39% and (c) 50% PVC LNR91 primers.

parameter of $R_{sn(0.1Hz)}$, to a certain extent, can be used to monitor the degradation of coating films, including the new Mg alloy pigmented primer systems, though a large collection of ENM data is preferred to reduce the disturbance of the abnormal data.

In many ENM studies, it has been proposed that, in some way, the inverse ratio of $R_{sn(0.1Hz)}$ is related to the corrosion rate.[6] In Figure 5-14, the reciprocal of $R_{sn(0.1Hz)}{}^f$ of the samples coated with 35%, 39% or 50% PVC LNR91 primers are shown as the function of exposure time.

It can be observed that, with the increase of exposure time, the reciprocals of $R_{sn(0.1Hz)}{}^f$ for the 35% and 39% PVC samples gradually increased at a similar rate, but the 50% PVC sample showed much higher $1/R_{sn(0.1Hz)}{}^f$ values and a much larger increasing rate. It

indicates that the corrosion rate of the 50% PVC sample was the highest and the consumption to Mg in primer was much faster than the other two. It is because that the 50% PVC sample (without topcoat) had the worst barrier properties due to its porous nature, and electrolyte penetrated easily into the primer film to speed up the corrosion processes. These results are in agreement with what obtained from the ENM data analysis in time and frequency domains. Moreover, further correlation study between EIS and ENM data showed the potential utility for the future application of ENM in Mg alloy rich primer system as a complementary sensing technique.

5.4. Conclusions

ENM measurements were carried out on Mg alloy rich primer systems samples to evaluate the performance changes as a function of Prohesion exposure time. ENM data collected on the Al alloy 2024 T3 substrates coated with LNR91 primers at different PVCs are reported.

The baseline drift was observed in the plots of potential/current noise versus time of various samples. A method of linear drift removal was applied on each ENM raw data and the results showed that the averages of potential/current noise were close to zero. Then, the detrended ENM data were analyzed by various methods, in the time and frequency domains. FFT and MEM were used to transform the ENM data in time domains into the frequency domains. The PSD_E/PSD_I plots obtained from both FFT and MEM were very similar. In addition, the interception of A_E/A_I and the slope of S_E/S_I were extracted from the linear fitting of PSD_{MEM}. The information obtained from ENM data in time domain and in frequency domain showed that the 35% and 39% PVC samples degraded with relatively low corrosion rate but various corrosion mechanisms. On the contrary, the 50% PVC

sample degraded at a high corrosion rate but with a constant mechanism.

The correlation between ENM and EIS was studied by comparing six important parameters, $|Z|_1$, $|Z|_2$, $|Z|_a$, R_n, $R_{sn(0.1Hz)}{}^f$ and $R_{sn(0.1Hz)}{}^m$. Trend correlations, not the numerical correlations, were found between the EIS parameters ($|Z|_1$, $|Z|_2$, $|Z|_a$) and ENM parameter (R_n, $R_{sn(0.1Hz)}{}^f$, $R_{sn(0.1Hz)}{}^m$), especially between $|Z|_a$ and $R_{sn(0.1Hz)}{}^f$. It indicates that ENM could be used to monitor the corrosion processes and coating degradations for the LNR91 primer system. Also, $R_{sn(0.1Hz)}{}^f$ could be a good indicator for monitoring the electrochemical performance of different coating systems.

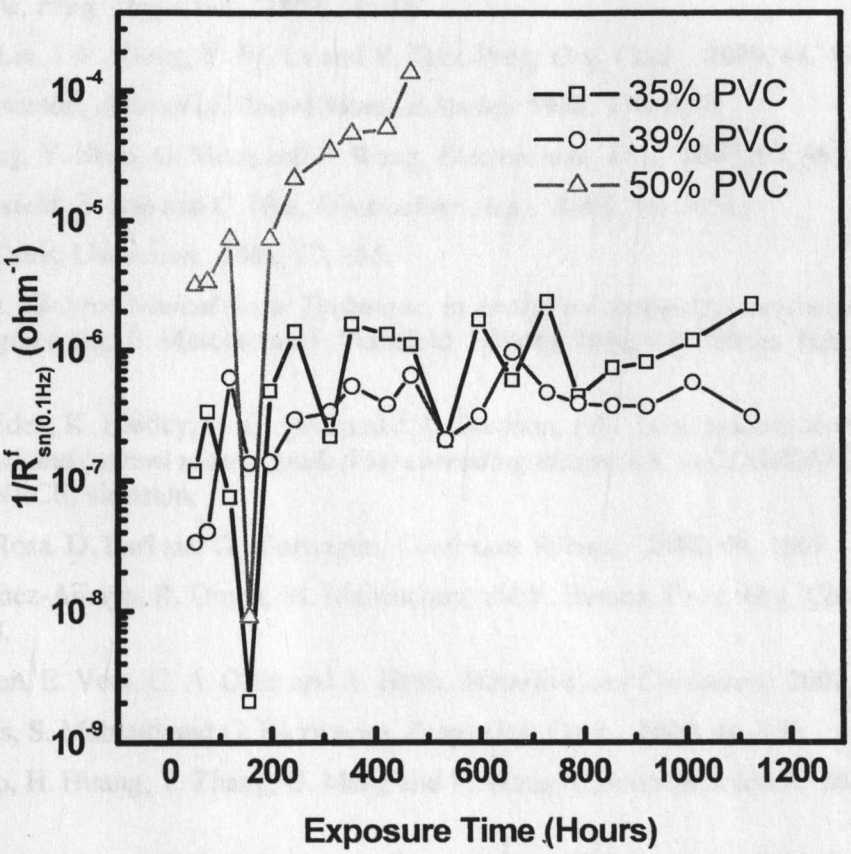

Figure 5-14. Inverse of $R_{sn(0.1Hz)}{}^f$ of the LNR91 primer coated samples change as the function of exposure time.

The influence of the non-stationary system or the unequal coupled samples was noted

but could not be rigorously analyzed. Further, there was some anomalous data present without a known source. It suggests that all the ENM data should be treated with care. EIS was in parallel with ENM to provide reference data for helps to interpret the ENM data, but more work needs to be done to utilize the application of ENM on this type coating primer.

5.5. References

1 P. Sorensen, S. Kiil, K. Dam-Johansen and C. Weinell, *J. Coat. Technol. Res.*, **2009**, 6, 135.

2 G. Bierwagen, D. Battocchi, A. Simoes, A. Stamness and D. Tallman, *Prog. Org. Coat.*, **2007**, 59, 172.

3 I. Sekine, *Prog. Org. Coat.*, **1997**, 31, 73.

4 X. W. Liu, J. P. Xiong, Y. W. Lv and Y. Zuo, *Prog. Org. Coat.*, **2009**, 64, 497.

5 W. P. Iverson, *Journal of Electrochemical Society* **1968**, 115, 617.

6 T. Zhang, Y. Shao, G. Meng and F. Wang, *Electrochim. Acta*, **2007**, 53, 561.

7 F. Mansfeld, Z. Sun and C. Hsu, *Electrochim. Acta*, **2001**, 46, 3651.

8 R. A. Cottis, *Corrosion*, **2001**, 57, 265.

9 F. Huet, *Electrochemical Noise Technique*, in *Analytical methods in corrosion science and engineering*, P. Marcus and F. Mansfeld, Editors, **2006**, CRC Press, Boca Ration, FL.

10 D. A. Eden, K. Hladky, D. G. John and J. L. Dawson, *EN - simultaneous monitoring of potential and current noise signals from corroding electrodes*, in *CORROSION'86*. **1986**, NACE, Houston, 1.

11 R. De Rosa, D. Earl and G. Bierwagen, *Corrosion Science*, **2002**, 44, 1607.

12 J. Sanchez-Amaya, R. Osuna, M. Bethencourt and F. Botana, *Prog. Org. Coat.*, **2007**, 60, 248.

13 O. Duran, E. Vera, C. A. Ortiz and A. Heyn, *Materials and Corrosion*, **2007**, 58, 997.

14 D. Mills, S. Mabbutt and G. Bierwagen, *Prog. Org. Coat.*, **2003**, 46, 176.

15 Y. Shao, H. Huang, T. Zhang, G. Meng and F. Wang, *Corrosion Science*, **2009**, 51, 2906.

16 G. Bierwagen, C. Jeffcoate, J. Li, S. Balbyshev, D. Tallman and D. Mills, *Prog. Org. Coat.*, **1996**, 29, 21.

17 D. Mills, G. Bierwagen, D. Tallman and B. Skerry, *Characterization of Corrosion under Marine Coatings by Electrochemical Noise Methods* in *Proc.12th International Corrosion Congress*, **1993**, Houston, TX.

18 D. Mills, G. Bierwagen, D. Tallman and B. Skerry, *Materials Performance*, **1995**, 34, 33.

19 S. Mabbutt, D. Mills and C. Woodcock, *Prog. Org. Coat.*, **2007**, 59, 192.

20 X. Wang, G. bierwagen, S. Mabbutt and D. Tallman, *Some Non-conventional Measurement Electrode Configurations for Electrochemical Impedance Spectroscopy and Electrochemical Noise Measurements of Coated Metals and Their Possible Uses*, in *EuroCorr 2001*. **2001**, CD-ROM Conf. Proc., Lake Garda, Italy.

21 X. P. Wang, *Studies on novel electrode configurations for in situ corrosion monitoring on coated metal systems*, in *Coatings and Polymeric Materials*. **2002**, North Dakota State University, Fargo.

22 Q. Su, *The application of embedded sensors for in-situ monitoring of protective coatings on metal substrates*, in *Coatings and Polymeric Materials*. **2008**, North Dakota State University, Fargo.

23 Q. Su, K. Allahar and G. Bierwagen, *Electrochim. Acta*, **2008**, 53, 2825.

24 G. Bierwagen, X. Wang and D. Tallman, *Prog. Org. Coat.*, **2003**, 46, 163.

25 N. Fawcett, C. Stearns and B. Bufkin, *JCT Coatings Tech*, **1984**, 56, 49.

26 F. Mansfeld and H. Xiao, *Journal of the Electrochemical Society*, **1993**, 140, 2205.

27 M. Moon and B. Skerry, *J. Coat. Technol.*, **1995**, 67, 35.

28 S. E. Faidi, J. D. Scantlebury, P. Bullivant, N. T. Whittle and R. Savin, *Corrosion Science*, **1993**, 35, 1319.

29 U. Bertocci, J. Frydman, C. Gabrielli, F. Huet and M. Keddam, *J.Electrochem.Soc.*, **1998**, 145, 2780.

30 C. Gouveia-Caridade, M. Pereira and C. Brett, *Electrochim. Acta*, **2004**, 49, 785.

31 H. Xiao and F. Mansfeld, *J. Electrochem. Soc.*, **1994**, 141, 2332.

32 U. Bertocci, F. Huet, R. P. Nogueira and P. Rousseau, *corrosion*, **2002**, 58, 337.

33 H. Greisiger and T. Schauer, *Prog. Org. Coat.*, **2000**, 39, 31.

CHAPTER 6. THE STUDIES OF THE OXIDATION PRODUCTS OF MG ALLOY-RICH PRIMERS DURING ACCELERATED WEATHERING

6.1. Introduction

In Mg alloy-rich primer systems, Mg alloy particles are used as pigments in polymer matrix to provide cathodic protection for AA 2024 T3 substrate in parallel to the barrier protection of the topcoat system. The understanding of the aspects of a new metal-rich primer system, such as corrosion processes, protective mechanisms, interaction between the primer and environment, and the failure modes of primers are of importance to the development and implementation of the novel Cr-free protection coating systems.

Therefore, the studies of the oxidation products formed in Mg alloy-rich primers after the accelerated weathering exposure are important. The discovery of the chemical composition and morphology of the oxidation products can provide useful information of the probable corrosion protection mechanisms, the possible electrochemical and chemical reactions, and the interactions between Mg alloy-rich primer systems and environment. The identification of the oxidation products is also necessary to understand whether passivation or the related phenomena are occurring.

Moreover, the oxidation products can change the environment, such as the local pH near the Mg alloy pigments and influence the protection mechanisms due to the variation in the coating system and its exposure. For example, the oxidation products of zinc-rich primers have been identified to include zinc oxide and hydrated zinc oxide, and zinc oxychlorides. These oxidation products of zinc exhibit a large volume increase relative to

the metallic zinc. It has also been found that the mixture of zinc oxidation products can seal the voids and cracks in the polymer binder through swelling and result in some extra barrier protection to the steel substrate. [1, 2] Thus, the studies of oxidation products in the exposed zinc-rich primer have helped to explain that the outstanding corrosion protection of zinc-rich primer for steel is not only dependent on the cathodic protection provided by the active zinc particles but also possibly the incremental barrier protection supplied by Zn oxidation products.

Similarly, the studies of the oxidation products formed in the exposed Mg alloy-rich primer may help to understand the sacrificial protection provided by Mg alloy pigments, the solubility of oxidation products, the pH control issues, and the transport of the chemical species in primer system. Also, the identification of oxidation products may give the important information about how the secondary elements present in Mg alloy pigments affect the cathodic protection and provide the insight to the relationship between the composition of Mg alloy and the protection efficiency of cathodic protection or barrier protection of the primer system. Moreover, the better understanding of the Mg alloy pigmented primer systems may help the future work of designing and developing an optimal Mg/Mg alloy-rich primer system.

The effective and accurate identification of oxidation products is highly dependent on the analytical techniques used for measurement. The proper techniques need to perform the non-destructive analysis on the oxidation products qualitatively, quantitatively and sensitively. In this study, due to their unique capabilities, scanning electron microscopy (SEM), X-ray photoelectron spectroscopy (XPS) and confocal Raman microscopy were chosen to identify the oxidation products of the exposed Mg alloy primers.

XPS is a widely used and powerful surface analysis method for determining the elemental composition on the material surfaces. [3-7] XPS is based on photoelectric effects. As shown in Figure 6-1, a beam of monochromatic X-ray is used to irradiate the surface of testing material under ultra high vacuum condition, the kinetic energy of the escaped photoelectrons is measured by an electron energy analyzer, and the number of photoelectrons is counted by an electron detector. Since the energy of photoelectrons from element is specific and the counts of photoelectrons are proportional to the amount of corresponding element, the elemental composition of material surface can be obtained by analysis XPS spectra. XPS can provide both qualitative and quantitative information of existing elements in high sensitivity (~0.1 atom %). Furthermore, the chemical state of each element can be identified from XPS spectra, which cannot be obtained by other methods, such as EDX. Based on the information provided by XPS, the formula of the target compounds can be actually identified.

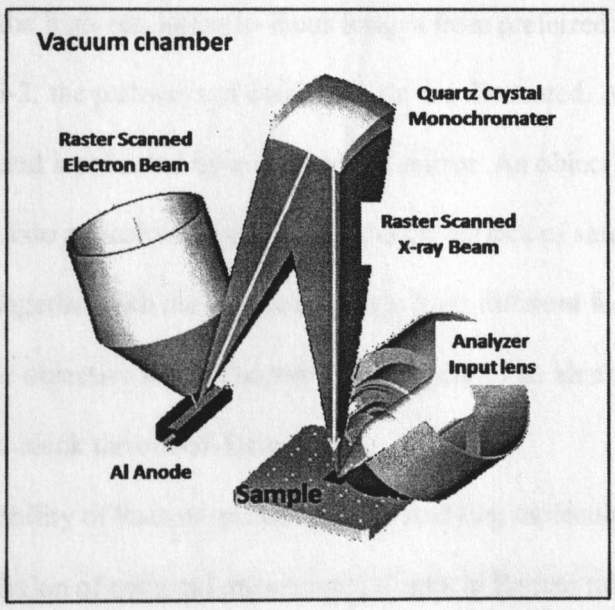

Figure 6-1. Schematic of XPS. (Courtesy of Physical electronics, Inc)

Confocal Raman microscopy is a microscopic analysis technique that incorporates Raman spectroscopy with confocal microscopy. Raman spectroscopy is a mature technique and has been widely used to analyze the structures of inorganic and organic compounds based on Raman scattering phenomenon: being interrupted by the photons of the incident light, molecules of the testing materials are excited from the ground state to the effective energy states. During the consequent relaxation, part of molecules return to the new rotation or vibration states and meanwhile release the photons with energy different from that of incident light. These shifts of photo energy reflect the energy differences between the original and final states, i.e. the energy level of molecular vibration. Raman spectroscopy can provide information of molecular vibration similar as IR spectroscopy does and is very useful in the identification of molecular structure or the study of chemical bonds' changes. One of the advantages of Raman technique is that the interference of the presented water or OH ion can be neglected. Confocal microscopy is a well-developed new technique by which the high-resolution in-focus images from preferred depths can be obtained. In Figure 6-2, the pathways of confocal light are illustrated. A laser beam passes through an aperture and is refracted by a dichromatic mirror. An objective lens is used to center the laser light into a focal volume on or within the surface of sample. The scattered and reflected lights together with the illuminated light from different focal planes are collected by the same objective lens. A barrier filter in front of an identical aperture as the former one is used to block the out-of-focus signal.

Combining the ability of Raman spectroscopy in studying molecular vibration and the superior spatial resolution of confocal microscopy, Confocal Raman microscopy can analyze samples at unique lateral resolution and depth resolution of micrometer level and is

very powerful in the investigation of oxidation products and degradation of polymer binders. [8-13]

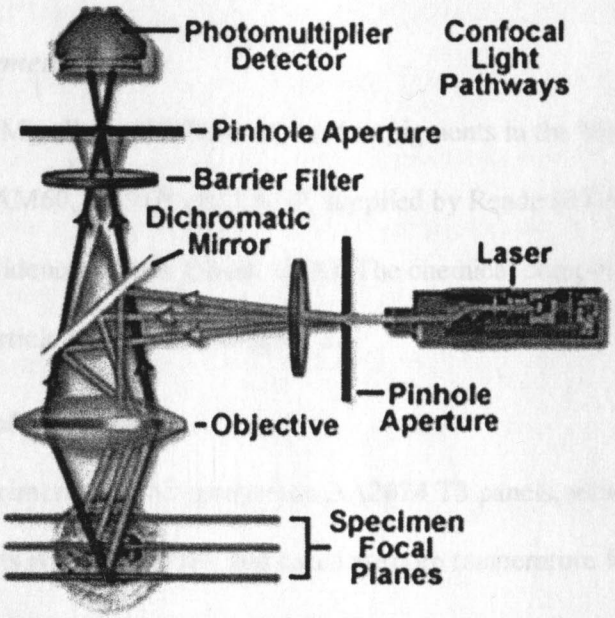

Figure 6-2. Principle of confocal microscopy. (Copied from http://www.olympusfluoview.com/theory/index.html)

In this chapter, the identification of the oxidation products of three exposed Mg alloy rich primers will be reported. Three Mg alloy-rich primers having AM60, AZ91B and LNR91 as pigment were formulated at 34% PVC, 38% PVC and 44% PVC, respectively. The AA2024 T3 panels coated with these Mg alloy-rich primers were exposed in Prohesion chamber for accelerated weathering tests.

The oxidation products of the exposed Mg alloy-rich primers have been studied and identified by SEM, XPS and confocal Raman microscopy. Based on the results, the mechanism study is carried out mainly on three aspects: the possible reactions forming the identified oxidation products; the possible local environment causing these reactions; the possible influences of Al content in Mg alloys on the local environment. In addition, the impacts of oxidation products on corrosion protection performance will be discussed at the

end of this chapter.

6.2. Experimental

6.2.1. Mg alloy pigments

Three different Mg alloy particles were used as pigments in the Mg alloy rich primer system. They were AM60, AZ91B and LNR9, supplied by Reade (READE Advanced Materials, East Providence, Rhode Island, USA). The chemical composition and properties of each Mg alloy particle are given in Chapter 3.

6.2.2. Primer sample preparation

Mg alloy rich primers were air sprayed on AA2024 T3 panels, which are supplied by Q Panel Lab products (Cleveland OH) and cured at room temperature for two days. The substrates were polished with 220 grit and 600 grit sand paper to clean the surface, rinsed with hexane, and dried with paper towel. AM60, AZ91B and LNR91 pigmented primers were using an epoxy-amide system as binder and formulated at PVC of 34%, 38% and 44%, respectively. The thickness of the dry primer film was approximately 120 μm.

6.2.3. Sample characterization

6.2.3.1. SEM measurement

SEM and EDX measurement were conducted by using a JEOL JSM-6300 Scanning Electron Microscope equipped with X-ray energy dispersion detector. SEM images were taken with 15KV acceleration voltage with backscattering mode. SEM and EDX measurement were carried out by Mr. Scott Payne in USDA. The schematic details of SEM are given in Chapter 3.

6.2.3.2. XPS measurement

XPS measurements were carried out with a PHI Quantera XPS microprobe system located at College of Engineering, Alfred University (Alfred, NY). It was equipped with an electron neutralizing gun and an Ar ion sputter gun. The base pressure of chamber was less than 1 x 10^{-8} torr during measurement. All the results were obtained with an Al K_α ($h\nu$ = 1486.6 eV) X-ray beam at beam diameter of 200 microns. During the whole range spectra scanning, the pass energy of analyzer was fixed at 224 eV and the scanning step was 0.4eV. During the high resolution scanning, the pass energy was 55 eV and the scanning step was 0.1 eV. The binding energy was calibrated using Au $4f_{7/2}$ = 84.0 and Cu $2p_{3/2}$ = 932.67 eV.

The deconvolution of the high resolution spectra was conducted by using XPS Peak v4.1 software (by Raymund Kwok, Department of Chemistry, The Chinese University of Hong Kong, Shatin, Hong Kong and distributed as freeware). In all deconvolution, Shirley (non-linear) baselines and Gauss-Lorentz synthetic peaks were used.

XPS experiments were carried out by Dr. Jinhai Wang in CPM at Alfred University, Alfred, NY.

6.2.3.3. Confocal Raman Microscopy

Confocal Raman microscopy experiments were carried out by using a Horiba Aramis confocal Raman microscope at Center of Nano Science and Engineering, NDSU. All Raman spectra were obtained with excitation laser at λ = 532 nm at 180° configuration. The diameter of the aperture for confocal operation was 150 μm. An Olympus 50× (NA 0.75) objective lens was used for collecting both optical images and Raman spectra. This setup yielded a laser beam with diameter of 2 μm at focal plane and the theoretical depth resolution of 1.0 μm. Confocal Raman microscopy experiments were carried out on a

cross-section prepared by ultra low angle microtome (ULAM). During measurement, the sample was placed on the same stage used for ultra low angle microtome to keep the section surface at the same height. The details of ULAM are described in Chapter 3.

The work of sample preparation by ULAM and Confocal Raman measurement was performed by Dr. Jinhai Wang in CPM at NDSU.

6.3. Results

6.3.1. AM60 Mg alloy-rich primer

Figure 6-3(A) and (B) show SEM surface images of an unexposed 34% PVC AM60 Mg alloy-primer sample with magnification of 25× and 200×, respectively. It can be seen that the unexposed 34% AM60 primer is porous and has rough surface, and the AM60 particles are covered by a layer of polymer. In addition, the porous pathway extending into the film can be observed; Figure 6-3(C) and (D) show SEM images of 34% AM60 pigmented primer of 715 hours exposure with magnification of 25× and 600×, respectively. After exposure, a white-gray layer can be observed on the surface of sample in Figure 6-3(C). With the larger magnification of Figure 6-3(D), loose precipitates with a specific crystal structure can be seen both on the surface of sample and in the interstices between pigments. The morphology of the precipitate seems to be similar to those observed in exposed pure Mg-rich primer sample. [14]

The elemental composition of the oxidation products formed after exposure was studied by EDX. Figure 6-4 (a-1) shows a SEM image of 34% AM60 pigmented primer after 715 hours exposure in Prohesion chamber. Two different areas, zone #1 and zone #2, represent the regions of AM60 pigment and the precipitate, respectively. Figure 6-4 (a-2) and (a-3) are the EDX spectra obtained from zone #1 and zone #2, respectively. The data of

the corresponding elemental composition are listed in Table 6-1.

From Table 6-1, it can be seen that AM60 pigment in zone #1 contains 9.08 atom % Mg and 0.56 atom % Al, which correspond to 93.6 wt % Mg and 6.4 wt % Al if Mg and Al are normalized. This result is in agreement with the composition of AM60, which contains about 94 wt % Mg and 5.8 wt % Al. However, the composition of the precipitate in zone #2 has no Al detected, which indicating that the oxidation products derived from Mg are the major compounds in the precipitate.

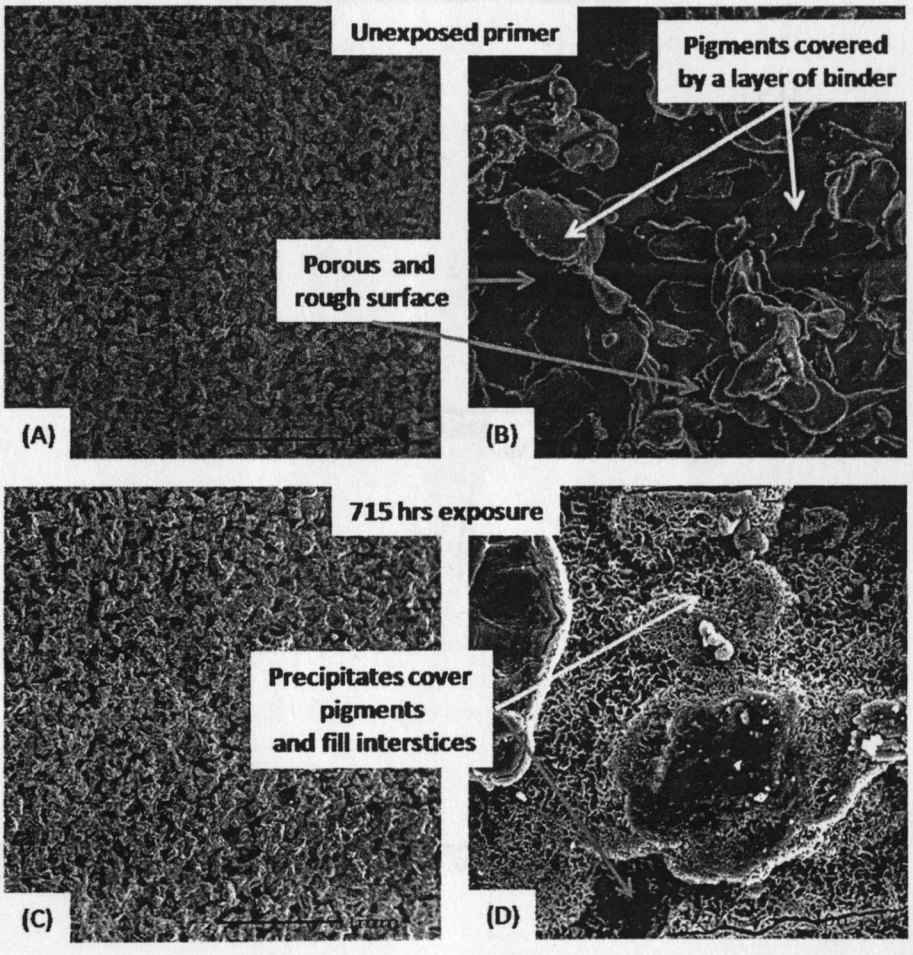

Figure 6-3. SEM surface image of AM60 pigmented primer formulated at 34% PVC: (A) unexposed sample with 25× magnification, (B) unexposed sample with 200× magnification, (C) sample of 715 hours exposure with 25× magnification, (D) sample of 715 hours exposure with 600× magnification.

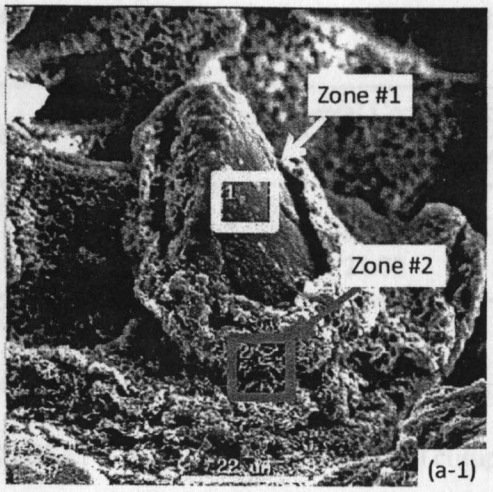

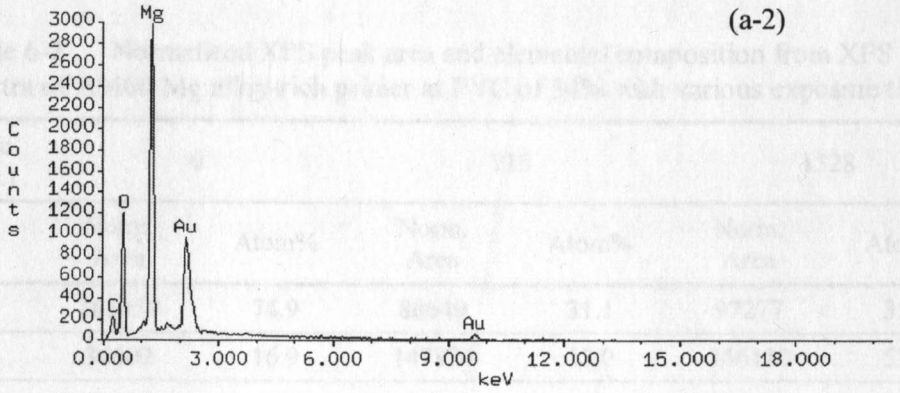

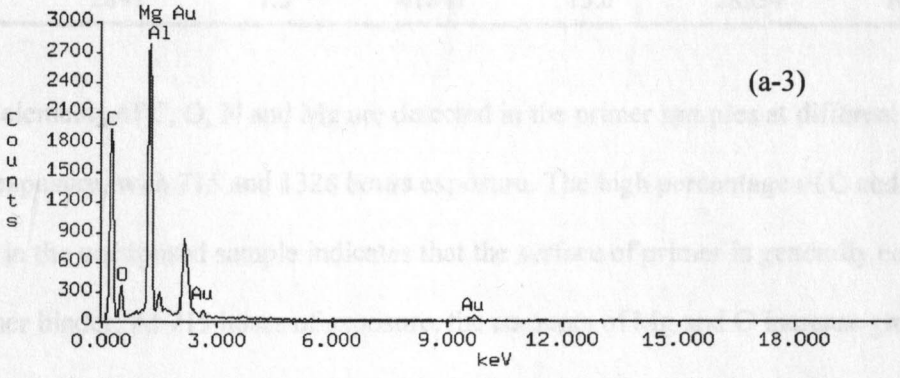

Figure 6-4. SEM image (a-1) and EDX spectra of 34% AM60 Mg alloy-rich primer after exposed in Prohesion chamber for 715 hours. The colored boxes mark the zones for EDX measurement: (a-2) spectrum from box #1(on AM60 pigment particle) and (a-3) spectrum from box #2 (on precipitate).

Table 6-1. Elemental composition as detected in EDX spectra shown in Figure 6-4.

Sample	Exposure time	Zone	Elemental Composition (atom%)					
			C	O	Mg	Al	Cl	S
AM60 34% PVC	715 hours	#1	75.54	14.42	9.08	0.56	0.21	0.19
		#2	25.16	52.16	21.00	/	0.20	1.49

The results obtained from XPS measurement have confirmed the observation of EDX. Table 6-2 lists the normalized XPS peak areas, and elemental compositions of 34% PVC AM60 primer sample at 0, 715 and 1328 hours exposure in Prohesion chamber.

Table 6-2 Normalized XPS peak area and elemental composition from XPS spectra of AM60 Mg alloy-rich primer at PVC of 34% with various exposure time.

Exposure Time (hr.)	0		715		1328	
	Norm. Area	Atom%	Norm. Area	Atom%	Norm. Area	Atom%
C	163039	74.9	86649	31.1	97277	35.5
O	36602	16.9	147894	53.0	146110	53.3
N	15014	6.9	2601	0.9	2137	0.8
Mg	2897	1.3	41841	15.0	28534	10.4

The elements of C, O, N and Mg are detected in the primer samples at different stages: without exposure, with 715 and 1328 hours exposure. The high percentage of C and O obtained in the unexposed sample indicates that the surface of primer is generally covered by polymer binder. At 715 hours of exposure, the amounts of Mg and O increase greatly; meanwhile, very little of N and no Al are detected at the surface. These results are in agreement with EDX data. The XPS results obtained from the sample of 1328 hours exposure are very similar as the ones of 715 hours. It may suggest that there was no new

type of oxidation product formed after 715 hours exposure.

High resolution XPS spectra give further information about the chemical shifts of these elements. Figure 6-5 shows the high resolution XPS spectra obtained on 34% PVC AM60 pigmented Mg alloy primer at various stages of exposure. All these XPS peaks have been deconvoluted to determine the different chemical states of each element, and the results are shown in thin lines in Figure 6-5. In the C 1s spectrum obtained on as-prepared primer surface, four different carbon states, which belong to C-C/C-H, C-O/C-N, C=O (carbonyl) and COO (carboxyl), [15] can be assigned to the polymer binder. The corresponding O 1s peak for polymer binder is observed at 532.3 and 533.2 eV, too. [16]

For the sample of 715 hours exposure in Prohesion chamber, a new peak at 290.2 eV, which is attributed to carbon in $MgCO_3$, [3, 5, 17] appears and is accompanied by the decrease of the C1s peaks originating from polymer binder. Moreover, Mg 2p peak and O 1s peak from $MgCO_3$ are also observed at 50.4 eV and 532.0 eV, respectively. [3, 7, 18]

Besides the increase of O 1s peak for carbonate, the intensity of O 1s peak at 533.2 eV increases, too. The O 1s binding energies of C=O in polymer binder, hydroxyl group and water overlap in this position. [3, 16] The degradation of the polymer has been shown by diminishing C 1s peaks of polymer binder, so polymer binder cannot contribute to the increase of the intensity of O 1s peak at 533.2 eV. Therefore, the increase in intensity of O 1s peak at 533.2 eV after exposure has to be assigned to the formation of hydroxyl and/or water. Considering that the formation of carbonate has been confirmed, hydrated/hydroxy magnesium carbonates probably formed due to the presence of water in Prohesion chamber.

In addition, the XPS results show that the features changed little when the exposure time increased from 715 to 1328 hours. The constancy in the analysis results of XPS and

EDX indicates that there was no new type of oxidation product formed after 715 hours exposure. Thus, it seems that the protection mechanisms were invariant during the exposure from 715 to 1328 hours.

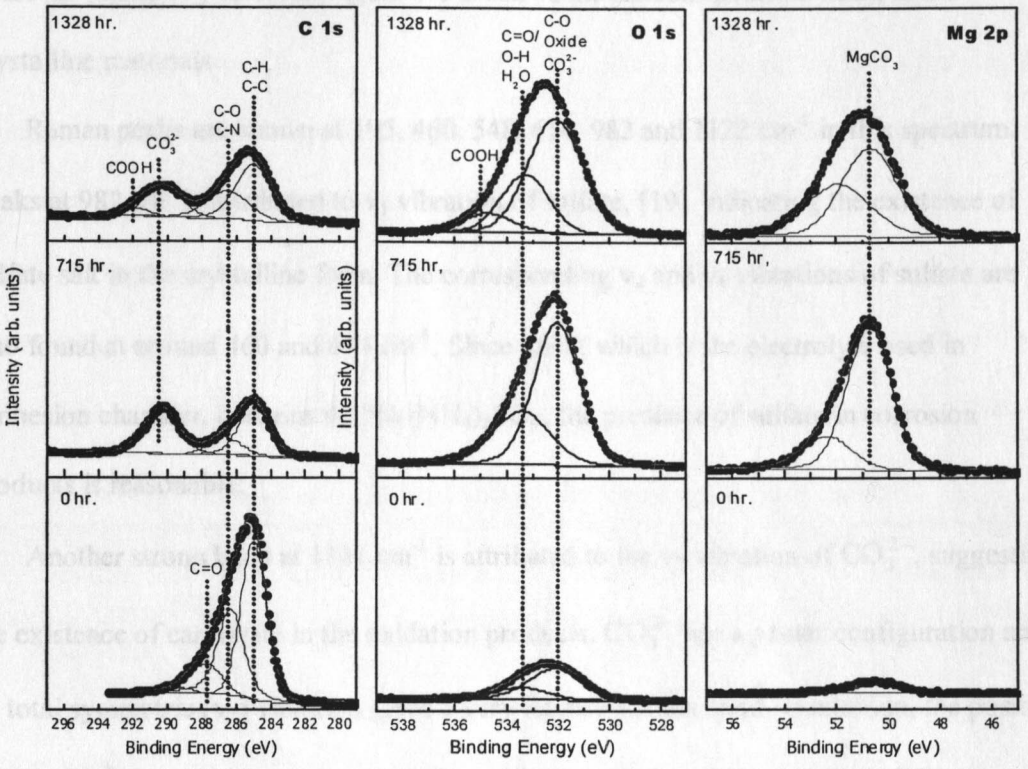

Figure 6-5. High resolution XPS spectra of AM60-Mg alloy-rich primer at PVC of 34% after exposed in Prohesion chamber for (a) 0 hr, (b) 715 hrs., (c) 1328 hrs.

Moreover, no Al-containing compound was detected in the samples of 715 and 1328 hours exposure by XPS. It implies that hydrated/hydroxyl magnesium carbonate compounds are the major oxidation products presented in the precipitates of the exposed AM60 Mg alloy-rich primer samples. The absence of Al-containing compound in the precipitates may be due to that Al, still in the metallic form, is left in Mg alloy particles.

Additional identification of oxidation products has been given by confocal Raman microscopy. Figure 6-6A shows the confocal optical image obtained from the cross-section

of 34% PVC AM60 Mg alloy-rich primer at 1328 hours exposure. In this image, bright Mg alloy particles, dark polymer matrix and blurry voids can be observed. Furthermore, some crystalline materials, which might be some oxidation products, can be seen in some blurry voids (as marked by arrows). Figure 6-6 B shows the Raman spectrum taken at the crystalline materials.

Raman peaks are shown at 195, 460, 548, 614, 982 and 1122 cm^{-1} in this spectrum. Peaks at 982 cm^{-1} is attributed to ν_1 vibration of sulfate, [19] indicating the existence of sulfate salt in the crystalline form. The corresponding ν_2 and ν_4 vibrations of sulfate are also found at around 460 and 614 cm^{-1}. Since DHS, which is the electrolyte used in Prohesion chamber, contains 0.35% $(NH_4)_2SO_4$, the presence of sulfate in corrosion products is reasonable.

Another strong band at 1121 cm^{-1} is attributed to the ν_1 vibration of CO_3^{2-}, suggesting the existence of carbonate in the oxidation products. CO_3^{2-} has a planar configuration and its total symmetric (ν_1) vibration gives a very intense Raman band. In addition, the position of this CO_3^{2-} band, varied between 1094 and 1121 cm^{-1}, is corresponding to different magnesium carbonate compounds. Table 6-3 shows some corresponding relations between the specific position of ν_1 vibration band and the probably magnesium carbonate compounds. The information shown in Table 6-3 has been reported in literatures and can be used as a fingerprint for identifying the particular type of carbonate compound. According to the data in Table 6-3, the ν_1 vibration band at 1121 cm^{-1} is assigned to hydromagnesite; moreover, the presence of the weak band at 190 cm^{-1} can confirm this assignment according to the work of Edwards et al. [20].

As a result, the crystalline material in the voids of Figure 6-6 A can be identified as a

mixture of sulfate and hydromagnesite ($MgSO_4/Mg_5(CO_3)_4(OH)_2 \cdot 4H_2O$) by confocal Raman microscopy. The sulfates might come from DHS electrolyte and the hydromagnesites could be from the oxidation of Mg alloy particles as an oxidation product.

With the analysis of SEM/EDX, XPS and confocal Raman Microscopy, the major oxidation product formed in the exposed 34% PVC AM60 primer samples is identified as hydromagnesite; and in some voids the presence of sulfate and chloride ions can be observed. However, the results from both EDX and XPS show that there is no Al containing product presented in corrosion products. The possible reason is that the high percentage Mg in AM60 particles provides cathodic protection for the low content of Al. As a result, Al may maintain its metallic form in AM60 particles without being oxidized.

Table 6-3. Raman peak assignment of various magnesium carbonates.

Name	Chemical Formula	Band position (cm^{-1})	Reference
Magnesium carbonate	$MgCO_3$	1094 1117	[20] [21]
Artinite	$Mg_2CO_3(OH)_2 \cdot 3H_2O$	1094	[20]
Lansfordite	$MgCO_3 \cdot 5H_2O$	1098	[22]
Nesquehonite	$MgCO_3 \cdot 3H_2O$	1100	[20, 22, 23]
Hydromagnesite	$Mg_5(CO_3)_4(OH)_2 \cdot 4H_2O$	1119 1121	[20] [23]

6.3.2. AZ91B Mg alloy-rich primer

Figure 6-7 (A) and (B) show the SEM images of unexposed 38%PVC AZ91B pigmented primer by 25× and 200× magnification, respectively. Similar to the unexposed

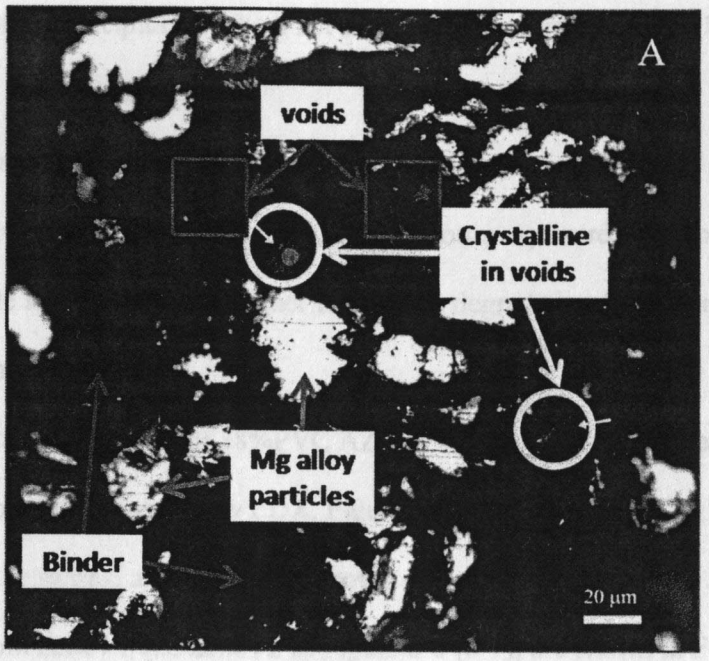

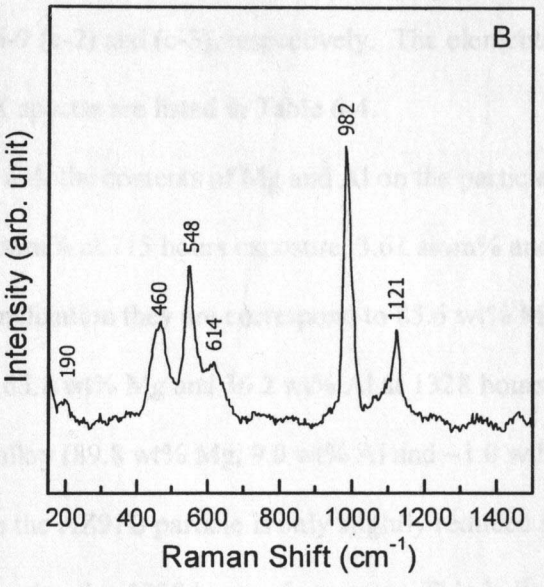

Figure 6-6. (A) Confocal optical image of low angle cross section of AM60 Mg alloy-rich primer after exposed in Prohesion chamber for 1328 hrs.; (B) Raman spectra collected in spots marked as crystalline in voids in (A).

34% AM60 primer sample, a porous and rough surface can be observed as well as a layer of polymer covering AZ91B particles. At 715 hours exposure, Figure 6-7 (C) and (D) show

the appearance of the precipitates, which not only cover the surface of AZ91B pigments but also partially fill the interstices.

The precipitates have similar structures as those found in both exposed primers based on pure Mg and AM60 pigments. However, at 1328 hours exposure, these precipitates disappeared while leaving a porous primer film with a degraded polymer binder, as shown in Fig. 6-7 (E) and (F).

The elemental composition of 38%PVC AZ91B Mg alloy-rich primer after exposure in Prohesion chamber was measured by EDX. Figure 6-8 (b-1) and Figure 6-9 (c-1) are the SEM images of the sample at 715 and 1328 hours of exposure, respectively. The EDX spectra, taken from zone #1 and zone #2 of Figure 6-8 (b-1), are shown in Figure 6-8 (b-2) and 6-8 (b-3), respectively; and the EDX spectra of zone #1 and zone #2 in Figure 6-9 (c-1) are exhibited as Figure 6-9 (c-2) and (c-3), respectively. The elemental compositions calculated from the EDX spectra are listed in Table 6-4.

According to Table 6-4, the contents of Mg and Al on the particle zone (zone #1) are 21.53 atom% and 3.63 atom% at 715 hours exposure, 3.61 atom% and 2.05 atom% at 1328 hours exposure. By normalization they are correspond to 85.6 wt% Mg and 14.4 wt% Al at 715 hours exposure and 63.8 wt% Mg and 36.2 wt% Al at 1328 hours. Compared with the composition of AZ91B alloy (89.8 wt% Mg, 9.0 wt% Al and ~1.0 wt% Zn), it can be seen that the content of Mg in the AZ91B particle is only slightly reduced after 715 hours exposure but reduced greatly after 1328 hours of exposure. This indicates that, in the beginning of exposure, Mg in the AZ91B particle is preferentially oxidized. Al in AZ91B is protected as the cathodes and left in AZ91B particle. This is also supported by the fact that Al was absent in the oxidation products after 715 hours exposure (the precipitate in

zone #2 of Figure 6-7).

In the SEM image of Figure 6-7(D), the oxidation products have a crystalline structure similar as the one observed on the exposed AM60 Mg alloy-rich primer in Figure 6-3(D). Since hydromagnesite has been identified as the major oxidation product in the case of AM60 Mg alloy, we tentatively assign these precipitates as hydromagnesite.

Table 6-4. Elemental composition of 38% AZ91B Mg alloy-rich primer after various exposure time, as detected by EDX spectra in Figures 6-7 and 6-8.

Sample	Exposure time	Zone	Elemental Composition (atom%)					
			C	O	Mg	Al	Cl	S
AZ91B 38% PVC	715 hours	1	35.72	36.33	21.53	3.63	0.78	2.02
		2	30.25	46.12	22.87	/	0.09	0.66
	1328 hours	1	78.95	13.54	3.61	2.05	/	1.86
		2	58.74	24.99	7.07	4.54	/	4.65

Different from the sample of 715 hours exposure, 4.54 atom% of Al content was observed in the oxidation products after 1328 hours exposure in zone #2 of Figure 6-9. It indicates that Al in AZ91B Mg alloy was also oxidized along with the oxidation of Mg after a longer exposure.

The oxidation of Al in AZ91B particles is also reflected by the XPS results obtained from the 38% PVC AZ91B sample after 1328 hours exposure. The normalized XPS peak area and elemental composition of the unexposed and after 1328 hours exposure AZ91B Mg alloy-rich primers are listed in Table 6-5.

As shown in Table 6-5, C, O and N are dominant in the unexposed AZ91B primer and only a little Mg is detected. Considering that XPS is a surface sensitive technique, this result clearly indicates that chemical species at the surface are mainly organic compounds, in which C, O and N are major component; meanwhile, there is a little Mg detected by XPS.

It may imply that the polymer binder covered most of AZ91B particles before the primer was exposed.

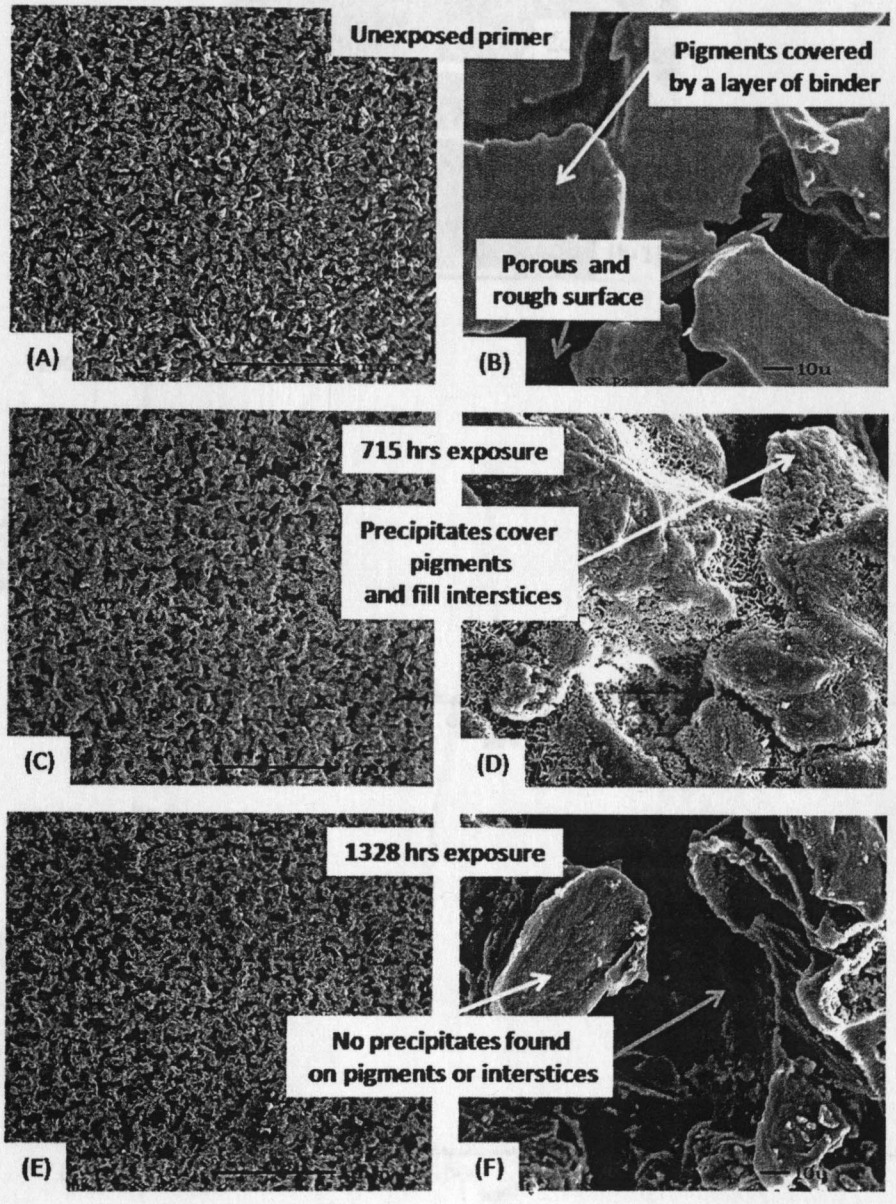

Figure 6-7. SEM surface image of AZ91B pigmented primer formulated at 38% PVC: (A) Fresh sample with 25× magnification, (B) Fresh sample with 600× magnification, (C) 715 hours exposure with 25× magnification, (D) 715 hours exposure with 600× magnification, (E) 1328 hours exposure with 25× magnification and (F) 1328 hours exposure with 600× magnification.

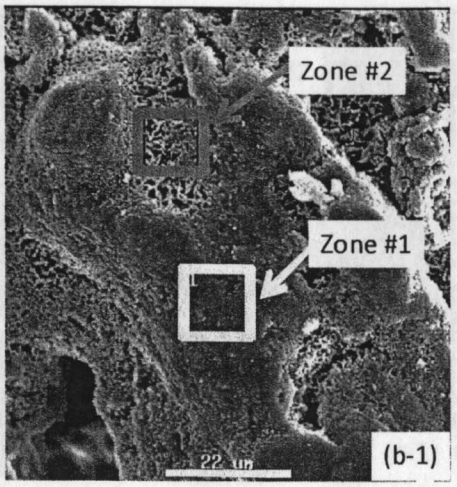

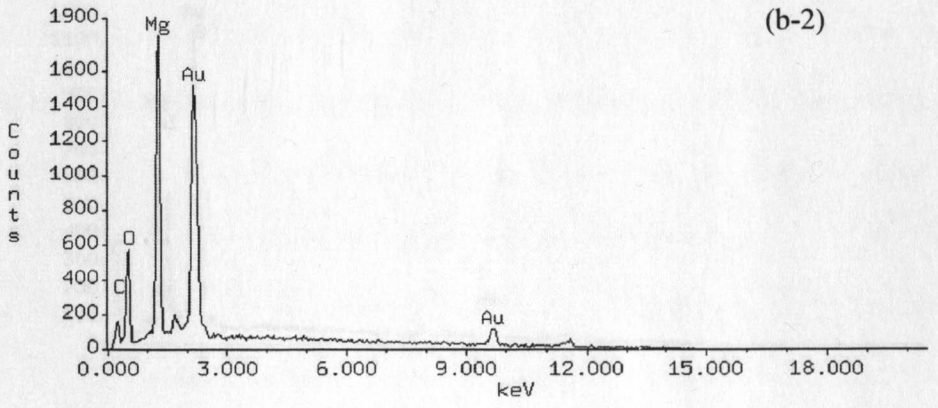

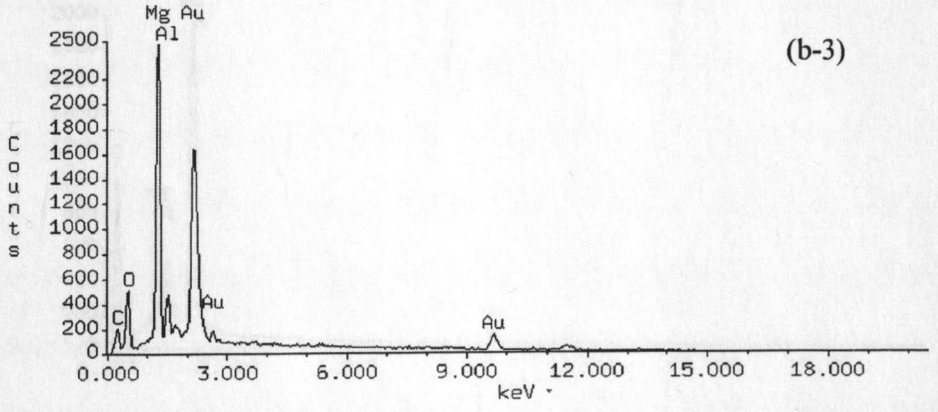

Figure 6-8. EDX spectra of 38% AZ91B Mg alloy-rich primer after exposed in Prohesion chamber for 715 hours. (b-2) spectrum was obtained from box #1 (on AZ91B pigment particle) and (b-3) spectrum was obtained from box #2 (on precipitate).

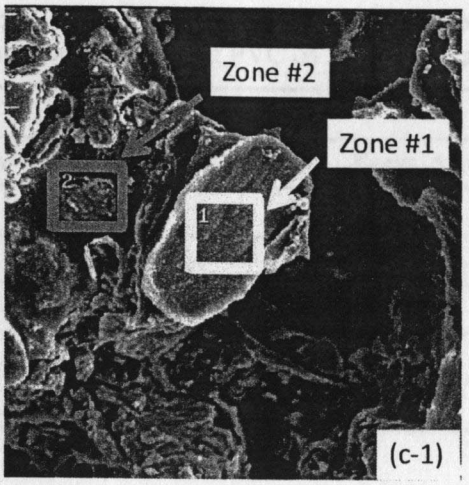

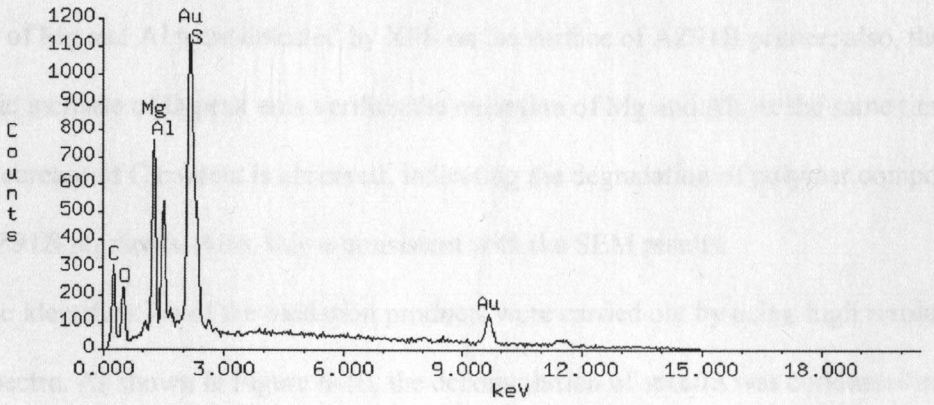

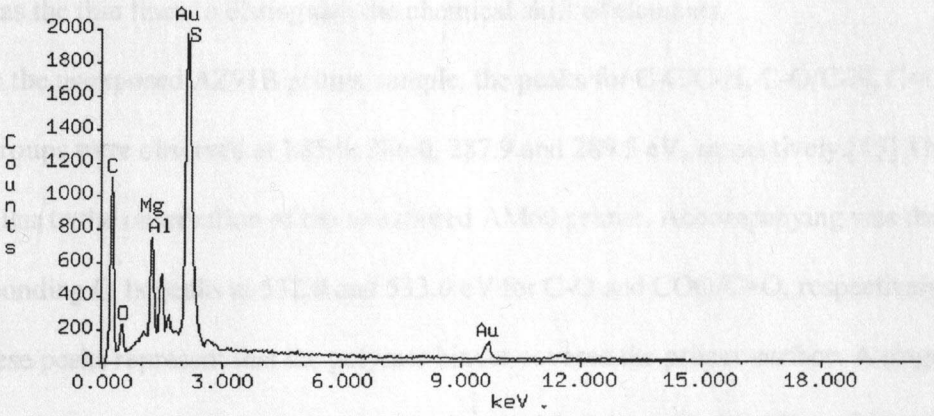

Figure 6-9. EDX spectra of 38% AZ91B Mg alloy-rich primer after exposed in Prohesion chamber for 1328 hours. (b-2) spectrum was obtained from box #1 (on AZ91B pigment particle) and (b-3) spectrum was obtained from box #2 (off pigment particle).

Table 6-5. Normalized XPS peak area and elemental composition from XPS spectra of AZ91 Mg alloy-rich primer at PVC of 38% with various exposure time.

Exposure Time (hr.)	0		1328	
	Norm. Area	Atom%	Norm. Area	Atom%
C	135596	77.9	57119	24.2
O	19738	11.4	126000	53.3
N	16668	9.6	2564	1.1
Mg	1839	1.1	26126	11.0
Al	/	/	24628	10.4

However, after 1328 hours exposure, the oxidation products containing more than 10 atom% of Mg and Al were detected by XPS on the surface of AZ91B primer; also, the dramatic increase of O peak area verifies the oxidation of Mg and Al. At the same time, a sharp decrease of C content is observed, indicating the degradation of polymer compounds near AZ91B pigments. Also, this is consistent with the SEM results.

The identification of the oxidation products were carried out by using high resolution XPS spectra. As shown in Figure 6-10, the deconvolution of spectra was conducted and shown as the thin lines to distinguish the chemical shift of elements.

On the unexposed AZ91B primer sample, the peaks for C-C/C-H, C-O/C-N, C=O and COO groups were observed at 285.0, 286.0, 287.9 and 289.5 eV, respectively.[15] They are similar to the observation of the unexposed AM60 primer. Accompanying was the corresponding O 1s peaks at 532.0 and 533.0 eV for C-O and COO/C=O, respectively.[15, 16] These peaks represent that the polymer binder covered the primer surface. A single small Mg 2p peak at 50.8 eV can be assigned to the MgO layer [5, 16, 17] on the surface of the AZ91B particles.

The exposure of AZ91B Mg alloy-rich primer in Prohesion chamber resulted in the

significant changes in XPS spectra. As shown in Figure 6-10, after 1328 hours exposure, an Al 2p peak appears at 74.9 eV, which actually consists of two components at 75.0 eV and 76.3 eV, as revealed by deconvolution. The peak at 75.0 eV is attributed to Al_2O_3[24, 25] and the peak at 76.3 eV is attributed to AlOOH. [26] Meanwhile, Mg 2p peak at 50.8 eV is assigned to MgO and its intensity significantly increases. The assignment of a new Mg 2p peak at 52.0 eV is not clear yet, but it possibly belongs to an oxidized Mg compound due to its high binding energy. Along with the appearance of those typical peaks for oxidized Mg and Al compounds, corresponding O 1s for their oxide and hydroxide are also observed at 532.0 eV and 533.0 eV, respectively.

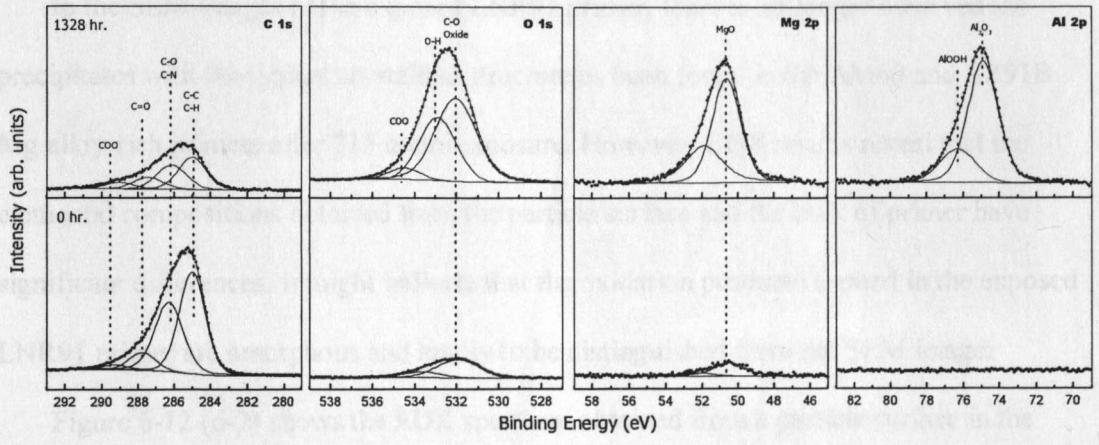

Figure 6-10. High resolution XPS spectra obtained from the surface AZ91B Mg alloy-rich primer, 38% PVC after (a) 0 hour; (b) 1328 hours exposure in Prohesion chamber.

As a summary, there is probably two stages in the formation of the oxidation products of the 38% AZ91B Mg alloy-rich primer being exposed in Prohesion chamber: after 715 hours exposure, hydromagnesite was the major oxidation product; after 1328 hours, Al_2O_3, AlOOH and MgO were formed as the final oxidation products.

6.3.3. LNR91 Mg alloy-rich primer

In Figure 6-11 (A) and (B) are shown the SEM images of the unexposed 44% PVC LNR91 Mg alloy-rich primer with 25× and 600× magnification, respectively. It can be seen that 44% PVC LNR91 primer is not as porous as the other two Mg alloy-rich primer samples. Its surface is rough due to the large size of the LNR91 particles.

Figure 6-11 (C) and (D) show the SEM images of 44% LNR91 Mg alloy-rich primer after 467 hours exposure with 25× and 600× magnification. It can be seen that the surface of the exposed LNR91 primer is very rough in comparison to the unexposed one. In addition, some LNR91 particles are observed to lose the adhesion with polymer binder.

In the SEM images of the exposed LNR91 primer, there is no longer observed the precipitates with the typical crystalline structure as been found in the AM60 and AZ91B Mg alloy-rich primers after 715 hours exposure. However, EDX results reveal that the elemental compositions obtained from the particle surface and the bulk of primer have significant differences. It might indicate that the oxidation products formed in the exposed LNR91 primer are amorphous and hardly to be distinguished from the SEM image.

Figure 6-12 (d-2) shows the EDX spectrum obtained from a particle surface in the LNR91 primer after 467 hours exposure (marked as zone #1 with a box in the SEM image of Figure 6-11). The corresponding elemental composition is listed in Table 6-6.

In Table 6-6, it can be seen that the contents of Mg and Al in the LNR91 primer sample after 467 hours exposure are 4.15 atom% and 23.6 atom%, respectively. It equals to a composition of 13.5 wt% Mg and 86.5 wt % Al if only Mg and Al are normalized. But, the global chemical composition of the unexposed LNR91 pigment is 50 wt% of Mg and 50 wt% of Al. Therefore, the pigment surface in the exposed LNR91 primer possibly has

been covered by Al-rich oxidation products.

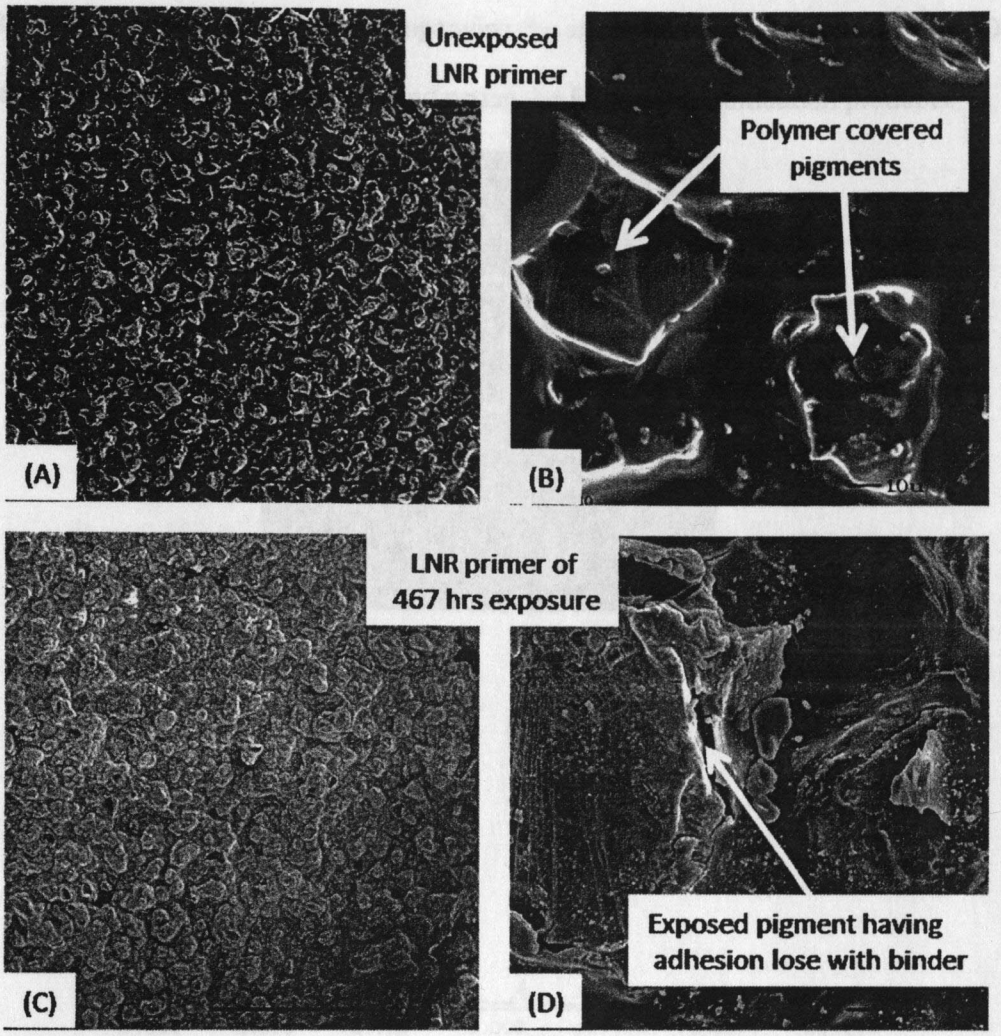

Figure 6-11. SEM surface images of 44% PVC LNR91 pigmented primer: (A) unexposed sample with 25× magnification, (B) unexposed sample with 600× magnification, (C) sample of 467 hrs exposure with 25× magnification and (D) sample of 467 hrs exposure with 600× magnifications.

In Table 6-7, the elemental compositions of the unexposed and after 467 hours exposure LNR91 Mg alloy-rich primers via XPS analysis are listed. Similar to the unexposed AM60 and AZ91B Mg alloy-rich primers, the surface of unexposed LNR91 primer seems to be dominated by polymer binder, since neither Mg nor Al was detected by

XPS. After 467 hours exposure in Prohesion chamber, Al was observed on the surface of LNR91 primer sample by XPS. Accompanying the appearance of Al, the peak area of O increased by more than 100%, which indicating the formation of oxidation products.

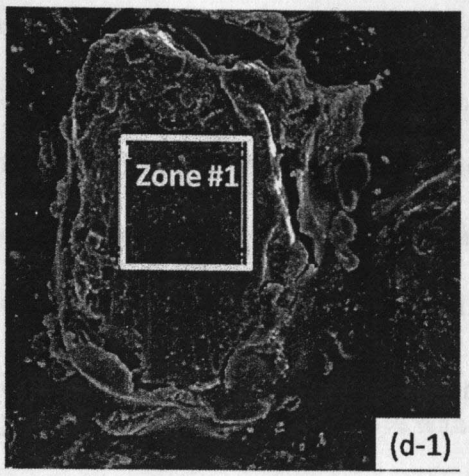

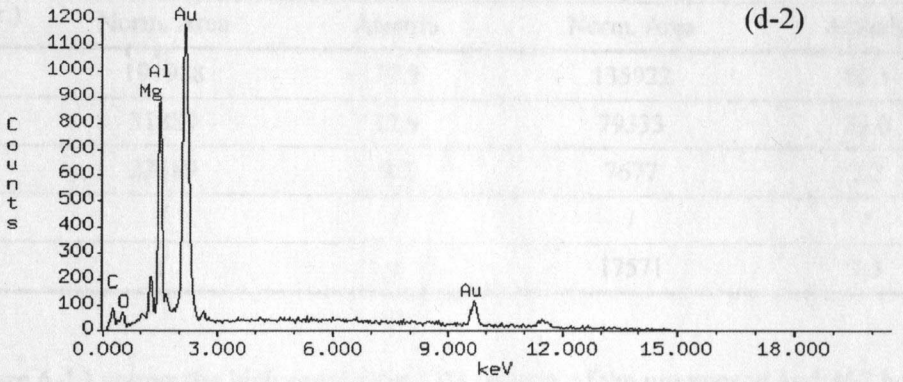

Figure 6-12. (d-1) SEM image of 44% LNR91 Mg alloy-rich primer after 467 hours exposure, and (d-2) EDX spectrum of zone #1 marked by box.

Table 6-6. Elemental composition by EDX of pigment particle surface of 44% LNR91Mg alloy-rich primer after exposed in Prohesion chamber for 467 hours.

Sample	Exposure time	Zone	Elemental Composition (atom%)					
			C	O	Mg	Al	Cl	S
LNR91 44% PVC	467 hours	1	55.69	16.70	4.15	23.46	/	/

However, dissimilar as EDX, XPS did not detect Mg in the LNR91 primer after 467 hours exposure, as shown in Table 6-7. The possible reason is that the detection depth of EDX is much larger than that of XPS. The results from XPS reflect the chemical composition of the outermost layer of the sample surface; but the EDX spectrum probably includes the signals from the area beneath the surface. Therefore, if the outermost layer mainly consists of Al oxidation products, and Mg oxidation products or even unexposed LNR 91 particles are presented under the surface, the results obtained from EDX and XPS can be different, low percentage Mg can be detected by EDX but not XPS.

Table 6-7. Normalized XPS peak area and elemental composition from XPS spectra of LNR91 Mg alloy-rich primer at PVC of 44% with various exposure time.

Exposure Time (hr.)	0		437	
	Norm. Area	Atom%	Norm. Area	Atom%
C	191988	77.9	135922	56.5
O	31889	12.9	79333	33.0
N	22589	9.2	7677	3.2
Mg	/	/	/	/
Al	/	/	17571	7.3

Figure 6-13 shows the high resolution XPS spectra of the unexposed and 467 hours exposed 44% PVC LNR91 primers. Before exposure, the surface consists of polymer binder, as indicated by the C1s peak that consists of components from C-C/C-H at 285.0 eV, C-O/C-N at 286 eV, C=O at 288.0 and COO group at 289.3 eV[15] as well as the O1s peak consists of components from C-O at 532.0 and COO at 534.5 eV[15, 16]. After exposure, an Al 2p peak appears at 75.1 eV. It is composed by two peaks, the one at 75.2 eV is assigned to Al_2O_3[24, 25] and the one at 76.6 eV is assigned to AlOOH. [26] The corresponding O 1s peak can be observed arising at 532.0 eV for oxide and 533.1 eV for

OH. Thus, Al_2O_3 and AlOOH are identified in the oxidation products formed during the exposure of 44% LNR91 pigmented primer in Prohesion chamber.

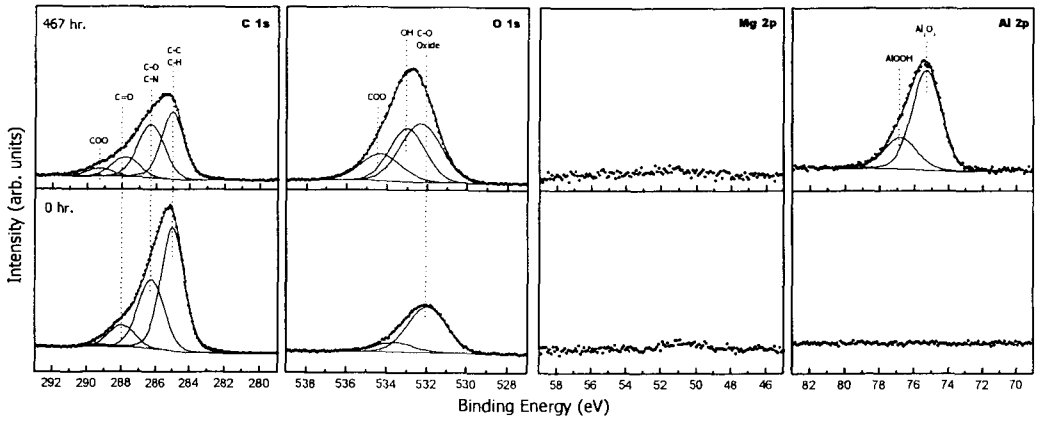

Figure 6-13. High resolution XPS spectra for LNR Mg alloy-rich primer at PVC of 44%. (a) unexposed in Prohesion chamber; (b) after exposed in Prohesion chamber for 467 hrs.

6.4. Discussion

6.4.1. Features of oxidation products

By using XPS, EDX and confocal Raman microscopy, the oxidation products of various Mg alloy-rich primers after being exposed in Prohesion chamber have been identified and the results are listed in Table 6-8.

The identification of the oxidation products can provide necessary information for comprehending the probable reactions occurred during the exposure of the Mg alloy-rich primers coated panels in Prohesion chamber; furthermore, the probable mechanisms by which the Mg alloy primers provide corrosion protection for Al alloy substrate, e.g. cathodic protection and barrier protection, can be understood. However, in order to analyze these data properly, some specific features of the oxidation products of the exposed Mg alloy rich primers have to be mentioned.

Table 6-8. Oxidation products of Mg alloy-rich primer after exposed in Prohesion chamber for various time.

Mg alloy	Exposed time (hrs)	Major oxidation products
AM60	715	$Mg_5(CO_3)_4(OH)_2 \cdot 4H_2O$ (hydromagensite)
	1328	$Mg_5(CO_3)_4(OH)_2 \cdot 4H_2O$ (hydromagensite)
AZ91B	715	$Mg_5(CO_3)_4(OH)_2 \cdot 4H_2O$ (hydromagensite)
	1328	MgO, Al_2O_3, AlOOH
LNR91	467	Al_2O_3, AlOOH

First, all the oxidation products mainly came from the oxidation reactions of Mg alloy pigments. Samples used for oxidation products analysis were cut from the inscribed area; also, by visual inspection, it has been found that Al alloy substrates were intact. It can be deduced that the oxidation products hardly derived from the corrosion of Al alloy substrate. Therefore, the Al-containing oxidation products, which were detected in the samples of AZ91B and LNR91 Mg alloy-rich primers, mainly came from the oxidation of Al in the Mg alloy particles.

Second, the observed oxidation products actually are final results of a series of reaction processes, in which various chemical and/or electrochemical reactions and ionic transport are probably involved. There might be some intermediate products, but they were consumed in the subsequent reactions. In this work, only *ex-situ* analysis approaches are used, therefore the possible intermediate products could not be detected.

Third, only those oxidation products that remain on the surfaces of primers after exposure can be determined. In Prohesion chamber, each cycle includes electrolyte spraying and condensing on the testing panels, thus, the soluble oxidation products could probably be dissolved and washed away. Only those insoluble oxidation products were left in primers and later detected and identified by different analysis methods. This

presumption is supported by the facts from many literature results that all the identified oxidation products are insoluble.

Fourth, all the samples used for exposure and surface analysis were bare primers only, there was no topcoat used to cover them. As we known, Mg alloy pigmented primers are porous due to the high content of Mg alloy particles. Thus, electrolyte can easily penetrate the voids presented in the primer to contact Mg alloy particles directly. However, in a real-life use, metal-rich coating systems are always coated with an exterior durable topcoat, which can provide excellent barrier protection to keep the primer from direct exposure to the aggressive electrolyte. Therefore, for a complete anticorrosion organic coating system consisted of a metal-rich primer and a topcoat, the reactions initiated by the penetration of electrolyte to form various oxidation products probably still occur but at a much slower rate in comparison to the bare primer system without a topcoat. To test the bare primers without a topcoat in Prohesion chamber can compress the time frame of Mg alloy particles oxidation, but the much more aggressive environment may cause some reactions that might not take place in real life exposure.

6.4.2. Influencing factors on the formation of oxidation products

From Table 6-8, it can be seen that there are four major oxidation products: $Mg_5(CO_3)_4(OH)_2 \cdot 4H_2O$, MgO, Al_2O_3 and AlOOH. For the samples of AM60 pigmented primers at 715 and 1328 hours exposure as well as AZ91B pigmented primer at 715 hour exposure, hydromagensite is the major compound detected on the sample surfaces; for the sample of AZ91B pigmented primer at 1328 hour exposure, hydromaensite disappeared, MgO, Al_2O_3 and AlOOH were left as the insoluble corrosion products; for the sample of LNR91 primer at 467 hour exposure, Al_2O_3 and AlOOH are the major compounds.

As we have mentioned above, all the three Mg alloy pigments, AM60, AZ91B and LNR91, contain Al as the secondary element at 4.5 wt%, 9 wt% and 50 wt%, respectively. Although the three Mg alloy pigments have similar elements, i.e. Mg and Al, different oxidation products were detected on these exposed Mg alloy-rich primers. It implies that different reaction processes have taken place in the three Mg alloy-rich primers at different exposure time. Thus, based on the exposure conditions, four factors are considered to probably influence the electrochemical/chemical reactions and the oxidation products during Prohesion exposure: potential difference between the galvanic coupled metals, pH of local environment, species present and the equilibriums between ions and their insoluble compounds.

6.4.2.1. Potential difference

In Mg alloy-rich primer system, two or three metals can be involved in galvanic coupling: Mg, Al and Zn. Mg and Zn mainly exist in Mg alloy particles, Al can be found in Mg alloy particles as well as Al alloy substrate. Since Mg is the most electrochemically active metal, it is preferentially oxidized when it couples with others. [27] Thus, the anodic reaction is

$$Mg \rightarrow Mg^{2+} + 2e$$

And the cathodic reactions are

$$2H^{+} + 2e \rightarrow H_2(g) \text{ or } O_2 + 2H_2O + 4e \rightarrow 4OH^{-}$$

$$e_{Mg/Mg^{2+}} = -2.372 + 0.0295 \log[Mg^{2+}] \qquad (6.1)$$

$$pH = -\frac{1}{2}(\log K + \log[Mg^{2+}]) \qquad (6.2)$$

It can be seen that $e_{Mg/Mg^{2+}}$ will increase with the increase of $[Mg^{2+}]$. However, in the

environment of Prohesion chamber, the continuous electrolyte spray will remove the Mg^{2+} ions from the primer system. Therefore, as long as Mg has good electrical conductivity with the other coupling metals, the anodic reaction of Mg will persist. On the other hand, pH of the local environment can increase with the accumulation of $[Mg^{2+}]$ in the microenvironment near the cathodic sites.

6.4.2.2. pH of local environment

In Prohesion chamber, dilute Harrison's solution (DHS) is used as electrolyte. DHS contains 0.35wt% $(NH_4)_2SO_4$ and 0.05wt% NaCl and its pH is about 5.6. With the oxidization of Mg, pH of the solution near the cathodic sites will increase. As a result, different chemical reactions can occur. In Table 6-9, all the possible chemical reactions as well as the probably presented ions and insoluble oxidation products at different pH ranges are listed.

It can be seen that Mg is preferentially dissolved when pH is below 10.5; $Mg(OH)_2$ precipitates can be formed at higher pH. Al and Al_2O_3 are stable when pH is below 8.6 and start to dissolve when pH is higher than 8.6. Moreover, most oxidation products are soluble and probably present in ionic forms.

6.4.2.3. Species present

When the panels coated with Mg alloy pigmented primers are exposed in Prohesion chamber, some species presented in environment can affect the oxidation processes of Mg alloy particles. For example, DHS solution contains Cl^- ions, which have the significant influence on Mg or Mg alloys: Cl^- ions can convert the slightly soluble $Mg(OH)_2$ or $MgCO_3$ to more soluble $MgCl_2$. As a result, the presence of Cl^- ions can easily breakdown the protective films of $Mg(OH)_2$ and/or $MgCO_3$ and enhance the solubility of Mg

compounds. [17] [28] [29] The hindrance of Cl^- ions to the precipitation of Mg oxidization products may explain the previous observation that the simple $Mg(OH)_2$ or $MgCO_3$ were absent on the surfaces of the exposed three Mg alloy pigmented primers.

Table 6-9. The possible chemical reactions occurred in Mg alloy primers and the presented ions at various pH ranges.

pH range	Chemical reactions	Ions present	Insoluble compounds
5.6 to 7	$MgO + 2H^+ = Mg^{2+} + H_2O$ $Mg + 2H^+ = Mg^{2+} + H_2(g)$	Mg^{2+}, H^+, NH_4^+, SO_4^{2+}, Cl^-, Na+	Al , Al_2O_3
7 to 8.6	$Mg + 2H_2O = Mg^{2+} + 2OH^- + H_2(g)$ $CO_2 + OH^- = HCO_3^-$ $HCO_3^- + OH^- = CO_3^{2-} + H_2O$ $Mg^{2+} + CO_3^{2-} = MgCO_3$	Mg^{2+}, OH^-, NH_4^+, SO_4^{2+}, Cl^-, Na^+, CO_3^{2-} and HCO_3^-,	Al , Al_2O_3
8.6 to 10.5	$Mg + 2H_2O = Mg^{2+} + 2OH^- + H_2(g)$ $CO_2 + OH^- = HCO_3^-$ $HCO_3^- + OH^- = CO_3^{2-} + H_2O$ $Mg^{2+} + CO_3^{2-} = Mg\,CO_3$ $Al_2O_3 + 2OH^- = 2AlO_2^- + H_2O$ $Al_2O_3 + 2H_2O + 2OH^- = 2AlO_2^- + 3H_2$ (g)	Mg^{2+}, OH^-, NH_4^+, SO_4^{2+}, Cl^-, Na^+, CO_3^{2-}, HCO_3^-, AlO_2^-	
> 10.5	$Mg^{2+} + 2OH^- = Mg(OH)_2$ (s) $CO_2 + OH^- = HCO_3^-$ $HCO_3^- + OH^- = CO_3^{2-} + H_2O$ $Al_2O_3 + 2OH^- = 2AlO_2^- + H_2O$ $Al_2O_3 + 2H_2O + 2OH^- = 2AlO_2^- + 3H_2$ (g)	Mg^{2+}, OH^-, NH_4^+, SO_4^{2+}, Cl^-, Na^+, CO_3^{2-}, HCO_3^-, AlO_2^-	$Mg(OH)_2$

On the other hand, the presence of carbon dioxide (CO_2) in environment seems to benefit the formation of the protective films on the surface of Mg or Mg alloy particles. There is about 390 ppm CO_2 in atmosphere,[30] which can be dissolved in water in the forms of HCO_3^- and CO_3^{2-}.[28]

$$CO_2\,(g) + H_2O \leftrightarrow H_2CO_3\,(aq)$$

$$H_2CO_3\,(aq) \leftrightarrow HCO_3^- + H^+$$

$$HCO_3^- \leftrightarrow CO_3^{2-} + H^+$$

Neutral or alkali conditions will promote the dissolution of CO_2 in solution. HCO_3^- and CO_3^{2-} can react with magnesium hydroxides to form the less soluble magnesium hydrate or hydroxyl carbonates. For example, $Mg_4(CO_3)_3(OH)_2 \cdot 3\,H_2O$, $Mg_4(CO_3)_3(OH)_2 \cdot 3\,H_2O$, $Mg_6(CO_3)_5(OH)_2 \cdot 9\,H_2O$, $MgCO_3 \cdot 3\,H_2O$ (nequehonite) and $MgCO_3 \cdot 5\,H_2O$ (lansfordite) have been reported as the oxidation products for Mg in natural environment [31]. In the corrosion products of the exposed Mg alloy pigmented primers, e.g. AM60 primers at 715 and 1328 hours exposure, AZ91B primer at 715 hours exposure, $Mg_5(CO_3)_4(OH)_2 \cdot 4\,H_2O$ (hydromagensite) had been identified. It suggests that the presence of CO_2 has influenced the formation of oxidation products of Mg alloy pigments.

In addition, the alternatives of temperature and humidity can also affect the final corrosion products. In Prohesion chamber, there are two alternative cycles: one-hour wet cycle, in which temperature is set at 25 °C and the humidity is very high due to the DHS spray; one-hour dry cycle, in which the temperature is maintained at 35 °C and there is no DHS spray. Therefore, many soluble species, such as $MgCl_2$, $(NH_4)_2SO_4$, $AlCl_3$, can be washed away during the wet cycle, and the insoluble precipitates, e.g. $Mg(OH)_2$, $Al(OH)_3$ and $MgCO_3$, can remain; during the dry cycle, the insoluble precipitates can lose water to form MgO, Al_2O_3, AlOOH or $Mg_5(CO_3)_4(OH)_2 \cdot 5H_2O$, which had been identified as the final corrosion products on the surface of the exposed Mg alloy pigmented primers.

6.4.2.4. Equilibriums present

When the Mg alloy particles in Mg alloy-rich primers underwent oxidation in the environment of Prohesion chamber, several equilibriums probably were present between the soluble ions and the insoluble compounds. In Table 6-10 are listed some important equilibrium reactions and the corresponding equilibrium constants.

Table 6-10. Equilibrium reactions and their equilibrium constants.

No. of Reaction	Reaction	Constant
1	$Mg(OH)_2$ (s) $\leftrightarrow Mg^{2+} + 2OH^-$	$K_{sp} = 5.6 \times 10^{-12}$
2	$Al(OH)_3$ (s) $\leftrightarrow Al^{3+} + 3OH^-$	$K_{sp} = 1.1 \times 10^{-33}$
3	$Al(OH)_3$ (s) $+ OH^- \leftrightarrow AlO_2^- + 2H_2O$	$K_{sp} = 2.98 \times 10^{-1}$
4	CO_2 (g) $+ H_2O \leftrightarrow H_2CO_3$ (aq)	$K_H^* = 29.4$(atm/M)
5	H_2CO_3 (aq) $\leftrightarrow HCO_3^- + H^+$	$K_{a1} = 4.5 \times 10^{-7}$
6	$HCO_3^- \leftrightarrow CO_3^{2-} + H^+$	$K_{a2} = 4.7 \times 10^{-11}$
7	$MgCO_3$ (s) $\leftrightarrow Mg^{2+} + CO_3^{2-}$	$K_{sp} = 3.16 \times 10^{-8}$
8	$MgCO_3$ (s) $+ 2H^+ \leftrightarrow Mg^{2+} + CO_2$ (g) $+ H_2O$	$K_{sp} = 4.39 \times 10^{10}$

K_H^* is the Henry's constant and has the form $K_H^* = P_{CO2}/[H_2CO_3(aq)]$

Reaction (8) is obtained by reaction (7) minus the summation of reaction (4) to (6) as follows:

	$MgCO_3$ (s)	$\leftrightarrow$	$Mg^{2+} + CO_3^{2-}$	$K_{sp} = 3.16 \times 10^{-8}$
-	CO_2 (g) $+ H_2O$	$\leftrightarrow$	H_2CO_3 (aq)	$K_H^* = 29.4$(atm/M)
-	H_2CO_3 (aq)	$\leftrightarrow$	$HCO_3^- + H^+$	$K_{a1} = 4.5 \times 10^{-7}$
-	HCO_3^-	$\leftrightarrow$	$CO_3^{2-} + H^+$	$K_{a2} = 4.7 \times 10^{-11}$
	$MgCO_3$ (s) $+ 2H^+$	$\leftrightarrow$	$Mg^{2+} + CO_2$ (g) $+ H_2O$	$K_{sp} = 4.39 \times 10^{10}$

Thus, its $K_{sp} = (3.16 \times 10^{-8}) /[(1/29.4) \times (4.5 \times 10^{-7}) \times (4.7 \times 10^{-11})] = 4.39 \times 10^{10}$

From the data listed in Table 6-10, it can be seen that the equilibriums are significantly affected by pH. The variance of pH determines the existence forms of Mg and Al, e.g. ions, insoluble compounds or soluble species. Therefore, based on the information supplied by Table 6-10, the relationship between the concentrations of ions (Mg^{2+}, AlO_2^-, Al^{3+}) and pH are calculated as follows:

$$Mg(OH)_2 (s) \leftrightarrow Mg^{2+} + 2OH^-, \quad K_{sp} = [Mg^{2+}][OH^-]^2 = 5.6 \times 10^{-12}$$

$$\text{Log}[Mg^{2+}] = 16.75 - 2 \times \text{pH} \qquad (6.3)$$

$$Al(OH)_3\ (s) \leftrightarrow Al^{3+} + 3OH^-,\ K_{sp} = [Al^{3+}][OH^-]^3 = 1.1 \times 10^{-33}$$

$$\text{Log}[Al^{3+}] = 9.04 - 3 \times \text{pH} \qquad (6.4)$$

$$Al(OH)_3\ (s) + OH^- \leftrightarrow AlO_2^- + 2H_2O,\ K_{sp} = [AlO_2^-]/[OH^-] = 2.98 \times 10^{-1}$$

$$\text{Log}[AlO_2^-] = \text{pH} - 14.53 \qquad (6.5)$$

$$MgCO_3\ (s) + 2H^+ \leftrightarrow Mg^{2+} + CO_2\ (g) + H_2O,\ K_{sp} = 4.39 \times 10^{10}$$

$$\text{Log}[Mg^{2+}] = 14.01 - 2 \times \text{pH} \qquad (6.6)$$

6.4.3. Probable local environment for forming the identified oxidation products

According to the discussions above, it seems that the local pH is a key parameter related to the concentrations of various ions, the formation of insoluble compounds, the stability of Al_2O_3 and solubility of CO_2. Therefore, it will be very useful to extrapolate the probable local environment where the identified oxidation products of various Mg alloy rich primers were formed.

Based on equation (6.3) to equation (6.6), the log([ion]) as a function of pH is plotted in Figure 6-14. The four solid lines represent the borders between the insoluble compound and its corresponding ion of $Mg(OH)_2$ / Mg^{2+}, $Al(OH)_3$ / Al^{3+}, $Al(OH)_3$ / AlO_2^-, $MgCO_3$ / Mg^{2+}. On the left of these lines, the insoluble compounds are the stable species; on the right of the lines, the soluble ions are stable.

In Figure 6-14, a pH region from 5.6 to 11 is marked by a dash and a short dot vertical lines, which is considered as the "possible pH region of Prohesion environment". In Prohesion chamber, DHS is the major electrolyte with pH of 5.6, which presents the lowest pH condition. On the other hand, the highest pH of environment is depended on the oxidation of Mg. In our lab, the experimental results of immersing pure Mg-rich primer in

different solutions (e.g. DHS, 3 wt% NaCl solution) showed that the final pH of the solutions were lower than 9.6. In addition, the work of Pathak et.al also suggested that pH was stable at the value of 9.75 when pure Mg particles were added into carbonic acid solution. [28] Thus, pH of 11 can be regarded as the highest pH value during Prohesion exposure.

In Figure 6-14, the two horizontal dot lines stand for the boundary of possible ion concentration: below the lower dot line, the concentration of a certain species is lower than 1 ppm and can be considered as undetectable; above the upper dot line, the ion concentration needs to be larger than 5M, which is impossible for $[Mg^{2+}]$, $[Al^{3+}]$,$[AlO_2^-]$ to achieve.

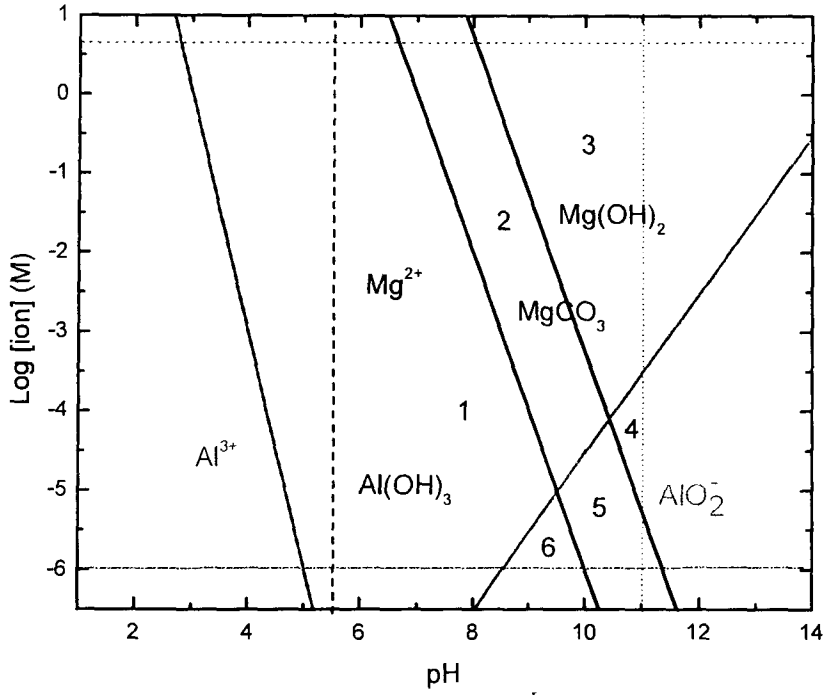

Figure 6-14. Phase diagram of system of Mg alloy oxidation in Prohesion exposure of Mg alloy primer.

In Figure 6-14, six regions can be distinguished: region 1 is where $Al(OH)_3$ is stable

and Al is passivated; region 2 is where $Al(OH)_3$ and $MgCO_3$ can precipitate; region 3 is where $Al(OH)_3$, $MgCO_3$ and $Mg(OH)_2$ can precipitate together; region 4 is where $MgCO_3$ and $Mg(OH)_2$ can co-precipitate; region 5 is where only $MgCO_3$ precipitation can be found; and region 6 is where the oxidation products of Mg and Al are soluble.

For AM60 primer, the identified oxidation products were hydromagensite alone, which indicates that the probable environment was region 3 and 4; for AZ91B primer, the oxidation products changed from hydromagensite to a mixture of MgO, Al_2O_3, AlOOH, which implies the environment changed from region 4 to region 2 and 3; for LNR91 primer, the only Al_2O_3 and AlOOH present suggests the environment was region 1.

Again, the identification of the oxidation products can help us to extrapolate the probable environment which influenced the equilibriums.

6.4.4. Impact of Al content of Mg alloy to oxidation products

As mentioned above, all the Mg alloy rich primers were formulated by using a same epoxy-amide system as polymer binder. Also, the samples were exposed to a same accelerated weathering condition. However, the oxidation products of each Mg alloy rich primer were different from others: AM60 contains 4.5 wt% Al, its oxidation product is mainly hydromagnesite; AZ91B has 9 wt% Al, after 1328 hours exposure, Al_2O_3 and AlOOH were formed besides MgO in AZ91B primer; for LNR91, which constitutes of 50 wt% Al, the oxidation products are mainly Al containing products, e.g. Al_2O_3 and AlOOH. It has suggested that the formation of different oxidation products attributed to the different pH of local environment. But, what caused the different pH of the local environment?

One possible reason is the different Al content of Mg alloy particles. When Mg alloy rich primer is exposed in Prohesion chamber, Mg in Mg alloy particles starts to oxidize

first due to its high activity. Thus, pH of local environment increases, and so does the $[Mg^{2+}]$. Without the presence of Al, such as pure Mg pigments used in Mg-rich primer, pH can increase until the precipitation of $MgCO_3$ and $Mg(OH)_2$ initiates. However, in the case of Mg alloy particles used as pigments in primer system, the passivation of Al breaks down when pH is higher than 8.6. According to Reaction 3 in Table 6-10, OH^- ions are consumed when $Al(OH)_3$ dissolves. Therefore, the presence of Al can buffer the pH of environment due to the equilibrium between $Al(OH)_3$ and AlO_2^-.

Mg alloy AM60 particles have Mg 95.5wt% and Al 4.5wt%. The identification of hydromagnesite as the only oxidation product indicates that its high Mg content resulted in an environment of high pH and high $[Mg^{2+}]$, at which the precipitation of $MgCO_3$ and $Mg(OH)_2$ occurs. The absence of Al oxidation product might be due to the formation of AlO_2^-, which could be washed out by electrolyte.

Mg alloy AZ91B contains 91.5wt% Mg and 8.5wt% Al. In the beginning of exposure of AZ91B primer, Mg is oxidized first which resulted in a similar local environment as AM60 primer. So, hydromagnesite was the major oxidation product of 715 hour exposure. But, during the further exposure, the higher Al content of AZ91B (8.5wt%) could reduce the pH to region 2, where $Mg(OH)_2$ dissolved and $Al(OH)_3$ precipitated. As a result, the final oxidation products of the exposed AZ91B primer at 1328 hour exposure were MgO, AlOOH and Al_2O_3, which were left by the thermal decomposition of $MgCO_3/Mg(OH)_2$ and the dehydration of $Al(OH)_3$, respectively.

LNR91 Mg alloy contains 50 wt% Mg and 50 wt% Al. The high Al content could buffer the pH of local environment as low as 8.6, where neither $MgCO_3$ nor $Mg(OH)_2$ could precipitate. Therefore, only AlOOH and Al_2O_3 dehydrated from $Al(OH)_3$ were

identified as the final corrosion products of the exposed LNR91 primer.

It must be pointed out that the above discussions regarding to the probable corrosion processes of different Mg alloy pigmented primers are mainly based on the information from several aspects: the identification of oxidation products, the properties of Mg alloy pigments, the condition of Prohesion chamber and the knowledge of the possible equilibrium reactions between some species, e.g. Mg^{2+}, Al^{3+}, AlO_2^-, $Mg(OH)_2$, $Al(OH)_3$, $MgCO_3$, H^+, OH^-, HCO_3^-, CO_3^{2-}. The actual oxidation processes of Mg alloy rich primers in Prohesion chamber could be much more complicate than what discussed above.

However, the simplified framework is given as one possibility to explain the impact of Al content on the formation of oxidation products. We only have the information of the final oxidation products to extrapolate the different corrosion mechanisms. Furthermore, the relationship between the oxidation processes and Al content of Mg alloy pigments can be roughly revealed, which is very useful for making the proper choice on future Mg alloy pigment selection.

6.4.5. Influences of oxidation products on corrosion protection performance

In galvanic coating systems, the oxidation products are the results of a series of electrochemical and chemical reactions through which the active particles embedded in primers interacting with the corrosive environment. However, the formed oxidation products can also affect the corrosive mechanism by changing the microstructure of primer system. For instance, it has been found that the outstanding corrosion protection performance of ZRP relies on two factors: the galvanic protection of Zn particles during the first stages and the excellent barrier protection provided by the oxidation products of Zn particles, such as zinc carbonate [32] and ZnO [33], which are believed to fill the voids to

enhance the barrier property of ZRP. It shows that the involvement of oxidation products and their interaction with the coating can influence the mechanisms of ZRP corrosion protection.

According to the results of the observed oxidation products of the exposed Mg alloy pigmented primers, in this section, the probable influences of the pigment oxidation products on the performance of Mg alloy primers will be briefly discussed below and compared with ZRP.

6.4.5.1. Conductivity of oxidation products

Effective cathodic protection requires that good electrical connection among metallic particles as well as between metallic particles and substrate should be maintained. Metallic particles of Mg, Al and Zn have very good electrical conductivity. However, when metallic particle is exposed to atmosphere, a thin oxidation layer, usually in the form of oxide or hydroxide, can grow over the surface of particle. The thickness, morphology, density and conductivity of the oxidation layer can be varied depending on the environment. In general, the conductivity of these oxidation products is poorer in comparison to the corresponding metal. It indicates that the overall conductivity between metallic particles will be reduced due to the formation of the oxidation products layer. In Table 6-11, the electrical resistivity of metallic Mg, Al, Zn and their oxidation products are listed.

In Table 6-11, it can be seen that dry MgO has a very high resistivity (1.3×10^{15} Ω•cm). From the previous work in our Lab, [34, 35] it has been found that there is a thin MgO layer with thickness of ~100 nm formed over the surface of Mg or Mg alloy pigment particles. It explains why dry Mg/Mg alloy particles or the dry Mg/Mg alloy-rich primers have the resistance larger than 10^6 Ω. However, when Mg/Mg alloy particles are in contact

with electrolyte, MgO can hydrolyze into $Mg(OH)_2$ because the latter one is more thermodynamically stable. [36-42] $Mg(OH)_2$ has a much less resistivity (3.45×10^{1} ~ 3.7×10^{2} Ω•cm) in comparison to MgO. Furthermore, as mentioned above, Cl^- ions presented in electrolyte can speed the breakdown the $MgO/Mg(OH)_2$ films due to the formation of more soluble $MgCl_2$. As a result, when Mg/Mg alloy-rich primer is wetted by electrolyte, the fresh Mg/Mg alloy surface can be exposed again because of the breakage of oxidation films and the relatively good conductivity between Mg/Mg alloy particles can be established. The experimental results from EIS and ENM showed that the impedances of Mg/Mg alloy-rich primers at low frequency were in the range of 10^{3}~10^{9} Ω.

Table 6-11. Electrical resistivity of several metals and possible oxidation products in metal-rich primer system. (At 20°C if not notified)

Metal/compound	Resistivity (Ω•cm)	Reference
Mg	4.39×10^{-6}	[43]
Zn	5.9×10^{-6}	[43]
Al	2.65×10^{-6}	[43]
MgO	1.3×10^{15}	[44]
$Mg(OH)_2$*	3.45×10^{1} ~ 3.7×10^{2}	[45]
Al_2O_3	$>1.0\times10^{15}$	[44]
ZnO	$1.4\sim2\times10^{-4}$	[46]

* brucite at 500 K.

Differently, dry ZnO has a resistivity of $1.4\sim2\times10^{-4}$ Ω•cm, which is only two orders of magnitude higher than metallic Zn. It suggests that the formation of ZnO will not significantly reduce the conductivity of ZRP. Some studies even revealed that the presence of a low percentage of ZnO, e.g. 18 to 27 wt%, actually can improve the cathodic protection. [47]

The passivative layer of Al_2O_3 has a very high resistivity. Also, it is insoluble unless

the pH of electrolyte is higher than 8.6. Therefore, physical removal of the dense Al_2O_3 layer from Al alloy substrate right before the application of primer is the most effective way to make the substrate have good conductivity with the metallic particles in primer system. On the other hand, since Mg alloy particles, e.g. AM60, AZ91B and LNR91, contain Al as the secondary element, the formation of $Al(OH)_3$ may reduce the conductivity between Mg alloy particles. However, the presence of Cl^- and alkaline environment will promote the fracture of Al passivating layer.

6.4.5.2. Solubility of oxidation products

The solubility of oxidation products also affects the conductivity of primer system and further the efficiency of cathodic protection. If the oxidation products of Mg alloy particles are soluble in electrolyte, the good electrical contact between Mg/Mg alloy particles may maintain due to the emergence of the fresh surface of Mg alloy particles. Table 6-12 lists the solubility of some inorganic compounds possibly present in Mg/Mg alloy rich primer during Prohesion exposure.

From Table 6-12, it can be seen that $MgCl_2$, $MgSO_4$ and $Al_2(SO_4)_3$ have high solubility, which may explain the absent of sulfate in the final oxidation products. Since the K_{sp} of $Mg(OH)_2$ is 5.6×10^{-12}, the equilibrium pH of $Mg(OH)_2$ solution is 10.4. When pH is lower than 10.4, Mg^{2+} is more stable in electrolyte and $Mg(OH)_2$ will dissolve. As mentioned before, the probably highest pH of the microenvironment in Mg alloy rich primer film is about 10. Thus, $Mg(OH)_2$ can dissolve under this condition. Also, $Al(OH)_3$ can dissolve when pH is lower than 5 or higher than 8.6. As the discussion in section 6.4.3, the increase of Al content in Mg alloy can cause pH to drop due to the consumption of OH^- by Al oxidation. Therefore, the high Al content cannot benefit the dissolution of $Al(OH)_3$ and

may retard the electrical connection between Mg alloy particles. Therefore, the formation of $Mg(OH)_2$ over Mg alloy particle surface may not affect the electrical conductivity because $Mg(OH)_2$ can dissolve in the environment of Prohesion chamber, especially with the presence of Cl^-. In contrast, the presence of $Al(OH)_3$ could influence electrical conductivity based on the instant local pH. In general, the low Al content in Mg alloy particles will benefit the dissolution of $Al(OH)_3$.

Table 6-12. Solubility of some inorganic compounds. (Data from CRC Handbook of Chemistry and Physics [43])

Formula	Solubility (Gram/ 100 g H_2O)	Qualitative Solubility
$MgSO_4$	35.7	
$Mg(OH)_2$	0.00069	soluble in dilute acid
$MgCl_2$	56.0	
$MgCO_3$	0.18	soluble in acid
MgO		slightly soluble in water
Al_2O_3		insoluble in water, slightly soluble in acid
$Al(OH)_3$		insoluble in water, soluble in alkaline and acid
$Al_2(SO_4)_3$	38.5	

6.5. Conclusions

By using SEM, EDX, XPS and confocal Raman microscopy, the oxidation products formed due to the exposure of three Mg alloy-rich primers in Prohesion chamber were determined. It was found that the composition of oxidation products were highly dependent on the Al content in the Mg alloy. The oxidation product of the 715 hours and 1328 hours exposed AM60 primer was hydromagnesite; the major oxidation product of AZ91B primer was hydromagnesite at 715 hours exposure stage and changed to be MgO, Al_2O_3 and AlOOH as the exposure time increased to 1328 hours; Al_2O_3 and AlOOH were the final

oxidation products for the exposed LNR91 primer. It is proposed that the variance of the oxidation products may be attributed to the different Al content in Mg alloy particles. When Mg content of Mg alloy was high, the oxidation of Mg was the major reaction which caused the formation of hydromagnesite in the presence of CO_2; with the increase of Al percentage in Mg alloy particles, more Al could be oxidized and meanwhile more OH^- ions were consumed. As a result, the pH of the local environment decreased to a region where the $Mg(OH)_2$ precipitate start to dissolve and $Al(OH)_3$ became stable. Thus, Al_2O_3 and AlOOH became the major corrosion products. The identification of oxidation products provides the necessary information to reveal the probable corrosion mechanisms based on the knowledge of the chemistry of Mg alloy particles and environment.

6.6. References

1 H. Marchebois, S. Joiret, C. Savall, J. Bernard and S. Touzain, *Surf. Coat. Technol.*, **2002**, 157, 151.

2 H. Marchebois, S. Touzain, S. Joiret, J. Bernard and C. Savall, *Prog. Org. Coat.*, **2002**, 45, 415.

3 S. Ardizzone, C. L. Bianchi, M. Fadoni and B. Vercelli, *Appl. Surf. Sci.*, **1997**, 119, 253.

4 D. K. Aswal, K. P. Muthe, S. Tawde, S. Chodhury, N. Bagkar, A. Singh, S. K. Gupta and J. V. Yakhmi, *J. Cryst. Growth*, **2002**, 236, 661.

5 S. Feliu, M. C. Merino, R. Arrabal, A. E. Coy and E. Matykina, *Surf. Interface Anal.*, **2009**, 41, 143.

6 M. Liu, S. Zanna, H. Ardelean, I. Frateur, P. Schmutz, G. L. Song, A. Atrens and P. Marcus, *Corrosion Science*, **2009**, 51, 1115.

7 H. B. Yao, Y. Li and A. T. S. Wee, *Appl. Surf. Sci.*, **2000**, 158, 112.

8 P. Dhamelincourt, *Raman Microscopy*, Handbook of Vibrational Spectroscopy, ed. J. M. Chalmers and P. R. Griffiths, Vol. 2, **2002**, Chichester, John Wiley & Sons.

9 L. Baia, K. Gigant, U. Posset, R. Petry, G. Schottner, W. Kiefer and J. Popp, *Vib. Spectrosc.*, **2002**, 29, 245.

10 K. E. Chike, M. L. Myrick, R. E. Lyon and S. M. Angel, *Appl. Spectrosc.*, **1993**, 47, 1631.

11 M. Claybourn, *Polym. Mater. Sci. Eng.*, **1994**, 71, 143.

12 N. Everall, *Spectroscopy*, **2004**, 19, 16.

13 N. Everall, *Spectroscopy*, **2004**, 19, 22.

14 D. Battocchi, A. Simoes, D. Tallman and G. Bierwagen, *Corrosion Science*, **2006**, 48, 1292.

15 S. G. Hong, *Polymer Degradation and Stability*, **1995**, 48, 211.

16 J. Moulder, W. Stickle and P. Sobol, *Handbook of X Ray Photoelectron Spectroscopy*, 1 ed, **1993**, Perkin-Elmer, Physical Electronics Division.

17 V. Fournier, P. Marcus and I. Olefjord, *Surface and Interface Analysis*, **2002**, 494.

18 D. Y. Zhang, Q. Y. Fei, H. M. Zhao, M. Geng, X. C. Zeng and P. K. Chu, *Thin Solid Films*, **2005**, 484, 215.

19 K. Nakamoto, *Infrared and Raman Spectra of Inorganic and Coordination Compounds*, in *Handbook of Vibrational Spectroscopy*, J. Chalmers and P. Griffiths, Editors, **2002**, John Wiley & Sons Ltd.

20 H. G. M. Edwards, S. E. J. Villar, J. Jehlicka and T. Munshi, *Spectrochim. Acta, Part A*, **2005**, 61A, 2273.

21 M. de Veij, P. Vandenabeele, T. De Beer, J. P. Remonc and L. Moens, *J. Raman Spectrosc.*, **2009**, 40, 297.

22 E. E. Coleyshaw, G. Crump and W. P. Griffith, *Spectrochim. Acta, Part A*, **2003**, 59A, 2231.

23 L. Hopkinson, K. Rutt and G. Cressey, *Journal of Geology*, **2008**, 116, 387.

24 A. K. Dua, V. C. George and R. P. Agarwala, *Thin Solid Films*, **1988**, 165, 163.

25 W. M. Mullins and B. L. Averbach, *Surface Science*, **1988**, 206, 29.

26 J. R. Lindsay, H. J. Rose, W. E. Swartz, P. H. Watts and K. A. Rayburn, *Applied Spectroscopy*, **1973**, 27, 1.

27 D. A. Jones, *Principles and prevention of corrosion*, **1996**, Prentice-Hall, Inc.

28 S. S. Pathak, *Corrosion science*, **2010**, in press.

29 F. H. Cao, V. H. Len, Z. Zhang and J. Q. Zhang, *Elektrokhimiya (Russian)*, **2007**, 43, 878.

30 R. Lindstrom, J. E. Svensson and L. G. Johansson, *J. Electrochem. Soc.*, **2002**, 149, B103.

31 M. R. Bothwell, in *The Corrosion of Light Metals*, H. P. Godard, Editor, **1967**, John Wiley and Sons, New York.

32 J. Krzywicki, *Fastener Technology International*, **2006**, August, 34.

33 R. N. Jagtap, P. P. Patil and S. Z. Hassan, *Prog. Org. Coat.*, **2008**, 63, 389.

34 G. Bierwagen, *J. Coat. Technol. Res.*, **2008**, 5, 133.

35 G. Bierwagen, R. Brown, D. Battocchi and S. Hayes, *Progress in Organic Coatings*, **2010**, 67, 195.

36 A. Pardo, M. C. Merino, A. E. Coy, R. Arrabal, F. Viejo and E. Matykina, *Corrosion Science*, **2008**, 50, 823.

37 A. Pardo, M. C. Merino, A. E. Coy, F. Viejo, R. Arrabal and S. Feliu, *Electrochim. Acta*, **2008**, 53, 7890.

38 M. C. Zhao, P. Schmutz, S. Brunner, M. Liu, G. L. Song and A. Atrens, *Corrosion Science*, **2009**, 51, 1277.

39 R. Lindstrom, L. Johansson and J. Svensson, *Materials and Corrosion*, **2003**, 54, 587.

40 S. Feliu, A. Pardo, M. C. Merino, A. E. Coy, F. Viejo and R. Arrabal, *Appl. Surf. Sci.*, **2009**, 255, 4102.

41 G. Song, A. Atrens, D. S. John, X. Wu and J. Nairn, *Corrosion Science*, **1997**, 39, 1981.

42 G. Song, A. Atrens, D. Stjohn, J. Nairn and Y. Li, *Corrosion Science*, **1997**, 39, 855.

43 D. Lide, ed. *CRC Handbook of Chemicstry and Physics*. 84th ed., **2003**, CRC Press, Boca Raton

44 *Electrical properties of materials*, in *CRC Maerial Science and Engineering Handbook*, J. F. Shackelfork and W. Alexander, Editors, **2001**, CRC Press, Boca Raton, FL.

45 K. Fuji-ta, T. Katsura, T. Matsuzaki and M. Ichiki, *Earth Planets Space*, **2007**, 59, 645.

46 K. Ellmer, *Journal of Physics D: Applied Physics*, **2001**, 34, 3097.

47 N. Fawcett, C. Stearns and B. Bufkin, *JCT Coatings Tech*, **1984**, 56, 49.

CHAPTER 7. SUMMARY AND CONCLUSION

This research work focused on the studies of a new metal-rich coating system by using Mg alloys as pigments for corrosion protection of aerospace Al alloy substrate, especially AA2024 T3. New Mg alloy rich primer systems were formulated with various Mg alloy particles dispersed in an epoxy-amide binder at PVCs near the critical pigment volume concentration (CPVC). Based on the new Mg alloy rich primer system, different studies have been carried out on three major formulation aspects: CPVC, electrochemical performance and oxidation products' characterization.

The CPVC study focused on the Mg alloy particles' characterization, the experimental determination of the CPVCs of new Mg alloy rich primer systems, e.g. electrochemical impedance spectroscopy (EIS) and fluorescence microscopy, the modification of a mathematic model proposed by Bierwagen (GPB model) for CPVC predication and experimental coarseness measurement.

Results showed that Mg alloy pigments, AM60, AZ91B and LNR91, were different in shape, size, particle size distribution and Oil absorption (OA). Moreover, the CPVCs of the three Mg alloy rich primer systems experimentally obtained were various from the corresponding predicted CPVC values through GPB model. By taking the influences of the irregular particle shapes of Mg alloy pigments into account, a modified mathematical model was proposed, through which the predicted CPVC values showed better agreement with the experimental CPVC values obtained by EIS and fluorescence microscopy. Furthermore, a practical method for experimental coarseness measurement was proposed for the first time. The experimental results obtained from AM60 primer films confirmed the presence of coarseness in coating film, and showed that coarseness was a function of PVC

and the onset of coarseness is 0.85 of Λ, which was theoretically predicted by Bierwagen ten years ago.

The electrochemical performance study of Mg alloy-rich primers was carried out by using different electrochemical methods, such as EIS and electrochemical noise method (ENM).

In the EIS study, five different Mg alloys, AM60, AZ91B, LNR91, AM503 and AZG, were used as pigment in Mg alloy-rich primers at two PVCs, 32% and 42%, giving 10 different Mg alloy rich primer systems in total. The samples representing different primer systems were exposed in Prohesion chamber and taken out for EIS measurement after certain exposure time. Three important parameters obtained from EIS tests, open circuit potential (OCP), impedance modulus at low frequency ($|Z|_{0.01Hz}$) and capacitance at high frequency ($|C|_{10^4Hz}$), were used to reflect the performance changes of Mg alloy rich primers.

The non-topcoated Mg alloy-rich primers of 42% PVC had the OCP values that were higher than the OCP of Mg but lower than the one of bare AA2024 T3. It indicated that all the Mg alloy rich primers exhibited cathodic protection for Al substrates. In addition, it was found that the changes of OCP with exposure time consisted of three stages. The first stage was characterized by a sharp increase of OCP with increasing exposure time between 0 and 250 hours. This behavior of a fast OCP change indicates the quick consumption of Mg alloy particles by the penetrating electrolyte when topcoat was not applied. After the first stage, the OCP tended to fluctuate in a range of about 0.25 V until up to 1200 hours of exposure. The fluctuation of OCP was probably caused by the oscillation of the surface area ratio of the activated Mg alloy particle to the exposed Al alloy substrate. The decrease of Mg to Al surface area ratio could be caused by the oxidation of Mg in Mg alloy particles

and the dissolution of the passivation layer of Al_2O_3; the increase of Mg to Al surface area ratio could be due to the exposure of fresh Mg after Mg oxidation dissolving. This stage also represented the timeframe of Mg alloy rich primer providing stable cathodic protection to Al alloy substrate. After 1200 hours, OCP continuously increased and finally approached to the OCP value of bare AA2024 T3, which implied the gradual loss of cathodic protection.

Mg alloy rich primers with 32% PVC also exhibited cathodic protection for Al alloy substrate because their mixed OCPs were located between the OCPs of Mg alloys and bare AA2024 T3. It indicated that the electrical connection between Mg alloy particles and between the primers and Al alloy substrate existed due to percolation even when PVC was below CPVC. Similar three-stage changes of OCPs were observed on 32% PVC Mg alloy rich primers, but with shorter first and second stages, since there were less Mg alloy particles available in the low PVC primers to provide cathodic protection.

The $|Z|_{0.01Hz}$ is related with the impedance of a coating film, such as the porous resistance R_{pore} and the polarization resistance R_p. The EIS results showed that the $|Z|_{0.01Hz}$ values of 42% PVC Mg alloy rich primers (non-topcoated) decreased with the increasing exposure time. It may be related to the drop of R_{pore} and R_p. Reducing of R_{pore} could be associated with the penetration of electrolyte into primer film, and the drop of R_p could be due to the increase of underfilm corrosion. Meanwhile, the $|C|_{10^4Hz}$ values of 42% Mg alloy rich primers were found increasing with exposure time, which indicated the water uptake of Mg alloy rich primer films increased with the longer exposure.

For the 32% PVC non-topcoated Mg alloy rich primers, the changes of $|Z|_{0.01Hz}$ and $|C|_{10^4Hz}$ with exposure time showed in a similar trend but at much slower rates. It suggested

that the Mg alloy rich primer films with low PVC exhibited better barrier properties due to their high polymer contents.

The EIS results of the topcoated Mg alloy rich primers confirmed that the practical coating system (Mg alloy rich primer + topcoat) provided effective cathodic protection for Al alloy substrates, as shown by the fact that the OCP values of each system were in the proper potential range for cathodic protection. The uses of topcoat over Mg alloy rich primers significantly increased the $|Z|_{0.01Hz}$ values of 42% PVC Mg alloy rich primers, and as a result, the barrier properties of Mg alloy rich primer systems were increased as expected, with the combination of topcoat.

ENM measurement, as a non-destructive technique, was also carried out on Mg alloy rich primer systems to obtain useful information of the electrochemical processes occurred. Noise signals of Mg alloy rich primer systems were collected based on a three-electrode configuration. A parameter of noise resistance, R_n, was used to evaluate the performance of primer films. Results showed that, for some samples, the value of R_n had big difference with the $|Z|_{0.1\ Hz}$ values. By analysis the PSD spectra obtained from ENM measurement on LNR91 primer system via fast Fourier transformation (FFT) and MEM, it was found that the noise signals carried a DC drift which might be due to the active nature of Mg alloy rich primer system. After data detrend treatment to remove the linear DC drift, the plot of $R_{sn}(f)$ showed good agreement with the plot of $|Z|(f)$ from EIS. Meanwhile, a new parameter $R_{sn}(0.1\ Hz)$ obtained from the $R_{sn}(f)$ plot exhibited high correlation with $|Z|_{0.1\ Hz}$ from EIS. This suggests that $R_{sn}(0.1\ Hz)$ can be used as a reliable parameter for monitoring the performance when ENM measurement was carried out on an active coating system.

The identification of the oxidation products of the exposed Mg alloy rich primers were

accomplished through various techniques, scanning electron microscope (SEM), energy dispersion X-ray spectroscopy (EDX), X-ray photoelectron spectroscopy (XPS) and confocal Raman microscopy. Results showed that various oxidation products were formed on the different Mg alloy rich primer system though all of them were exposed in Prohesion chamber. The major oxidation product of the 715 and 1328 hours exposure AM60 primer were hydromagnesite; the oxidation products of the exposed AZ91B primers at 715 and 1328 hours were hydromagnesite and a mixture of MgO, $Mg(OH)_2$, Al_2O_3 and AlOOH, respectively; for LNR91 Mg alloy-rich primer, the final oxidation products were Al_2O_3 and AlOOH. The different oxidation products indicated that different chemical reactions occurred to each Mg alloy rich primer mainly depending on the local pH. It was proposed that the different Al content of Mg alloy particles resulted in various pH of local environment due to some equilibriums present in electrolyte solution. The higher Al content of Mg alloy pigment may cause the lower pH of local environment and result in less precipitates of $MgCO_3$ and $Mg(OH)_2$ and more Al_2O_3. In addition, the results suggested that a high Al content, e.g. Al% near 50%, in Mg alloy pigment could hinder the good performance of cathodic protection.

In summary, the new Mg-rich primer systems have been formulated by using different Mg alloy particles as pigment in an epoxy-amide polymer system. CPVC studies provided a practical PVC window to ensure good contact between Mg alloy particles and also between the primer film and Al alloy substrate. The electrochemical testing results showed that all the Mg alloy rich primer systems, regardless of the types of Mg alloy particles, the PVC or with/without topcoat, exhibited cathodic protection for Al alloy substrates, as the pure Mg-rich primer does. Better performance of cathodic protection can be expected when

a Mg alloy rich primer system possesses a higher PVC, has the Mg alloy particles with less Al content and/or is combined with a topcoat. The initial work of using Mg alloy particles as pigment in Mg-rich primer system provided useful information of the influences of particle shape on CPVC, the effects of chemical composition of Mg alloy particles on the electrochemical behavior of Mg alloy primer and also on the oxidation products. This work is a good starting point for selecting the suitable Mg alloy particles among a large number of available Mg alloys and tuning the formulation of Mg-rich primer system to achieve the optimal performance of corrosion protection for Al alloy substrates.

CHAPTER 8. FUTURE WORK

Based on the information obtained from the research work of using Mg alloys as pigment in metal-rich coating system to provide corrosion protection for Al alloy substrates, the future work can be carried out on four aspects.

8.1. CPVC study

A modified mathematical model for CPVC predication has proposed in this work. The application of this new model in a more complicate pigmentation coating systems is necessary. For example, ZRP powder coating system uses a combination of spherical and flake Zn particles as pigments to compensate for the low PVC. [1-5] The mixing ratio of spherical/flakes Zn particles will significantly affect the particle packing and further CPVC. The application of this new model in ZRP powder coating system can help to predict the CPVC theoretically and to find the optimal mixing ratio without the massive bench work.

8.2. Coarseness study

A new method used to experimentally measure the coarseness of a pigmentation coating system has succeeded in this study. But more work needs to be done based on various coating systems to testify this method. As a practical application of coarseness in coating system, the relationship between the coarseness and the quality control of manufacturing should be studied. In general, the small and constant coarseness of a coating system means good quality control in manufacturing.

8.3. New Mg alloy particles

Although the five Mg alloy particles used in this study exhibited cathodic protection

for AA2024 T3 when being formulated in an epoxy-amide matrix, the study results showed that Al, the major alloying element in Mg alloy, could hinder cathodic protection due to the poor conductivity of Al_2O_3. The more promising Mg alloy particles for the Mg alloy rich primer system could be Mg/Zn alloys. Zn not only has the similar ability to reduce the local pH of local environment as Al, but also its major oxidation product, ZnO, possesses good electrical conductivity. [6] The improvement of Mg alloy rich primer system can focus on using Mg alloy particles with different Zn contents or the mixing Mg/Zn powders at various ratios. Other Mg alloys, such as Mg-Ce alloys and Mg-Ca alloys, can also be considered as the potential pigments for Mg alloy rich primer systems.

8.4. Characterization of oxidation products

The combination of several techniques, such as SEM, EDX, XPS and confocal Raman microscopy, has successfully characterized the oxidation products of the complicate Mg alloy rich primer systems and provided important information to the mechanism study. In the same way, these techniques can help the comparison between outdoor exposure and different accelerated weathering methods, such as salt spray, wet/dry cycling, and QUV. Generally, same oxidation products can always be formed if the corrosion mechanisms keep constant. Thus, by using SEM, EDX, XPS and confocal Raman microscopy to study the oxidation products formed after different exposure methods, the corrosion mechanisms of the different accelerated weathering methods can be compared to the natural exposure. [7, 8]

8.5. References

1 C. Giudice, J. Benitez and A. Pereyra, *J. Coat. Technol. Res.*, **2004**, 1, 291.

2 A. Kalendova, *Prog. Org. Coat.*, **2003**, 46, 324.

3 H. Marchebois, S. Joiret, C. Savall, J. Bernard and S. Touzain, *Surf. Coat. Technol.*, **2002**, 157, 151.

4 H. Marchebois, C. Savall, J. Bernard and S. Touzain, *Electrochim. Acta*, **2004**, 49, 2945.

5 H. Marchebois, S. Touzain, S. Joiret, J. Bernard and C. Savall, *Prog. Org. Coat.*, **2002**, 45, 415.

6 N. Fawcett, C. Stearns and B. Bufkin, *JCT Coatings Tech*, **1984**, 56, 49.

7 S. S. Pathak, *Corrosion science*, **2010**, in press.

8 S. S. Pathak, M. D. Blanton, S. K. Mendon and J. W. Rawlins, *Corrosion Science*, **2010**, 52, 1453.